Production, Characterization and Stability of Organic Solar Cell Devices

Gevorgyan, Suren; Krebs, Frederik C

Publication date:
2010

Document Version
Publisher's PDF, also known as Version of record

Production, Characterization and Stability of Organic Solar Cell Devices

Risø-PhD-Report

PhD Thesis

Suren Ashot Gevorgyan

Risø DTU
National Laboratory for Sustainable Energy

Production, Characterization and Stability of Polymer Solar Cell Devices

PhD Thesis

Suren Ashot Gevorgyan

Submitted: January 2010

Academic Advisor: Prof. Frederik C. Krebs
Solar Energy Program
Risø DTU National Laboratory for Sustainable Energy

Author: Suren Ashot Gevorgyan
Title: Production, Characterization and Stability of Organic Solar Cell Devices
Academic advisor: Prof. Frederik C. Krebs
Division: Solar Energy Program

Report number: Risø-PhD-55(EN)
Submitted: January 2010

ISBN 978-87-550-3798-4

Information Service Department
Risø National Laboratory for
Sustainable Energy
Technical University of Denmark
P.O.Box 49
DK-4000 Roskilde
Denmark
Telephone +45 46774005
bibl@risoe.dtu.dk
Fax +45 46774013
www.risoe.dtu.dk

Preface

The presented PhD project was carried out at Risø National Laboratory for Sustainable Energy, Denmark Technical University from January 2007 to January 2010 under supervision and guidance of Professor Frederik C. Krebs. The work was financed by the Danish Strategic Research Council (DSF). The project also involves 3 months of research carried out during my external stay at Eindhoven University of Technology, where I worked in the department of Molecular Science & Technology under supervision of Professor René A. J. Janssen.

Structure of the Report

The title of the thesis is rather general and involves a number of projects with broad variation of topics. The report is divided into 5 chapters. Chapter 1 is aimed for the reader barely familiar with the field. It gives a brief introduction to solar cells and particularly describes the structure and the operating principle of organic photovoltaic devices with the further discussion of issues and challenges to be met. Chapter 2 is discussing various designs for solar cells as well as demonstrating some techniques for processing the active layer in the device with the aim to find the optimal processing method that would assure the highest photovoltaic performance for the given material. While most of the results presented in Chapter 2 have been probably already shown by others, my purpose in this chapter is to demonstrate that when a new material is developed, it requires a large number of experiments and characterization studies for efficiently exploring the potential of the material in photovoltaic applications. Chapter 3 and 4 are presenting my main results, major parts of which have been published in articles that can be found attached at the end of this report. In particular, Chapter 3 presents a number of projects that involve studying and characterization of various materials including thermocleavable polymers as donor materials and metal oxides as buffer layers and studying of inverted devices. Chapter 4 is devoted to degradation studies of devices in different atmospheres and comparison of lifetimes of devices with various materials and structures. Chapter 5 presents the summary of the project and the future challenges. While all the presented projects succeeded in demonstrating the applicability of studied materials and structures in photovoltaic devices to certain extent, they still leave “plenty of room at the bottom” for further studies, since it was not possible to accomplish them within the time given for this project. It is my hope that the presented report will not be covered by dust lying on the shelves, but will initiate further research for developing efficient products.

Acknowledgments

Above all my deepest gratitude goes to Frederik C. Krebs for giving me the opportunity to carry out this project in his group and for his supervision and guidance along the project. I genuinely thank him for his continuous positive and encouraging attitude and I thank him for always being a great leader to look up to. I finally thank him for all the projects, tasks and challenges that have been given to me and that helped me increase significantly my knowledge in the field.

I sincerely thank Kristian O. Sylvester-Hvid and Mikkel Jørgensen for valuable scientific discussions and advices, for designing and software assistance and for always willingly helping me out with any scientific problems. Jan Alstrup and Torben Kjær are particularly thanked for their technical support. Without them this project would not go half through.

Nishit Shah is thanked for his contribution in some of the experiments while he was carrying out a short project in our group under my supervision for 2 months.

Frederik and Mikkel are greatly acknowledged for comments on my report. Contributions of Thomas Tromholt and Martin Petersen in translation of abstract are greatly appreciated.

I would like to stress my gratitude to our whole Solar Cell group at Risø DTU, particularly to: Frederik, Mikkel, Kristian, Kion, Jens, Torben, Thomas, Martin, Eve, Roar, Ole, Jan, Jon, Mette, Nikolas, Mathilde, AJ, Nishit, Morten for everything. It's been a real pleasure to experience their company and support both in working area and in social life. Torben is particularly thanked for shearing his views on economical aspects of the field.

Genuine thanks go to the administrative stuff of SOL department, particularly to the Group Leader Peter Sommer-Larsen, Secretary Bente Overgaard Schlichting, Ole Kristoffersen and Birgit Jensen. I would like to thank also Maria, Senior Scientist David Plackett, Istvan, Natanya, Nini, Vimal, Honghao, Luise and the rest of SOL department for creating a nice working environment full of cheerful and helpful people.

Danish Strategic Research Council (DSF) is acknowledged for financing the project.

I would like to thank also Denmark and Danish people, as living and working here for the last three years was one of the greatest experiences I ever had in my life.

My deepest gratitude goes to Professor René Janssen for giving me the opportunity to study in his group at Eindhoven University of Technology during my external stay. The experience I gained in Eindhoven was invaluable. Particularly I would like to thank René Janssen and Jan Gilot for fruitful scientific discussions and I would like to express my gratitude to the whole group of Molecular Science & Technology for making my stay unforgettable.

Finally, I would like to express my thankfulness to my family and all my friends for their love, support and friendship that helped me a lot during the last three years.

Abstract

Despite the fact that the field of organic photovoltaics (OPVs) is in a rapid progress, organic solar cells continue taking backstage roll in the growing markets of various solar technologies. The main challenge of the field is to develop devices that would possess all the optimal properties required for efficient, stable and cheap solar cells, i.e. devices that can deliver high photoconversion efficiencies and long lifetimes and can be efficiently produced in large scales using roll-to-roll coating technologies.

This dissertation is primarily devoted to the issues of photoconversion efficiency and device lifetimes. In particular, descriptions of some practical approaches for different device designs and processing of active layer for typical small scale OPV devices were presented. The emphasis was put on some optimizing techniques for processing of active layer that can significantly improve the device photoconversion efficiency. The techniques were further applied for manufacturing and characterization of solar cell devices based on various materials.

In particular, a number of thermocleavable polymers were studied and devices based on such materials were produced and characterized. The applicability of such materials in photovoltaic devices was shown and further challenges were discussed. Another task of this work was to manufacture and study inverted device structures and compare their properties with normal structure based devices. Device based on both structure were successfully produced with same level of performance in terms of photoconversion efficiency, yet with totally different stability performance. As another task, metal oxides, such as MoO_3 or V_2O_5 were studied in solar cell devices as buffer layers instead of PEDOT:PSS. Although the device efficiencies obtained with metal oxides were inferior to PEDOT based device, it was shown that such materials can possibly improve the device efficiency if the processing of the layers is optimized.

The final part of the work is devoted to the issue of stability. In particular, a setup comprising an atmospheric chamber was presented for efficient lifetime evaluation of OPV devices and examples of exploitation of the setup were shown. Lifetime studies of various thermocleavable polymers were carried out and compared to commonly used thiophene based polymers. Comparative degradation studies were carried out for normal and inverted device structures under different atmospheric conditions, which revealed different degrading features for different structures. While the normal geometry devices were rather stable in oxygen and rapidly degraded in

humid environment, the inverted devices showed strong degradation in oxygen, but stayed rather stable in high humidity.

Resumé

På trods af den hurtige udvikling af organiske solceller står denne teknologi stadig i baggrunden sammenlignet med andre solcelle teknologier. Den største udfordring inden for forskningsområdet består af at kunne udvikle organiske solceller som besidder alle de optimale egenskaber nødvendige for en effektiv, stabil samt billig solcelle – det vil sige solceller, der kan give effektiv omsætning af lysenergy til elektricitet, har lang levetid, og som er produceret i stor skala med rulle til rulle teknologi.

Denne afhandling er primært dedikeret til solcelle effektivitet og deres levetid. Der er lagt vægt på praktiske tilgangsvinkler til forskellige solcelledesigns og processering af fotoaktive lag for solceller med små arealer, som kan øge solcellernes effektivitet betydeligt. De udviklede teknikker anvendes desuden til fremstilling og karakterisering af solceller baseret på forskellige materialer.

Der er fokuseret på studier af solceller baseret på termokløvbare polymerer. Anvendelsen af disse materialer til solceller er blevet vist og de tilhørende udfordringer er diskuteret.

Desuden er der fokuseret på fremstilling og studie af solceller med inverterede lagstrukturer, hvor deres egenskaber sammenlignes med solceller baseret på normale lagstrukturer. Solceller baseret på begge strukturer opnåede samme effektivitet, hvorimod stabiliteten af solcellerne varierede. Desuden blev metaloxider, så som MoO_3 og V_2O_5 undersøgt i solceller som buffer lag i stedet for PEDOT:PSS. Selvom solcelle effektiviteter opnået med disse metaloxider var mindre end for PEDOT:PSS baserede solceller, blev det påvist at disse materialer muligvis kan forbedre effektiviteten hvis fremstillingen af lagene forbedres.

Den sidste del af denne afhandling er dedikeret til stabilitet af solcellerne. En opstilling bestående af et kammer med kontrol af atmosfæren til effektiv evaluering af solceller præsenteres og anvendelser af dette beskrives. Levetidsstudier af forskellige termokløvbare polymerer udførtes og sammenlignedes med de ofte anvendte thiophene-baserede polymerer. Nedbrydningsstudier udførtes for solceller med hhv. inverterede og normale lagstrukturer under forskellige atmosfæriske forhold. Dette afslørede forskellige nedbrydningsegenskaber for de forskellige lagstrukturer. Mens solceller med normale lagstrukturer var forholdsvist stabile i ilt og blev nedbrudt i vandig atmosfære, viste solceller med inverterede lagstrukturer sig at være forholdsvist stabile i vandig atmosfære mens de blev nedbrudt i ilt.

Table of Contents

1 Introduction

1.1 Solar Energy

When the global warming and depletion of common energy supplies, such as fossil fuels started threatening the balance of human life, great attention was driven towards the renewable (alternative) energy sources. Among number of alternative sources, such as wind energy, hydroelectric energy, biomass and geothermal energy, solar energy has the highest amount potentially available on earth. A very small fraction of sun power (less than 0.02 %) reaching the earth surface can cover the whole energy demand of the world. Yet, by the end of year 2008, solar technology based sources have been providing only 0.1 % of all the energy consumed by man according to *Renewable Energy Policy Network (REN21)* report.[1]

There are various solar technologies for harvesting the sun energy, which can be divided to two categories: passive solar and active solar. An example of passive technique can be the designing of a building in such a way that it efficiently harvests and stores the sun energy in the building. Active solar technologies are the solar thermal collectors or photovoltaic (PV) devices. However, the fastest and most efficient direct conversion of sun light into electrical energy is possible only through photovoltaic devices. The photovoltaic (PV) effect discovered by Becquerel[2,3] is the basic physical process, by which the semiconductor material converts electromagnetic radiation (sun light) into electric power.

While our environment is surrounded with abundant solar power, the PV technology is still too expensive to become a primary energy source. Therefore, the main task of the solar cell field is to develop a technology, which can provide cheap PV products and make the photoconversion of sun light into electrical power cost efficient.

1.2 Solar Cell Generations

So far photovoltaic devices (solar cells) have been categorized in three generations according to the time sequence they started playing big role in the solar cell field.[4]

The first generation (1G) solar cells are large scale, single junction devices. Most of the production is based on silicon wafers including single crystal and multi-crystalline silicon. About

90 % of the current photovoltaic production is based on first generation. The efficiency of the single junction cells has a theoretical limit of about 30% (the *Shockley–Queisser* limit)[5,6] and currently the common silicon wafer based devices show nearly 20% efficiency with the highest reported efficiencies reaching 25%.[7] Yet, the cost per produced 1 Watt of power is nearly 4 times higher than conventional energy prices due to the high cost of the material (half of the cost of 1G devices is the silicon wafer) and cost of production technologies. Although, the price continuously goes down along with the progress of the technology, the 1G products will probably reach their price limit before achieving the competitive level in the market.

The second generation (2G) solar cells are addressing the cost issue and the primary task is to decrease the amount of expensive material used in the production process while keeping the efficiency of the device high. The foremost approach is producing thin film solar cells on low cost substrates (such as glass). Different techniques are utilized for production process such as solution deposition, vapor deposition, electroplating and etc. Most successful materials for 2G are amorphous silicon, CuIn(Ga)Se2 (CIGS), CdTe/CdS, which are being deposited on thin substrates. Devices based on these materials can deliver lab efficiencies up to 19 %, but the module efficiencies are reaching only 14 % due to difficulties in producing large scale uniform films.[7] Although thin film technology can significantly decrease the prices for PVs, 2G solar cells will also hit certain price limits per watt due to efficiency limits and the material costs.

The third generation (3G): The alternative way to get the cost down is to increase the efficiency by multiple stacking of solar cells. 3G solar cells introduce the idea of multi junction solar cells, which can significantly increase the devise efficiency via improvement in harvesting of photons and even overcome the theoretical limit of 30 %. Currently the highest efficiencies reported for multijunction solar cells are over 33 %.[7]

In addition, 3G utilizes completely new concepts in terms of device architectures and materials. As an example, two atypical approaches of photovoltaics are Dye – Sensitized Solar Cells (DSSCs)[8,9] and Organic Solar Cells (OSCs). DSSCs are based on combination of dyes with metal oxides and electrolyte. The efficiencies of DSSC are in the range of 12 % for small lab scale devices, while the lifetime of the devices is rather low compared to inorganic solar cells.

Anthracene was the first organic compound in which photoconductivity have been observed by Pochettino in 1906[10] and which started a new era for studying organic compounds for electronic applications. Especially in the last decade the field of organic photovoltaics (OPVs) has been

growing really fast and showing promising potential for rather cheap PV technology. For that reason, in recent years OPVs became one of the most fascinating fields of research.

1.3 Organic Solar Cells

"Our children will enjoy in their homes electrical energy too cheap to meter" (Lewis Lichtenstein Strauss, 1954). Although, the words referred to atomic energy, nowadays one could certainly ascribe the quote to solar energy due to promising progress in area of organic photovoltaics, which focuses on production of a technology that has considerable lower cost potential. There are a number of reasons that generated the big interest towards OPVs: polymers allow fast, simple, low cost and large volume processing, since polymers have the opportunity to be solution processed, which literally means printing solar cells on roll-to-roll (R2R) machinery like news papers. Typical organic solar cell devices have a layered structure and are commonly considered organic if the active absorbing layer comprises only organic materials, while for other layers (for example electrodes) metals and other inorganic materials can be used. Often the OPV field includes a category of hybrid solar cells, in which the active layer contains some inorganic quantum dots doped into the polymer matrix[11,12] or inorganic metal oxides combined with polymers.[13-15] The reader can find useful the review of Pedro Gomez-Romero, who presents different classifications of hybrid materials for applications in electronics.[16]

There have been a number of reviews discussing the development of OPVs nicely presenting the key events throughout the short history of the OPV field.[17-24] Although polymer solar cells are developing really fast, there are three main issues that are still remaining unsolved: the improvement of device photoconversion efficiency (PCE),[24] extension of device lifetimes[25] and large scale production.[26,27] There are a number of loss mechanisms that result in low PCEs and currently most of the groups in the field are struggling to overcome these mechanisms to improve the efficiency. More and more groups are addressing the stability issue and various approaches are reported for improvement of the device lifetimes. Yet, the improvements are minor and further studies are needed. Moreover, the experiments show that when a good polymer is developed and the small model devices based on such polymer deliver high efficiencies, it is still a big practical challenge to transfer the device structure to R2R process for large scale production.

1.4 Device Architecture and Operational Mechanism

The main criteria that distinguishes the working principle of the organic PVs from inorganic PVs is that upon absorption of a photon by inorganic material free charge carriers are created, while in the case of organic material an excited pair or so-called "exciton" is generated, from which charge carriers still need to be dissociated.[28]

The mechanism by which the light is converted to electric power in OPVs consists of 4 basic steps (Figure 1.1): 1) The photon is absorbed by the active material, which promotes the electron to the lowest unoccupied molecular orbital (LUMO), while leaving the positive charge carrier or so-called "hole" in the highest occupied molecular orbital (HOMO). The exited pair is still bounded by coulomb attraction forces forming an exciton; 2) The exciton diffuses to the interface of the donor and acceptor; 3) The exciton is dissociated into free carriers at the interface between donor and acceptor and 4) Finally the free carriers are being transported and collected at the opposite electrodes.

Each of the steps is crucial for the efficient power generation and there are many loss mechanisms involved in this sequence. The terms donor and acceptor refer to materials with either high ionization potential (donor) or high electron affinity (acceptor). The free charge collection at opposite electrodes is assured by the asymmetric ionization energy or work function of the electrodes.

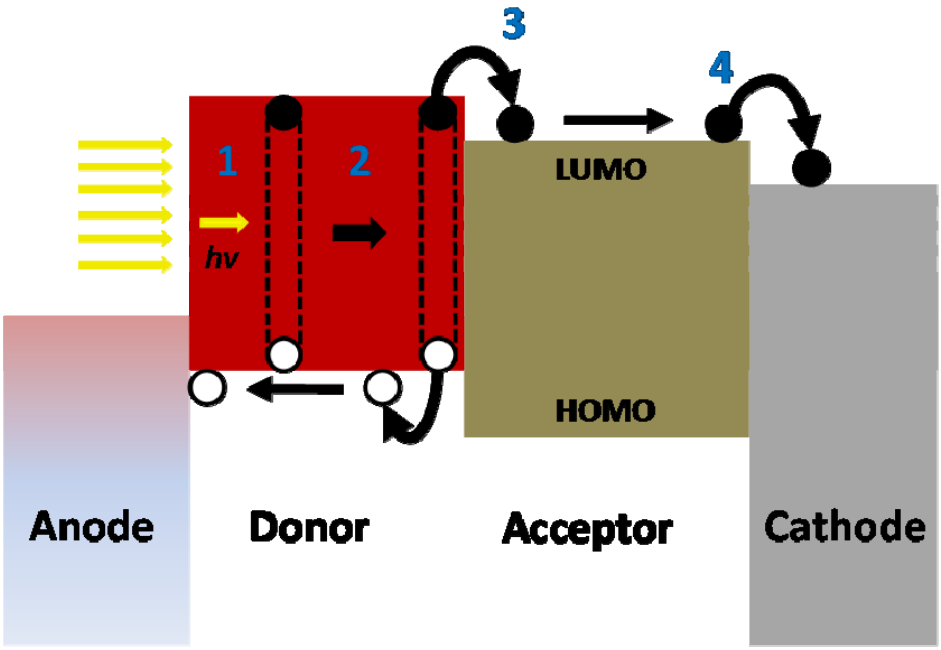

Figure 1.1: Schematic illustration of the photoelectric conversion mechanism

An important parameter of the absorbing material is its optical bandgap, which is defined by the difference of HOMO and LUMO. One of the main losses in the efficiency of OPVs is the poor matching of the absorption spectrum of the polymer with the solar emission spectrum. As an example, the band gap of commonly used poly(3-hexylthiophene) P3HT is around 1.9 eV, limiting the absorbance to wavelengths below 650 nm. Since the photon flux reaching the surface of earth from the sun has a maximum of approximately 1.8 eV (700 nm) P3HT is only able to harvest up to 22.4% of the available solar photons.[29-31]

In order to increase the efficiency of OPVs to their optimal value the band gap of the polymer has to be tuned to the light spectrum in the way that it collects the highest number of photons possible. While tuning the band gap one has to take into account also the alignment of the bands of donor and acceptor to ensure charge separation. The offset of LUMO levels between the two materials needs to be at least few hundred meV in order to efficiently separate the excitons to free carriers.[32,33] Often this offset is called exciton binding energy. The voltage of the device is theoretically defined by the difference of donor HOMO and acceptor LUMO, while the number of absorbed photons and consequently the current is defined by the lowest band gap of two materials. If commonly used derivative of fullerene C_{60}, phenyl-C_{61}-butyric acid methyl ester (PCBM) is considered as the acceptor then the optimum band gap of the polymer has to be in the range of 1.2-1.7 eV as was estimated by Dennler *et al*.[24]

The common structure of the organic solar cells is comprised of a stack of layers. Usually the active layer which is a combination of donor and acceptor materials is sandwiched between two electrodes. One of the electrodes needs to be transparent for illumination of the cell. In some cases certain buffer layers are being applied between the electrodes and the active layer to ensure charge selective transport. Figure 1.2 shows typical device architecture for OPVs. Excitons have a very short life time and the distance they can cross before recombination (Diffusion length) in several different conjugated polymers has subsequently been measured to be 4–20 nm.[34-36] Therefore, after the generation of an exciton it has to be separated to free charges very fast before recombination takes place.

The active layer can be designed in three different ways shown on the right hand side of Figure 1.2. It can be 1) a single layer, 2) double layer (bilayer heterojunction) or 3) bulk heterojunction (mixture of donor and acceptor in a bulk). The first OPVs were based on a single layer structure, where the excitons are separated into free charges at the interface between the active layer and the

electrode.[37-39] The separation of charges however is very inefficient in this concept. The efficiencies severely increased after the introduction of donor/acceptor bilayer structure, where the donor and acceptor layers are brought together forming a heterojunction.[40] However, only the excitons generated within the distance of the diffusion length from the interface can successfully diffuse to the interface and be separated to free carriers. Therefore, only the light absorbed by a very thin layer next to the interface can contribute to the photocurrent, while the rest is lost due to recombination processes. For that reason the photocurrent delivered by these devices is quite low. The breakthrough came with the idea of bulk heterojunction, where the donor and acceptor materials are mixed in a bulk forming nanoscale morphology.[41-43] In that way the interface is distributed throughout the whole active layer providing more efficient charge separation.

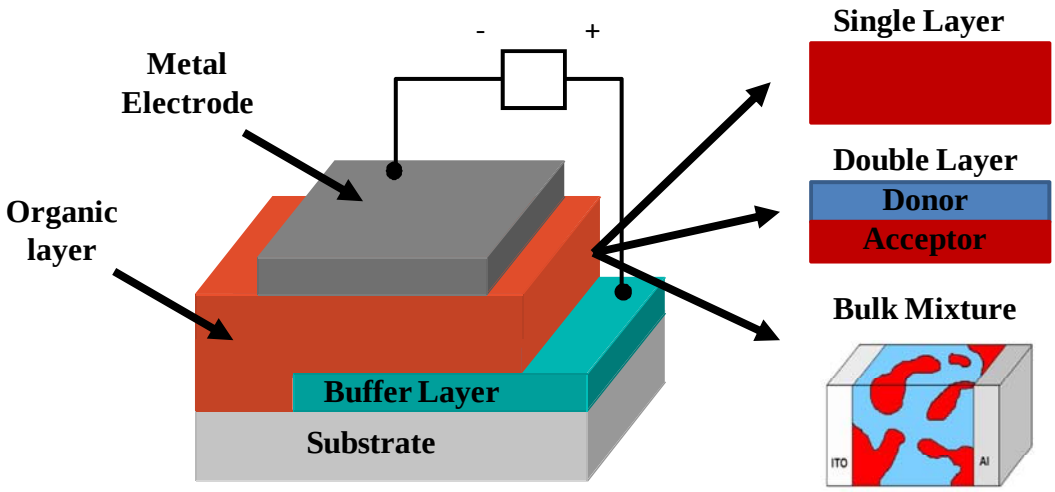

Figure 1.2: Device structure of a polymer solar cell. Three different designs of active layer are shown on the right hand side.

The solar cell in the dark acts as a simple diode. The equal electric circuit that approximates the organic solar cell performance is shown in Figure 1.3.[44] It is comprised of 1) A diode with ideality factor n and saturation current I_0 (current in the dark at the reverse bias), 2) A source to provide current that corresponds to photocurrent I_L generated during illumination, 3) R_s series resistance, which takes into account all the resistance at interfaces in the layers, the conductivity of the semiconductors and the electrodes, 4) Shunt resistance R_{sh}, which takes into account the leakage of the current through the shunts due to the defects in the films. For good performance of the device R_s needs to be low and R_{sh} has to have high values.

Figure 1.4 shows the current voltage characteristics (IV curves) for a typical solar cell. When light is shined on the device the IV curve of the cell becomes a superposition of the dark IV with the light generated current and the curve is shifted down to the 4th quadrant. The right hand side of Figure 1.4 presents the 4th quadrant of the IV curve, which shows the part where the actual power is being produced by the cell during the illumination. The figure also shows the key parameters that define the performance of the cell, which are the open circuit voltage V_{oc}, short circuit current I_{sc}, fill factor *FF*, the maximum power P_{max}, the voltage and the current at max power point V_{max} and I_{max}.

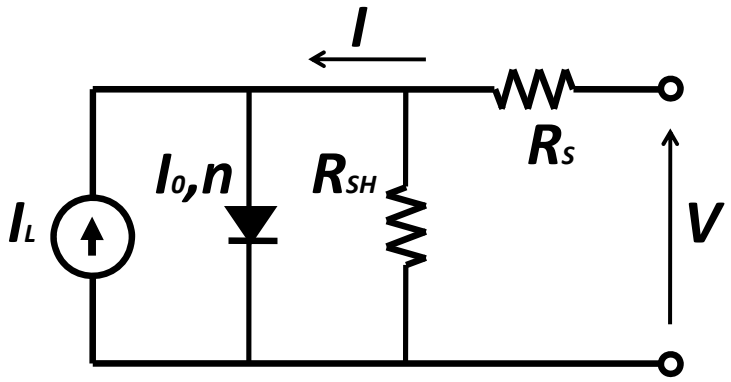

Figure 1.3: Electric circuit that approximates the operation principle of OPV device

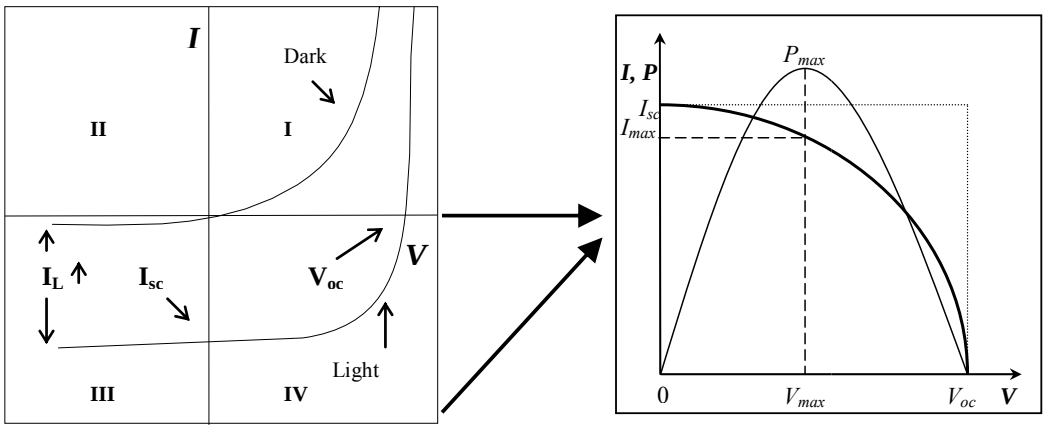

Figure 1.4: Dark and light IV characteristics of OPV device (left) and the inverted and enlarged 4th quadrant with additional power curve (right).

The following expression defines the current for the circuit:[45]

$$I = I_0\left(exp\left[\frac{e(V - IR_S)}{nkT}\right] - 1\right) + \frac{V - IR_S}{R_{Sh}} - I_L \qquad [1.1]$$

where e is the elementary charge, kT the thermal energy. From this equation V_{oc} and I_{sc} can be obtained by placing 0 values for I and V respectively (see eq. [1.2] and [1.3]). For the approximation on right hand side of the equations below it is considered that R_s is very small and R_{sh} is very big:

$$I_{sc} = I_0\left(exp\left[\frac{eI_{sc}R_S}{nkT}\right] - 1\right) - \frac{I_{sc}R_S}{R_{Sh}} - I_L \approx I_L \qquad [1.2]$$

$$V_{oc} = \frac{nkT}{e} ln\left[1 + \frac{I_L}{I_0}\left(1 - \frac{V_{oc}}{I_L R_{sh}}\right)\right] \approx \frac{nkT}{e} ln\left[1 + \frac{I_L}{I_0}\right] \qquad [1.3]$$

The power of the energy produced by the solar cell is defined by the product of the current and voltage and the maximum power will correspond to the maximum product of $I_{max} \times V_{max}$. Equation [1.4] below is the basic equation that defines the power conversion efficiency (PCE) η of the solar cell, which shows the ratio between maximum electric power produced by the cell and the power of the incident light on the cell with given active area of A:

$$\eta = \frac{I_{max}V_{max}}{P_{in}A} = FF\frac{I_{sc}V_{oc}}{P_{in}A} \qquad [1.4]$$

where fill factor (FF) is defined as:

$$FF = \frac{I_{max}V_{max}}{I_{sc}V_{oc}} \qquad [1.5]$$

Fill Factor FF is a relative measure of how much power is produced by the cell with given I_{sc} and V_{oc} in practice compared to the theoretically possible value. FF is significantly affected by parasitic resistances R_s and R_{sh}. Typically, good operating organic solar cell delivers FF values in a range of 60 – 65 %.

Another important quantity that defines the quality of energy conversion is the quantum efficiency (QE) of a solar cell. QE defines the number of charge carriers collected at the electrodes per number of incident photons on the solar cell area at a given wavelength. If every incident

photon results in one collected charge carrier then the QE is equal to unity (no recombination losses). There are two ways of defining the QE:

External Quantum Efficiency (EQE) or often called Incident Photon to Charge Carrier Efficiency (IPCE) is the ratio between number of collected carriers and number of all **incident** photons on the cell at a given wavelength.

Internal Quantum Efficiency (IQE) is the ratio between number of collected carriers and number of all **absorbed** photons by the active layer of the device at a given wavelength (IQE does not take into consideration the light transmitted through and reflected from the cell as well as the light collected by the other layers that do not contribute in photoconversion process).

1.5 Current State of the Art and Challenges of OPVs

Currently the world record PCE report is held by a new established company called *Solarmer Energy, Inc* and their latest reported PCE is 7.9 % for small cell device (certified by NREL), while for the large solar panel they have 3.9 % efficiency reported.[46]

Although, the numbers are modest compared to inorganic solar cells, OPVs are already applicable for different niche markets (see for example [47]). However, in order to compete with their inorganic counterparts not only in small product niche markets, but also in applications such as Building Integrated PVs (BIPV), OPVs have to perform at higher efficiency levels. The current challenge of the OPV field is to develop new donor and acceptor materials with better band gap alignment.[24] In addition, the improvement of the transport properties of the materials through better control of the morphology can significantly reduce the recombination losses.[48]

It is difficult to establish the current "state of the art" lifetimes of OPV devices, because the behavior of the devices varies from one cell type to another[49-51] and it is not an easy task to develop a standard measuring technique for evaluation of the lifetime.[25] OPVs are quite sensitive towards the surrounding environment (temperature, humidity, mechanical stress, light intensity) and probably the most reliable test that has been reported so far is the outdoor testing of the cells (see for example in the literature[50,52]). *Konarka Technologies, inc*, which is one of the leading companies in this field, proved that their devices could keep almost the same performance after 1 year of exposure to real outdoor conditions and sunlight.[52] The same company claims up to 3 to 5 years of stability for their products. There is an intensive research going on in the direction of developing different protecting techniques for OPVs and many different encapsulation and buffer

layer methods have been reported.[53-57] However, production of stable and at the same time flexible devices that will have lifetimes of a few years still remains as a challenging task.

Although a vast number of groups have reported high efficiencies for OPVs, all the reports are based on devices with small sizes (≤ 1 cm^2 of active area). When one attempts to increase the size of the cell the efficiency drastically decreases due to sheet resistance and increased amount of defects in the film. There are a very limited number of groups/companies that are capable of producing large scale OPVs with reasonable efficiencies and even fewer groups/companies use roll to roll techniques for production. In order to make the OPV technology cost efficient the processing needs to be cheap, fast and in large scales. Therefore, one of the primary goals of the OPV field is to develop efficient techniques for transferring the technology from small lab scale to large R2R production without any significant loss in efficiency.

The challenges presented above were the main reasons that generated the motivation for this project.

1.6 Project Goals

The title of the dissertation is rather broad and comprises a number of different tasks that have been accomplished during the project. The work is based on results, most of which have been published in 11 different articles attached as appendixes at the end of the report. The articles contain projects of different character and in some cases it is difficult to link them to each other. However, the attempt to group them in different sections led to generation of three chapters that are presented after the introduction (chapters 2 – 4). In particular, chapter 2 discusses the materials and the processing techniques that have been used for manufacturing OPVs throughout this work. Chapter 3 presents a number of small projects that involve characterization of various OPV devices and chapter 4 discusses the stability/degradation issue by presenting some experiments that have been carried out in that regard.

Four general goals have been extracted from the chapters that describe the aim of the presented work:

I. One of the primary tasks was to learn techniques for manufacturing OPV devices and further optimize them for fast and efficient characterization of organic solar cell devices based on various materials and structures.

II. Further tasks involved production of OPV devices based on various polymers, such as different kinds of P3HT materials as well as newly established thermocleavable polymers.

III. Other tasks involved studies of different materials for other layers in the devices structure, e.g. different metal oxide layers as buffer layers as well as various materials as front and back electrodes.

IV. Another important task was to establish efficient lifetime measuring methods for evaluating lifetimes of various devices. It also involved the detailed studies of degradation effect of devices with various materials stored in different conditions.

Reference List

1. http://www.ren21.net/globalstatusreport/g2009.asp
2. A. E. Becquerel, *Comptes Rendus De L'Académie Des Sciences*, 1839, **9**, 145.
3. A. E. Becquerel, *Comptes Rendus De L'Académie Des Sciences*, 1839, **9**, 561.
4. D. M. Bagnall and M. Boreland, Photovoltaic technologies, *Energy Policy*, 2008, **36**, 4390-4396.
5. W. Shockley and H. J. Queisser, Detailed Balance Limit of Efficiency of P-N Junction Solar Cells, *J.Appl.Phys.*, 1961, **32**, 510-519.
6. M. C. Hanna and A. J. Nozik, Solar conversion efficiency of photovoltaic and photoelectrolysis cells with carrier multiplication absorbers, *J.Appl.Phys.*, 2006, **100**, 074510.
7. M. A. Green, K. Emery, Y. Hishikawa, and W. Warta, Solar Cell Efficiency Tables (Version 34), *Prog.Photovolt: Res.Appl.*, 2009, **17**, 320-326.
8. M. Gratzel, Photoelectrochemical cells, *Nature*, 15-11-2001, **414**, 338-344.
9. M. K. Nazeeruddin, A. Kay, I. Rodicio, R. Humphry-Baker, E. Mueller, P. Liska, N. Vlachopoulos, and M. Graetzel, Conversion of light to electricity by cis-X2bis(2,2'-bipyridyl-4,4'-dicarboxylate)ruthenium(II) charge-transfer sensitizers (X = Cl-, Br-, I-, CN-, and SCN-) on nanocrystalline titanium dioxide electrodes, *J.Am.Chem.Soc.*, 1-5-2002, **115**, 6382-6390.
10. A Pochettino, *Acad.Lincei Rend.*, 1906, **15**, 355.
11. W. U. Huynh, J. J. Dittmer, and A. P. Alivisatos, Hybrid Nanorod-Polymer Solar Cells, *Science*, 29-3-2002, **295**, 2425-2427.
12. D. J. Milliron, I. Gur, and A. P. Alivisatos, Hybrid organic - Nanocrystal solar cells, *Mrs Bulletin*, 2005, **30**, 41-44.
13. A. Petrella, M. Tamborra, M. L. Curri, P. Cosma, M. Striccoli, P. D. Cozzoli, and A. Agostiano, Colloidal TiO2 nanocrystals/MEH-PPV nanocomposites: Photo(electro)chemical study, *Journal of Physical Chemistry B*, 3-2-2005, **109**, 1554-1562.
14. K. M. Coakley, Y. X. Liu, M. D. McGehee, K. L. Frindell, and G. D. Stucky, Infiltrating semiconducting polymers into self-assembled mesoporous titania films for photovoltaic applications, *Adv.Func.Mater.*, 2003, **13**, 301-306.
15. A. C. Arango, L. R. Johnson, V. N. Bliznyuk, Z. Schlesinger, S. A. Carter, and H. H. Horhold, Efficient titanium oxide/conjugated polymer photovoltaics for solar energy conversion, *Adv.Mater.*, 16-11-2000, **12**, 1689-1692.

16. P. Gomez-Romero, Hybrid organic-inorganic materials - In search of synergic activity, *Adv.Mater.*, 5-2-2001, **13**, 163-174.

17. C. J. Brabec, N. S. Sariciftci, and J. C. Hummelen, Plastic solar cells, *Adv.Func.Mater.*, 2001, **11**, 15-26.

18. J. Nelson, Organic photovoltaic films, *Current Opinion in Solid State & Materials Science*, 2002, **6**, 87-95.

19. H. Spanggaard and F. C. Krebs, A brief history of the development of organic and polymeric photovoltaics, *Sol.Energy Mater.Sol.Cells*, 15-6-2004, **83**, 125-146.

20. K. M. Coakley and M. D. McGehee, Conjugated polymer photovoltaic cells, *Chem.Mater.*, 16-11-2004, **16**, 4533-4542.

21. S. Gunes, H. Neugebauer, and N. S. Sariciftci, Conjugated polymer-based organic solar cells, *Chemical Reviews*, 2007, **107**, 1324-1338.

22. B. C. Thompson and J. M. J. Frechet, Organic photovoltaics - Polymer-fullerene composite solar cells, *Angew.Chem.- Int.Ed.*, 2008, **47**, 58-77.

23. B. Kippelen and J. L. Bredas, Organic photovoltaics, *Energy & Env.Sci.*, 2009, **2**, 251-261.

24. G. Dennler, M. C. Scharber, and C. J. Brabec, Polymer-Fullerene Bulk-Heterojunction Solar Cells, *Adv.Mater.*, 6-4-2009, **21**, 1323-1338.

25. M. Jørgensen, K. Norrman, and F. C. Krebs, Stability/degradation of polymer solar cells, *Sol.Energy Mater.Sol.Cells*, 2008, **92**, 686-714.

26. F. C. Krebs, Fabrication and processing of polymer solar cells: A review of printing and coating techniques, *Sol.Energy Mater.Sol.Cells*, 2009, **93**, 394-412.

27. C. J. Brabec and J. R. Durrant, Solution-processed organic solar cells, *Mrs Bulletin*, 2008, **33**, 670-675.

28. B. A. Gregg and M. C. Hanna, Comparing organic to inorganic photovoltaic cells: Theory, experiment, and simulation, *J.Appl.Phys.*, 15-3-2003, **93**, 3605-3614.

29. E. Bundgaard and F. C. Krebs, Low band gap polymers for organic photovoltaics, *Sol.Energy Mater.Sol.Cells*, 2007, **91**, 954-985.

30. R. Kroon, M. Lenes, J. C. Hummelen, P. W. M. Blom, and B. De Boer, Small bandgap polymers for organic solar cells (polymer material development in the last 5 years), *Polym.Rev.*, 2008, **48**, 531-582.

31. G. P. Smestad, F. C. Krebs, C. M. Lampert, C. G. Granqvist, K. L. Chopra, X. Mathew, and H. Takakura, Reporting solar cell efficiencies in solar energy materials and solar cells, *Sol.Energy Mater.Sol.Cells*, 2008, **92**, 371-373.

32. M. C. Scharber, D. Wuhlbacher, M. Koppe, P. Denk, C. Waldauf, A. J. Heeger, and C. L. Brabec, Design rules for donors in bulk-heterojunction solar cells - Towards 10 % energy-conversion efficiency, *Adv.Mater.*, 17-3-2006, **18**, 789-794.

33. J. L. Bredas, D. Beljonne, V. Coropceanu, and J. Cornil, Charge-transfer and energy-transfer processes in pi-conjugated oligomers and polymers: A molecular picture, *Chemical Reviews*, 2004, **104**, 4971-5003.

34. J. J. M. Halls, K. Pichler, R. H. Friend, S. C. Moratti, and A. B. Holmes, Exciton diffusion and dissociation in a poly(p-phenylenevinylene)/C-60 heterojunction photovoltaic cell, *Appl.Phys.Lett.*, 27-5-1996, **68**, 3120-3122.

35. L. A. A. Pettersson, L. S. Roman, and O. Inganas, Modeling photocurrent action spectra of photovoltaic devices based on organic thin films, *J.Appl.Phys.*, 1-7-1999, **86**, 487-496.

36. M. Theander, A. Yartsev, D. Zigmantas, V. Sundstrom, W. Mammo, M. R. Andersson, and O. Inganas, Photoluminescence quenching at a polythiophene/C-60 heterojunction, *Physical Review B*, 15-5-2000, **61**, 12957-12963.

37. G. A. Chamberlain, Organic Solar-Cells - A Review, *Solar Cells*, 1983, **8**, 47-83.

38. D. Wohrle and D. Meissner, Organic Solar-Cells, *Adv.Mater.*, 1991, **3**, 129-138.

39. R. N. Marks, J. J. M. Halls, D. D. C. Bradley, R. H. Friend, and A. B. Holmes, The Photovoltaic Response in Poly(P-Phenylene Vinylene) Thin-Film Devices, *Journal of Physics-Condensed Matter*, 14-2-1994, **6**, 1379-1394.

40. C. W. Tang, 2-Layer Organic Photovoltaic Cell, *Appl.Phys.Lett.*, 13-1-1986, **48**, 183-185.

41. J. J. M. Halls, C. A. Walsh, N. C. Greenham, E. A. Marseglia, R. H. Friend, S. C. Moratti, and A. B. Holmes, Efficient Photodiodes from Interpenetrating Polymer Networks, *Nature*, 1995, **376**, 498-500.

42. G. Yu and A. J. Heeger, Charge Separation and Photovoltaic Conversion in Polymer Composites with Internal Donor-Acceptor Heterojunctions, *J.Appl.Phys.*, 1995, **78**, 4510-4515.

43. G. Yu, J. Gao, J. C. Hummelen, F. Wudl, and A. J. Heeger, Polymer Photovoltaic Cells - Enhanced Efficiencies Via A Network of Internal Donor-Acceptor Heterojunctions, *Science*, 1995, **270**, 1789-1791.

44. H. Hoppe and N. S. Sariciftci, Organic solar cells: An overview, *Journal of Materials Research*, 2004, **19**, 1924-1945.

45. C. Waldauf, M. C. Scharber, P. Schilinsky, J. A. Hauch, and C. J. Brabec, Physics of organic bulk heterojunction devices for photovoltaic applications, *J.Appl.Phys.*, 15-5-2006, **99**, 104503.

46. http://www.solarmer.com/

47. F. C. Krebs, M. Jorgensen, K. Norrman, O. Hagemann, J. Alstrup, T. D. Nielsen, J. Fyenbo, K. Larsen, and J. Kristensen, A complete process for production of flexible large area polymer solar cells entirely using screen printing-First public demonstration, *Sol.Energy Mater.Sol.Cells*, 2009, **93**, 422-441.

48. X. Yang and J. Loos, Toward high-performance polymer solar cells: The importance of morphology control, *Macromolecules*, 6-3-2007, **40**, 1353-1362.

49. K. Kawano, R. Pacios, D. Poplavskyy, J. Nelson, D. D. C. Bradley, and J. R. Durrant, Degradation of organic solar cells due to air exposure, *Sol.Energy Mater.Sol.Cells*, 15-12-2006, **90**, 3520-3530.

50. E. A. Katz, S. Gevorgyan, M. S. Orynbayev, and F. C. Krebs, Out-door testing and long-term stability of plastic solar cells, *European Physical Journal-Applied Physics*, 2006, **36**, 307-311.

51. S. A. Gevorgyan, M. Jorgensen, and F. C. Krebs, A setup for studying stability and degradation of polymer solar cells, *Sol.Energy Mater.Sol.Cells*, 2008, **92**, 736-745.

52. J. A. Hauch, P. Schilinsky, S. A. Choulis, R. Childers, M. Biele, and C. J. Brabec, Flexible organic P3HT : PCBM bulk-heterojunction modules with more than 1 year outdoor lifetime, *Sol.Energy Mater.Sol.Cells*, 2008, **92**, 727-731.

53. M. O. Reese, A. J. Morfa, M. S. White, N. Kopidakis, S. E. Shaheen, G. Rumbles, and D. S. Ginley, Pathways for the degradation of organic photovoltaic P3HT : PCBM based devices, *Sol.Energy Mater.Sol.Cells*, 2008, **92**, 746-752.

54. F. C. Krebs, J. E. Carle, N. Cruys-Bagger, M. Andersen, M. R. Lilliedal, M. A. Hammond, and S. Hvidt, Lifetimes of organic photovoltaics: photochemistry, atmosphere effects and barrier layers in ITO-MEHPPV: PCBM-aluminium devices, *Sol.Energy Mater.Sol.Cells*, 2005, **86**, 499-516.

55. F. C. Krebs, Encapsulation of polymer photovoltaic prototypes, *Sol.Energy Mater.Sol.Cells*, 15-12-2006, **90**, 3633-3643.

56. G. Dennler, C. Lungenschmied, H. Neugebauer, N. S. Sariciftci, M. Latreche, G. Czeremuszkin, and M. R. Wertheimer, A new encapsulation solution for flexible organic solar cells, *Thin Solid Films*, 26-7-2006, **511**, 349-353.

57. P. Vivo, J. Jukola, M. Ojala, V. Chukharev, and H. Lemmetyinen, Influence of Alq(3)/Au cathode on stability and efficiency of a layered organic solar cell in air, *Sol.Energy Mater.Sol.Cells*, 2008, **92**, 1416-1420.

2 Materials and Processing

2.1 Introduction

The manufacturing of OPV devices involves many crucial steps and the processing of every layer in the device can significantly vary from one material to another. Especially the processing of active layer in the device is prompt to changes when different materials are used. Often even the same material synthesized using different approaches can result in different requirements for device processing. As a result often a large number of experiments are necessary for defining the optimal processing conditions during manufacturing of OPV devices in order to obtain the best performance.

This chapter contains two topics. One of the topics discusses various device structures and geometries and presents comparative studies of different designs used throughout this project. The second topic demonstrates an example of defining the optimal processing parameters and techniques for the active layer in the device based on polythiophene. Advanced processing methods for improving film morphology are also demonstrated.

Most of the results presented in this chapter have been further used as a guide for manufacturing and characterization of all the devices presented in the whole dissertation.

2.2 Layer Structure and Layout of OPV Devices

2.2.1 Structure of OPV Devices

As was already discussed in the first chapter the typical structure of polymer solar cells comprises a number of layers, which gives plenty of choice for different materials and material combinations. The frontface of the cell is usually considered the substrate and accordingly the next electrode after the substrate is the front electrode. One of the requirements while building a solar cell is to keep one of the faces transparent for illumination. It can be frontface or backface illumination depending on whether the substrate is transparent or not as shown in Figure 2.1.

One has to choose also the positions of the cathode and anode while building a solar cell. In case of “normal geometry” the anode is the front electrode and in case of “inverted geometry” the

anode is the back electrode. Two typical device structures have been chosen for each of these geometries that will be frequently referred to throughout the context of the presented work. The reference structures are outlined in the tables below:

Normal Geometry

Substrate	Anode	Hole Conductor	Active Layer	Electron Conductor	Cathode
Glass or PET	ITO	PEDOT:PSS	P3HT:PCBM	LiF	Aluminum

PET – Polyethyleneterphthalate;

ITO – Indium Tin Oxide;

PEDOT:PSS – Poly(3,4-ethylenedioxythiophene):poly(styrenesulfonate);

P3HT – Poly(3-hexylthiophene);

PCBM – Fullerene derivative [6,6]-phenyl C61 butyric acid methyl ester;

LiF – Lithium fluoride

Inverted Geometry

Substrate	Cathode	Electron Conductor	Active Layer	Hole Conductor	Anode
Glass or PET	ITO	ZnO	P3HT:PCBM	PEDOT:PSS	Ag Silver

ZnO – Zinc oxide

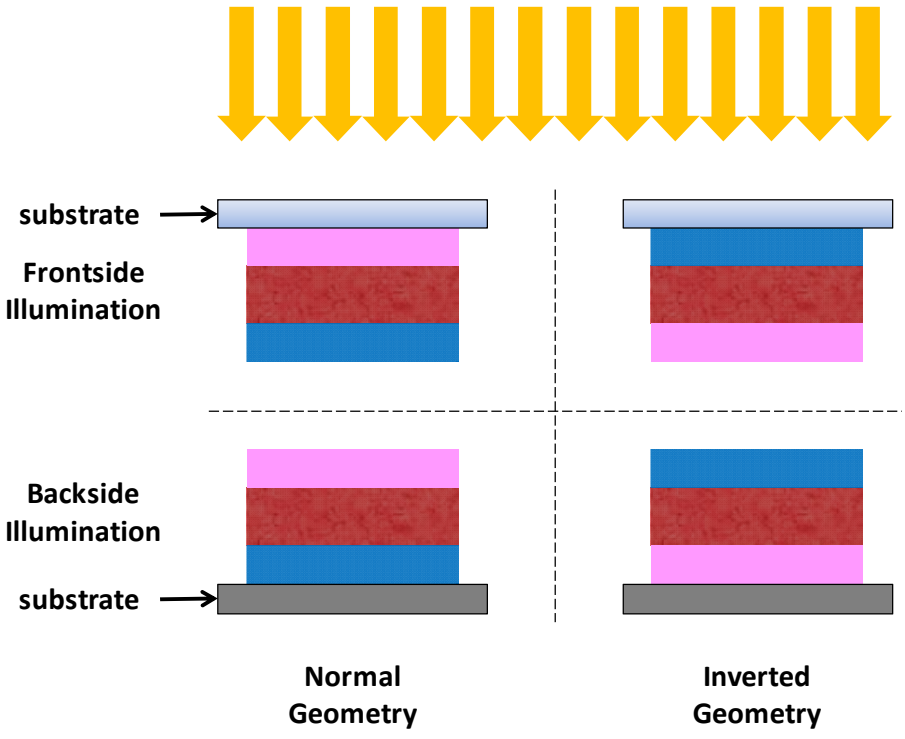

Figure 2.1: Different geometries of OPV devices with frontside or backside illumination.

The normal geometry reference cell will be called the "traditional device". The traditional device has been considered to be the optimal for a long period of time, since it can deliver relatively high efficiencies and is relatively easy to produce.[1,2] Yet, in the context of operational stability and large scale solution processing without vacuum coating steps the inverted geometry has proven to be more useful[3] and thus has been given a lot of attention in this work as well.

2.2.2 Designing OPV Devices

An important step in building organic solar cells is choosing the optimal geometrical layout for the device. The layout is very crucial for optimizing the charge transport through the electrodes by reducing the sheet resistance.[4] In addition, layout can play important role in accurate definition of the device PCE values.[5]

This section presents measurements carried out for different device layouts to establish the optimal geometry for small model devices that would deliver highest efficiencies and allow accurate characterization of the cells.

As an example, four different size devices have been produced on one substrate and tested for photovoltaic performance. The cells active area, which is defined by the overlap of the front and back electrodes, had the following area sizes: (a) – 0.091 cm^2, (b) – 0.161 cm^2, (c) – 0.361 cm^2, (d) – 1 cm^2. Figure 2.2 shows the change of the photovoltaic parameters while going from small to big size cells. The parameters are normalized to the values of the parameters of the smallest device. The value of V_{oc} is not shown, because it stays the same for all the cells. The data of the curves is averaged over 7 modules of 28 solar cells. The cells have the traditional structure and the best cell with area (a) and PCE of 3.14 % is shown in Figure 2.3.

The typical sheet resistance of the transparent electrode ITO is in the range of 5 – 15 $\Omega\square^{-1}$, which causes a decrease of J_{sc} and FF when the area of the cell is increased. As a result, by increasing the active area from 0.1 cm^2 to 1 cm^2 one can lose up to 30 % of PCE value (Figure 2.2). Also the larger area results in bigger number of defects in the film morphology, which can also be detrimental for device performance.

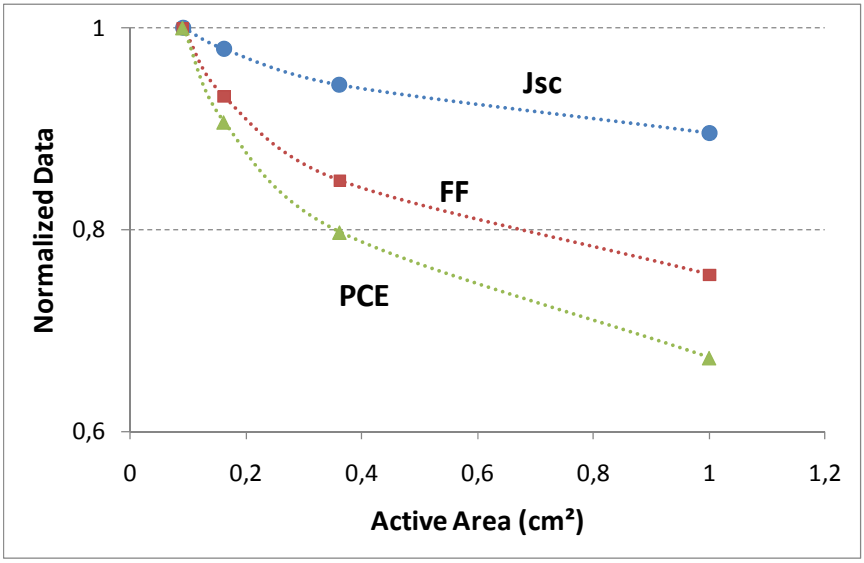

Figure 2.2: Photovoltaic parameters vs. size of active area. The parameters are normalized to the values of the smallest device parameters. Voc stays constant for all the sizes. The curves are averaged over 7 modules with 28 cells in total.

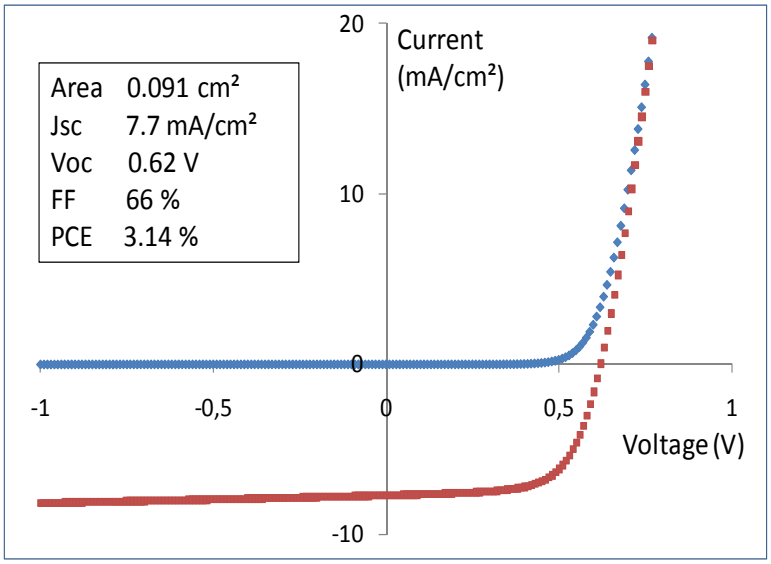

Figure 2.3: Dark and Light IV curves of the best performing device. The inset shows the PV parameters of the cell

On the other hand, different size cells were measured under 1 sun illumination with and without a mask, which covers the complete module leaving only the active area exposed to the light. Figure 2.4 shows the difference of the J_{sc} for different size cells with and without mask. The vertical axes

represent the following value $\frac{(J_{sc}op - J_{sc}m)}{J_{sc}op} \times 100\%$, where $J_{sc}m$ and $J_{sc}op$ are the short circuit current densities of the cell with and without masking respectively.

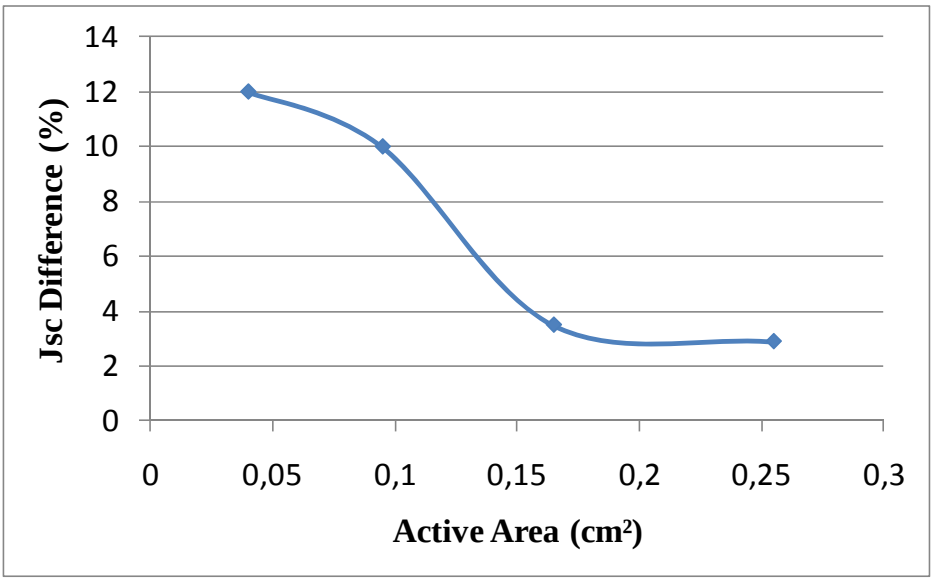

Figure 2.4: The change of the short circuit current due to the edge effect for different size solar cells. The vertical axes show the value defined by $\frac{(J_{sc}op - J_{sc}m)}{J_{sc}op} \times 100\%$, where $J_{sc}m$ and $J_{sc}op$ are the short circuit current densities for the cells with and without masking respectively.

Although the cell active area is defined by the overlap of front (ITO) and back (Al) electrodes, there is still so called "edge effect", which results in significant contribution of the edges where Al goes over the active layer and PEDOT:PSS. Although there is no ITO, PEDOT:PSS can still transport some carriers to the ITO thus contribute to the overall current. One way to avoid this is patterning the active layer in the way that it covers only the ITO pattern, which technically is not easy if spin coating technique is used. From Figure 2.4 it appears that for small area solar cells (≤ 0.1 cm^2) contribution from edges can reach more than 10 %. Increasing the cell area to 0.2 cm^2 creates a difference of only 3 %. Building solar cells with larger active areas can significantly reduce the edge effect. Thus if accurate evaluation of a solar cell is required one has to ether mask the cells while measuring or produce cells in scales large enough for neglecting the edge effects. For characterization of large amount of cells masking is not very applicable, since it is a time consuming process.

There were many different outlines designed by our group and some of them are shown in Figure 2.5 for a substrate with the size 2.5 × 5 cm^2 and the table below the figure outlines the pros

and cons of each design. Outline (1) is the most inefficient design among all four in all terms and the only benefit of (1) is that it shows the potential of the device in larger scales. Outline (2) allows having 4 cells on one substrate, which is useful for statistical analyses. However, the sheet resistance due to ITO for such a design is relatively high. Outlines (3) and (4) reduce the sheet resistance by reducing the distance that the charge carriers have to cross via ITO and both designs are useful for achieving high fill factors. However, (3) has only one cell per module and half of the space on the substrate is not used and (4) is very elaborate for production, since one has to pattern stripes on active layer, which is not easy if spin coating technique is used.

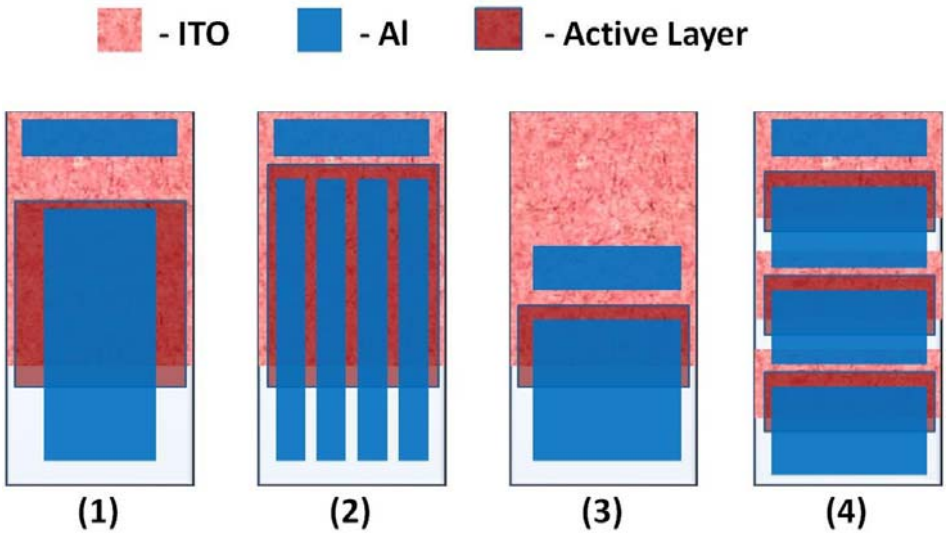

Design	Active Area (cm^2)	Sheet Resistance	Statistics	Area Usage	Production
(1)	3	High	No	Effective	Simple
(2)	0,5	High	4 cells	Effective	Simple
(3)	1	Lowered	No	Poor	Simple
(4)*	3	Lowered	3 cells	Effective	Elaborate

*The cells are connected in series and the area for each cell is 1 cm^2

Figure 2.5: Different outlines of solar cell devices designed by Risø DTU Solar cell group. The table below the figure shows the pros and cons of each design.

It was not possible to design an outline that would satisfy all the requirements, thus different outlines were used for different purposes within the scopes of this work. If quick and statistical characterization was required, then outline (2) was the choice for producing the cells and if accurate evaluation of optimal PCE was required, then outlines (3) or (4) were used during this project. A

possible complete solution can be a module with 4 different size cells of a squared shape on each corner of a squared substrate.

2.3 Materials and Processing Methods for Active Layer

Currently the challenge of OPV field is to develop donor and acceptor materials that when brought together can deliver optimal device efficiencies and will have high stability in different environmental conditions. At the same time the materials have to be abundant, cost efficient and easy to process for large scale productions. While there are no such "full package materials" developed yet, there are countless numbers of reports on different materials that steadily lead to progress.

The following subsection describes some of the materials that have been used as donor and acceptor during this project. Further, methods for optimization of the processing of the active layer as well as some advanced processing for improving film morphology based on polythiophene are presented.

2.3.1 Donor and Acceptor Materials

The 'kick-off' for polymer based solar cells happened in 1992 with the first results of photo induced charge transfer from a conjugated polymer to a buckminster fullerene (C_{60}) reported by Sariciftci *et al,*[6] and since then the field of polymer/fullerene solar cells experienced a continuous evolution. In 1995 Yu *et al* showed that charge separation is greatly improved when donor and acceptor materials are mixed in a bicontinuous interpenetrating network.[7] In their report the bulk heterojunction of the photoactive layer had 2-methoxy-5-(2-ethylhexyloxy)-polyphenylenevinylene (MEH-PPV) as the electron donor and the soluble fullerene derivative [6,6]-phenyl C_{61} butyric acid methyl ester (PCBM) as the electron acceptor. This was followed by countless number of reports with various donor and acceptor materials.

A big number of materials for donors and acceptors have been characterized throughout this project and Figure 2.6 outlines the molecular structure of some of the most successful materials in terms of PV performance.

Acceptors

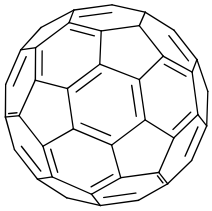

C_{60} Buckminster fullerene

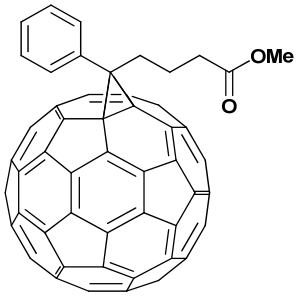

[60]PCBM

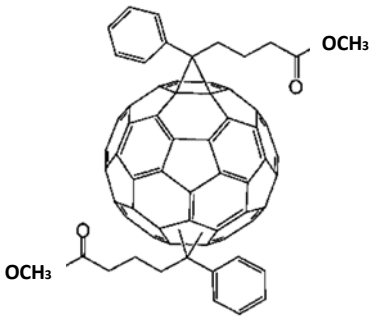

[60]bis-PCBM

Donors

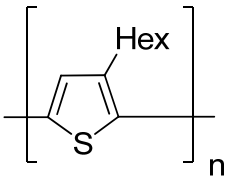

P3HT

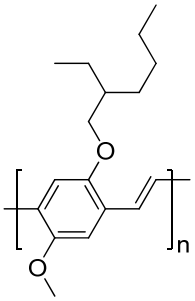

MEH-PPV

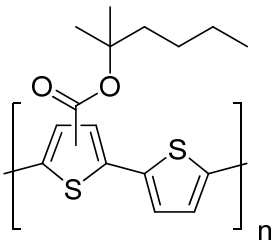

P3MHOCT

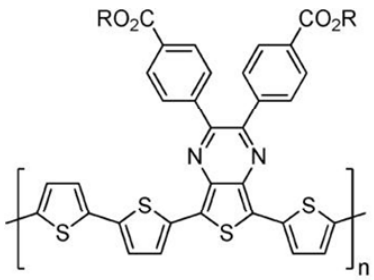

8j

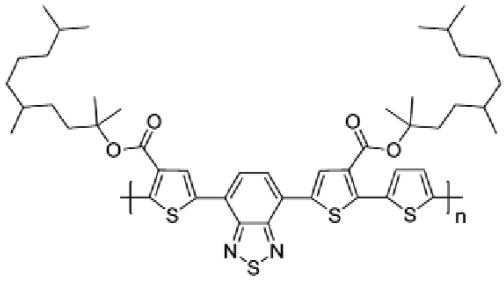

10

[60]PCBM – [6,6]-phenyl C61 butyric acid methyl ester

P3HT – poly(3-hexylthiophene)

MEH-PPV – 2-methoxy-5-(2-ethylhexyloxy)-polyphenylenevinylene

P3MHOCT – poly-(3-(2-methylhex-2-yl)-oxy-carbonyldithiophene)

Description of **8j** and **10** can be found in sections 3.3.3 and 3.3.4 respectively

Figure 2.6: Molecular structures of the materials commonly used in this work as donors and acceptors in the active layer. The description of the polymers **8j** and **10** can be found in Chapter 3.

From an active layer materials point of view, the state of the art have long been dominated by the bulk heterojunctions prepared from poly(3-hexylthiophene) (P3HT) and the fullerenes [60]PCBM and [70]PCBM (Figure 2.6). A lot of research has been put into this and efficiencies in the range of 4 – 5 % have been achieved.[1,2,8-10]

Part of this project was devoted to characterization of P3HT based devices, particularly, developing manufacturing techniques for optimal, fast and efficient production of P3HT based devices and using the techniques as a reference for characterization of other polymers.

Another part of this project was devoted to characterization of so called thermocleavable polymers (Figure 2.6 **P3MHOCT**, **8j** and **10**). This is a category of materials which can be cleaved thermally after producing films from soluble polymer. The cleaving process converts the films from soluble to more rigid form, which can improve the stability of the devices. The characterization details for such polymers can be found in Chapter 3.

2.3.2 Optimization of Active Layer Processing

As was already mentioned in first chapter the active layer can be single layer, double layer heterojunction or bulk heterojunction. Since the latter has proven to be the most efficient one, we will focus only on bulk heterojunctions.

When a new polymer is produced, the best way to test it for photovoltaic applications is to build a solar cell with active layer based on that polymer. However, in order to efficiently evaluate the photovoltaic potential of the material one has to carefully choose the processing parameters for the particular material to obtain the best device performance, which requires large amount of experiments and comparative studies.

As an example the carrier mobility can be different for various materials, which can affect the ratio of the bulk mixture. If the charge transport throughout the cell is not balanced then there will be an accumulation of charges during transport (the device becomes space charge limited), which leads to recombination losses.[11,12] One way to avoid such accumulation is to control the distances that the carriers have to cross to reach the electrodes in such a way, that they compensate the mobility difference. The distance can be tuned by choosing the donor/acceptor ratio in the bulk. For example in the case of MEH:PPV/PCBM blend the mobility of the holes is one order of magnitude lower compared to the electron mobility.[11] As a result the optimal ratio between MEH-PPV and

PCBM in terms of performance was found to be 1:4. While for the P3HT:PCBM blend in the traditional device the mobility ratio is close to unity and therefore the optimal ratio is around 1:1.[1]

This subsection presents some methods for optimization of the active layer processing that have been realized during this project.

The processing of active layer based on a blend of P3HT polymer synthesized by Risø DTU group and PCBM was studied and optimized for the best device performance in this work. Figure 2.7 presents PV parameters versus the combined concentration of P3HT:PCBM in the active solution for the traditional device. The values are averaged over 6 cells. The spin speed of coating the films is kept the same. Thus, the thickness is defined by the concentration of the solution. The fill factor is gradually decreasing with the concentration, since the layer thickness is increasing (coating spin speed was kept the same), which results in increased recombination losses. Contrary to *FF* the short circuit current density J_{sc} is increasing until around 45mg/ml and decreasing again. The light absorption by the active layer is increased with the increase of the concentration (due to increase of film thickness) resulting in higher currents and possibly due to interference effects[13] after reaching to a peak the current starts decreasing again. The concentrations chosen for this particular project was mostly in the range of 40 to 45 mg/ml, since this concentration allows having reproducible devices at the same time with high PCE values. However, the highest PCEs were achieved using 20 mg/ml concentration although with lower reproducibility (the thicknesses of the films were adjusted accordingly using different coating speeds). The reason that the high concentrations provide better reproducibility is probably due to the fact that the defects density (dust particles, pin holes etc.) decreases with the increase of solution concentration.

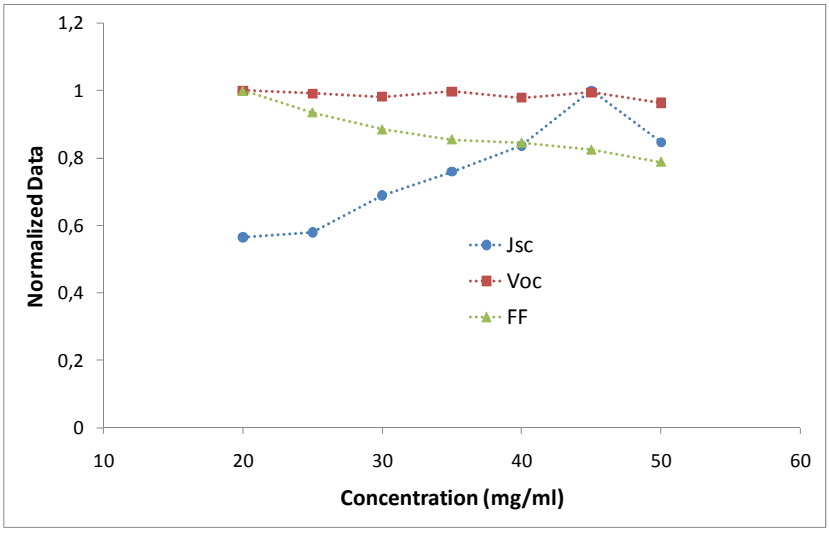

Figure 2.7: Photovoltaic parameters vs. the combined concentration of P3HT:PCBM in the solution for devices with traditional structure.

An important factor is also the ratio between the donor and acceptor materials in the blend as was mentioned earlier. Figure 2.8 (a) and (b) show the device performance for different ratios of PCBM/P3HT for devices with traditional structure without and with postproduction thermal annealing respectively. The values are averaged over 6 cells. The devices for this particular set of experiments show the best performance for the ratio 9/10 for PCBM/P3HT.

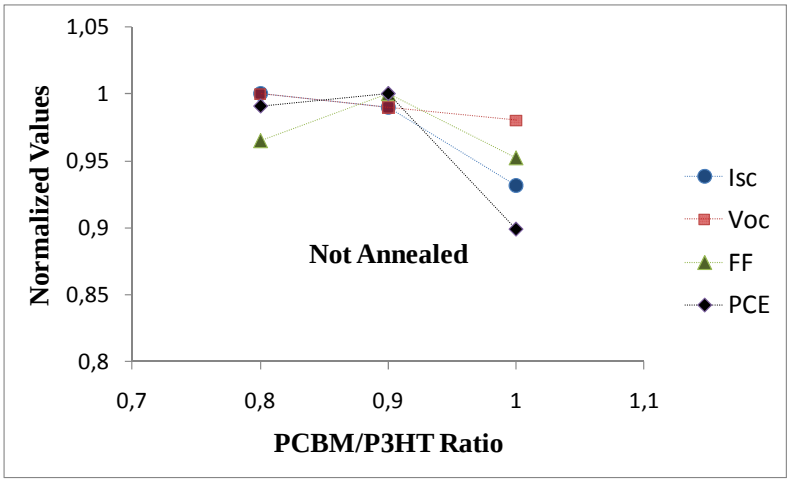

(a)

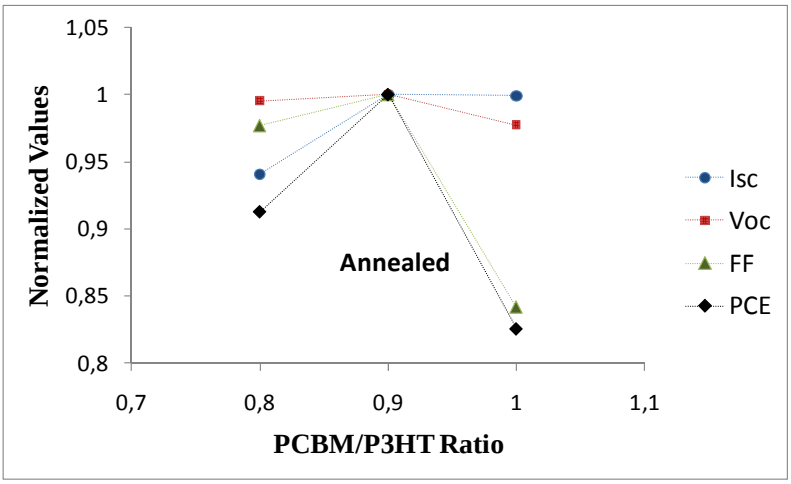

(b)

Figure 2.8: Photovoltaic parameters vs. the concentration ratio of PCBM/P3HT for devices without (a) and with (b) annealing. The data are average values for 6 cells.

As will be shown later the annealing of polythiophene based devices is very crucial, since it can drastically improve the morphology of the active layer and thus the performance of the device. Typical annealing of a device is carried out in glove-box or room environment on a hot plate. The devices with traditional structure were tested for different annealing temperatures and the optimal temperature was found to be in the range of 150 to 160 ^{o}C with 5 minutes annealing time (Figure 2.9). The chosen temperature for traditional devices in this project was 150 ^{o}C.

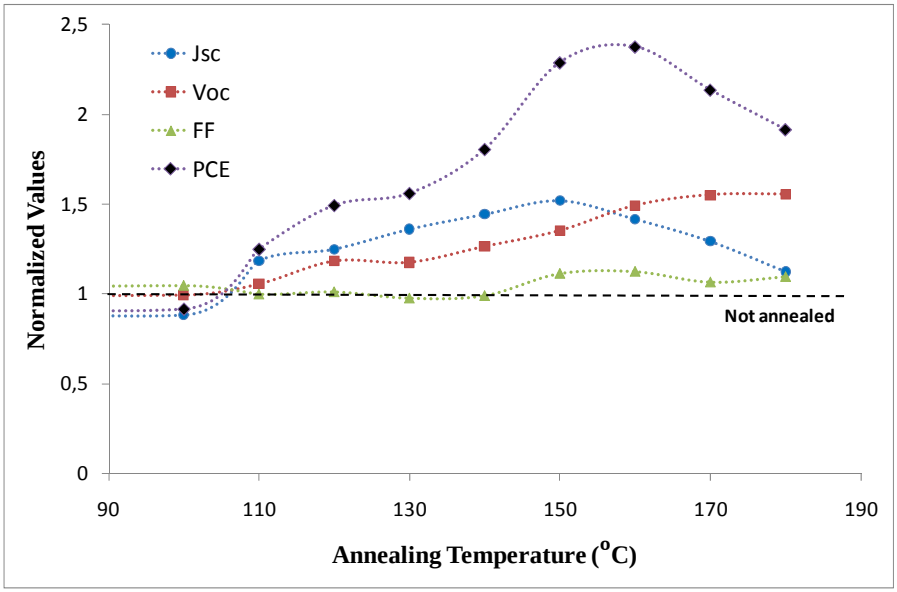

Figure 2.9: Photovoltaic parameters vs. postproduction annealing temperature. The annealing time was 5 minutes. The data are the average of 6 cells. The values are normalized to the parameters for device with no annealing shown with a black striped line.

The choice of the solvent for P3HT based blends was commonly Chlorobenzene (CLB). However, different solvents have been tested as well, such as 1,4-Dichlorobenzene (DCB), m-Xylene (mXl), Chloroform (CLF). The layers spin coated from mXl deliver very homogenous films and thus the devices based on such a blend have high reproducibility. However, homogeneity of the film does not necessarily define the best performance. Thus, the common choice of the solvent during this project was CLB, since it delivers the best performance. Cells with DCB can also perform equally good or even better than CLB, but it is much harder to achieve homogeneous layer by spin coating from DCB.

2.3.3 Advanced Processing and Characterization of P3HT Based Devices

What makes P3HT so unique is that it allows improving the morphology and crystalline structure of the polymer by certain postproduction techniques. This subsection describes few approaches that have been studied and optimized for our particular devices during this project.

Thermal processing to alter the morphology: One way to improve the performance of devices based on polythiophene is post-production thermal treatment.[14-16] The treatment is realized by simply annealing the complete device on a hot plate. Especially P3HT has the property to crystallize when the temperature is increased above the glass transition temperature.

P3HT:PCBM based devices with traditional structure were manufactured and thermally annealed. Figure 2.10 presents the IV curves and the IPCE data of measured devices before and after thermally annealing at 150 ^{o}C for 5 minutes. Table in Figure 2.10 shows the corresponding PV parameters. Clearly there is a significant increase in the performance after the thermal treatment due to improvement in short circuit current density J_{sc} and fill factor *FF*. Figure 2.11 shows the absorption spectra of the P3HT:PCBM films before and after annealing. More pronounced peaks are seen on the curve of the annealed film, especially the shoulders on right hand side, which are originated from the planar stacking of the polymer chains. In addition, a remarkable red shift of the absorption is also observed after the thermal treatment. In the literature it was suggested earlier that the heating induces slow crystallization of the polymer, resulting in better ordering and staking of the polymer chains. This results in an increase of the charge carrier mobility in the polymer, which improves the performance.[17] Apart from that the heating causes a decrease in the free volume and in the density of defects at the interface due to the solvent evaporation from the layer, which could improve the morphological structure of the organic active layer.[18] Furthermore, the heating enhances the interaction between the chains in the polymer, which changes the absorption properties of the polymer and improves the morphology.[19] The red shift is caused by the change of the average conjugation length in the polymer.

There have been various reports on improvement of the device efficiency by thermal treatment (see for example[20-23]), but all the best devices reported by different groups have different optimal annealing temperatures for the same polymer materials, which is probably due to the concentration of the PCBM.[22,24] During the annealing process, the PCBM clusters are growing. Such a phenomenon can improve the phase separation between compounds. At the same time while being

heated the average conjugation length of the polymer is increased due to the ordering of the chains into more crystalline structure that leads to creation of borders around PCBM clusters, which to some extent hamper the large-scale growth of PCBM crystals and create fine phase separation in the interface.[20] However, in case of excess amount of PCBM overgrown clusters of PCBM can appear which can lead to destruction of the homogeneity of phase separation.

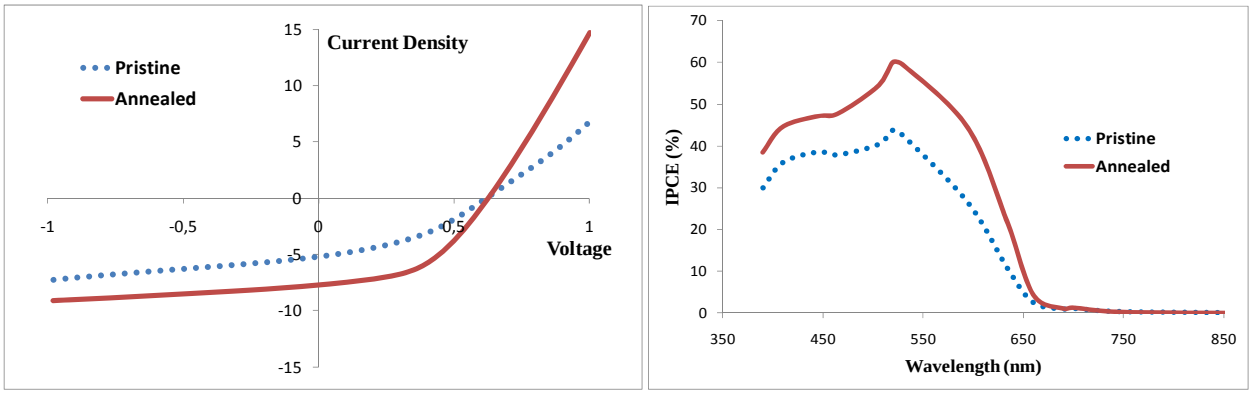

PV parameters	J_{sc} (mA/cm^2)	V_{oc} (V)	FF (%)	PCE (%)
Pristine	5.2	0.62	38	1.24
Annealed	7.7	0.62	48	2.3

Figure 2.10: IV curves (left) and IPCE data (right) of both pristine (blue dots) and thermally annealed (solid red line) devices with structure of Glass/ITO/PEDOT:PSS/P3HT:PCBM/Al. The table below the figures shows the PV parameters for both pristine and annealed devices.

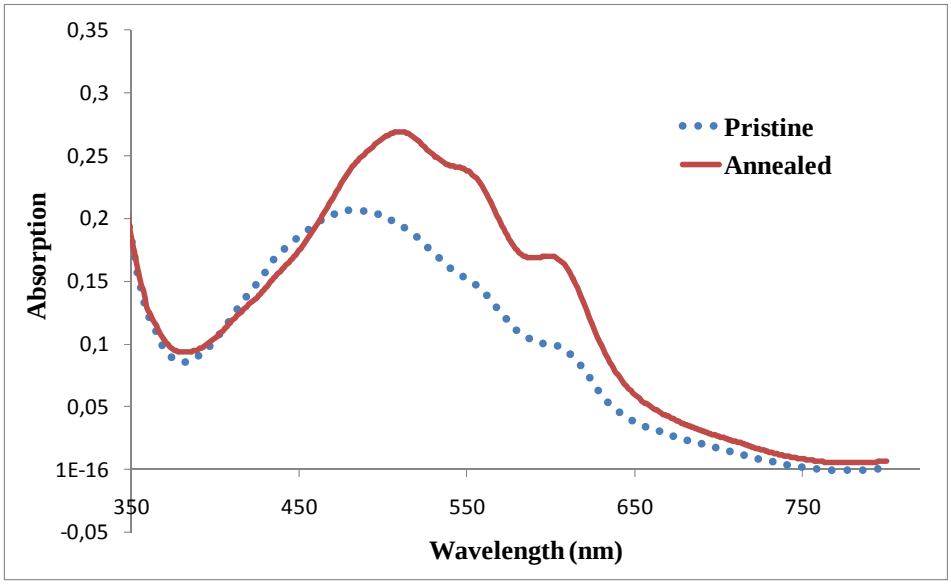

Figure 2.11: Absorption spectra for both pristine (blue dots) and thermally annealed (solid red line) films with structure of Glass/ITO/PEDOT:PSS/P3HT:PCBM.

As possible evidence, in some cases during the annealing of the devices "bubbles" are formed on the back electrode. Figure 2.12 presents the three cells with polymer/PCBM ratios of 5/4, 5/5 and 5/6 annealed at 155 ^{o}C for 5 minutes. The one with the highest concentration of PCBM (5/6) has the strongest effect of bubble formation, while no bubbles are evident in case of lower concentration of PCBM (5/4). In the same experiment the devices based on active solution that had been filtered with micro filter prior to spin coating of the film had strong bubble formation effect independent of PCBM concentration. This indicates that during filtering certain amount of polymer is lost in the filter resulting in significantly dominating concentration of PCBM.

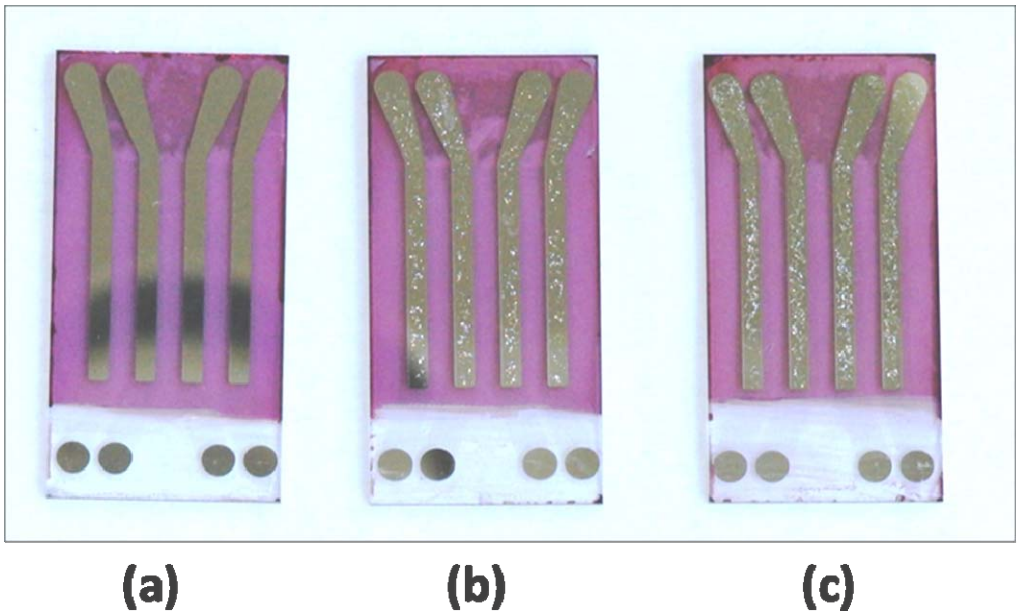

Figure 2.12: The image of the back side of devices with following layers: Glass/ITO/PEDOT:PSS /P3HT:PCBM/Al. The ratio of P3HT/PCBM is (a) 5/4; (b) 5/5; (c) 5/6.

Solvent vapour treatment to alter the morphology: Another way to improve the photovoltaic performance of thiophene-based polymer devices is to alter the morphology of the polymer thin films by so-called solvent annealing or solvent vapor treatment. Solvent annealing is a technique for controlling the slow drying process of freshly spin-coated films in a controlled atmosphere with a certain solvent vapor. This technique has been explored generally since the 1980s for different organic material-based thin films.[1,25-32] In the case of polythiophenes, similar to thermal annealing

the solvent annealing results in self-organization of the polymer chain structure into an ordered structure. The degree of such self-organization can be controlled by drying conditions of the film.

Solvent annealing is realized by placing the films right after the spin coating into an environment with saturated solvent vapour, which slows down the drying process and facilitates the crystal structure growth.

Devices with P3HT:PCBM dissolved in CLB have been prepared. Half of the devices after spin coating were placed in a rack with dichlorobenzene (DCB) solvent covering the bottom, which creates a saturated vapour environment in the rack. The cells after the treatment had more purple color compared to the pristine films, which could be easily distinguished by eye. Figure 2.13 shows the IV curves and the IPCE data for the pristine and solvent annealed devices together with the table showing the PV parameters of the devices. Similar to the thermal annealing there is a significant improvement of the performance after the treatment. Figure 2.14 shows the absorption spectra of the devices without the back electrode and again behavior resembling the thermal treatment can be seen in the absorption spectrum.

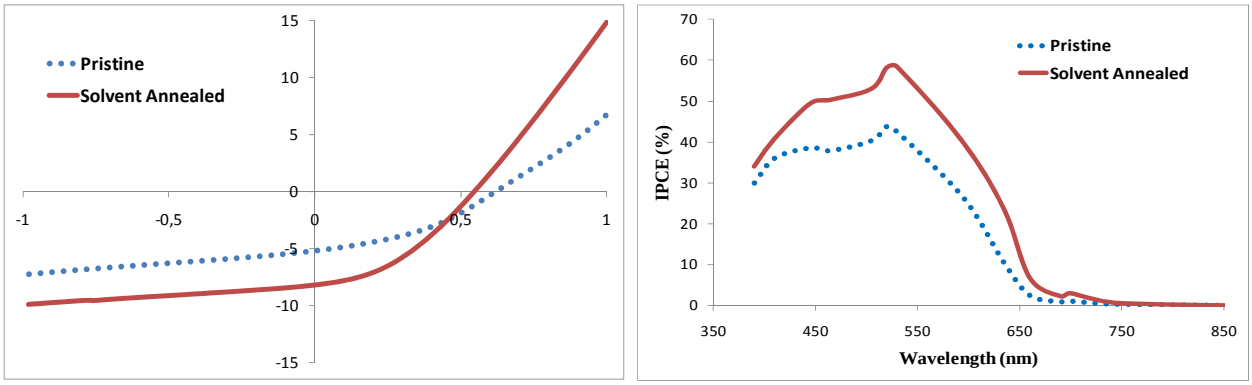

PV parameters	J_{sc} (mA/cm^2)	V_{oc} (V)	FF (%)	PCE (%)
Pristine	5.2	0.62	38	1.24
Solv. Annealed	8.2	0.54	39	1.74

Figure 2.13: IV curves (left) and IPCE data (right) of both pristine (blue dots) and solvent annealed (solid red line) devices with structure of Glass/ITO/PEDOT:PSS/P3HT:PCBM/Al. The table below the figures shows the PV parameters for both pristine and solvent annealed devices.

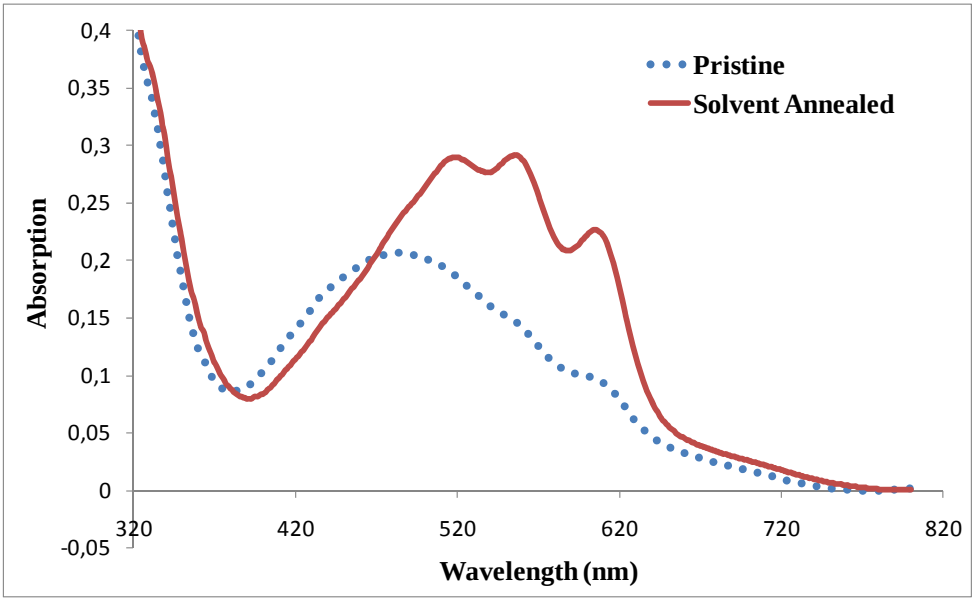

Figure 2.14: Absorption spectra for both pristine (blue dots) and thermally annealed (solid red line) films with structure of Glass/ITO/PEDOT:PSS/P3HT:PCBM.

Atomic force microscopy (AFM) studies were carried out and AFM images of the surface of the studied films confirm a remarkable change in morphology of the film. Figure 2.15 show the AFM images of pristine (top left) and solvent annealed (top right) samples. The roughness of the film is increased after treatment showing more pronounced peaks, which can be a possible evidence of growing units of donor and acceptor materials. However, it is difficult to conclude anything specific from just AFM image, since it only represents the topography of the surface.

The results confirmed that the slow grown film can improve the crystalline structure of the polymer and the ordering of the interface network of the bulk. However, it was obvious also that just solvent annealing in this case is not improving the device as much as the thermal annealing and thus additional thermal annealing is still required for complete improvement.

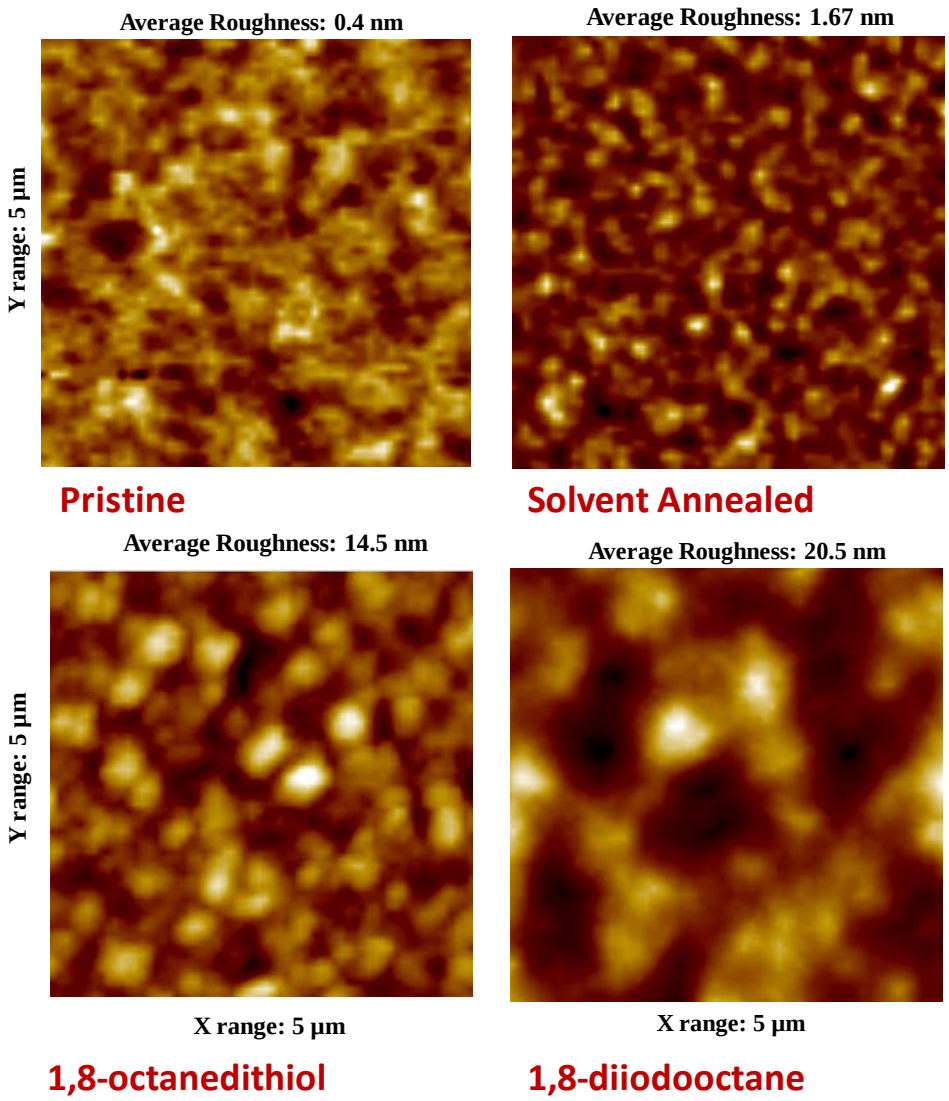

Figure 2.15: AFM images of the surface of pristine (top left), solvent annealed (top right), 1,8-octanedithiol (bottom left) and 1,8-diiodooctane (bottom right) films with structure of Glass/ITO/PEDOT:PSS/P3HT:PCBM together with the average roughness values.

Additives approach: Often organic solar cells are fabricated on flexible substrates, such as poly(ethylene terephthalate) (PET) and due to low glass transition temperature of PET thermal annealing cannot be applied for such devices. At the same time the technique of solvent vapour annealing is a time consuming process and therefore puts constrains on production speeds and scales. For that reason a number of new approaches have been suggested for improving the morphology, which does not require any further treatment after film formation.

It was shown by a number of groups that adding some amount of certain solvents unfavorable for the polymer in the solution of photoactive blend results in strong aggregation of the polymer,

which can lead to improvement of the morphology of the interface. Efficiencies above 5 % have been reported by adding 2.5 % of 1,8-diiodooctane or 1,8-octanedithiol in the active solution dissolved in CLB.[33] According to Lee *et al.* the fullerene component is dissolved by the additive, while the polymer is not. As a result the fullerene is removed from the polymer mixture and fine structures of donor rich and acceptor rich domains are created.[33]

OPV devices have been prepared with traditional structure by adding 2,5 % of 1,8-diiodooctane or 1,8-octanedithiol in the active solution based on CLB. Figure 2.16 shows the IV curves and IPCE data together with the table of PV parameters for the devices with and without additives. For both additives the performances were significantly improved compared to the devices without treatment. The best performance was achieved with 1,8-diiodooctane. Figure 2.17 shows the absorption spectra of the devices with the same structure without the back electrode. Similar behavior can be seen as in the previous two cases. The additives also result in better morphology and ordering of the nanostructure in the bulk. The AFM images show a strong increase in roughness when 1,8-octanedithiol (Figure 2.15 bottom left) or 1,8-diiodooctane (Figure 2.15 bottom right) are mixed in the solution. Similar results of roughness change were shown by Peet *et al.*[34] The additives approach proves to be very easy and applicable method especially when other methods such as thermal annealing cannot be employed.

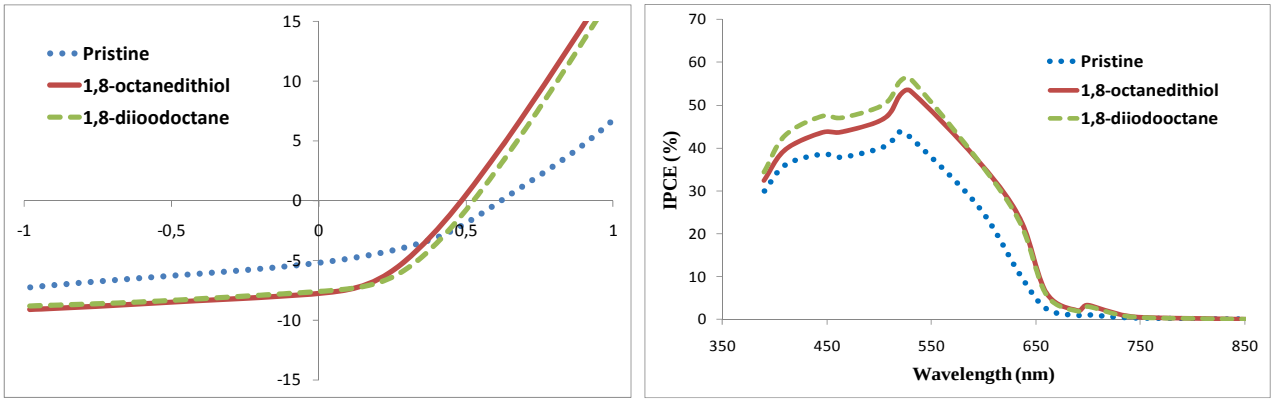

PV parameters	J_{sc} (mA/cm^2)	V_{oc} (V)	FF (%)	PCE (%)
Pristine	5.2	0.62	38	1.24
1,8-octanedithiol	7.7	0.48	39	1.49
1,8-diiodooctane	7.6	0.52	43	1.71

Figure 2.16: IV curves (left) and IPCE data (right) for pristine (blue dots), 1,8-octanedithiol (solid red line) and 1,8-diiodooctane (green broken line) devices with structure of Glass/ITO/PEDOT:PSS /P3HT:PCBM/Al. The table below the figures shows the PV parameters of the measured devices.

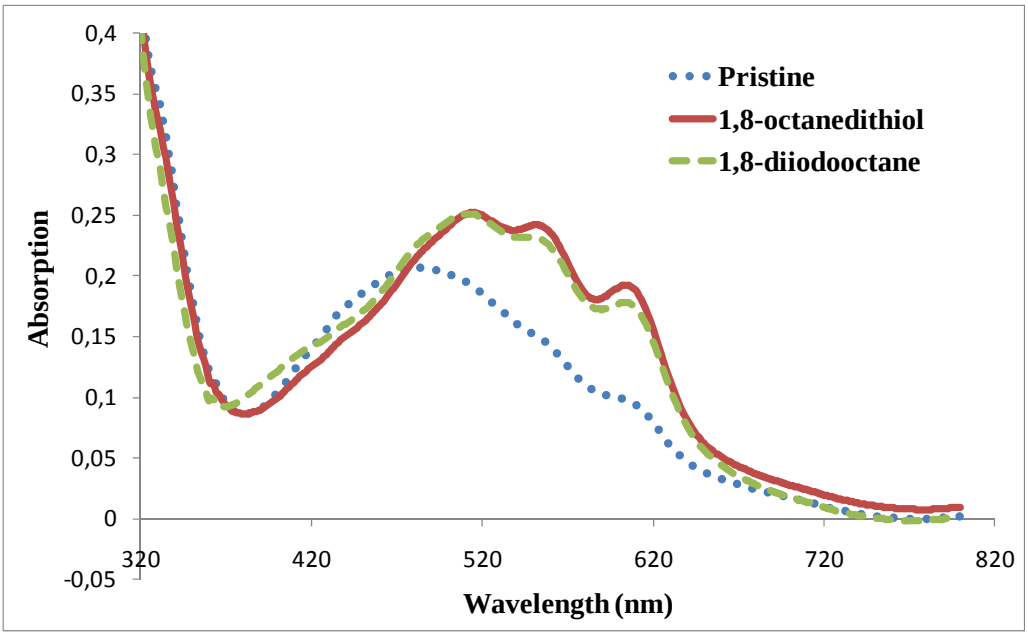

Figure 2.17: Absorption spectra for pristine (blue dots), 1,8-octanedithiol (solid red line) and 1,8-diiodooctane (green broken line) films with structure of Glass/ITO/PEDOT:PSS /P3HT:PCBM.

More detailed description of such processing techniques has been published in a short overview discussing the polythiophene based materials for photovoltaic applications. The overview is a chapter contribution to "Handbook of THIOPHENE-BASED MATERIALS" edit. I. F. Perepichka, D. F. Perepichka.[35]

"Hairy" P3HT: Other annealing free methods have been reported as well for the improvement of the film morphology. For example, Senkovskyy *et al.* demonstrated a new strategy for the preparation of (nano)structured conjugated polymer hybrids, that was exemplified by the synthesis of hairy poly(3-alkylthiophene) particles (see Appendix 1). In particular, poly(3-alkylthiophenes) were selectively grown via a quasi-living surface-initiated Kumada catalyst transfer polycondensation (SI-KCTP) reaction from particles bearing surface-immobilized Ni catalysts supported by bidentate phosphorus ligands. This resulted in hairy particles with endtethered P3HT chains. Densely grafted P3HT within the μ-P3HT particles exhibits strongly altered optical properties as compared to the untethered counterparts or to P3HT grafted onto small nanoparticles with a high surface curvature. This was attributed to strong interchain interactions within the densely grafted P3HT chains, which can be tuned by changing of the surface curvature (or size) of the supporting particle.

My task in this particular project was to prepared and characterize devices based on the bulk heterojunction of hairy P3HT:PCBM. The traditional device structuring approach was used for manufacturing and the devices were tested under 1 sun illumination. The devices showed a reasonably good PV performance for relatively large area devices with an active area of 1 cm^2: *PCE* = 1.8 - 2.3 %; *Isc* = 5.5 - 6.8 mA/cm^2; V_{oc} = 0.60 - 0.62 V; *FF* = 55 – 58 %. Figure 2.18 shows the IV curve of the measured device before and after annealing.

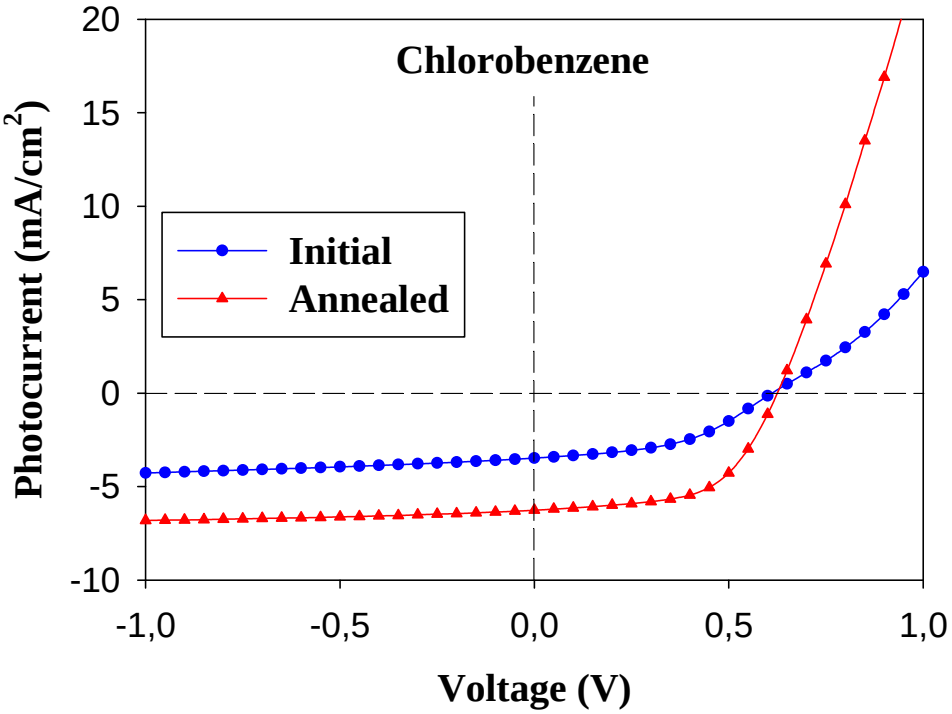

Figure 2.18: IV curves of Glass/ITO/PEDOT/PSS/nano-P3HT particles/PCBM/Al device before (blue circles) and after (red triangle) thermal annealing (130 °C for 5 min).

Although the PV performance of the nano-P3HT particles is lower than for the best reported P3HT-PCBM devices, the observed performance for the nano-P3HT particles when employed in a bulk heterojunction with PCBM is similar to what is obtained with linear P3HT with a rather high molecular weight (Mw – 36 600 g/mol) for relatively large active area devices of 1 cm^2.[3] On the other hand, it is even somewhat better than the performance of previously reported small-area devices that utilized relatively low molecular weight P3HTs of M_w < 13000 g/mol.[36-39] This result demonstrates that the developed SI-KCTP procedure, at least, does not affect the optoelectronic properties of P3ATs. Although more studies are necessary to comprehensively establish the influence of the polymer architecture on the PV performance, it becomes clear that the molecular

weight of linear P3HT constituents of branched P3HT structures must be subjected to further optimization in order to enhance the PV performance.

The detailed description of the synthesis of the hairy P3HT can be found in the reprint of the published article in Appendix 1.

2.4 Conclusions

To summarize, the importance of the device layout was discussed and the influence of sheet resistance and edge effects on performance were demonstrated. Device structures and designs that have been mostly used in this work were presented. In addition, an example of defining the processing parameters of the active layer for given material was shown together with some advanced technique for improving the film morphology and thus the device efficiency. It was demonstrated that there are many crucial steps while processing the active layer and each step can significantly vary from one material to another.

The designs and methods presented in this chapter have been used for most of the devices presented in the whole dissertation.

Reference List

1. G. Li, V. Shrotriya, J. S. Huang, Y. Yao, T. Moriarty, K. Emery, and Y. Yang, High-efficiency solution processable polymer photovoltaic cells by self-organization of polymer blends, *Nat.Mater.*, 2005, **4**, 864-868.

2. W. L. Ma, C. Y. Yang, X. Gong, K. Lee, and A. J. Heeger, Thermally stable, efficient polymer solar cells with nanoscale control of the interpenetrating network morphology, *Adv.Func.Mater.*, 2005, **15**, 1617-1622.

3. F. C. Krebs, S. A. Gevorgyan, and J. Alstrup, A roll-to-roll process to flexible polymer solar cells: model studies, manufacture and operational stability studies, *J.Mater.Chem.*, 2009, **19**, 5442-5451.

4. S. Choi, W. J. Potscavage, and B. Kippelen, Area-scaling of organic solar cells, *J.Appl.Phys.*, 1-9-2009, **106**, 054507.

5. A. Cravino, P. Schilinsky, and C. J. Brabec, Characterization of organic solar cells: the importance of device layout, *Adv.Func.Mater.*, 17-12-2007, **17**, 3906-3910.

6. N. S. Sariciftci, L. Smilowitz, A. J. Heeger, and F. Wudl, Photoinduced Electron-Transfer from A Conducting Polymer to Buckminsterfullerene, *Science*, 1992, **258**, 1474-1476.

7. G. Yu, J. Gao, J. C. Hummelen, F. Wudl, and A. J. Heeger, Polymer Photovoltaic Cells - Enhanced Efficiencies Via A Network of Internal Donor-Acceptor Heterojunctions, *Science*, 1995, **270**, 1789-1791.

8. C. J. Ko, Y. K. Lin, F. C. Chen, and C. W. Chu, Modified buffer layers for polymer photovoltaic devices, *Appl.Phys.Lett.*, 2007, **90**, 063509.

9. M. Reyes-Reyes, K. Kim, and D. L. Carroll, High-efficiency photovoltaic devices based on annealed poly(3-hexylthiophene) and 1-(3-methoxycarbonyl)-propyl-1-phenyl-(6,6)C-61 blends, *Appl.Phys.Lett.*, 2005, **87**, 083506-3.

10. M. Reyes-Reyes, K. Kim, J. Dewald, R. Lopez-Sandoval, A. Avadhanula, S. Curran, and D. L. Carroll, Meso-structure formation for enhanced organic photovoltaic cells, *Org.Lett.*, 2005, **7**, 5749-5752.

11. C. Melzer, E. J. Koop, V. D. Mihailetchi, and P. W. M. Blom, Hole transport in poly(phenylene vinylene)/methanofullerene bulk-heterojunction solar cells, *Adv.Func.Mater.*, 2004, **14**, 865-870.

12. M. M. Mandoc, L. J. A. Koster, and P. W. M. Blom, Optimum charge carrier mobility in organic solar cells, *Appl.Phys.Lett.*, 26-3-2007, **90**, 133504.

13. G. Dennler, M. C. Scharber, and C. J. Brabec, Polymer-Fullerene Bulk-Heterojunction Solar Cells, *Adv.Mater.*, 6-4-2009, **21**, 1323-1338.

14. X. Yang and J. Loos, Toward high-performance polymer solar cells: The importance of morphology control, *Macromolecules*, 6-3-2007, **40**, 1353-1362.

15. T. L. Benanti and D. Venkataraman, Organic solar cells: An overview focusing on active layer morphology, *Photosynthesis Research*, 2006, **87**, 73-81.

16. H. Hoppe and N. S. Sariciftci, Morphology of polymer/fullerene bulk heterojunction solar cells, *J.Mater.Chem.*, 2006, **16**, 45-61.

17. J. J. Dittmer, E. A. Marseglia, and R. H. Friend, Electron trapping in dye/polymer blend photovoltaic cells, *Adv.Mater.*, 1-9-2000, **12**, 1270-1274.

18. T. Ahn, H. Lee, and S. H. Han, Effect of annealing of polythiophene derivative for polymer light-emitting diodes, *Appl.Phys.Lett.*, 21-1-2002, **80**, 392-394.

19. P. J. Brown, D. S. Thomas, A. Kohler, J. S. Wilson, J. S. Kim, C. M. Ramsdale, H. Sirringhaus, and R. H. Friend, Effect of interchain interactions on the absorption and emission of poly(3-hexylthiophene), *Physical Review B*, 1-2-2003, **67**, 064203.

20. X. N. Yang, J. Loos, S. C. Veenstra, W. J. H. Verhees, M. M. Wienk, J. M. Kroon, M. A. J. Michels, and R. A. J. Janssen, Nanoscale morphology of high-performance polymer solar cells, *Nano Letters*, 2005, **5**, 579-583.

21. F. Padinger, R. S. Rittberger, and N. S. Sariciftci, Effects of postproduction treatment on plastic solar cells, *Adv.Func.Mater.*, 2003, **13**, 85-88.

22. D. Chirvase, J. Parisi, J. C. Hummelen, and V. Dyakonov, Influence of nanomorphology on the photovoltaic action of polymer-fullerene composites, *Nanotechnology*, 2004, **15**, 1317-1323.

23. Y. Kim, S. A. Choulis, J. Nelson, D. D. C. Bradley, S. Cook, and J. R. Durrant, Device annealing effect in organic solar cells with blends of regioregular poly(3-hexylthiophene) and soluble fullerene, *Appl.Phys.Lett.*, 7-2-2005, **86**, 063502.

24. X. N. Yang, J. K. J. van Duren, M. T. Rispens, J. C. Hummelen, R. A. J. Janssen, M. A. J. Michels, and J. Loos, Crystalline organization of a methanofullerene as used for plastic solar-cell applications, *Adv.Mater.*, 17-5-2004, **16**, 802-806.

25. F. Iwatsu, T. Kobayashi, and N. Uyeda, Solvent Effects on Crystal-Growth and Transformation of Zinc Phthalocyanine, *Journal of Physical Chemistry*, 1980, **84**, 3223-3230.

26. J. C. Conboy, E. J. C. Olson, D. M. Adams, J. Kerimo, A. Zaban, B. A. Gregg, and P. F. Barbara, Impact of solvent vapor annealing on the morphology and photophysics of molecular semiconductor thin films, *Journal of Physical Chemistry B*, 4-6-1998, **102**, 4516-4525.

27. S. H. Kim, M. J. Misner, and T. P. Russell, Solvent-induced ordering in thin film diblock copolymer/homopolymer mixtures, *Adv.Mater.*, 27-12-2004, **16**, 2119-2123.

28. F. L. Zhang, M. Svensson, M. R. Andersson, M. Maggini, S. Bucella, E. Menna, and O. Inganas, Soluble polythiophenes with pendant fullerene groups as double cable materials for photodiodes, *Adv.Mater.*, 17-12-2001, **13**, 1871-1874.

29. Y. Zhao, Z. Y. Xie, Y. Qu, Y. H. Geng, and L. X. Wang, Solvent-vapor treatment induced performance enhancement of poly(3-hexylthiophene): methanofullerene bulk-heterojunction photovoltaic cells, *Appl.Phys.Lett.*, 22-1-2007, **90**, 043504.

30. G. Li, Y. Yao, H. Yang, V. Shrotriya, G. Yang, and Y. Yang, "Solvent annealing" effect in polymer solar cells based on poly(3-hexylthiophene) and methanofullerenes, *Adv.Func.Mater.*, 9-7-2007, **17**, 1636-1644.

31. G. H. Lu, L. G. Li, and X. N. Yang, Achieving perpendicular alignment of rigid polythiophene backbones to the substrate by using solvent-vapor treatment, *Adv.Mater.*, 5-11-2007, **19**, 3594-3598.

32. S. Miller, G. Fanchini, Y. Y. Lin, C. Li, C. W. Chen, W. F. Su, and M. Chhowalla, Investigation of nanoscale morphological changes in organic photovoltaics during solvent vapor annealing, *J.Mater.Chem.*, 2008, **18**, 306-312.

33. J. K. Lee, W. L. Ma, C. J. Brabec, J. Yuen, J. S. Moon, J. Y. Kim, K. Lee, G. C. Bazan, and A. J. Heeger, Processing additives for improved efficiency from bulk heterojunction solar cells, *J.Am.Chem.Soc.*, 19-3-2008, **130**, 3619-3623.

34. J. Peet, J. Y. Kim, N. E. Coates, W. L. Ma, D. Moses, A. J. Heeger, and G. C. Bazan, Efficiency enhancement in low-bandgap polymer solar cells by processing with alkane dithiols, *Nat.Mater.*, 2007, **6**, 497-500.

35. S. A. Gevorgyan and F. C. Krebs, Photovoltaics Based on Thiophene Polymers: a Short Overview, *John Wiley & Sons Ltd*, 2009, ch. 18,673-693.

36. C. H. Woo, B. C. Thompson, B. J. Kim, M. F. Toney, and M. J. Frechet, The Influence of Poly(3-hexylthiophene) Regioreigularity on Fullerene-Composite Solar Cell Performance, *J.Am.Chem.Soc.*, 2008, **130**, 16324-16329.

37. R. C. Hiorns, R. De Bettignies, J. Leroy, S. Bailly, M. Firon, C. Sentein, A. Khoukh, H. Preud'homme, and C. Dagron-Lartigau, High molecular weights, polydispersities, and annealing temperatures in the optimization of bulk-heterojunction photovoltaic cells based on poly(3-hexylthiophene) or poly(3-butylthiophene), *Adv.Func.Mater.*, 3-11-2006, **16**, 2263-2273.

38. W. Ma, J. Y. Kim, K. Lee, and A. J. Heeger, Effect of the molecular weight of poly(3-hexylthiophene) on the morphology and performance of polymer bulk heterojunction solar cells, *Macromolecular Rapid Communications*, 3-9-2007, **28**, 1776-1780.

39. P. Schilinsky, U. Asawapirom, U. Scherf, M. Biele, and C. J. Brabec, Influence of the molecular weight of poly(3-hexylthiophene) on the performance of bulk heterojunction solar cells, *Chem.Mater.*, 19-4-2005, **17**, 2175-2180.

3 Characterization

3.1 Introduction

An important part in the research of OPVs is the proper understanding and characterization of the devices in terms of both chemical and morphological properties and photovoltaic performance. There are numerous techniques for characterization, which can be divided into two categories: (i) techniques that provide either morphological and/or chemical information from specific spatial locations in the device, and (ii) techniques that provide information from e.g. all layers and typically averaged over a large area perpendicular to the thickness of the device. The usage of such techniques has been already demonstrated in Chapter 2 when studying the processing of P3HT based devices.

This chapter starts with short introductions to the most of the characterizing techniques that have been used during the PhD project.

Recently, new types of thermocleavable polymers have been developed, which show rather promising properties regarding the morphological stability. Part of this chapter presents studies of various thermocleavable polymers and detailed characterization of the devices based on such materials.

Another part involves studies of inverted devices. Number of advantages of inverted devices over the normal geometry is discussed and comparison of PV performance for both types of devices is demonstrated. The last section of the chapter presents the studies of MoO_3 and V_2O_5 as buffer layers instead of PEDOT:PSS in traditional devices.

3.2 Various Characterizing Techniques

3.2.1 IV Curve and IPCE Measurements

One of the primary technique for evaluation of device performance is based on simple measurements of the diode characteristics of the solar cell. The method requires a source meter. By varying the applied voltage in a certain range and measuring the corresponding current of the device

the IV curves can be built. Values such as V_{oc}, I_{sc}, FF, PCE, R_{sh}, R_s can be then extracted from the measured IV curves during device illumination, which are the most important parameters that define the device performance (see Chapter 1). Dark IV characteristics are also very useful for extracting information about series resistance, shunt resistance, saturation currents and ideality factors.[1]

While studying the degradation of devices it is essential to measure all the diode characteristics periodically, since depending on the type of material and measuring conditions each photovoltaic parameter might behave differently. Often the decay of device efficiency is a direct result of the decay of photocurrent. However, in some cases the decay of FF and even V_{oc} can result in decrease of PCE as well (see for example Appendix 2.1).

In addition, an important quantity to measure is the quantum efficiency (QE) or incident photon to charge carrier efficiency (IPCE). IPCE gives information whether the absorbed photons are being efficiently converted to charge carriers and collected at the electrodes. Systems with different operational mechanisms have been developed for measuring IPCE. The most common principle for measuring IPCE relies on shining a monochromatic light with known intensity (number of photons) on a device and measuring the generated current (number of electrons) while changing the wavelength of the light throughout the absorption spectrum range of the device.

3.2.2 UV-vis Spectroscopy

UV–vis spectroscopy is a straight forward technique for measuring the spectral absorption distribution of the films in the wavelength range from near ultraviolet to near infrared. The method is simply realized by shining monochromatic light on the sample film and recording the transmitted light. The sample can be a pure glass substrate with coated film to be tested. The absorption for given wavelength can be calculated from the value of the transmitted light. From the absorption measurements one can roughly estimate the optical bandgap of the absorbing semiconductor. The absorption spectrum measurements can also help in recording morphology changes (such as crystallinity of the polymer) in the materials or blends during device processing (for example after thermal annealing) as was shown in Chapter 2.

3.2.3 Photoluminescence Spectroscopy

Photoluminescence (PL) spectroscopy is a contactless, nondestructive method of probing the electronic structure of materials. Light is directed onto a sample, where it is absorbed and imparts excess energy into the material. One way this excess energy can be dissipated by the sample is through the emission of light, or luminescence. In the case of photo-excitation, this luminescence is called photoluminescence.

This technique can be used for defining the effectiveness of the excited charge separation at the interface between donor and acceptor. When the polymer material is shined with light, the polymer emits light through the photoluminescence process. When an acceptor material such as PCBM is added in the mixture a quenching of photoluminescence takes place, since some of the excitons are separated at the interface and the radiative recombination is reduced. When a complete quenching is achieved it indicates that all the excited pairs are successfully separated to free carriers. As an example, Figure 3.1 shows the absorption spectrum of polymer **10** (described in Section 3.4.4) together with PL of films spin coated from blends of the polymer with different ratio of PCBM. Clearly over 60% of PCBM in the mixture is already resulting in significant quenching of PL due to the effective exciton dissociation to free carriers at the interface.

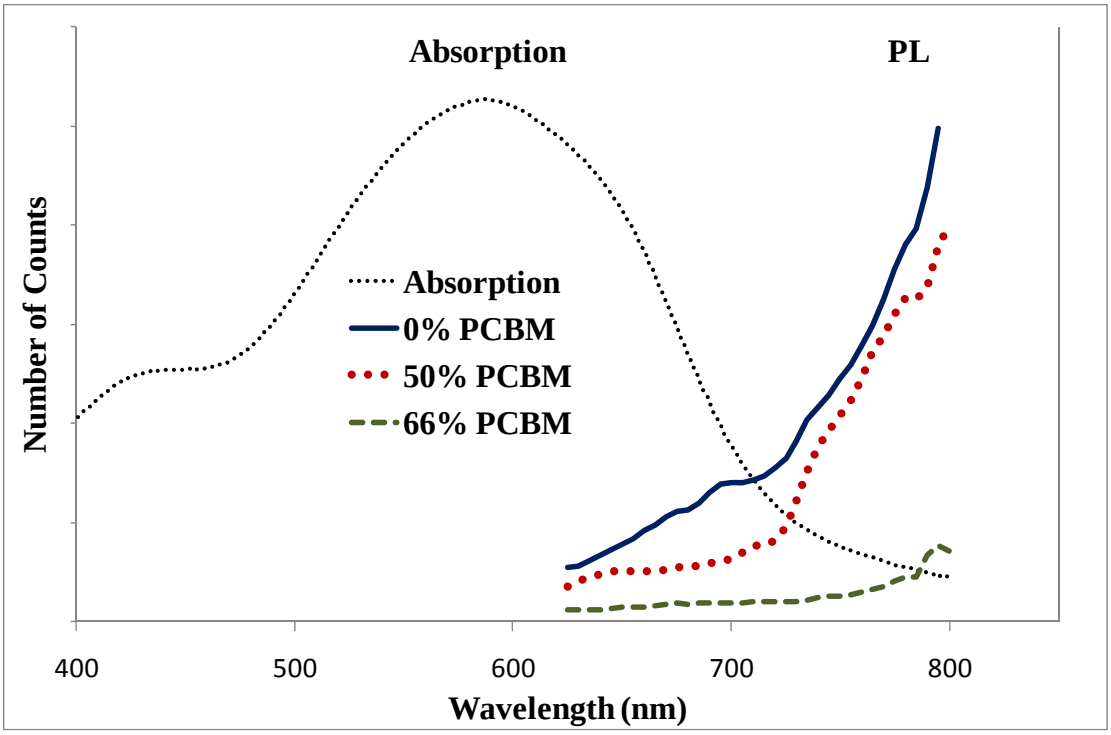

Figure 3.1: Absorption spectra and photoluminescence of polymer **10** described in Section 3.4.4. The photoluminescence was measured for three different rations of the polymer with PCBM.

3.2.4 Atomic Force Microscopy

Atomic Force Microscopy (AFM) is an imaging technique that typically maps the surface with respect to surface topography (can, however, provide chemical contrast information if used in alternative modes). AFM can cover only a limited analysis area, but has an excellent lateral resolution (Ångstrøm range) and an excellent height resolution (Ångstrøm range), which makes it the obvious choice for the study of OPV film morphology. The typical application for AFM with regard to OPVs has been to monitor and thus optimize the nanostructure of bulk heterojunction blend films in order to optimize the OPV efficiency. It is also a powerful tool to investigate the degradation of the devices due to morphology changes.

The operating principle of AFM is as follows: The AFM consists of a cantilever with a sharp tip (probe) used to scan the specimen surface. When the tip is brought into proximity of a sample surface, forces between the tip and the sample lead to a deflection of the cantilever. The amount of reflection of the cantilever is recorder by the reflection of the laser beam from the cantilever surface. By scanning certain area the 3 dimensional image of the surface can be plotted. Some examples of AFM studies of active layer surface were presented in Chapter 2.

3.2.5 Scanning Electron Microscopy

Scanning Electron Microscopy (SEM) is an imaging technique and has become a standard tool for visualizing morphology in OPVs. The strength of the technique is the superior lateral resolution and the capability of analyzing a broad range of scales from nanometer range to millimeter range. The weakness is the lack of a depth scale. Just as AFM the typical application for SEM with regard to OPVs has been to monitor and thus optimize nanostructures in order to optimize the OPV efficiency. SEM is, mainly because of the superior lateral resolution, capable of visualizing the bulk morphology of OPVs by imaging a cross-section of the device.

SEM operation is based on directing the accelerated electron beam on specimen, where by interacting with the material the electrons decelerate emitting various signals. These signals include secondary electrons (that produce SEM images), backscattered electrons (BSE), diffracted backscattered electrons (EBSD that are used to determine crystal structures and orientations of minerals), photons (characteristic X-rays that are used for elemental), visible light (cathodoluminescence – CL), and heat.

3.3 Thermocleavable Polymers

A large part of this project was devoted to production and characterization of devices based on thermocleavable materials. One way to increase the stability of organic solar cells is to render the active layer more rigid, which can slow down the degradation processes in the film.[2] (A detailed description of stability issues is described in the next chapter) One way of doing this by solution processable precursors is to use thermocleavable materials. [2-15] The general principle of the method is shown in Figure 3.2, where insolubility is induced *post* film formation by removal of the solubilising side chains.

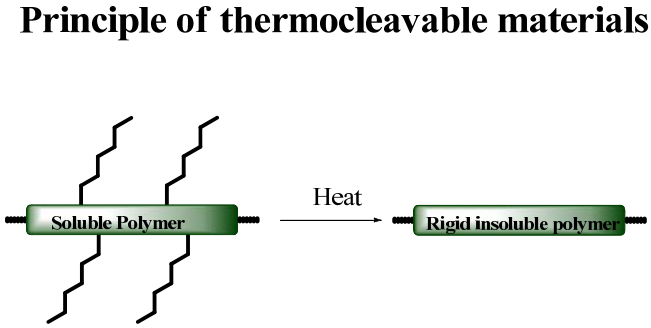

Figure 3.2: Schematic illustration of the side chain removal.

One important aspect to the principle is that it opens up the possibility of creating multilayered structures by sequential processing. After rendering the first layer insoluble a subsequent layer can be applied, since the insoluble layer is no longer influenced by the processing.

The use of thermocleavable materials addresses the issue of stability as well as the issue of optimisation of device performance by removal of non-absorbing material from the active layer. As most of the polymer solar cell production is based on solution processing, it requires for the materials to be soluble. Native polythiophene (PT) for example is an insoluble material and in order to achieve solubility, solubilising side chains such as alkyl groups are attached onto the conjugated polymer backbone. However, after thin film formation there is no need for side chains anymore as they make up a significant proportion of the polymer (in the case of P3HT, the hexyl groups account for 50% of the material weight) and are passive in terms of light harvesting and charge transport. In addition, the side chains make the material soft, which affects the morphological and

chemical stability of the active layer.[16,17] As a consequence, devices based on materials with side chains can be rather unstable, while films that at a final stage do not have solubilising chains can form a more rigid and stable morphology, which can lead to an increase of the glass transition temperature of the material and therefore to thermally stable devices.[2,4,16,18]

The following subsections are briefly presenting the studies of thermocleavable materials and characterization of the devices based on such materials carried out during this project.

3.3.1 Bulk Heterojunctions Based on Native Polythiophene

This section presents the overview of a published article, the reprint of which can be found in Appendix 2.1.

As was mentioned above it is a subject of a great interest to prepare devices with a solution processed active layer, which after processing doesn't contain solubilizing chains. From a fundamental point of view, a bulk heterojunction between native polythiophene and a soluble fullerene derivative such as [60]PCBM or [70]PCBM represents a challenge that cannot be met using known procedures as native (unsubstituted) polythiophene is an insoluble and intractable material. The polymer material poly-(3-(2-methylhex-2-yl)-oxy-carbonyldithiophene) (P3MHOCT) developed by the group of J. M. J. Fréchet was shown to convert to poly-3-carboxydithiophene (P3CT) at temperatures of ~200 °C through elimination of 2-methylhexene.[12] It was later shown by ^{13}C labeling studies and solid-state NMR that P3CT could be further converted to native polythiophene (PT) at temperatures of ~300 °C by decarboxylation.[3] Figure 3.3 schematically represents the conversion of P3MHOCT to P3CT and further to PT.

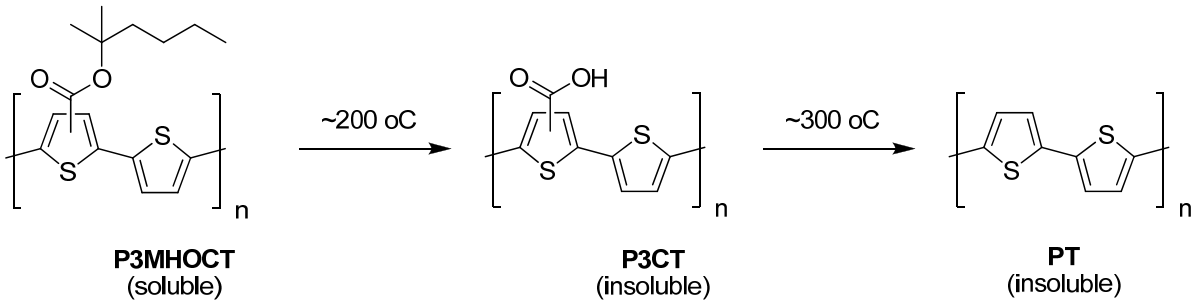

Figure 3.3: Chemical transformation of P3MHOCT to P3CT at ~200 °C and further transformation to PT at ~300 °C.

The task of this work was to produce films based on solution processed bulk heterojunction blend of P3MHOCT:PCBM and to study the subsequent chemical conversion of the polymer via thermal processing into P3CT and PT followed by production of solar cell devices based on such films and characterization of these devices.

Regiorandom P3MHOCT had the following properties: M_n = 11 624 g mol^{-1}, M_w = 28 266 g mol^{-1}, M_p = 27 505 g mol^{-1}, PD = 2.564. For the film production the bulk mixture of the polymer and PCBM dissolved in dichlorobenzene (DCB) (with combined concentration of 40 mg/ml and ration of 1:1 between the donor and acceptor) was spin coated on pure glass slide and annealed on a hot plate at required temperatures for desired chemical conversion. For production of solar cell devices a PEDOT:PSS as a 1.3 wt % aqueous solution was spin-coated on top of a glass substrate with 100 nm thick ITO (sheet resistivity 8-12 Ω □$^{-1}$) at a rotational speed of 2800 rpm, and the slides were annealed at 160 °C for 5 min. Subsequently, an active layer of a mixture containing P3MHOCT and [60]PCBM or [70]PCBM was spin-coated onto the PEDOT:PSS. The samples were then annealed at the different temperatures chosen in the range between room temperature and 310 °C. The annealing time was kept at 30 s for the temperatures up to 250 °C and at 10 s for temperatures above 250 °C. Longer annealing times lowered the V_{oc}. The aluminum metal electrode was evaporated on top after the thermal annealing to complete the devices. The devices had an active area of 3 cm^2 and were tested for photovoltaic performance and stability. The photovoltaic performance was tested under a solar simulator where the irradiance and emission spectrum were checked carefully using an optical spectrum analyzer in conjunction with a precision radiometer from Eppley Laboratories. The spectrum during characterization of the solar cell efficiency was AM1.5G with an incident light power of 1000 W m^{-2}.

As a first step, for testing the absorption properties the films of P3MHOCT/[60]PCBM or [70]PCBM blends were coated on glass substrates and annealed at different temperatures. For obtaining P3CT the samples were annealed at temperatures in the range from 190 to 270 ^{o}C for more than 30 seconds period. For obtaining PT the cells were annealed at 300 ^{o}C or more (technical limitation 310 ^{o}C). The chemical conversions were accompanied by color change of the film visible for eye: color changes from red to yellow for conversion from P3MHOCT to P3CT and again from yellow to purple-red indicating conversion from P3CT to PT. The brief periods of heating time involved here possibly do not give rise to full chemical conversion of the device film, and it is reasonable to assume that the films are composite mixtures representative of the chemistry that is accessible at the given processing temperatures. Figure 3.4 (a) shows the image of the films

annealed at different temperatures, while Figure 3.4 (b) shows the UV-vis absorption spectra of the films spin coated from blends of P3MHOCT:[60]PCBM or [70]PCBM. The change of absorption during the annealing of the film is evident. In addition, a small shift of the absorption peak at 500 nm toward longer wavelength can be seen.

As a next step solar cell devices were produced based on different compounds of active material (P3MHOCT, P3CT or PT as donors and [60]PCBM or [70]PCBM as acceptors).

Figure 3.5 (a) shows the plot of the efficiency of the cells versus annealing temperature. The vertical lines separate regions that correspond to different polymers. The decrease of the efficiency in the first region was mostly due to the open circuit voltage of the cells being rather sensitive to thermal stresses (complete sets of IV-curves and graphs of V_{oc}, I_{sc}, and FF are provided in the Supporting Information in Appendix 2.2). The devices in the range of P3CT had the lowest PCE, while the cells with native polythiophene had the best performance with highest PCE reaching 1.5 % for the device with PT:[70]PCBM combination.

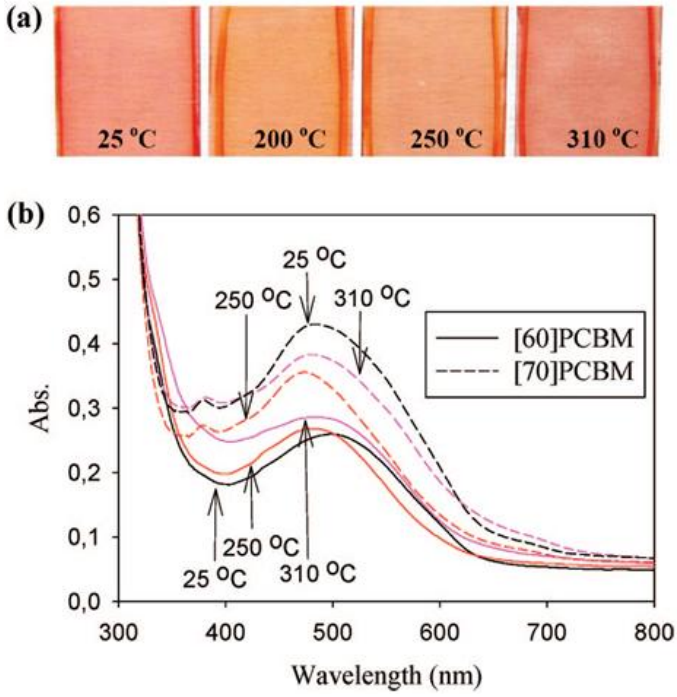

Figure 3.4: (a) A photograph showing the appearance of films based on [70]PCBM when heated to different temperatures. (b) UV-vis spectra of films based on P3MHOCT and [60]PCBM or [70]PCBM mixtures spin coated on glass slides and annealed at three different temperatures (25, 250, and 310 °C). Vertical axes correspond to the absorption of the films as measured in transmission geometry neglecting the reflection losses.

SEM analyses were carried out on the device surface after pilling of the aluminum electrode. Figure 3.5 (b, c and d) shows the images for devices annealed at three different temperatures. From the images of P3MHOCT and P3CT (Figure 3.5 (b) and (c) respectively) it is hard to see the nature of the phase separation in the bulk, while in the case of PT (Figure 3.5 (d)) certain grainy features are evident, which are most probably due to PCBM clusters grown during the annealing process.

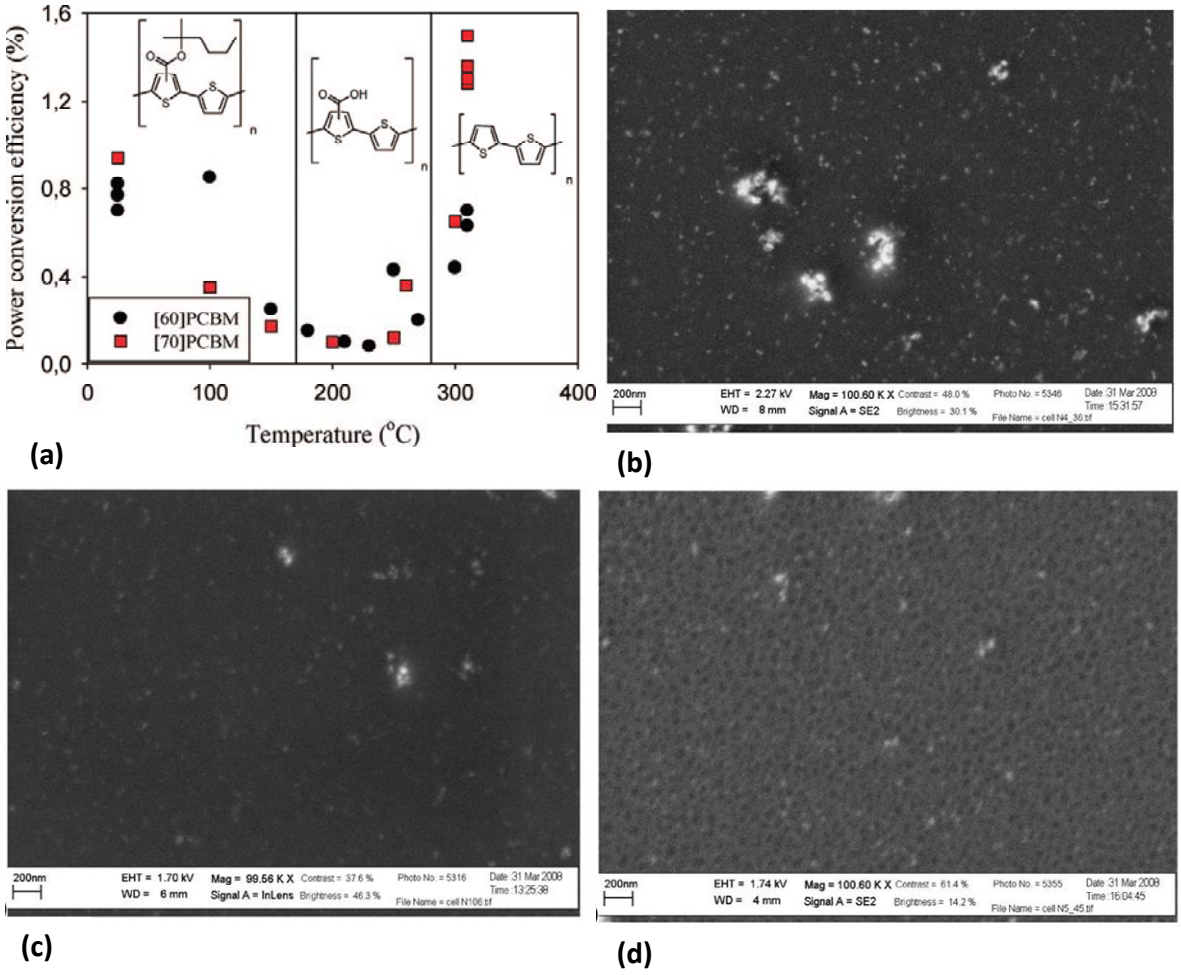

Figure 3.5: Efficiency versus annealing temperature for the cells with P3MHOCT polymer and [60]PCBM (●) or [70]PCBM (red ■) mixture measured under 1000 W m-2, AM1.5G, 70 °C conditions. The vertical lines show the temperatures at which the thermocleavage becomes significant upon increasing the temperature. The conversion is irreversible. SEM images of the surfaces of films based on P3MHOCT and [60]PCBM compound treated at (a) room temperature, (b) 200 °C, and (c) 310 °C are shown as well.

The PCE of the bulk heterojunctions in the as-formed films was generally observed to be in the range of 0.7 - 0.9% and was found to decrease as the device film was annealed in the range of temperatures below the transformation of P3MHOCT to P3CT. A broad minimum is then seen as the first cleavage temperature is reached, and all the devices based on P3CT were the poorest performing (PCE was in the range of 0.1 - 0.4%). When reaching the temperatures of the second transformation from P3CT to PT, an increase in power conversion efficiency was observed from the low value of 0.1 - 0.4% up to 0.6% in the case of [60]PCBM and as high as 1.5% in the case of [70]PCBM. [70]PCBM devices showed the largest improvement, which may be linked not only to morphology but also to better light harvesting properties of [70]PCBM as compared to [60]PCBM. It should, however, be noted that devices based on [60]PCBM and [70]PCBM generally gave the same result at processing temperatures below 300 °C. One possible explanation of the decrease in performance at annealing temperatures below 190 – 210 °C could be that the morphology changes and that the fullerene component grows to form large crystallites. However, from SEM images it is hard to link the device performance to the morphology changes in the films.

Two possible explanations are given for such performance of devices: first, slight changes in the optical properties may account for some of the degradation and further increase in performance (the effect of this is expected to be minor if present). The second and more likely explanation is that the performance of the three different devices based on respectively P3MHOCT, P3CT, PT, and [60]PCBM exhibits typical performances in the ranges of 0.7 - 0.8%, 0.1 - 0.2%, and 0.6 - 0.7%. For the three different devices based on respectively P3MHOCT, P3CT, PT, and [70]PCBM, typical performances in the ranges of 0.9%, 0.1%, and 1.3 - 1.5% are observed. At the intermediate temperatures, cleavage may take place to a small extent as evidenced from the weight loss during TGA experiments.[3] We thus propose that the observed changes in performance with temperature represent a complex interplay between morphological changes and changes in the chemistry of the film.

In addition, lifetime measurements were carried out for aforementioned devices. The detailed discussion of the degradation experiments and results can be found in Section 4.4.1.

To summarize, it was shown that a simple bulk heterojunction precursor film can be prepared from P3MHOCT thermocleavable polymer by solution processing compatible with the state of the art procedures. It was shown also how it can be processed into chemically different bulk heterojunctions through a simple thermal treatment. While there was no difference in the processing

conditions, there was a slightly lower performance in terms of the power conversion efficiency than the current state of the art, while there was a relative increase in performance as the processing temperature was increased, and efficiencies up to 1.5% could be achieved for bulk heterojunctions based on native polythiophene and [70]PCBM under simulated sunlight (1000 W/m^2, AM1.5G, 70 °C).

We believe that a better understanding of the complex interplay between morphological changes and the chemistry of the film as a function of temperature could lead to significant improvements in both device performance and operational stability.

3.3.2 Thermocleavable Materials for OPVs with High Open Circuit Voltages

Lenes *et al.* reported improvement of P3HT device V_{oc} and therefore PCE using bis-adduct (bisPCBM) as an acceptor in the active bulk. The V_{oc} was increased from 0.58 to 0.73 V and PCE from 3.8 % to 4.5 % by substituting regular PCBM with bisPCBM in the blend with P3HT. According to the cyclic voltammetry (CV) measurements performed by the group the LUMO level of bisPCBM is higher by 0.1 eV relative to LUMO of PCBM. Thus, an increase of V_{oc} is expected.

Since P3MHOCT is delivering higher V_{oc} values compared to regular P3HT, it was interesting to test it in combination with bisPCBM in attempt to achieve high voltage devices. bisPCBM was tested in combination with both P3HT and P3MHOCT polymers. The experimental procedures for production of solar cells were similar to the ones described in the previous section.

Figure 3.6 presents the IV curves together with a table showing the PV parameters for devices with various blends. The V_{oc} for P3HT based devices was improved by only 20 mV (from 0.58 to 0.6 V) and the PCE from 2.1 to 2.4 % when substituting PCBM with bisPCBM. A significant increase of V_{oc} was however achieved for thermocleavable polymer. The voltage improved by 100 mV for P3MHOCT based devices and by 200 mV for PT based devices. V_{oc} of 0.97 V was obtained for the device with PT:bisPCBM combination although accompanied with significant decrease of PCE (0.63 %) due to the lost in photocurrent.

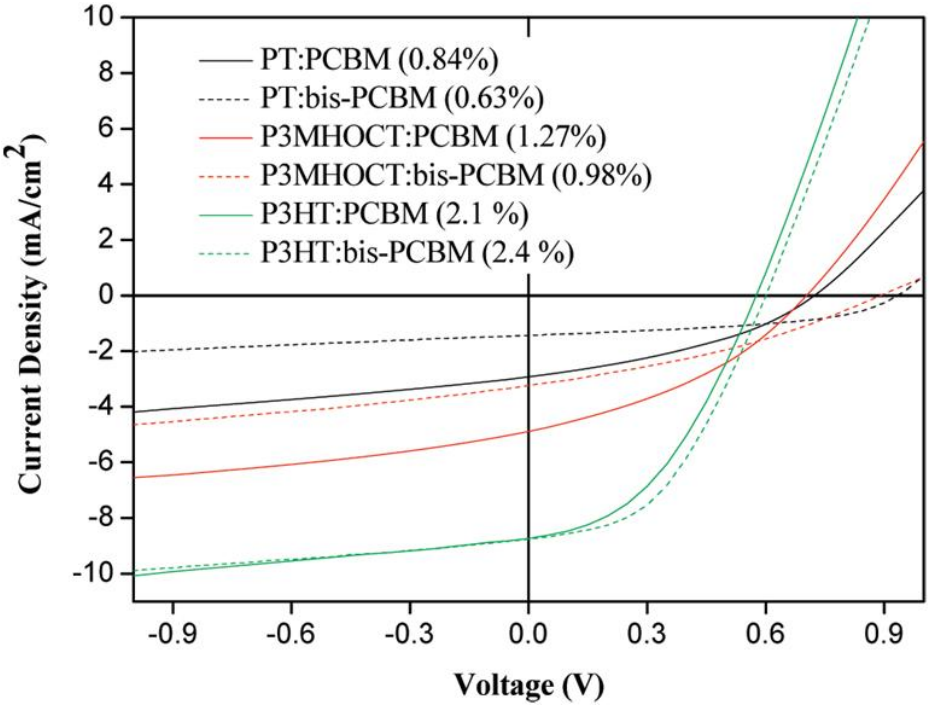

PV parameters	J_{sc} (mA/cm^2)	V_{oc} (V)	FF (%)	PCE (%)
PT:PCBM	3.26	0.75	41.16	0.84
PT:bisPCBM	1.53	0.97	51.07	0.63
P3MHOCT:PCBM	4.9	0.73	39.53	1.27
P3MHOCT:bisPCBM	3.23	0.9	35.61	0.98
P3HT:PCBM	8.95	0.58	44.38	2.12
P3HT:bis-PCBM	8.76	0.6	45.57	2.4

Figure 3.6: I-V curves for the best solar cells obtained for P3HT, PT and P3MHOCT under 1 sun illumination. The PCE values of the cells are also shown.

Interestingly the short circuit current density J_{sc} is not affected by using bisPCBM instead of PCBM in P3HT based devices, while it is nearly halved in P3MHOCT or PT. One of the possible explanation can be that the offset of LUMO levels of P3HT and acceptor is so big (nearly 0.8 eV) that 0.1 eV shift up by bisPCBM does not affect the charge separation efficiency, while in case of the thermocleavable polymer the offset somewhat smaller and therefore further decrease of the offset is detrimental for the performance.

More detailed discussion on the proposed scenario can be found in the article presented in Appendix 3, which further discusses the characterization of these devices. The article presents the comparative studies of these devices and discusses the possible reasons for such device performance.

To summarize, it was possible to achieve devices with V_{oc} approaching 1 V by substituting regular PCBM material with bisPCBM, although the PCEs were rather low. Such devices show a potential for high efficiency and further research can lead to production of devices with high efficiency and high voltage output.

3.3.3 Thermocleavable Low Band Gap Polymers

Similar to studies in previous sections characterization of low band gap thermocleavable polymers was carried out. Polymers based on diphenyldithienylthienopyrazine with different ester groups synthesized by Petersen *et al.* (see Appendix 4) have been characterized for photovoltaic performance. The reason it was interesting to study this polymer is because it has rather low optical band gap (in the range of 1.17 -1.37 eV), which can possibly increase the harvesting of photons.

Figure 3.7 shows the process of syntheses of the polymer together with the list of different ester groups. Figure 3.8 shows the deesterification process by heating the polymer.

The polymers with different ester groups varied by their solubility and for some of them it was impossible to use solution processing techniques, since they could not be dissolved in solvents. For the ones that were soluble DCB was found to be the optimal solvent. The optimal ratio of the polymer and PCBM was found to be 1:1 with combined concentration of 40 mg/ml. The cleaving process for these polymers differs from P3MHOCT discussed in the previous sections, since in this case the thermal cleavage is not accompanied by color change. It was tested by manually removing the polymer off the substrate with cotton stick soaked in a solvent. In case of complete cleaving it was impossible to remove the polymer from the surface of the substrate. The TGA measurements showed that the ester elimination for all the polymers starts at temperatures in the range from 210 to 290 ^{o}C, while the decarbolization starts only at 400 – 500 ^{o}C range. In this study, only the first step of deesterification was studied.

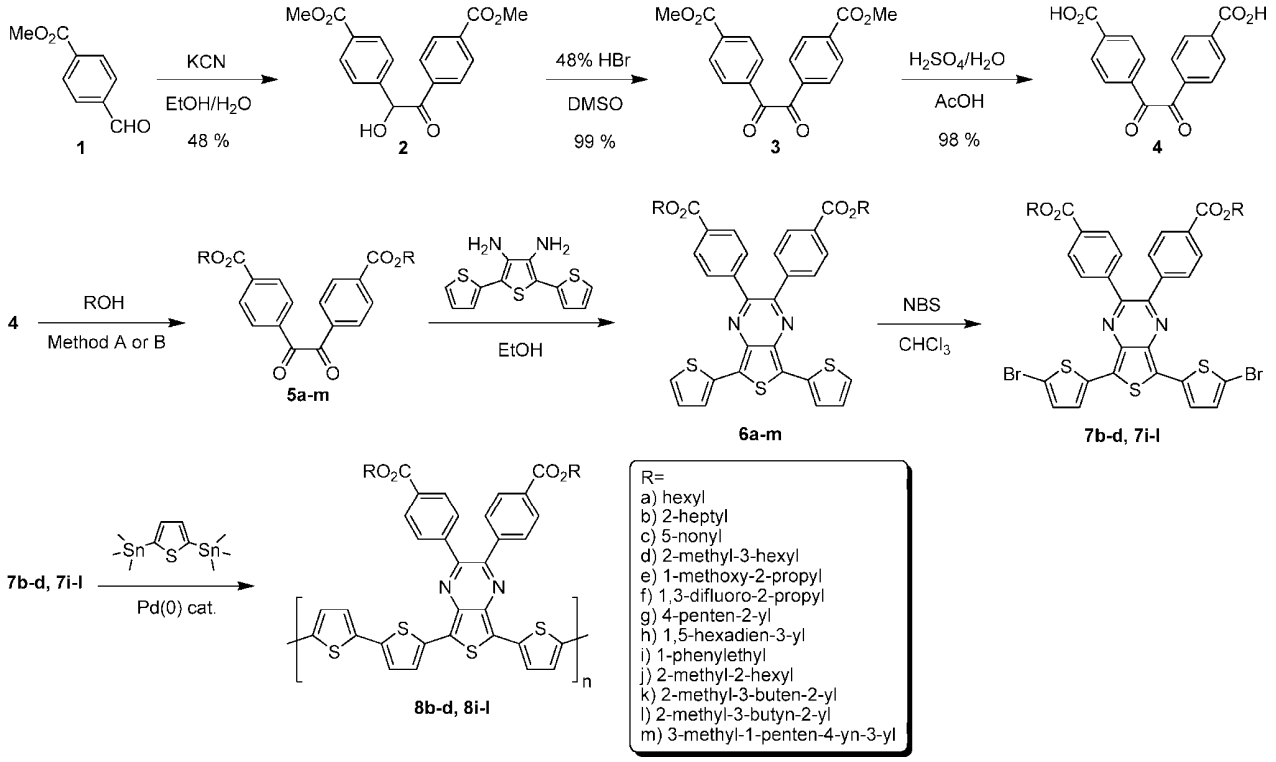

Figure 3.7: Synthesis of the Dithienylthienopyrazines 6a-m and the Polymers 8b-d, 8i-l with Thermocleavable Benzoate Esters Substituted on the Pyrazine Ring

Figure 3.9 left shows the IV curves for the polymers that have been studied (the rest of the polymers were impossible to process due to insolubility). Figure 3.9 right shows the IV curves for the same polymers after cleaving. Apart from the polymer **8j** the cleaving of other polymers resulted in drastic decrease of performance.

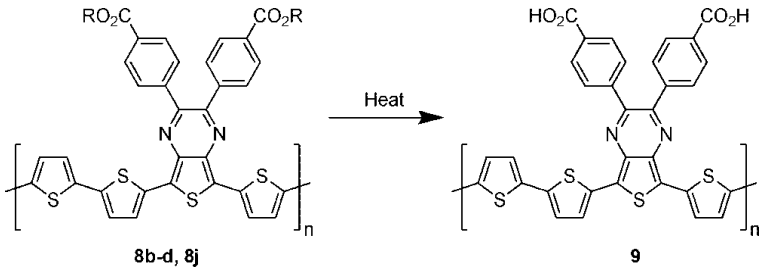

Figure 3.8: Thermocleavage of the the Polymer Materials 8b, 8c, 8d, or 8j All Lead to the Same Polymer Material **9**.

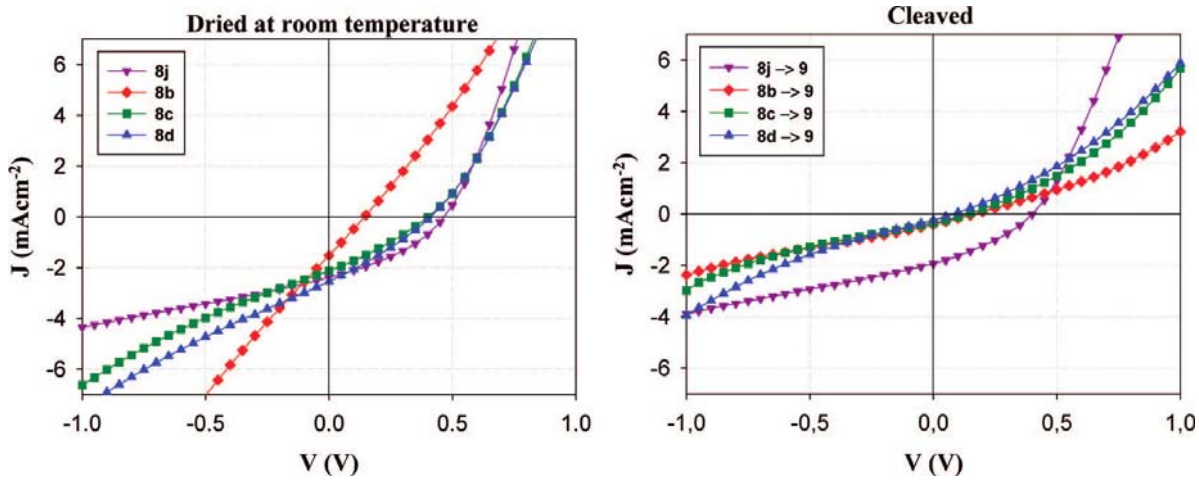

Photovoltaic Parameters of the Reported Materials with and without Thermocleaving[a]

Polymers	J_{sc} (mA/cm^2)	V_{oc} (V)	FF (%)	PCE (%)	Cleaving Temp. °C[b]	Solubility
8b	1.52	0.14	25	0.05	Not cleaved	Good
	0.41	0.16	26	0.017	310	
8c	2.1	0.4	29	0.25	Not cleaved	Poor
	0.36	0.14	27	0.013	310	
8d	2.55	0.41	29	0.3	Not cleaved	Good
	0.24	0.08	26	0.05	310	
8j	2.4	0.46	36	0.4	Not cleaved	Good
	1.94	0.4	33	0.25	230	

a The devices had a glass/ITO/PEDOT:PSS/polymer:PCBM/Al geometry and the performance was recorded immediately after preparation in the ambient atmosphere (1000 W m-2, AM1.5G, 72 (°C, humidity 30 (5% rh)
b The duration of cleaving at 230 °C was 1 min and at 310 °C was 10 min

Figure 3.9: IV-curves of the devices based on 4 different polymers (**8b**, **8c**, **8d** and **8j**). Left image corresponds to uncleaved and right to cleaved devices. The polymers **8b**, **8c**, and **8d** were cleaved at 310 °C for 10 min and the polymer **8j** was cleaved at 230 °C for 1 min.

The Table in Figure 3.9 shows the photovoltaic parameters of the measured cells. The devices had a glass/ITO/PEDOT:PSS/polymer:PCBM/Al geometry and the performance was recorded immediately after preparation in the ambient atmosphere (1000 W/m^2, AM1.5G, 72 ± 2 °C, humidity 30 ± 5% rh). Despite the fact that the photovoltaic performance of such devices was rather poor, polymer 8j showed some potential for higher efficiencies in case of further optimization. More interestingly, stability of such devices was rather promising, as will be shown in Section 4.4.2.

To summarize, while production of OPV devices based on low band gap thermocleavable polymers was demonstrated, it was not possible to obtain devices with reasonably high efficiencies

within the scope of this work. However, further characterization and optimization of such materials is vital, since such materials can provide devices with rather high stability as will be shown in Chapter 4.

The further description of the polymer synthesis and device production and characterization can be found in the reprint of the published article in Appendix 4.

3.3.4 Characterization of Substituted 2,1,3-Benzothiadiazole- and Thiophene-Based Thermocleavable Polymers

Another type of a thermocleavable polymer (numbered as **10**) based on 2,1,3-benzothiadiazole (PDTBT) and thiophene units synthesized by Petersen *et al.* (see Appendix 5) was characterized as well. The choice of materials with such molecular structure was motivated by the fact that PDTBT based polymers in combination with PCBM deliver devices with efficiencies more than 6%.

Figure 3.10 shows the molecular structure of this material together with specific parameters, such as average molecular weight, polydispersity index (PDI) and the optical band gap E_g. The cleaving temperature was found to be around 285 ^{o}C. Using the photoluminescence quenching technique it was found that the optimal donor:acceptor ratio for this material is 1:4 with PCBM having the 80 % of the volume. Figure 3.11 shows the absorption spectrum for the polymer **10** in a solution and as a film cleaved at different temperatures. A shift towards the shorter wavelength is evident for the cleaved films. Figure 3.12 shows the IV curves for the corresponding devices based on polymer **10**:PCBM combination together with the table showing the PV parameters and the thickness of the active layers. The maximum efficiency was achieved for the cell cleaved at 285 ^{o}C for 15 seconds. The cell delivered 0.42 % PCE.

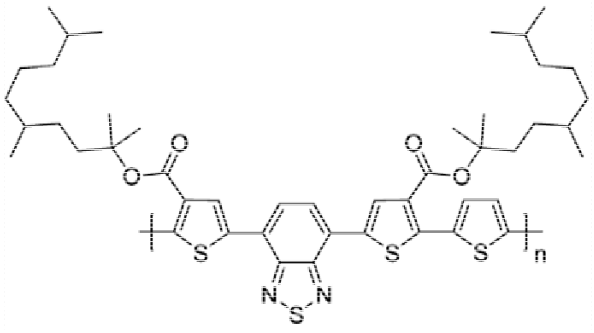

10

Mw (g/mol) = 173000

PDI = 2.6

Solution Eg (eV) = 1.96

Film Eg (eV) = 1.69

Figure 3.10: Molecular structure of thermocleavable polymer 10 based on 2,1,3-benzothiadiazole and thiophene units.

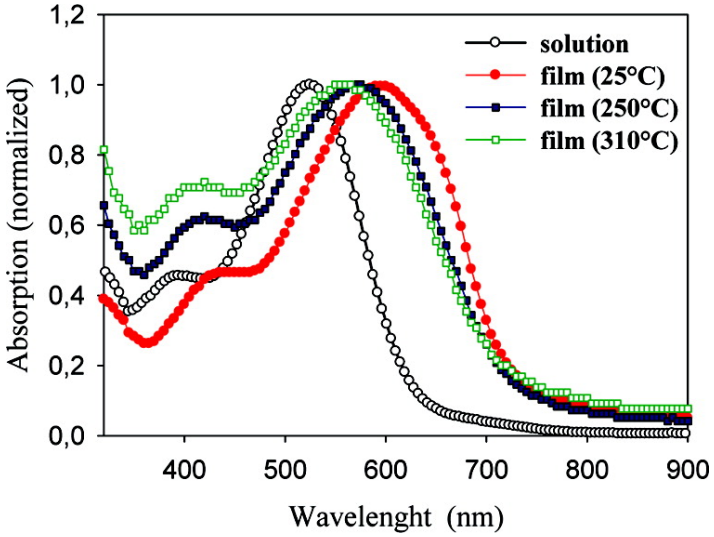

Figure 3.11: UV-vis absorption spectra of polymer **10** in chloroform solution and as a thin film cleaved at different temperatures.

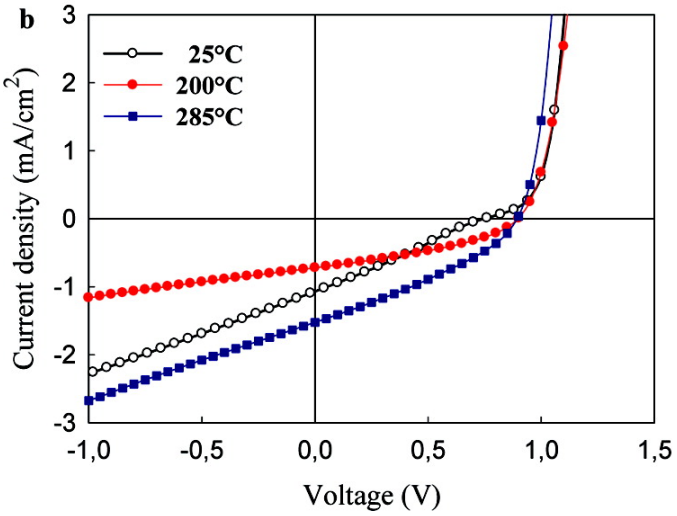

Cleaving (°C)	Layer Thick. (nm)	J_{sc} (mA/cm^2)	FF (%)	V_{oc} (V)	PCE (%)
-	92	1.07	26	0.75	0.21
200	92	0.72	37	0.9	0.24
285	78	1.36	34	0.9	0.42

Figure 3.12: IV curves for the polymer**10**:PCBM based devices with different cleaving temperatures and the table with PV parameters and thickness of the active layer.

Although the obtained PCE values are rather modest, these particular studies revealed a new category of thermocleavable polymers that show a potential for PV applications and deliver quite high voltage. Such polymers can also possibly result in very stable devices. Further synthesis and characterization of such materials are planned to be continued.

Further details of the synthesis and characterization of these polymers can be found in the article in Appendix 5.

3.4 Inverted Devices

Traditionally, the regular device structures are based on front transparent electrode (commonly ITO) acting as anode and back nontransparent electrode as cathode. If however the direction of the charge carriers is changed inside the device using electrode materials with different work functions, the device is then commonly named "inverted". There are a number of reasons why inverted geometry has became the choice of many groups for OPV production in the recent years.

i) The inverted device geometry gives the possibility to replace the interfacial layer of PEDOT:PSS as a buffer layer between ITO and active layer, which has been shown to introduce chemical and morphological instabilities at the interface with ITO.[19,20] In addition, PEDOT:PSS has non-negligible absorption in the visible region of the light spectrum[21] and substitution of PEDOT with more transparent TiOx or ZnO can drastically improve the absorption.

ii) Carrying out measurements on field effect transistors Waldauf *et al.* showed that the mobility of holes can be higher than that for electrons (in case of P3HT:PCBM combination).[22] While such difference might create unbalanced charge transport and space charge buildup in the device, in case of the inverted geometry this might be beneficial. Since illumination occurs through the bottom ITO electrode in both cell architectures, in inverted solar cells the holes have to travel over a longer distance compared to the slower-moving electrons (more excited carriers are created at the illuminated side of the layer). However, it must also be mentioned that the slight asymmetries in the charge transport become less relevant in the thin film devices, in which the carrier drift length under short circuit conditions is larger than the active layer thickness.

iii) Normally in the traditional devices Al metal is used for the back electrode, which has very good electron conduction properties, but it is also very reactive with surrounding environment. Therefore, the lifetime of the devices based on Al is significantly reduced. The inverted geometry allows choosing different materials less reactive with the surrounding environment, which can lead to more stable devices. The stability issue is discussed in details in Chapter 4.

iv) In addition the use of Al in normal geometry devices puts constrains on the speed and scale of the device production, since in order to make a good contact between organic layer and the metal Al electrode has to be evaporated, which requires slow vacuum processing step. Inverted geometry allows using silver instead of Al as a metal electrode and the advantage is that printable silver formulations are commercially available making solution processing of the silver electrode a possibility.[23]

For the aforementioned reasons part of this work was devoted to characterization of inverted devices. This section presents results of some of the most successful inverted devices produced during PhD project and comparison of the performance of inverted and normal device structures.

Devices with small active area size (1 cm^2) and various inverted structures have been produced on glass substrates and characterized. The most successful combination was substrate/ITO/ZnO/P3HT:PCBM/PEDOT:PSS/Ag. ZnO nanoparticles dissolved in CLB with 50 mg/ml ratio were used for the first intermediate layer. Since the spincoating of PEDOT:PSS on active layer is not easy (due to hydrophobicity of the active layer) special type of printable high viscosity PEDOT:PSS was used. Silver electrode was thermally evaporated using vacuum chamber.

Same level of performance was achieved for inverted device compared to the normal geometry. Figure 3.13 shows the device structures for both normal and inverted geometries and Figure 3.14 shows the measured IV curves together with the table showing the corresponding photovoltaic parameters for these devices. Both devices were characterized to efficiencies reaching 2.7 % value.

In addition, there have been attempts to produce inverted device based on P3HT polymer with silver paste as a back electrode using manual doctor blading, but the devices were short circuited probably due to the diffusion of the paste into the active layer. However, in the case of thermocleavable polymers, such as P3MHOCT (discussed in previous sections) it was possible to produce working solar cells possibly due to rigidity of the active layer after thermocleavage. Thus, in case of small model devices based on P3HT:PCBM active layer Ag electrode was commonly

applied via thermal evaporation. As was shown by Frederik Krebs in case of large printed devices the application of Ag paste was possible via a thick layer of PEDOT:PSS coated in between the active layer and the Ag electrode, which prevented the diffusion of the paste into the device. Device produced in such way were reported in the literature (see for example Appendix 6).

There was also an attempt to produce a device with Mg paste as a back electrode. The devices showed some photovoltaic performance. However the current density was very low due to low conductivity of Mg paste. Other metal pastes were also tested with no success in getting working devices. Thus, the only choice for electrode paste remained silver, which is commercially available and is being used for many electronic applications as printable electrode.

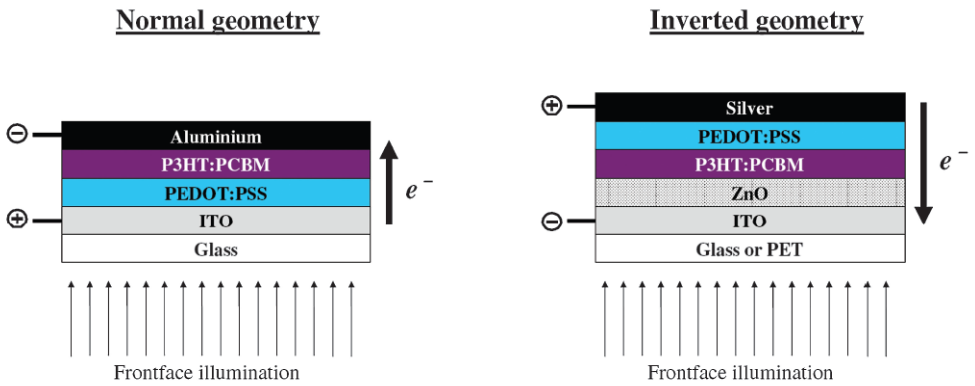

Figure 3.13: Schematic structures for normal and inverted geometry devices.

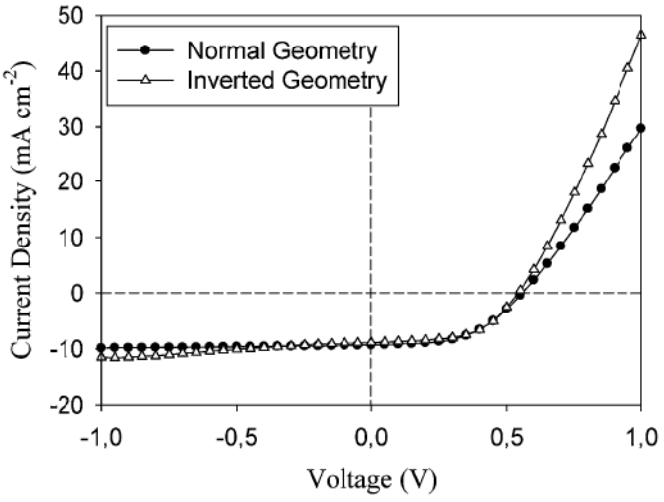

Module	J_{sc} (mA/cm^2)	V_{oc} (V)	FF (%)	PCE (%)
Normal Geometry (evaporated Al)	9.3	0.56	52	2.7
Inverse Geometry (evaporated Ag)	8.85	0.54	56	2.67

Figure 3.14: IV curves for both normal and inverted geometry devices together with the table of the PV parameters.

Tom summarize, it was demonstrated that inverted devices can be produced with performance as good as traditional devices. It was shown that such devices widen the range of materials that can be used for production of OPV devices and open up the possibility for complete vacuum free roll-to-roll production of OPVs. In addition, comparative stability studies were carried out for both normal and inverted devices, which are discussed in Section 4.5.

Further details on production and characterization of inverted devices can be found in a reprint of a published article in Appendix 6 together with discussion on same structure devices printed using roll to roll coating techniques.

3.5 MoO_3 and V_2O_5 as Buffer Layers Instead of PEDOT:PSS

As a part of the PhD project I spent three months at Eindhoven University of Technology working in the group of Molecular Science & Technology under supervision of Prof. Dr. Ir. R.A.J. Janssen. This section presents the results of the studies carried out during my external stay in Eindhoven.

Various groups have reported on successful production of devices with evaporated thin layers of MoO_3 or V_2O_5 instead of PEDOT:PSS and the photoconversion efficiencies (PCE) were reaching up to 3 %.[24-28] The benefit of these metal oxides is that by tuning the layer thickness it is possible to significantly decrease the light absorption by the buffer layer and also it allows substituting PEDOT:PSS, which is a source of instabilities. In addition, metal oxides are possible to deposit on active layers for inverted device structures, while depositing PEDOT:PSS is not an easy task due to hidrophilicity of PEDOT:PSS.

Figure 3.15 presents the energetic levels suggested by Shrotriya *et al*.[28] According to the picture it should be energetically possible to substitute PEDOT:PSS with the other materials.

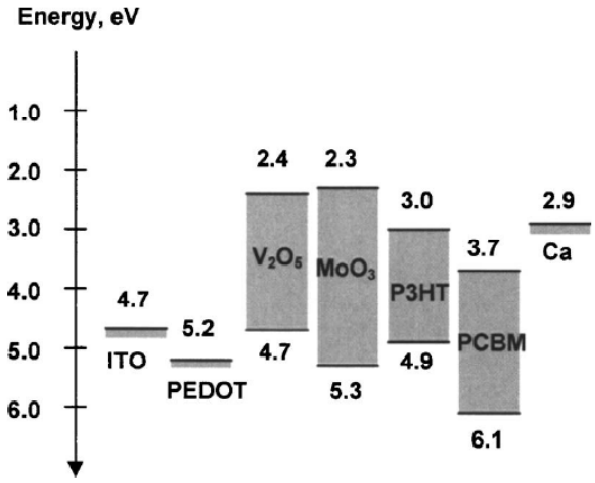

Figure 3.15: Energy levels of the bottom electrode ITO, various buffer layer materials (PEDOT:PSS, V_2O_5, MoO_3), donor polymer P3HT, acceptor PCBM, and top electrode Ca.

The aim of this work was to find the optimal thickness for the metal oxide layers for obtaining the best PCEs for the devices and in case of success applying the technique for building tandem solar cells.

Figure 3.16 (a), (b) and (c) present the results of transmission, reflection and absorption spectrum of the buffer layers using the integrating sphere based measuring system. The studies were carried out for spin coated 50 nm thick PEDOT:PSS layer and thermally evaporated V_2O_5 and MoO_3 of 20 nm all on ITO/Glass substrates. One can see that both V_2O_5 and MoO_3 are transmitting less light in the polymer absorption range compared to PEDOT. Therefore, less than 20 nm should be used. Melvin ten Kate from Eindhoven University of Technology in his graduation project presented the transmission of light for different thicknesses of MoO_3 layer (Figure 3.16 (d)) and according to the results a thickness below 5 nm is sufficient to gain in light harvesting compared to 50 nm PEDOT:PSS. However, studies showed that evaporating such thin closed layers is rather difficult task.

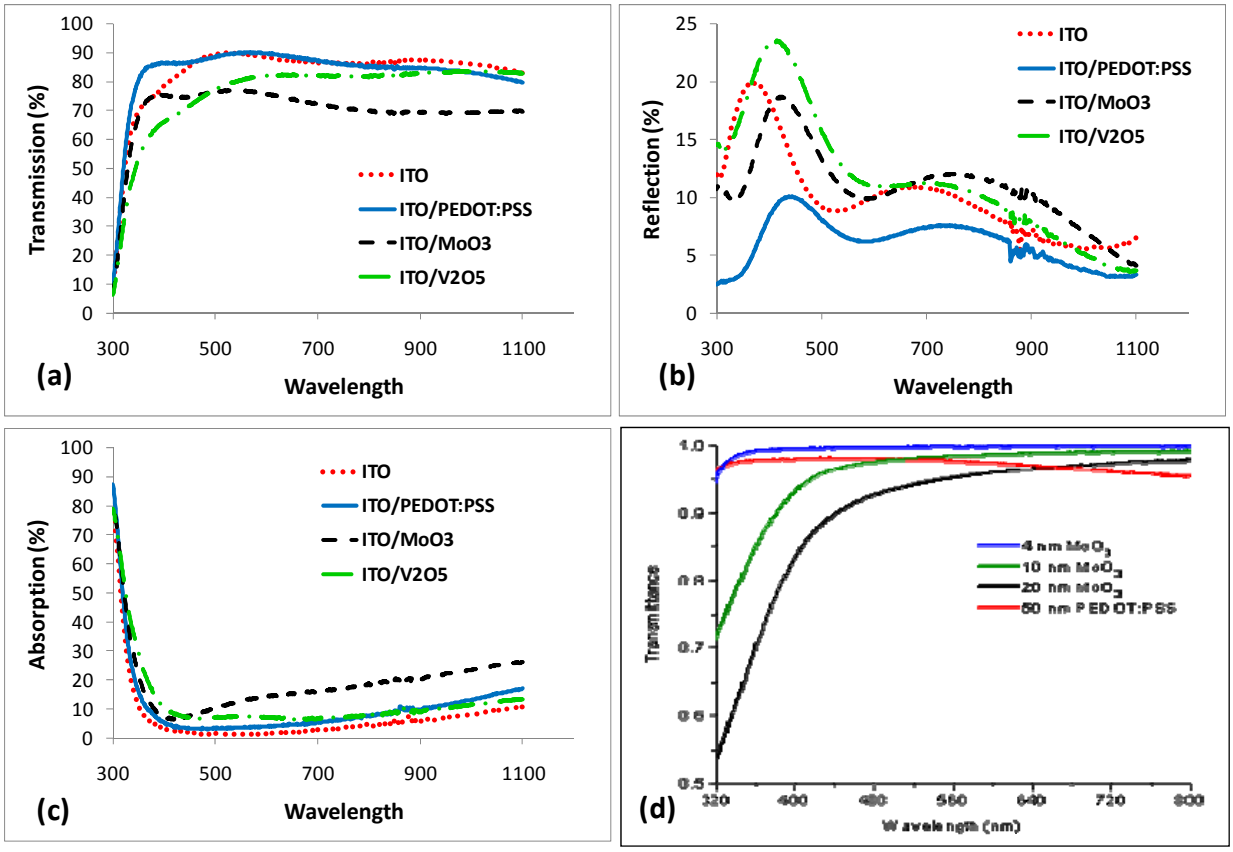

Figure 3.16: Transmission (a), Reflection (b) and Absorption (c) of different layers in combination with ITO. PEDOT:PSS was spin coated and had 50 nm thickness, while V_2O_5 and MoO_3 where thermally evaporated and had 20 nm thickness. (d) shows Transmission spectra of pure MoO_3 layer with different layer thicknesses (4, 10, 20 nm) compare to 50 nm thick PEDOT:PSS layer.

Organic solar cells have been prepared using the following structures:

1. Glass/ITO/Buffer Layer/P3HT:PCBM/LiF/Al – Regular structure
2. Glass/ITO/ZnO/P3HT:PCBM/Buffer Layer/Ag – Inverted structure

3 different materials were used as buffer layers: PEDOT:PSS, MoO_3, V_2O_5. For devices with MoO_3 two common features were recorded, curves with good fill factor and "s-shaped" curves. Various thicknesses of MoO_3 were tested (from 3 to 10 nm) and the thinner the layer was the more difficult it was to achieve a good performance. The UV-O_3 treatment of the MoO_3 layer for about 10 minutes before the active layer spin coating would lessen the s-shape effect or completely remove it delivering nice IV-curves. Just pure UV – light treatment of the layer seems not to have an effect on the curves. In addition, the UV-O_3 treatment of ITO before MoO_3 evaporation didn't have any effect on the IV-curves either. One could suggest that UV-O_3 treatment of MoO_3 layer simply changes the chemical composition of the surface, which results in different wetting

properties of the surface. Thus the adhesion of the next layer can be significantly improved, which can increase the device efficiency. Figure 3.17 (left) presents the IV-curves for regular devices with 10 nm MoO_3 with and without UV-O_3 treatment or PEDOT:PSS as buffer layers

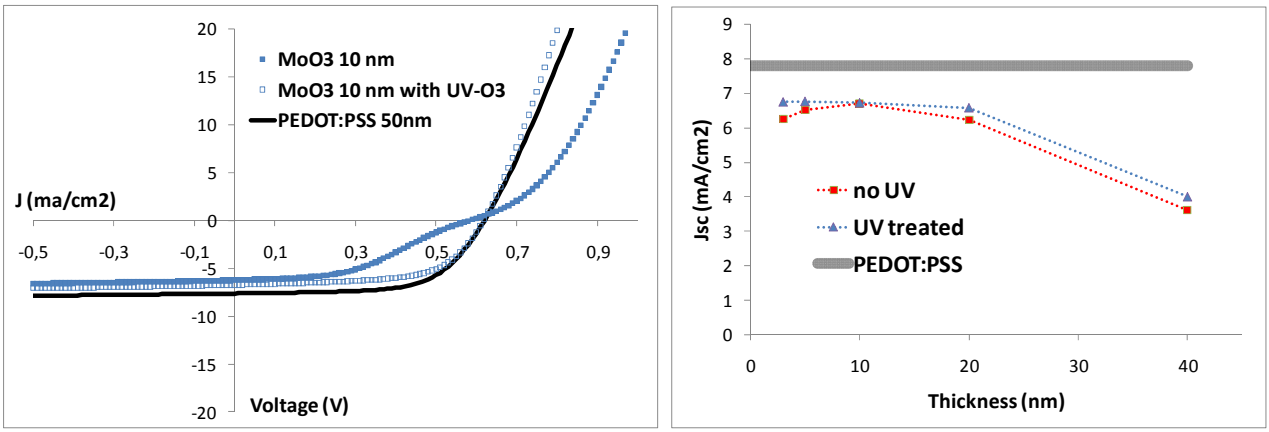

Figure 3.17: IV-curves for devices with 10 nm MoO_3 with (open blue squares) and without (solid blue squares) UV-O_3 treatment or PEDOT:PSS as buffer layers (left). Right hand side shows the short circuit current density versus MoO_3 layer thickness for both UV-O_3 treated and not treated layers. The grey line above corresponds to the current of the reference cell with 50 nm PEDOT:PSS.

Figure 3.17 (right) shows the short circuit current density of the devices versus the thickness of MoO_3 layer. The grey line corresponds to the current of the reference cell with 50 nm PEDOT:PSS buffer layer. The cells with MoO_3 deliver less photocurrent even for thin layers and the reason for that could be the optical properties of MoO_3 layer, which might change the electromagnetic field distribution in the whole device.

Similar picture can be seen in the case of V_2O_5 (Figure 3.18). However, in case of V_2O_5 the s-shaped curves were more frequent and in some cases the devices were simply short circuited. The UV-O_3 treatment of V_2O_5 didn't improve the device performance, but rather increased the s-shape effect contrary to MoO_3. The possible ways to remove the s-shape effect were by using 40 nm thick V_2O_5 layer or by building inverted structure mentioned above. However, in both cases the achieved short circuit current was significantly lower compared to regular PEDOT:PSS. In the first case the reason could be the absorption of the light by thick (40 nm) V_2O_5 and in case of inverted device the electromagnetic field distribution in the device might not be efficient.

The advantage of V_2O_5 over MoO_3 is that it was possible to achieve almost similar short circuit currents compared to PEDOT:PSS even with 20 nm thick layer (Figure 3.18 right). It can be partly ascribed to the transmission properties of V_2O_5 (Figure 3.16), since in the range of polymer absorption V_2O_5 transmits more light compared to MoO_3. Table 3.1 shows the photovoltaic parameters of the best cells for different materials.

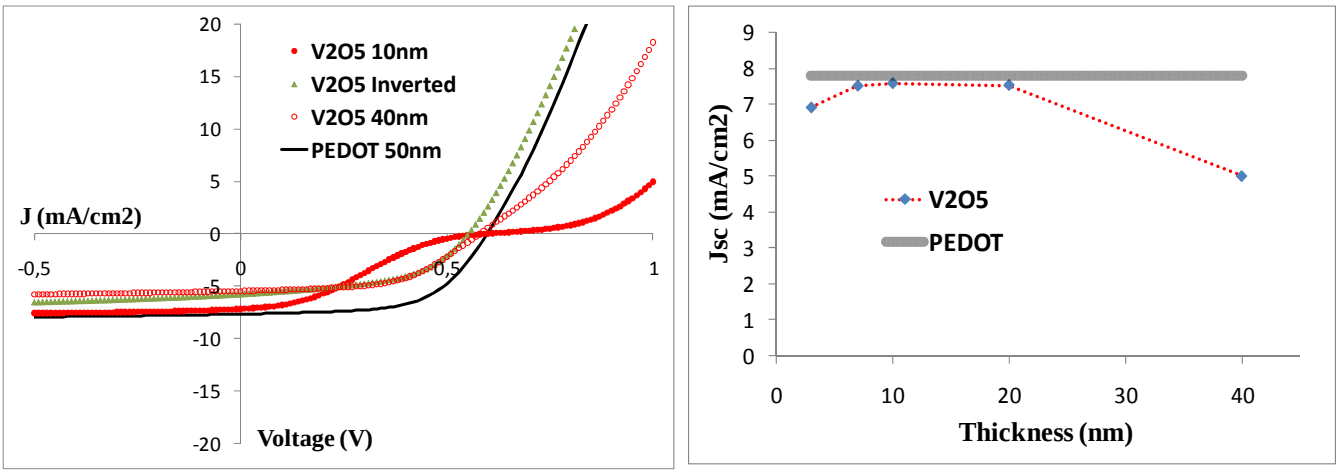

Figure 3.18: IV-curves for devices with 10 nm V_2O_5 (solid red circle), 40 nm (open red circle), inverted structure (green rectangular) and 50 nm PEDOT:PSS (solid line) as buffer layers (left). Right hand side shows the short circuit current density versus V_2O_5 layer thickness. The grey line above corresponds to the current of the reference cell with 50 nm PEDOT:PSS.

Table 3.1 Phtovoltaic parameters of the devices with different structures

Device	Jsc (mA/cm^2)	Voc (V)	FF	PCE (%)	UV-O_3 treatment	B. L. (nm)*
ITO/PEDOT:PSS/P3HT:PCBM/LiF/Al	7.7	0.62	0.65	3.14	No	50
ITO/MoO_3/P3HT:PCBM/LiF/Al	6.2	0.58	0.43	1.55	No	20
ITO/MoO_3/P3HT:PCBM/LiF/Al	6.6	0.59	0.62	2.41	Yes	20
ITO/V_2O_5/P3HT:PCBM/LiF/Al	5.5	0.58	0.53	1.7	No	40
ITO/V_2O_5/P3HT:PCBM/LiF/Al	5.3	0.58	0.5	1.5	Yes	40
ITO/ZnO/P3HT:PCBM/ V_2O_5/Ag	6	0.51	0.52	1.59	No	20
ITO/ZnO/P3HT:PCBM/ V_2O_5/Ag	5.8	0.55	0.51	1.64	Yes	20

***Buffer Layer thickness have been measured by profilometer**

AFM studies have been conducted for both buffer layers and the results revealed that both materials formed quite rough surfaces after thermal evaporation. The variation of the height was up to 15 nm with average value of 10 nm. Therefore, only films with more than 15 nm thickness could

assure closed layer. However, the films often had peaks higher than 20 nm, which probably explains the short circuits and the s-shaped IV-curves for even 20 nm thick films. In most cases probably the films with such high roughness did not have closed layer.

During the evaporation of the metal oxides the rate of the evaporation was in the range of 0.05 nm/s. Higher and lower rates have been tested as well, but due to the strongly scattering data it is hard to conclude in which way the evaporation rate affects the film morphology.

To summarize, in order to produce solar cells with MoO_3 or V_2O_5 buffer layers with efficiencies as good as or higher than the traditional PEDOT:PSS based devices, films with thickness below 7 nm are required to assure enough light transmission. However, to be able to produce such thin films at the same time avoiding short circuits better morphology control of the buffer layers and interfaces is needed. It can possibly be done by:

1. Proper cleaning treatments of the Glass/ITO substrates.
2. Finding the optimal evaporation rates for the metal oxides for decreasing the roughness.
3. Using after-treatments of the layers (for example UV-O_3 treatment in case of MoO_3).

One has to take into account also the electromagnetic field distribution in the device if the highest PCEs are aimed, which means optical spacers might be required in order to improve the photocurrent of the device.

3.6 Conclusions

To summarize, a number of projects for characterization of various materials and devices have been presented in this chapter. Applicability of various thermocleavable polymers in PV devices was shown. Characterization of inverted devices and comparison of the performance with traditional structured devices was carried out. Buffer layers such as MoO_3 and V_2O_5 were tested instead of PEDOT:PSS in traditional and inverted devices. While it was not possible to obtain devices with better performance compared to the one with PEDOT:PSS, the results showed that better control of the processing can potentially lead to higher efficiency devices.

Reference List

1. E. Q. B. Macabebe and E. E. van Dyk, Parameter extraction from dark current-voltage characteristics of solar cells, *South African Journal of Science*, 2008, **104**, 401-404.

2. F. C. Krebs and H. Spanggaard, Significant improvement of polymer solar cell stability, *Chem.Mater.*, 2005, **17**, 5235-5237.

3. M. Bjerring, J. S. Nielsen, N. C. Nielsen, and F. C. Krebs, Polythiophene by solution processing, *Macromolecules*, 2007, **40**, 6012-6013.

4. M. Bjerring, J. S. Nielsen, A. Siu, N. C. Nielsen, and F. C. Krebs, An explanation for the high stability of polycarboxythiophenes in photovoltaic devices- A solid-state NMR dipolar recoupling study, *Sol.Energy Mater.Sol.Cells*, 2008, **92**, 772-784.

5. J. H. Burroughes, D. D. C. Bradley, A. R. Brown, R. N. Marks, K. Mackay, R. H. Friend, P. L. Burns, and A. B. Holmes, Light-Emitting-Diodes Based on Conjugated Polymers, *Nature*, 1990, **347**, 539-541.

6. C. Edder, P. B. Armstrong, K. B. Prado, and J. M. J. Frechet, Benzothiadiazole- and pyrrole-based polymers bearing thermally cleavable solubilizing groups as precursors for low bandgap polymers, *Chem.Comm.*, 2006, 1965-1967.

7. J. H. Edwards, W. J. Feast, and D. C. Bott, New Routes to Conjugated Polymers: 1. A 2 Step Route to Polyacetylene, *Polymer*, 1984, **25**, 395-398.

8. S. A. Gevorgyan and F. C. Krebs, Bulk heterojunctions based on native polythiophene, *Chem.Mater.*, 2008, **20**, 4386-4390.

9. T. J. Gordon, G. Vamvounis, and S. Holdcroft, Bilayer approach to laser-induced thermal patterning of pi-conjugated polymers, *Adv.Mater.*, 2008, **20**, 2486-2490.

10. O. Hagemann, M. Bjerring, N. C. Nielsen, and F. C. Krebs, All solution processed tandem polymer solar cells based on thermocleavable materials, *Sol.Energy Mater.Sol.Cells*, 2008, **92**, 1327-1335.

11. X. Han, X. W. Chen, and S. Holdcroft, Nanostructured morphologies and topologies of pi-conjugated polymers from thermally reactive polymer blends, *Adv.Mater.*, 2007, **19**, 1697-1702.

12. J. S. Liu, E. N. Kadnikova, Y. X. Liu, M. D. McGehee, and J. M. J. Frechet, Polythiophene containing thermally removable solubilizing groups enhances the interface and the performance of polymer-titania hybrid solar cells, *J.Am.Chem.Soc.*, 2004, **126**, 9486-9487.

13. M. H. Petersen, S. A. Gevorgyan, and F. C. Krebs, Thermocleavable Low Band Gap Polymers and Solar Cells Therefrom with Remarkable Stability toward Oxygen, *Macromolecules*, 2008, **41**, 8986-8994.

14. G. A. Power, P. Hodge, and N. B. McKeown, Synthesis of novel conjugated polymers containing alternating hexa-1,3,5-triene and bi-p-phenylene or ter-p-phenylene segments, *Chem.Comm.*, 1996, 655-656.

15. J. F. Yu and S. Holdcroft, Solid-state thermolytic and catalytic reactions in functionalized regioregular polythiophenes, *Macromolecules*, 2000, **33**, 5073-5079.

16. F. C. Krebs and K. Norrman, Analysis of the failure mechanism for a stable organic photovoltaic during 10000 h of testing, *Prog.Photovolt: Res.Appl.*, 2007, **15**, 697-712.

17. K. Norrman and F. C. Krebs, Lifetimes of organic photovoltaics: Using TOF-SIMS and $^{18}O_2$ isotopic labelling to characterise chemical degradation mechanisms, *Sol.Energy Mater.Sol.Cells*, 23-1-2006, **90**, 213-227.

18. E. A. Katz, S. Gevorgyan, M. S. Orynbayev, and F. C. Krebs, Out-door testing and long-term stability of plastic solar cells, *European Physical Journal-Applied Physics*, 2006, **36**, 307-311.

19. M. P. de Jong, L. J. van IJzendoorn, and M. J. A. de Voigt, Stability of the interface between indium-tin-oxide and poly(3,4-ethylenedioxythiophene)/poly(styrenesulfonate) in polymer light-emitting diodes, *Appl.Phys.Lett.*, 2-10-2000, **77**, 2255-2257.

20. G. Greczynski, T. Kugler, M. Keil, W. Osikowicz, M. Fahlman, and W. R. Salaneck, Photoelectron spectroscopy of thin films of PEDOT-PSS conjugated polymer blend: a mini-review and some new results, *Journal of Electron Spectroscopy and Related Phenomena*, 2001, **121**, 1-17.

21. L. A. A. Pettersson, S. Ghosh, and O. Inganas, Optical anisotropy in thin films of poly(3,4-ethylenedioxythiophene)-poly(4-styrenesulfonate), *Org.Electron.*, 2002, **3**, 143-148.

22. C. Waldauf, M. Morana, P. Denk, P. Schilinsky, K. Coakley, S. A. Choulis, and C. J. Brabec, Highly efficient inverted organic photovoltaics using solution based titanium oxide as electron selective contact, *Appl.Phys.Lett.*, 4-12-2006, **89**, 233517.

23. F. C. Krebs, All solution roll-to-roll processed polymer solar cells free from indium-tin-oxide and vacuum coating steps, *Org.Electron.*, 2009, **10**, 761-768.

24. L. Cattin, F. Dahou, Y. Lare, M. Morsli, R. Tricot, S. Houari, A. Mokrani, K. Jondo, A. Khelil, K. Napo, and J. C. Bernede, MoO3 surface passivation of the transparent anode in organic solar cells using ultrathin films, *J.Appl.Phys.*, 1-2-2009, **105**, 034507.

25. A. K. K. Kyaw, X. W. Sun, C. Y. Jiang, G. Q. Lo, D. W. Zhao, and D. L. Kwong, An inverted organic solar cell employing a sol-gel derived ZnO electron selective layer and thermal evaporated MoO3 hole selective layer, *Appl.Phys.Lett.*, 1-12-2008, **93**, 221107.

26. G. Li, C. W. Chu, V. Shrotriya, J. Huang, and Y. Yang, Efficient inverted polymer solar cells, *Appl.Phys.Lett.*, 19-6-2006, **88**, 253503.

27. H. Schmidt, H. Flugge, T. Winkler, T. Bulow, T. Riedl, and W. Kowalsky, Efficient semitransparent inverted organic solar cells with indium tin oxide top electrode, *Appl.Phys.Lett.*, 15-6-2009, **94**, 243302.

28. V. Shrotriya, G. Li, Y. Yao, C. W. Chu, and Y. Yang, Transition metal oxides as the buffer layer for polymer photovoltaic cells, *Appl.Phys.Lett.*, 13-2-2006, **88**, 073508.

4 Stability/Degradation of OPVs

4.1 Introduction

One of the main hurdles to overcome in OPV field is the lack of device stability. Organic solar cells are very sensitive towards the surrounding environment and tend to degrade during illumination and in the dark. There are few processes that take place during the degradation of polymers, which can have various natures such as chemical, physical, mechanical etc. Lifetimes up to one year under 1 sun irradiation[1] and more than 10000 hours of shelf lifetime[2] have been reported so far. Such short lifetimes put constraints on the applications of OPVs and in order to extend the possible market of OPVs the improvement of stability is a primary requirement.

When the performance of solar cells is measured as a function of time the resulting curves have degrading features that in most cases can be fitted with linear or exponential functions:

$$\eta = a - bt \qquad [4.1] \qquad\qquad \eta = ae^{-\alpha t} + be^{-\beta t} \qquad [4.2]$$

However, this is very general approach, since depending on the polymer material, surrounding environment and measuring conditions the decay properties can significantly change.[3,4] Yet, one of the repeatable features that can be recorded in many cases is that the curves tend to have an initial fast decay followed by more moderate decline. The active polymer layer in the device can chemically react with oxygen, water and electrode material. The experiments show that the initial fast decay is independent of whether the tested device is kept in air or in oxygen free atmosphere, while the slower degrading part is strongly correlated to the amount of oxygen the cell is being exposed to. As a result it was proposed that the initial decay is related to the reaction at the metal/polymer interface. It was experimentally shown also that by simply placing a buffer layer of C60 between the layers reduces the effect.[4,5] The slower part of the decay was ascribed to the reaction of the polymer with the oxygen and water diffused through the layers.

Oxygen and water are gradually diffusing into the device regardless of whether the cell is kept in the dark or light and it is considered as the major source for decay process. It was suggested that oxygen and water diffuse through the outer electrode (counter electrode to ITO)[4,6,7] and the microscopic pinholes in the electrode are the main channels for diffusion. In addition it was

proposed that diffusion of water molecules takes place also through the metal grains of the evaporated electrode. In case of oxygen diffusion a sublayer of organic material is oxidized, which causes the material to expand in all directions resulting in formation of protrusions on the surface of the electrode centered on the microscopic pinholes and the diffusion takes places through the microscopic holes in the surface regardless of whether the device is under illumination or in dark.

There are a number of other factors such as the light intensity, temperature, mechanical flexing, cyclic testing etc. that can effectively contribute in the decay process as well. It makes the proper studying and evaluation of device degradation processes much harder due to multiple effects that can take place at the same time. There were attempts to establish a standard measuring approach for OPVs, which can effectively evaluate and compare different device performances, but there is no complete solution proposed yet and the question still remains open.

This chapter starts with a presentation of a setup for studying device stability under different atmospheric conditions. Different behaviors of device degradation processes are discussed, which were revealed while applying various atmospheric conditions to the cells. A number of studies of degradation for various devices and device structures are presented as well and few challenges are discussed.

4.2 Practical Approach for Stability Measurements

The definition of operational lifetime in traditional engineering terms is given as the period of time that elapses between the initial performance and the point where 80% of the initial performance has been reached. However, since often degradation features are observed, which differ by their nature from one device to another, it is advised to make measurements of the complete lifetime curve that will enable an applications engineer to evaluate if a given material technology has a stable or flat degradation regime that can enable application in spite of for instance a fast initial decay.

In the following subsections a special setup for stability measurements is presented together with examples of stability studies as well as usage of the chamber for water induced degradation studies with time-of-flight secondary ion mass spectrometry.

4.2.1 Atmospheric Chamber for Stability Studies

Since the degradation of polymer solar cells strongly depends on the exposure to oxygen, water and temperature, it is important to be able to control these parameters in a lifetime experiment. This can be done if the solar cell is contained in an airtight chamber with suitable connections to inert air supply, cooling or heating and electronic connections.

A detailed description of a setup for studying ageing of polymer devices is presented. The system offers individual control of the environmental factors (oxygen, humidity, atmosphere, temperature and light intensity) causing the degradation of organic devices. The system was developed for accurate control of the conditions and data collection of photovoltaic (PV) parameters for organic solar cells during long-term testing. The atmosphere chamber (AC) can operate under vacuum conditions without temperature control. It is designed for operation at an internal gas pressure of around 1 atm. It is further equipped for isotopic labeling experiments of the internal atmosphere ($^{18}O_2$ and $H_2{}^{18}O$) such that degradation mechanisms can be studied using TOF-SIMS as a chemical probe. Experiments on both ‘‘accelerated’’ (by applying thermal stress to the devices) and ‘‘long-term’’ lifetime measurements of traditional organic bulk heterojunction solar cell devices have been realized while controlling the environmental conditions via the chambers.

The chamber is shown in Figure 4.1. Two solar cell modules can be placed inside. The chamber is then placed under an artificial sun with light entering through two small circular windows directly above the solar cells under investigation. During measurements the chamber can be evacuated to remove any oxygen or water via one of the flanges on the chamber connected to a pump. Devices can also be measured in a controlled atmosphere e.g. nitrogen. The ambient air is replaced by placing the entire chamber in a nitrogen-filled glove-box. If ambient or artificial atmosphere is present in the chamber inside fans are used to even out any temperature variations. The temperature inside the chamber is controlled through active water cooling system mounted in the chamber. The temperature is measured with two thermocouples (type K). One is placed on a spring fixed directly under the device to be tested and the other has thermal contact with the circulating atmosphere. A humidity sensor (Figure 4.2) is placed inside the chamber for measuring the humidity. The oxygen concentration inside the chamber is monitored using an O_2 analyzer connected to the chamber. The solar cell devices are mounted on a sample holder that ensures the correct placement and orientation beneath the windows in the AC. A close-up is seen in Figure 4.2.

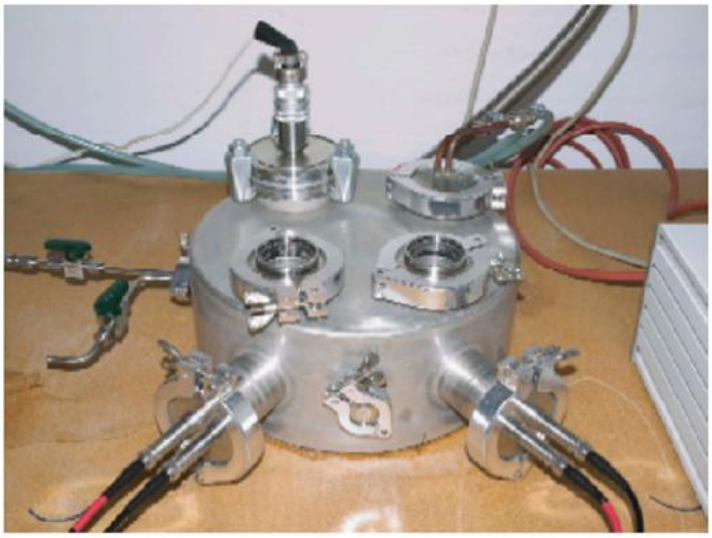

Figure 4.1: Chamber for controlling the atmosphere and temperature during a lifetime test of solar cells.

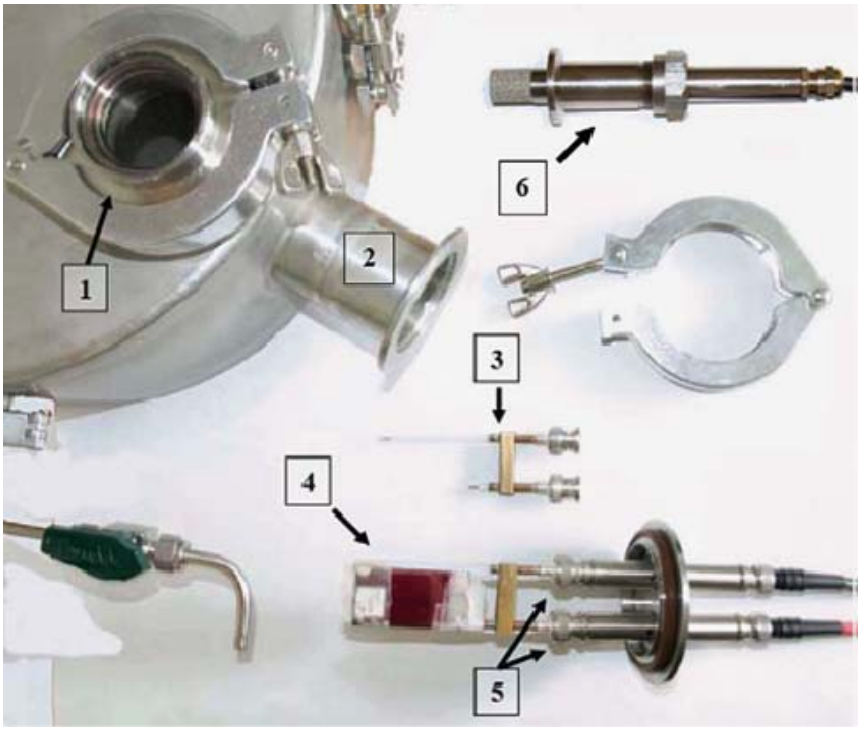

Figure 4.2: Viewport for exposing the sample to light (1), KF flange for introducing the samples (2), holder with BNC connections for fixing the samples (3), tested solar cell (4), cell with holder fixed on the flange through BNC connections (5) and humidity sensor with high-grade steel housing (6).

Devices with structure ITO/PEDOT:PSS/P3HT:[60]PCBM/Al have been prepared in similar fashion described in the previous chapters and have been characterized in the atmospheric chambers

for stability. Figure 4.3 shows an example of device short circuit current change during the device illumination while kept in room environment or pure nitrogen atmosphere at the same temperature. The decay curves show a fast initial decay followed by region with a constant decay that can be fitted with a linear or an exponential function. Clearly the one in ambient atmosphere degrades much faster due to the effect of oxygen and humidity. Similar relations between results in ambient atmosphere and nitrogen were seen also for other temperatures (25, 63 and 83 ^{o}C).

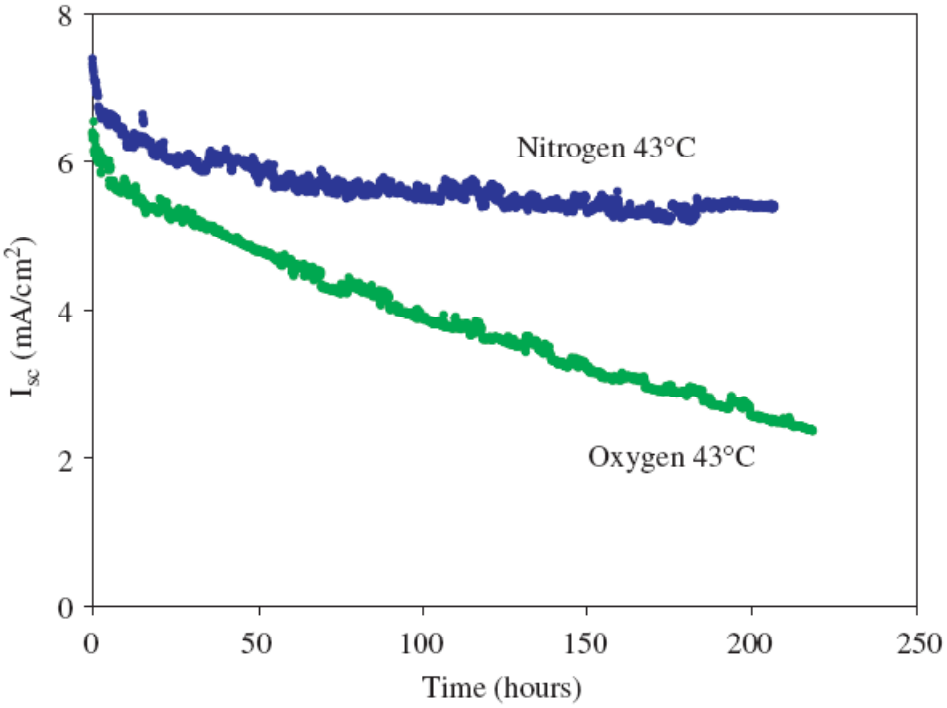

Figure 4.3: Comparing the lifetime curves for devices in ambient atmosphere and in nitrogen at 43 ± 1 ^{o}C.

The degradation of a PV device is characterized by a degradation constant that is obtained by fitting a suitable function to the decay curve for a device that shows the decay. The device current was chosen here and as mentioned above it can be fitted with either a linear or a single exponential function:

$$I_{sc}(t) = I_{sc}(t_0)\left(1 - k_{deg}t\right) \qquad [4.3]$$

$$I_{sc}(t) = I_{sc}(t_0)exp\left(-k_{deg}t\right) \qquad [4.4]$$

k_{deg} is the degradation constant and $I_{sc}(t_0)$ is the value of short circuit current at the initial stage.

In our case the curves exhibit at least two regions where the rate of degradation is different. We chose the constant region observed after 15 h and fitted a linear function (Eq. [4.3]). Our reason for this is that it seems to be the typical constant behavior of the devices. Assuming that the degradation constant k_{deg} depends on the temperature T given by the Arrhenius equation (Eq. [4.5]), an acceleration factor K can be calculated from Eq. [4.5] by fitting the values for k_{deg}.

$$k_{deg} = A\, exp\left(\frac{-E_a}{k_B T}\right) \qquad [4.5]$$

$$K = \frac{k_{deg}(T_2)}{k_{deg}(T_1)} = exp\left[\frac{E_a}{k_B}\left(\frac{1}{T_1} - \frac{1}{T_2}\right)\right] \qquad [4.6]$$

E_a is the activation energy and k_B is Boltzmann constant. Figure 4.4 shows the acceleration factor K plotted against $1/T$ for both ambient atmosphere and nitrogen and the exponential fit to the calculated values.

The calculated degradation constants k_{deg} for each device, the acceleration factors K and the activation energies E_a are shown in Table 4.1.

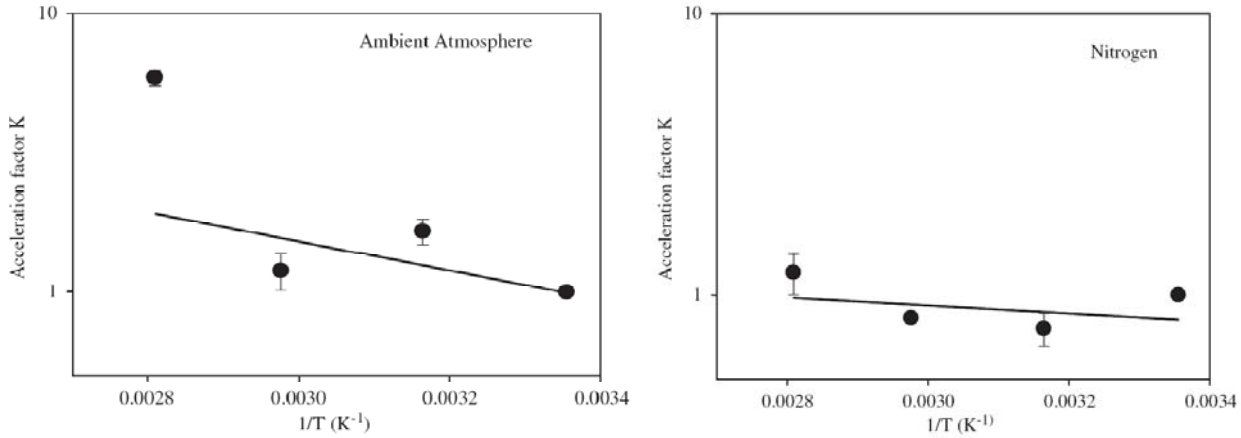

Figure 4.4: Log scale plots of the acceleration factor K, relative to 25 ^{o}C (298 K). The data were fitted using Eq. [4.4] and the parameters for the activation energy and the acceleration factor were obtained as shown in Table 4.1. The illumination intensity was 1/3 sun (330 W/m^2).

Table 4.1: Degradation constant, activation energies and acceleration constants obtained

Atmosphere	Temp. (^{o}C)	k_{deg} (h^{-1}) 10^{-3}	K^a	E_a (meV)

Ambient	25 ± 1	1.95 0.96	1 1	103
	43 ± 1	2.16 2.67	1.48 1.83	
	63 ± 1	1.7 1.78	1.17 1.22	
	83 ± 1	8 9.1	5.5 6.25	
Nitrogen	25 ± 1	0.92 0.93	1 1	29
	43 ± 1	0.8 0.6	0.86 0.65	
	63 ± 1	0.78 0.75	0.84 0.81	
	83 ± 1	1.3 0.94	1.4 1.1	

[a] K values were obtained by dividing each corresponding k_{deg} by average of k_{deg} values at 25 °C.

The activation energy has been extracted from the curves using Eq. [4.6] and in the case of ambient atmosphere it is rather low (103 meV), which might be due to the fact that the data at 63 °C is an outlier. There is naturally a certain degree of experimental variation due to the fact that we could not prepare and run all eight experiments at the same time but had to run the experiments in three consecutive batches. The calculation of activation energy with omission of the point at 63 °C gives an activation energy that is 3 times higher than the one we obtained. This however underlines the difficulty in obtaining a value for the activation energy from one experiment and then generally applying it. However, it is clear that the degradation proceeds much faster in the ambient atmosphere where oxygen and humidity are allowed to diffuse into the devices. Under inert conditions we obtain a totally different value for the activation energy and as a consequence a much slower acceleration factor indicating that there is no real acceleration of the degradation under inert conditions (albeit at lower light intensity and in the absence of UV-light). The degradation processes that take place in the presence of oxygen and humidity are most likely chemical processes involving the active polymer and perhaps the electrode materials. It is not so clear what causes the acceleration factor in our case to be much slower under nitrogen conditions. The limited data indicates that the process is not speeded up by increasing the temperature suggesting simple zero-order kinetics. This could happen if the rate of the process only depended on say the light intensity and not on the concentration and diffusion of molecular entities like oxygen and water.

While we see accelerated studies as a useful means to characterize polymer and organic solar cells we also see it as limited to a particular device technology that cannot be extended to other systems without verification of the generality. The general degradation we observed for the devices were as expected with a decrease in mostly the I_{sc} but also to some extend in the *FF* as the devices degraded as shown in Figure 4.5 where the change of the IV-curve is shown for the devices maintained in ambient atmosphere at 43 ^{o}C.

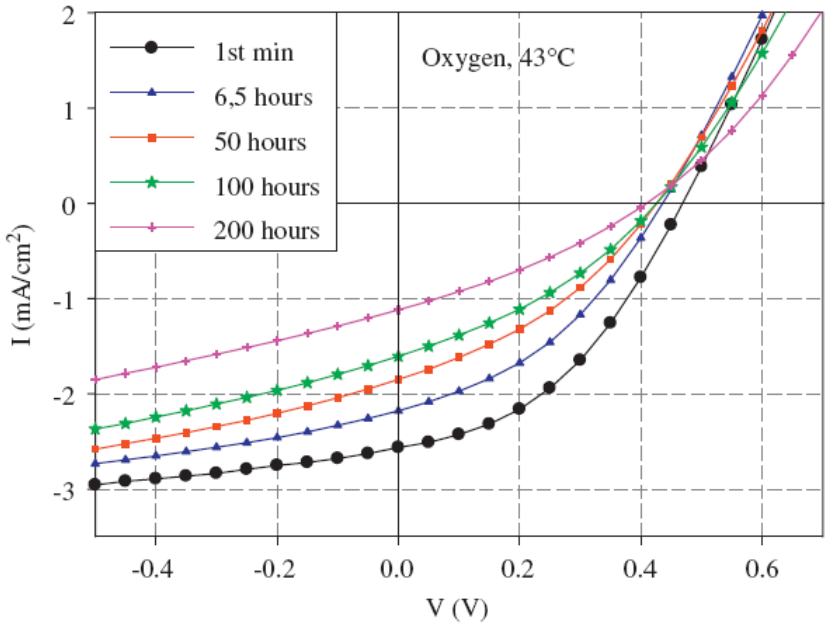

Figure 4.5: Evolution of IV-curves during decay at 43 ^{o}C and ambient atmosphere (under 1/3 sun illumination).

To summarize, the atmospheric chambers proved to be rather efficient tool for degradation studies of OPV devices under controlled atmosphere. Furthermore, the chambers allow eliminating some of the affecting environmental factors, while measuring the effect of the others on the degradation process. In addition, OPV devices have been tested under different temperatures for accelerated studies of degradation process and the results revealed that the degradation kinetics are strongly bounded to the environmental conditions and while the acceleration method is used for the evaluation of the solar cell decay one has to take care of the conditions being used and the type of the cells that are being tested.

The reprint of a published article based on these studies is presented in Appendix 7.

Further exploitations of atmospheric chambers in different experiments are presented in the following sections.

4.2.2 Water-Induced Degradation of Polymer Solar Cells

As another example, the atmospheric chambers were used for studying the effect of humidity on two types of solar cells.

Six solar cell devices were constructed: three with Al/P3HT:PCBM/PEDOT:PSS/ITO configuration and three with Al/MEH-PPV:PCBM/PEDOT:PSS/ITO configuration. The process of manufacturing is similar to the steps described in the previous chapters. Four of the devices were placed in a chamber with saturated humid atmosphere. The remaining two devices were placed in ambient air. One of each device type (P3HT or MEH-PPV) in the chamber was wrapped loosely in aluminum foil to exclude light, but not the atmosphere, for further studies with time – of – flight secondary ion mass spectrometry (TOF:SIMS). The temperatures of the devices in the chamber were similar because of the forced circulation of the atmosphere through a heat exchanger.[3] Two devices (not wrapped) in the chamber were then exposed to AM1.5G illumination (330 W m^{-2}). Two devices in ambient air were also exposed to AM1.5G illumination (1000 W m^{-2}). Table 4.2 shows what conditions each device was exposed to during the experiment. The degradation of the photovoltaic response was monitored during illumination, and normalized decay parameters were extracted using a fitting procedure for all illuminated cells.

Table 4.2: Experimental conditions for the six solar cells that were investigated in this study

Device No.	Polymer	Relative Humidity (%)	Temperature (^oC)	Illumination (W/m^2)
1	P3HT	90 ± 5	42 ± 2	0
2	P3HT	90 ± 5	42 ± 2	330
3	P3HT	25 ± 5	72 ± 2	1000
4	MEH-PPV	90 ± 5	42 ± 2	0
5	MEH-PPV	90 ± 5	42 ± 2	330
6	MEH-PPV	25 ± 5	72 ± 2	1000

[a]The content of molecular oxygen ($^{16}O_2$) in the atmosphere was ~ 20 % during all experiements

Figure 4.6 shows the corresponding IV curves measured immediately after device fabrication and prior to stability measurements for cells tested in ambient atmosphere (25 ± 5% relative humidity; 72 ± 2 °C) using AM1.5G illumination (1000 W/m^2). The photovoltaic parameters are outlined in the table in Figure 4.6.

Figure 4.7 shows the short circuit current-density decay curves for devices measured under different conditions (no. 2, 3, 5, and 6 in Table 4.2). The curves in Figure 4.7 clearly demonstrate a significant impact of humidity on the stability of the solar cells. Devices exposed to ~ 90 % relative humidity and ~ 42 °C showed significantly faster decay compared to the solar cells exposed to ~ 25 % relative humidity and ~ 72 °C in spite of the fact that the samples in ambient humidity were subjected to a temperature that is ~30 °C higher and subjected to a factor of 3 stronger light intensity compared to the conditions of the solar cells in the chamber with ~ 90 % relative humidity. The photovoltaic parameter that was changed most was the short-circuit current.

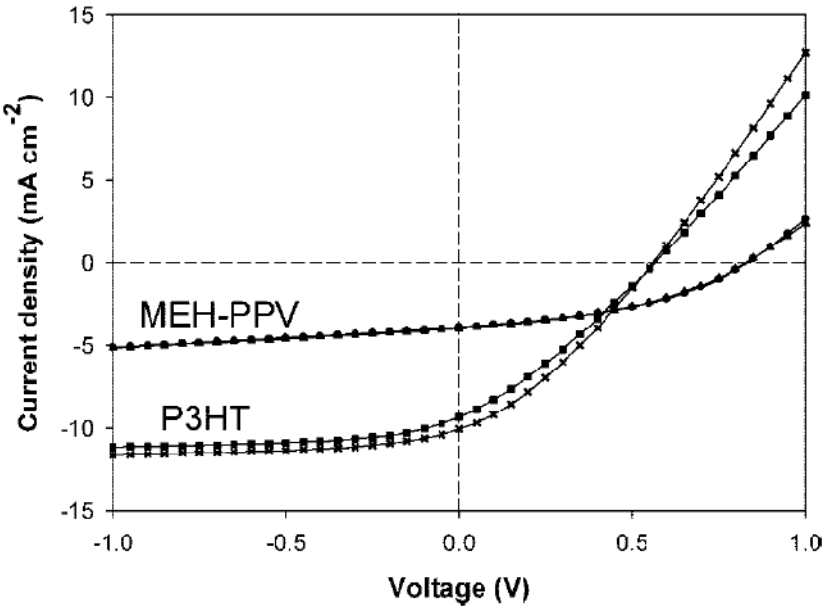

PV parameters of the measured devices [a]

Active Material	J_{sc} (mA/cm^2)	V (V)	FF (%)	PCE (%)
MEH-PPV	3.9 ± 0.03	0.83 ± 0.002	0.41 ± 0.01	1.3 ± 0.02
P3HT	9.7 ± 0.3	0.56 ± 0.002	0.31 ± 0.01	1.7 ± 0.1

[a] Average values are shown with corresponding standard deviations

Figure 4.6: IV curves for solar cell devices that where tested in the ambient atmosphere (25 ± 5% relative humidity; 72 ± 2 °C) using AM1.5G illumination (1000 W/m^2). Filled squares and crosses correspond to the P3HT:PCBM devices. Filled circles and triangles correspond to the MEH-PPV:PCBM devices.

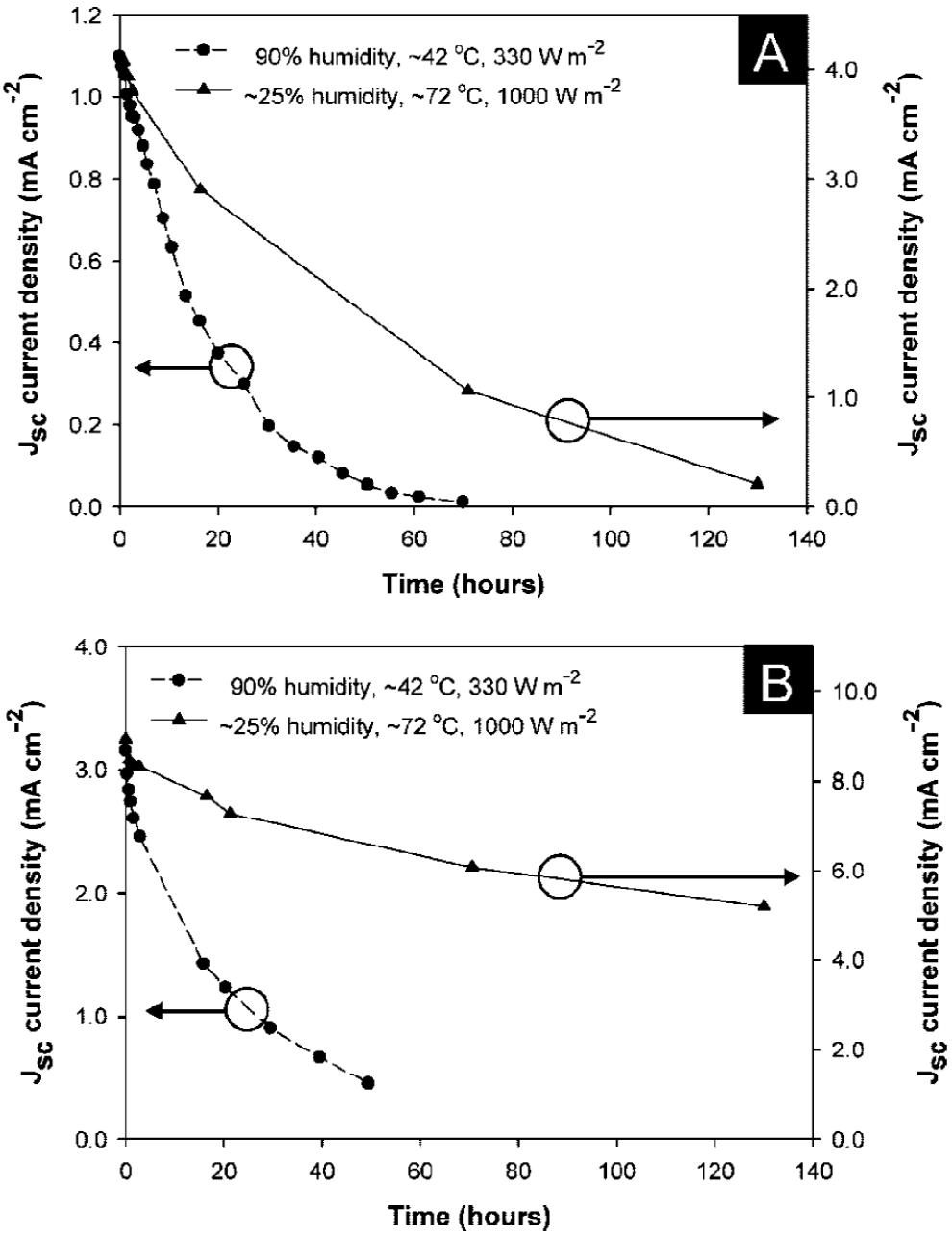

Figure 4.7: Short-circuit current-density decay curves for the MEH-PPV (A) and P3HT (B) based devices.

During the characterization the depth-profiling analysis carried out by Kion Norrman showed that water diffuses into the device through the aluminum electrode regardless of whether it is illuminated or not. Water appears to be incorporated more efficiently in aluminum oxide compared to molecular oxygen. Water incorporation is observed to be more pronounced in the MEH-PPV:PCBM layer for the illuminated device compared to the one that was stored in darkness; i.e.,

illumination increases the water-induced degradation, consistent with earlier observations using $^{18}O_2$.[7,8]

Furthermore, it was found that water reacts much more efficiently with MEH-PPV:PCBM compared to P3HT:PCBM and that illumination accelerates water-induced degradation, consistent with the depth-profiling results. The mass spectral investigation of the interfaces suggests that the relative stability of the donor/acceptor materials in question is P3HT: PCBM (darkness) > P3HT:PCBM (illuminated) > MEH-PPV: PCBM (darkness) > MEH-PPV:PCBM (illuminated).

Imaging analysis of all interfaces for all four devices suggest that water diffuses efficiently/rapidly through the aluminum electrode between the aluminum grains, causing homogeneous incorporation/degradation in all interfaces. This is a behavior opposite to that of molecular oxygen, which has been shown to at least mainly diffuse through the microscopic pinholes in the aluminum electrode, causing circular oriented incorporation/degradation, i.e., inhomogeneous incorporation/degradation.

In Appendix 8 the reader can find the reprint of the published article that presents the detailed description of further characterization of these devices by Kion Norrman using TOF:SIMS methodologies and discussion on the results.

4.3 Reversible Decay of Photovoltaic Parameters

During my master degree in Sde Boqer, Israel I participated in a project based on collaboration between the group of Israel and Risø DTU solar cell group. The task was to measure three different OPV devices in outdoor conditions. The cell structures were as follows:

Glass/ITO/PEDOT:PSS/X/Al, where X – P3HT:PCBM bulk heterojunction or MEH:PPV:PCBM bulk heterojunction or P3CT-C_{60} bilayer heterojunction manufactured by Frederik Krebs. The cells had a rigid encapsulation.

The cells were measured during the daytime under real sun and kept in the dark in nitrogen atmosphere over night. During the measurements it was discovered that V_{oc} and I_{sc} values are recovering to some extend over night. Figure 4.8 shows the values of V_{oc} and I_{sc} during the measurements. The starting values of the day are marked in solid black circles. The suggested reason of the recovery effect was the photoinduced generation of charge traps that then slowly disappear in the dark. The article presenting in details the aforementioned experiments can be found in literature.[4]

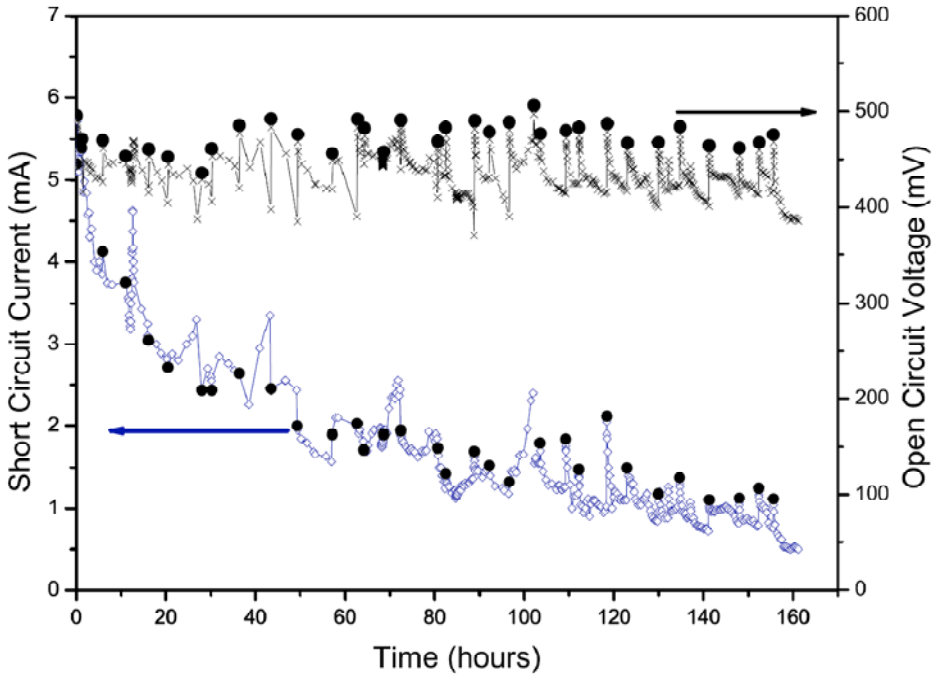

Figure 4.8: I_{sc} and V_{oc} behavior of the P3CT/C_{60} cell during last days of measurements. Vertical lines separate various days of measurements. Solid circles indicate the very first measurements every day while arrows and solid squares indicate the first measurements after the cell was shadowed for 10 or 30 minutes.

The effect was further studied in Denmark during my current project and the results are presented in this section. An article based on these studies was published in the proceedings of the 23rd European Photovoltaic Solar Energy Conference. The reprint of the article can be found in Appendix 9.

Presented work is a complementary to the article describing the outdoor measurements mentioned above. In this paper we further attempt to explain the reversible degradation by providing some additional experimental data and suggesting a physical mechanism responsible for the effect.

Similar to previous outdoor measurements, experiments were carried out on nonencapsulated cells with similar configuration and structure under indoor conditions while measuring the temperature on the back electrode of the device. Figure 4.9 presents the variation of V_{oc} and cell temperature while the cell was being subjected to light and dark and subsequently to 2V forward bias.

The steps were as follows:

0-5 min – cell is illuminated, no external field applied,

5-10 min – cell is in dark, no external field applied,

10-15 min – cell is illuminated again, no external field applied,

15-20 min – cell is in the dark, forward bias applied to the cell (+2V),

20-25 min – cell is illuminated, forward bias is released.

The temperature change clearly resembles the change of V_{oc} with opposite direction. The temperature of the cell is rising, when forward bias is being applied, which is due to the high current density flow through the device. The data is reproducible on different samples. Based on obtained data one can assume that the earlier reported V_{oc} recovery (Figure 4.8) can be a result of temperature variation in the device.

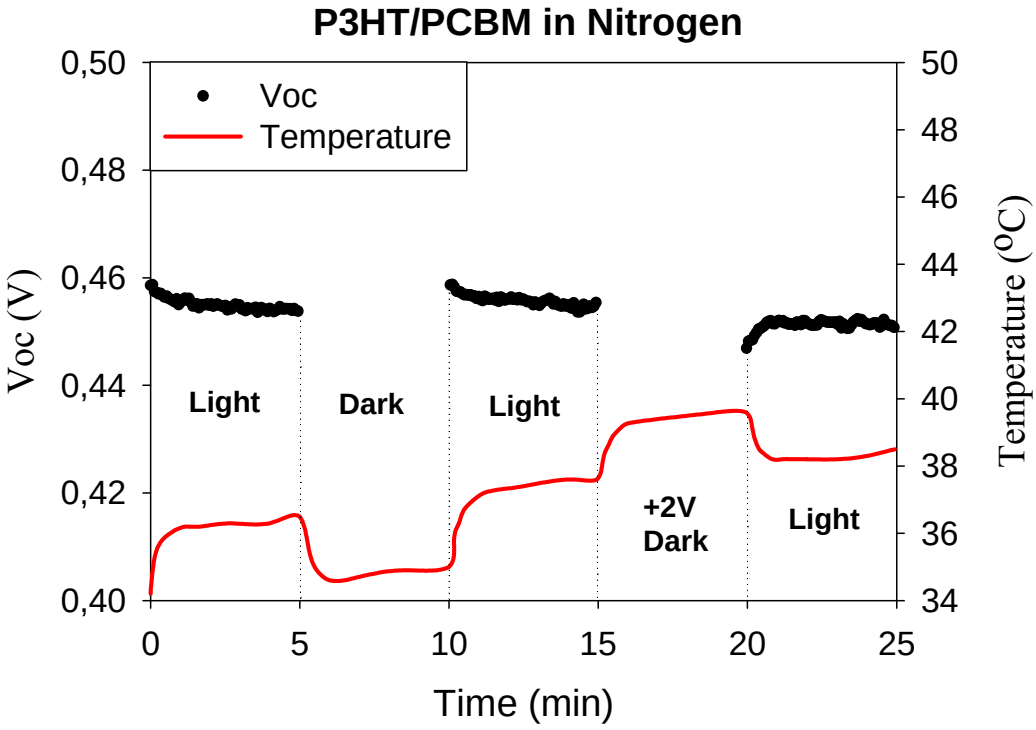

Figure 4.9: Measurements of V_{oc} and temperature, while applying voltage and light to the cell at different times. The cells were kept in a nitrogen atmosphere. The cell configuration: Glass/ITO/PEDOT:PSS/P3HT:PCBM/Al.

From Figure 4.8 it is clear that I_{sc} shows behavior similar to V_{oc}. It should be stressed out also that the I_{sc} recovery effect becomes more pronounced with ageing of the cell. Since the current increases with rising temperature [10] the effect cannot be attributed to the temperature change.

Therefore, it was suggested that there might be some photoinduced charge traps that result in decreased photocurrent, while they disappear in the dark. In 1996 Katz *et al.*[9] studied the phenomenon of persistent photoconductivity (PPC)[10] in C_{60} thin films. The authors found that after exposing the film to light it takes 5 days for the conductivity of the film to reach the initial value. Along with PPC the authors recorded another phenomenon of persistent internal photopolarization (PIPP) in C_{60} thin films, which is shown in Figure 4.10. After applying voltage (time: 0 - t_2) and light (time: 0 - t_1) to the film and releasing both light and then voltage a change of current direction in the film was found (time: t_2- t_3). Further illumination of the film (time: t_3 - t_4) increased the negative current without any external electric field. It was suggested that during the first irradiation period an internal field with opposite direction to the bias field is generated in the sample, due to a movement of photo-excited electrons and holes in opposite directions under the action of the external field, and their subsequent trapping at defect centers near the electrodes i.e. the sample was photopolarized. This internal field leads to a change of the current sign after switching off the external field and to the "negative" photocurrent flow after turning the light on the second time.

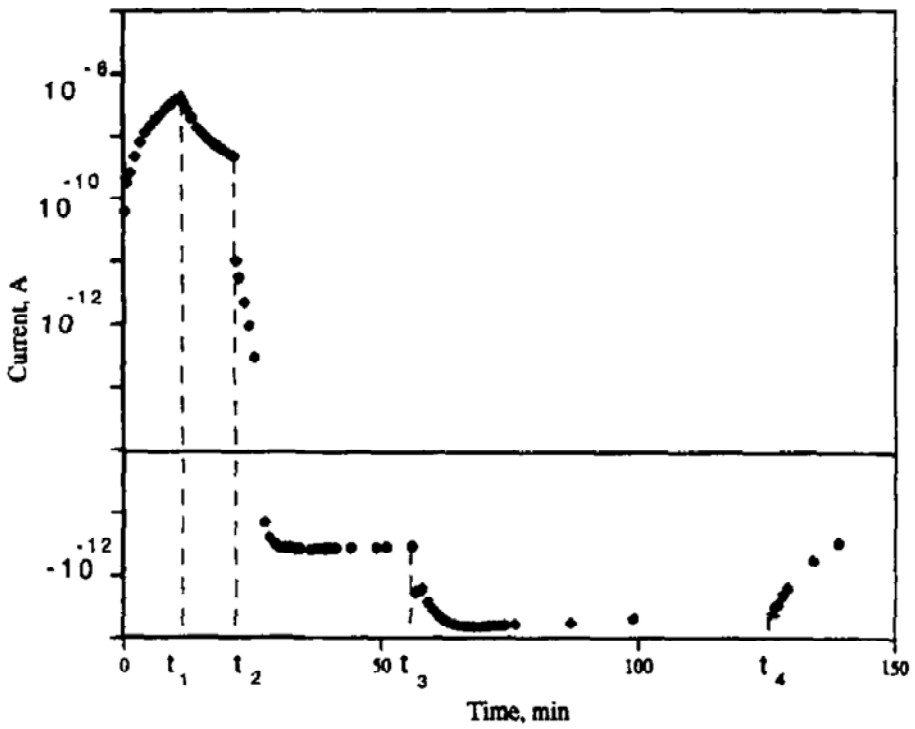

Figure 4.10: Kinetics of the current change in C_{60} thin film characteristic for PIPP effect.[9] t = 0 is the moment of turning the light on, t_1 is the moment of turning the light off, t_2 is the moment of turning the voltage bias off, t_3 and t_4 are the moments of second turning the light on and off, respectively.

A year later there was another report, where Zou *et al.* studied the degradation process in light emitting diodes (LEDs) and recorded recovery effect of current density and luminescence of the devices after applying external field to the device.[11] The authors suggested that when a forward bias is being applied to the device the ionic impurities in the material start to diffuse to the electrodes, the positive ions to one direction and cations to the other, creating an internal field, which is opposite to the external field. Thus, the internal field reduces the effective electric field for carrier injection. Once the forward bias is released the internal field decreases due to the depolarization of ionic impurities. As a matter of fact, the discovered recovery effect in LEDs and the earlier reported PIPP seemed to have similar nature.

Our first attempts to record recovery effect on photocurrent for freshly prepared nonencapsulated cells with traditional structure revealed no recovery phenomenon. However, after repeating the measurements on one month old cells the restoration of photocurrent was clearly recorded (Figure 4.11). This finding is completely consistent with the recovery recorded during the outdoor measurements (Figure 4.8) and confirms that the recorded phenomenon is reproducible also for nonencapsulated cells under indoor testing conditions. In addition, similar results were obtained for devices based on native polythiophene (PT)/PCBM bulk heterojunction (the route of device preparation is described in Appendix 2.1). Therefore, based on the earlier reports and the currently obtained results we suggest that PIPP in the photoactive layer of the bulk heterojunction solar cells can cause the observed reversible degradation of the cell under illumination. When the cell is kept in the dark for certain period the sample is depolarized and the internal field decreases. As a result, at a very first stage of cell illumination the photocurrent gives the highest value with subsequent decay within the time. The older the cell is, the more is the concentration of defects in the active layer and the stronger is the internal filed.

In conclusion, the further investigations of the reversible degradation effect in polymer solar cells confirmed that the phenomenon is observed independent of testing conditions and device configuration. The detailed studies showed that the recovery of V_{oc} can be resulted from temperature change in the device active layer, while the nature of the I_{sc} recovery resembles the earlier studied effect of photoinduced internal photopolarization (PIPP) and the effect becomes more apparent with ageing of the cell. These findings could further elucidate the decay processes that take place in the cell.

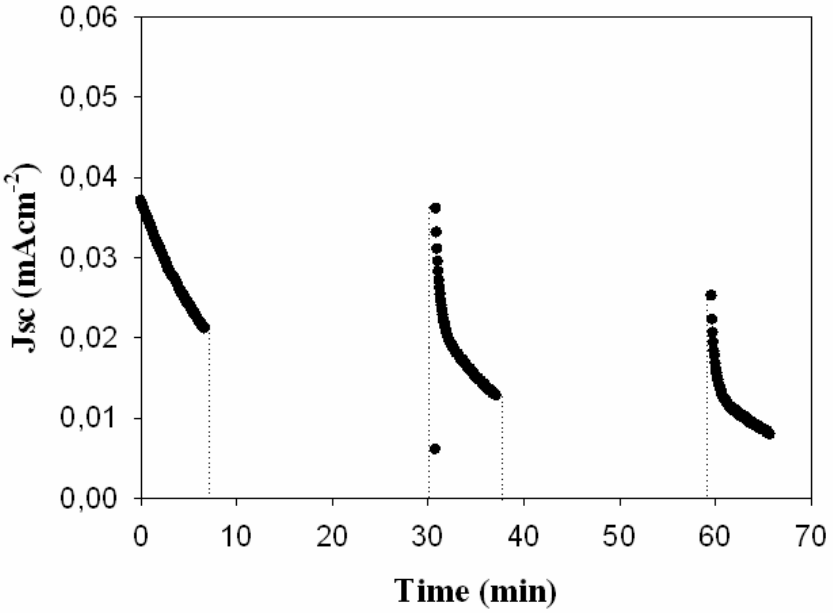

Figure 4.11: Short circuit current density J_{sc} versus time while the cell is being periodically exposed to 1sun irradiation and dark.

4.4 Stability of Thermocleavable Polymers

4.4.1 Degradation Measurements of Native Polythiophene

The degradation studies of thermocleavable P3MHOCT polymer discussed in Section 3.3.1 were carried out using the measuring setup presented in section 4.2.1. Figure 4.12 shows the decay of the photovoltaic parameters of the cell based on native polythiophene PT:[70]PCBM combination (PT is obtained by thermally cleaving the polymer P3MHOCT at 310^{o}C) during 500 hours kept in the atmospheric chamber under Nitrogen atmosphere, 0 % relative humidity, under illumination of 330 W/cm^2 light intensity. The measurements showed that V_{oc} of these types of cells is rather sensitive towards environmental impact. Figure 4.13 shows the IV curves of the device measured during the decay process, while Figure 4.14 shows the comparative decay measurements of I_{sc} of the devices cleaved at 250 ^{o}C (P3CT) and 310 ^{o}C (PT). It is clear that the device stability is improved after the cleaving process.

We believe that if one could improve the stability of V_{oc}, then this type of device could certainly challenge the commonly used traditional organic materials, such as P3HT and others.

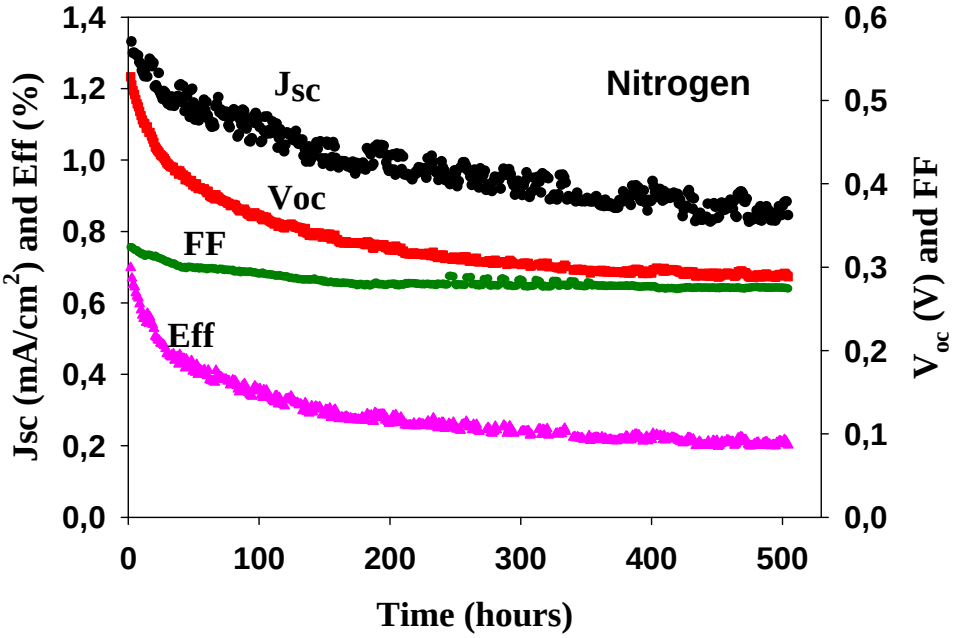

Figure 4.12: Variation of PV parameters of ITO/PEDOT:PSS/PT:[70]PCBM/Al device kept in nitrogen atmosphere under 1/3 sun irradiation for 500 h (330 W/m^2, AM1.5G, nitrogen, 0% relative humidity, 25 ^{o}C).

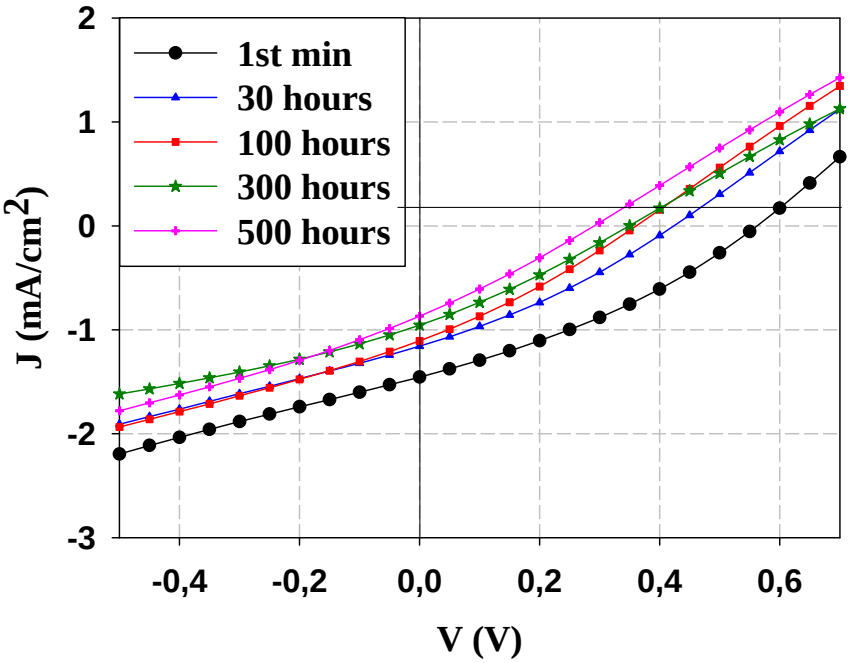

Figure 4.13: The evolution of IV-curves along the decay process in nitrogen for device with configuration Glass/ITO/PEDOT:PSS/PT:PCBM[70]/Al (330 W/m^2, AM1.5G, nitrogen, 0% relative humidity, 25 ^{o}C).

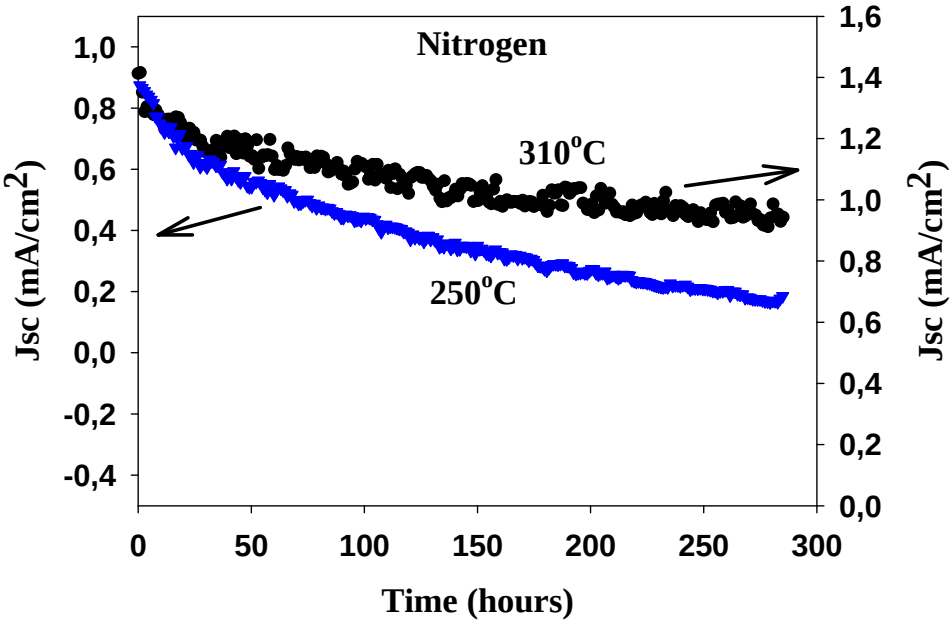

Figure 4.14: Decay of J_{sc} for devices Glass/ITO/PEDOT:PSS/Polymer:PCBM[70]/Al cleaved at two different temperatures (330 W/m^2, AM1.5G, nitrogen, 0% relative humidity, 25 ^{o}C).

4.4.2 Stability of Thermocleavable Low Band Gap Polymers

Similarly, stability studies were carried out for thermocleavable low band gap polymers presented in Section 3.3.3. To get an overview of the stability of the best performing **8j** polymer in relation to other known polymers and as a function of atmospheric reactants two studies were performed: one comparative study in an inert atmosphere and a study where devices were subjected to different atmospheres during continuous illumination.

Figure 4.15 shows the degradation of devices prepared in the same manner employing respectively P3HT, PT, and **8j**. The devices were measured inside the atmospheric chamber under controlled Nitrogen atmosphere. The performance of **8j** is inferior to both P3HT and PT in terms of efficiency, while the photovoltaic parameters are much more stable in time. The P3HT based device was annealed at 150 °C for 5 min after evaporation of the aluminum electrode. PT devices were prepared by heating P3MHOCT-PCBM films to 310 °C before evaporation of the aluminum electrode. The decay in the photovoltaic parameters were not affected significantly by the thermocleavage at 230 °C and the stability of **8j** is thus concluded to be very good without cleavage while there are processing advantages of thermally cleaved **8j**. Cleaving **8j** at higher temperatures

(310 °C) reduced the photovoltaic performance drastically and the decay of V_{oc} and *FF* was much faster.

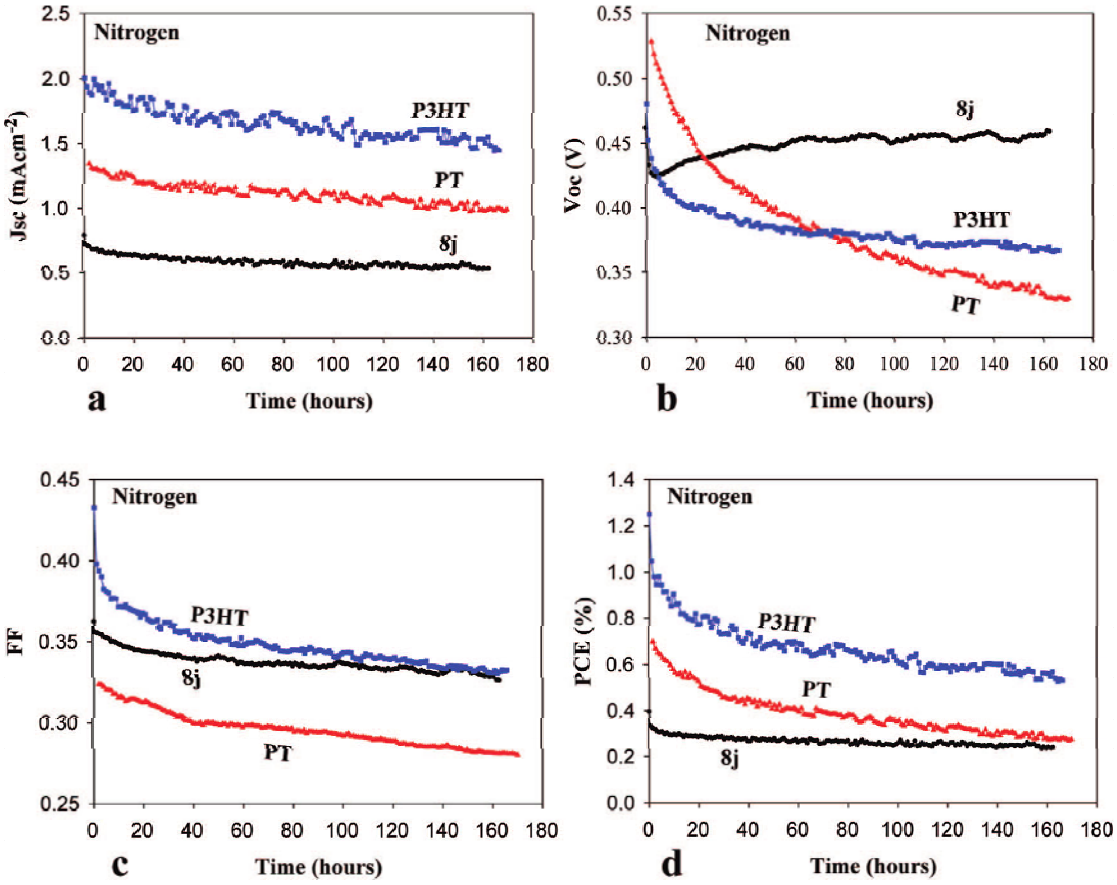

Figure 4.15: Comparison of the decay of the photovoltaic parameters for P3HT, PT, and **8j** polymers with a Glass/ITO/PEDOT:PSS/polymer:PCBM/Al device geometry in a nitrogen atmosphere (330 W/m^2, 30 °C, oxygen < 2 ppm, water < 2 ppm).

Further, **8j** polymer based devices were subjected to four different atmospheres to establish the inherent stability in nitrogen and the effect of water and oxygen taken separately and finally in combination in the real atmosphere. The conditions were as follows:

1) Pure nitrogen atmosphere 99.999 % (oxygen < 2 ppm, humidity < 2 ppm)
2) Dry oxygen atmosphere 99.5 % (humidity < 2 ppm)
3) Ambient atmosphere (20 ± 5 % relative humidity)
4) Humid nitrogen 99.999 % (oxygen < 2 ppm, 95 ± 5 % relative humidity)

It was found that oxygen had little effect on the stability as shown in Figure 4.16. The interesting finding was that the presence of pure oxygen at high concentration (i.e., five times more than in the ambient atmosphere) does not seem to speed up degradation significantly and we would

rate **8j** as stable toward oxygen under illumination. This is in stark contrast to conjugated materials containing vinylene bonds that are very sensitive toward oxygen. Humidity however was found to profoundly influence the stability leading to rapid degradation that is complete within less than 20 h whereas the absence of water leads to moderately stable operation.

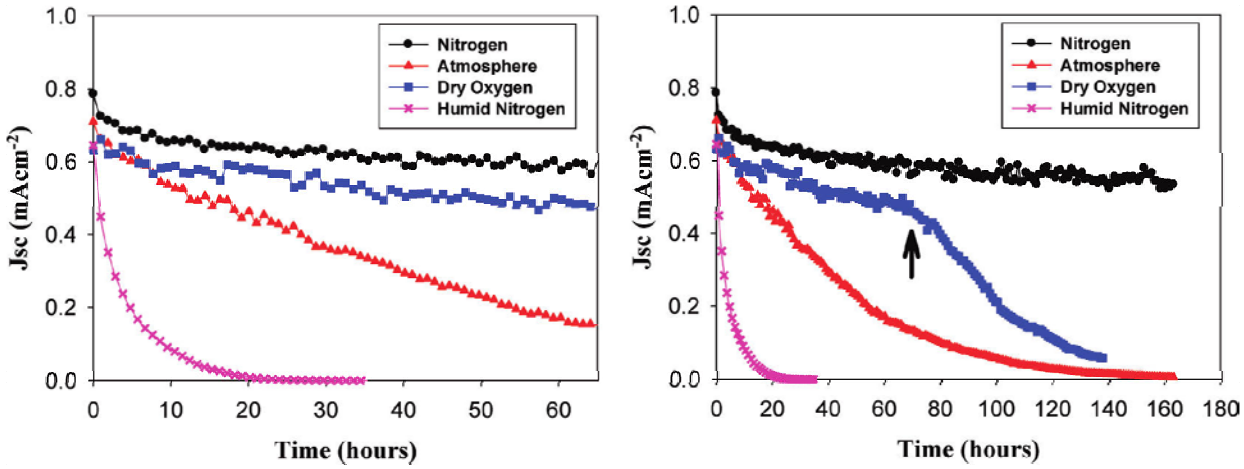

Figure 4.16: Decay of devices with configuration Glass/ITO/PEDOT:PSS/8j:PCBM/Al under conditions of: pure nitrogen atmosphere 99.999 % (oxygen < 2 ppm, humidity < 2 ppm), dry oxygen atmosphere 99.5 % (humidity < 2 ppm), ambient atmosphere (20 ± 5 % relative humidity), humid nitrogen 99.999 % (oxygen < 2 ppm, 95 ± 5 % relative humidity). The temperature was 30 ± 2 °C and the incident light intensity was 330 W/m^2 (left). The same experiment was repeated for a longer period of time while introducing ambient atmosphere after 70 h (see arrow) thus reducing the oxygen level by a factor of 5 and increasing the humidity by a factor of 105 (right).

The right hand side of Figure 4.16 shows results of measurements for longer period of time (170 hours) and the black arrow points the moment when dry oxygen atmosphere was substituted with ambient atmosphere. Clearly addition of humidity in the chamber resulted in significant acceleration of the decay process in the device. The devices dye rapidly in the presence of water (with and without oxygen present) and removal of water from this type of device gives devices with stability that exceeds hundreds of hours.

4.5 Stability of Inverted Devices

In terms of operational stability[12] the electron-collecting electrode is problematic because this implies that the electron carriers travel at high energy levels (LUMO). This is incompatible with operation in the presence of molecular oxygen and water molecules. The hole carriers do not have the same problems associated with transport in the presence of water molecules and molecular oxygen. It should thus in principle be possible to gain stability through an inverted device geometry towards both oxygen and water and to establish this model studies were performed using different atmospheres.

Stability measurements were conducted for normal vs. inverted devices with the following structures:

Normal – Substrate/ITO/PEDOT:PSS/P3HT:PCBM/Al

Inverted – Substrate/ITO/ZnO/P3HT:PCBM/PEDOT:PSS/Ag

Two types of substrates were used. Glass substrates were used for the model devices prepared using spin coating technique, while roll-to-roll coated devices using slot dye coating had flexible PET as a substrate. The details on roll-to-roll coating process can be found in the reprint of an article in Appendix 6. Similar to previous studies the stability measurements were carried out for devices kept in four different conditions:

1) Pure nitrogen atmosphere 99.999 % (oxygen < 2 ppm, humidity < 2 ppm)
2) Dry oxygen atmosphere 99.5 % (humidity < 2 ppm)
3) Ambient atmosphere (20 ± 5 % relative humidity)
4) Humid nitrogen 99.999 % (oxygen <2 ppm, 95 ± 5% relative humidity)

The temperature of the devices during the stability experiments was 40 ± 3 ^{o}C.

Similar to the results in the previous section the normal devices degraded as expected in the presence of humidity, but were quite stable in the presence of molecular oxygen (even in pure oxygen). Humidity (water) reacts efficiently with aluminum at unprotected interfaces leading to rapid degradation as shown in Figure 4.17 and as summarized in Table 4.3.

In the inverted device this was then expected to be efficiently solved as silver should not react with water at the metal-organic interface. Good operational stability in the presence of humidity was also observed confirming this hypothesis. However, the device presented poor stability towards oxygen. While it is problematic that we did not achieve stability towards both oxygen and humidity simultaneously it is reassuring that it is possible to make devices that are stable in the presence of oxygen (normal geometry) and in the presence of humidity (inverted geometry). This does hold

promise for the possibility of developing materials and device combination that exhibits stability in the presence of both oxygen and humidity.

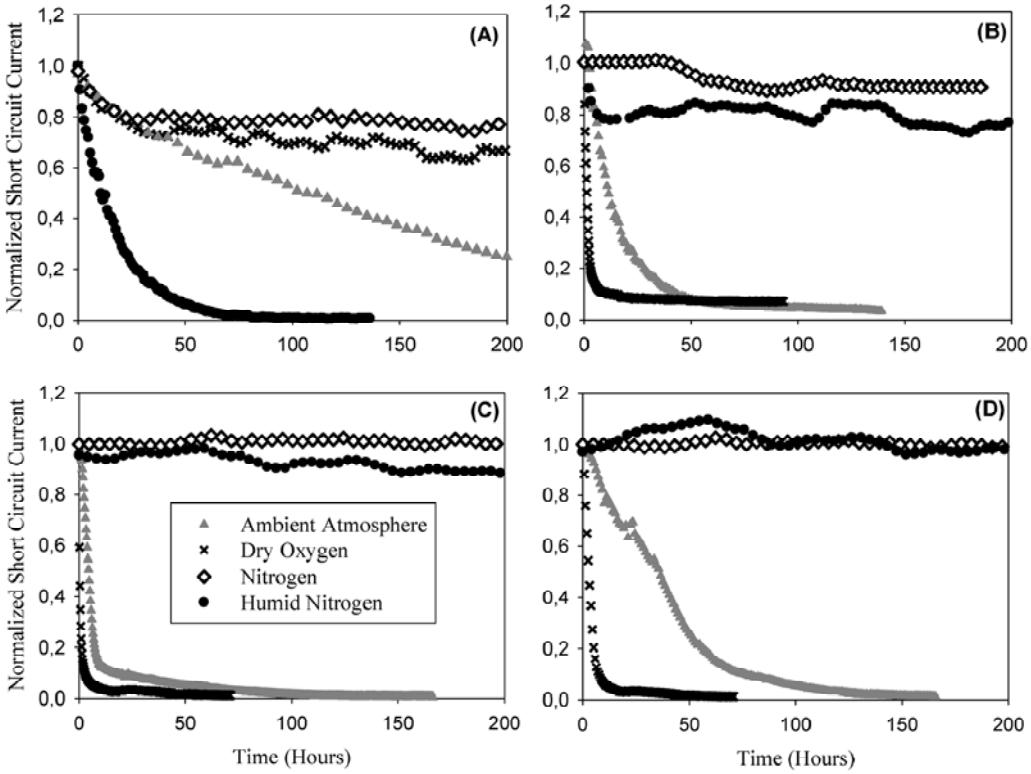

Figure 4.17: Curves showing the degradation as a function of illumination time under different atmospheric conditions for device models with normal geometry (A) and inverted geometry (B) and R2R processed inverted devices without encapsulation (C) and with simple encapsulation (D).

Table 4.3: Stability testing under different atmospheric conditions

Module	**N_2**	**H_2O**	**O_2**	**H_2O/O_2**
Normal Geometry (Evaporated Al) [a]	+	-	+	-
Inverted Geometry (Evaporated Ag) [a]	+	+	-	-
Inverted Geometry (solution processed Ag paste) [a]	+	+	-	-
Inverted Geometry (All R2R processed) [b]	+	+	-	-

[a] The active area was 3 cm^2, the measurement conditions were 330 W/cm^2, AM 1.5G, 40 ± 3 ^oC.
[b] The active area was 4.8 cm^2, the measurement conditions were 330 W/cm^2, AM1.5G, 40 ± 3 ^oC.

Simple cold back lamination with PET and an acrylic resin as the binder improved the operational stability significantly as shown in Figure 4.17. It is interesting that inverted devices that are based on zinc oxide work well in the absence of oxygen since this has been shown to be problematic earlier in bulk heterojunctions based on PPVs and metal oxide semiconductors

including zinc oxide[6,13] and also for poly-3- carboxydithiophene- ZnO bulk heterojunctions.[14,15] From this point of view dependence on the presence of oxygen for device function was expected. It should however be noted that the charge carrier separation processes in these devices are assumed to take place in the bulk of P3HT and PCBM and that zinc oxide in these devices only works as an electron transport layer. We ascribe the indifference of device function with respect to the presence of molecular oxygen to be due to this fact.

The further details of the presented studies can be found in the reprint of the published article in Appendix 6. In addition, a short overview with a title "Advanced Processing of New Materials for Extended Operational Lifetime of Polymer Solar Cells" has been published in 52nd Annual Technical Conference Proceedings, Santa Clara, CA, 2009 ISSN 0737-5921, where the stability of thermocleavable polymers and inverted device structures is discussed. The article can be found in Appendix 10.

4.6 Applicability of X-ray Reflectometry to Studies of Polymer Solar Cell Degradation

X-Ray Reflectometry is an analytical technique for investigating thin layers using the effect of total external reflection of X-rays. In reflectivity experiments, the X-ray reflection of a sample is measured around the critical angle. Below the critical angle of total external reflection, X-rays penetrate only a few nanometers into the sample. Above this angle the penetration depth increases rapidly. At every interface where the electron density changes, a part of the X-ray beam is reflected. The interference of these partially reflected X-ray beams creates the oscillation pattern observed in reflectivity experiments. From these reflectivity curves, layer parameters such as thickness and density, interface and surface roughness can be determined.

Paci *et al.* used a white incident X-ray beam produced by a standard 2 kW tungsten anode X-ray tube and detected by a solid-state germanium detector to study cells composed of the structure: glass/ITO/PEDOT/MDMO-PPV:PCBM/Al or glass/ITO/MDMO-PPV:PCBM/LiF/Al.[16,17] The results showed oscillations in the reflected intensity that were interpreted as due to the aluminum electrode layer. The cells were investigated both under illumination and in the dark and a significant thickening of the layer was observed. Two possible explanations were offered. The first was that a reaction occurred at the aluminum polymer interface with the formation of an aluminum oxide

layer. The second explanation was that indium atoms from the ITO layer diffused into the organic layer.

Inspired by this work, we have studied the layer and interface structure of glass/ITO/PEDOT:PSS/MEH-PPV/Al solar cells during operation with high-resolution angle-dispersive synchrotron X-ray reflectometry.

Samples representing different combinations of polymer solar cell layers were prepared as outlined in Table 4.4. After preparation, the samples were packed in diffusion and light tight bags made from a composite foil (70 μm polyethylene/9 μm Al/20 μm polyamide) inside the glove-box and transported to HASYLAB, Hamburg, for the X-ray reflectometry studies.

Table 4.4: Structure of the Tested Samples

Number	Structure of Prepared Samples
3	Glass/ITO/PEDOT:PSS/MEH-PPV/Al
4	Glass/ITO/PEDOT:PSS/Al
5	Glass/ITO/PEDOT:PSS
7	Glass/ITO

IV diode characteristics were measured for the device #3 (Table 4.4) simultaneously with reflectometry studies in order to record the rate of the decay process inside the solar cell. The cell was mounted on a holder designed for in situ measurements, which provides the necessary contacts for the IV characterization and keeps the cell surface accessible for X-ray reflectivity measurements. A spotlight halogen lamp (OSRAM Decostar IRC 20W 12V) was fixed approximately 10 cm below the holder to illuminate the cell (Figure 4.18). After the cell was removed from the sealed bag and mounted on the setup, initial reflectivity measurements on the cell were carried out in a dark room for about 5 h. Then the spotlight was turned on and IV data were collected using a source-measuring unit (Keithley 2400 and computer) connected to the cell, while continuing the reflectometry analyses.

Figure 4.19 presents the decay of short circuit current density of the cell measured within ~ 6 h and a double exponential fit normalized to the experimental data according to the following equation [4.7] in order to more clearly illustrate the degradation process:

$$\left|\frac{J_{sc}(t)}{J_{sc}(0)}\right| = A\, e^{-bt} + C\, e^{-dt} + \cdots \qquad [4.7]$$

The normalized decay parameters of the fit are collected in Table 4.5. The decay of this device type is consistent with earlier findings for ITO/PEDOT:PSS/MEHPPV/Al homojunctions.[5] One

can see that after 20 min of illumination the current dropped to 50% of its initial value. This fast decay is ascribed to the combination of a high intensity of the spotlight (measured irradiation was about 2 sun) and overheating of the tested cell by the lamp (the temperature of the cell during measurements reached 92 ^{o}C).

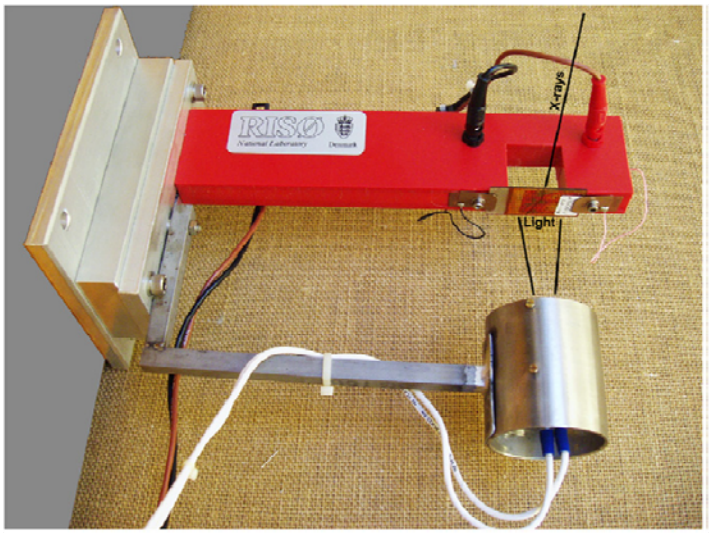

Figure 4.18: The sample-holder designed for in situ reflectivity measurements. The solar cell is seen mounted just above the word ‘‘Light’’, held in place by clamps ensuring contact with the electrodes for measuring IV characteristics.

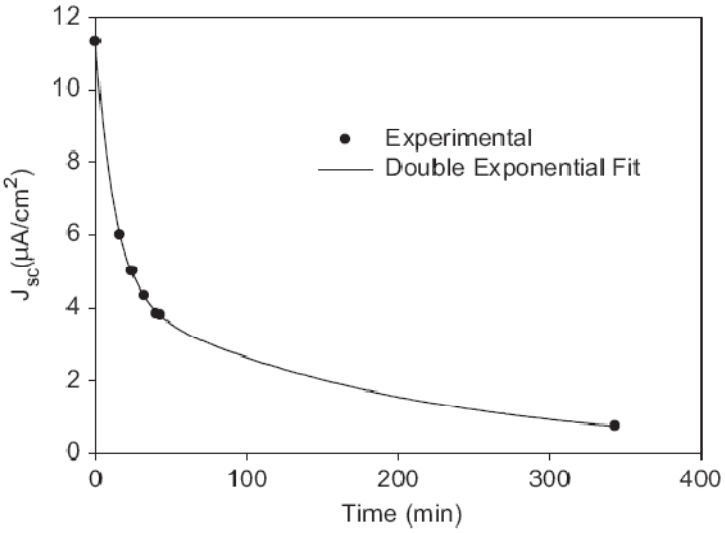

Figure 4.19: Experimental data (●) and double exponential fit (—) of short circuit current density measured for 6 h under 2 sun irradiation for the cell with geometry ITO/PEDOT:PSS/MEH-PPV/Al.

Table 4.5: Normalized parameters of the fit describing the current decay according to Eq. (4.7).

a (%)	b (s^{-1})	c (%)	d (s^{-1})	J_o ($\mu A/cm^2$)
6.9	79×10^{-3}	4.4	5.3×10^{-3}	11.3

The details of the reflectivity measurements and the discussion of the results can be found in the reprint of the published article in Appendix 11, while here short summary is presented only.

The results showed that even high-resolution angle-dispersive synchrotron X-ray reflectivity data, seemingly well fitted by detailed models, still leaves much uncertainty regarding the interpretation of the obtained density profiles. Although small changes in the reflectivity profile are observed, repeated model fits do not provide consistent results. No significant statistical change was obtained at the interface between polymer and Al electrode and the possible reason could be that the comparatively rough interface, even for a model system as studied here, seriously inhibits the observation of small changes, like the formation of a thin (sub-nm) interfacial oxide layer. Such a change or other morphological changes cannot be excluded, especially because a difference in reflectivity profiles before and during illumination is qualitatively observed, but the non-linear model fit cannot provide an unequivocal scattering length density profile of sufficient statistical validity. On these grounds, it was regarded as near impossible to detect such changes in more realistic devices, e.g. bulk hetero-junctions of P3HT–PCBM or PPV–PCBM for which much higher interfacial roughness was observed compared to the model system homo-junction studied in the work presented here.

4.7 Conclusions

A setup for degradation measurements of OPV devices was presented. It was possible to control the atmosphere via the setup thus choosing the conditions for degradation studies of the cells. Various devices have been studied using this setup and it was shown that thiophene based devices with Aluminum back electrode are rather stable in oxygen atmosphere, while they rapidly degrade in humid environment. Contrary to normal devices the cells with inverted structure showed promising stability in humid environment, while rapidly degraded in oxygen environment. In addition, comparative stability measurements were carried out for thermocleavable polymers, which show rather promising features in terms of stability. Studies of recovery phenomena of PV

parameters were carried out as well and further explanation of the effect via persistent internal photopolarization was given.

Reference List

1. J. A. Hauch, P. Schilinsky, S. A. Choulis, R. Childers, M. Biele, and C. J. Brabec, Flexible organic P3HT : PCBM bulk-heterojunction modules with more than 1 year outdoor lifetime, *Sol.Energy Mater.Sol.Cells*, 2008, **92**, 727-731.

2. F. C. Krebs and K. Norrman, Analysis of the failure mechanism for a stable organic photovoltaic during 10000 h of testing, *Prog.Photovolt: Res.Appl.*, 2007, **15**, 697-712.

3. S. A. Gevorgyan, M. Jorgensen, and F. C. Krebs, A setup for studying stability and degradation of polymer solar cells, *Sol.Energy Mater.Sol.Cells*, 2008, **92**, 736-745.

4. E. A. Katz, S. Gevorgyan, M. S. Orynbayev, and F. C. Krebs, Out-door testing and long-term stability of plastic solar cells, *European Physical Journal-Applied Physics*, 2006, **36**, 307-311.

5. F. C. Krebs, J. E. Carle, N. Cruys-Bagger, M. Andersen, M. R. Lilliedal, M. A. Hammond, and S. Hvidt, Lifetimes of organic photovoltaics: photochemistry, atmosphere effects and barrier layers in ITO-MEHPPV: PCBM-aluminium devices, *Sol.Energy Mater.Sol.Cells*, 2005, **86**, 499-516.

6. M. Lira-Cantu, K. Norrman, J. W. Andreasen, and F. C. Krebs, Oxygen release and exchange in niobium oxide MEHPPV hybrid solar cells, *Chem.Mater.*, 28-11-2006, **18**, 5684-5690.

7. K. Norrman, N. B. Larsen, and F. C. Krebs, Lifetimes of organic photovoltaics: Combining chemical and physical characterisation techniques to study degradation mechanisms, *Sol.Energy Mater.Sol.Cells*, 6-11-2006, **90**, 2793-2814.

8. K. Norrman and F. C. Krebs, Lifetimes of organic photovoltaics: Using TOF-SIMS and $^{18}O_2$ isotopic labelling to characterise chemical degradation mechanisms, *Sol.Energy Mater.Sol.Cells*, 23-1-2006, **90**, 213-227.

9. E. A. Katz, V. Lyubin, D. Faiman, S. Shtutina, A. Shames, and S. Goren, Persistent photoelectric phenomena in oxygenated C60 thin films, *Solid State Communications*, 1996, **100**, 781-784.

10. H. Kallmann and B. Rosenberg, Persistent Internal Polarization, *Phys.Rev.*, 15-3-1955, **97**, 1596.

11. D. C. Zou, M. Yahiro, and T. Tsutsui, Study on the degradation mechanism of organic light-emitting diodes (OLEDs), *Synthetic Metals*, 1997, **91**, 191-193.

12. M. Jørgensen, K. Norrman, and F. C. Krebs, Stability/degradation of polymer solar cells, *Sol.Energy Mater.Sol.Cells*, 2008, **92**, 686-714.

13. M. Lira-Cantu and F. C. Krebs, Hybrid solar cells based on MEH-PPV and thin film semiconductor oxides (TiO2, Nb2O5, ZnO, CeO(2)and CeO2-TiO2): Performance improvement during long-time irradiation, *Sol.Energy Mater.Sol.Cells*, 6-9-2006, **90**, 2076-2086.

14. F. C. Krebs, Air stable polymer photovoltaics based on a process free from vacuum steps and fullerenes, *Sol.Energy Mater.Sol.Cells*, 2008, **92**, 715-726.

15. F. C. Krebs, Y. Thomann, R. Thomann, and J. W. Andreasen, A simple nanostructured polymer/ZnO hybrid solar cell - preparation and operation in air, *Nanotechnology*, 22-10-2008, **19**, 424013.

16. B. Paci, A. Generosi, V. Rossi Albertini, P. Perfetti, R. De Bettignies, M. Firon, J. Leroy, and C. Sentein, In situ energy dispersive x-ray reflectometry measurements on organic solar cells upon working, *Appl.Phys.Lett.*, 7-11-2005, **87**, 194110-194113.

17. B. Paci, A. Generosi, V. R. Albertini, P. Perfetti, R. De Bettignies, J. Leroy, M. Firon, and C. Sentein, Controlling photoinduced degradation in plastic photovoltaic cells: A time-resolved energy dispersive x-ray reflectometry study, *Appl.Phys.Lett.*, 24-7-2006, **89**, 043507-3.

5 Conclusions and Future Challenges

Processing techniques were presented for manufacturing small scale solar cell devices. It was shown that many characteristics such as device geometry, material combinations, concentration and concentration ratios and layer thicknesses can significantly affect the device performance. In addition, it was shown that the accuracy of evaluation of device performance is correlated with the geometric design of the device. Furthermore, a number of characterization techniques were presented, which have been used in the presented work. Advanced processing of poly(3-hexylthiophene) (P3HT) based devices was described.

In addition, characterizations of various thermocleavable polymers and comparison with materials of traditional devices were presented. Inverted structure devices were manufactured as well and tested for PV performance and it was shown that inverted devices can perform as good as the normal geometry device. Utilization of MoO_3 or V_2O_5 materials as a buffer layer instead of PEDOT:PSS were presented as well. Although it was not possible to produce devices that would perform as good as traditional device with PEDOT, it was shown that there is a potential for obtaining higher efficiencies by improving the buffer layer morphology of MoO_3 or V_2O_5.

Stability issue was discussed. In particular, a setup for efficient device lifetime evaluation with controlled atmospheric conditions was presented. Examples of device degradation studies were shown using this setup. It was shown that devices under different atmospheric conditions (oxygen, nitrogen) have different decay kinetics. In addition, various polymer based devices were tested for stability. It was shown, that thermocleavable polymer based devices can have longer lifetimes compared to traditional device. Recovery effect of PV parameters during the decay process was further studied and it was shown that the effect is related to persistent internal photopolarization effect. The studies of inverted vs. normal geometry reveal that normal geometry devices with Al back electrode are rather stable in oxygen atmosphere, but rapidly degrade in humidity, while inverted devices with Ag back electrode show high stability in humid environment, but tend to quickly degrade when exposed to oxygen.

There are a number of challenges that still need to be addressed to accomplish the presented studies, which were not possible to do within the frames of this work. In particular:

a) Further characterization of thermocleavable polymers is required with attempt to increase the device performance via optimized processing.

b) Further studies of MoO_3 and V_2O_5 metal oxides have to be carried out with the attempt to establish the optimal processing of the layers for manufacturing efficient solar cells. A solution processing of such metal oxides is also a fascinating and challenging issue that needs to be addressed. After optimization of devices using such materials tandem solar cells can be possibly manufactured.

c) Further degradation studies should be carried out with optimized atmospheric chambers with improved atmosphere and temperature control, which would allow more thorough studies of the impact of humidity and oxygen on various active materials and electrodes.

List of Publications

Articles

2008

1. J. W. Andreasen, S. A. Gevorgyan, C. M. Schlepütz, and F. C. Krebs, Applicability of X-ray reflectometry to studies of polymer solar cell degradation, *Sol.Energy Mater.Sol.Cells*, 2008, **92**, 793-798. **(Appendix 11)**

2. S. A. Gevorgyan, M. Jorgensen, and F. C. Krebs, A setup for studying stability and degradation of polymer solar cells, *Sol.Energy Mater.Sol.Cells*, 2008, **92**, 736-745. **(Appendix 7)**

3. S. A. Gevorgyan, E. A. Katz, and F. C. Krebs, Reversible Degradation of Conjugated Polymer/Fullerene Solar Cells, 578, *23rd EU PVSEC*, Valencia, Spain,2008. **(Appendix 9)**

4. S. A. Gevorgyan, and F. C. Krebs, Bulk heterojunctions based on native polythiophene, *Chem.Mater.*, 2008, **20**, 4386-4390. **(Appendix 2.1 and 2.2)**

5. M. H. Petersen, S. A. Gevorgyan, and F. C. Krebs, Thermocleavable Low Band Gap Polymers and Solar Cells Therefrom with Remarkable Stability toward Oxygen, *Macromolecules*, 2008, **41**, 8986-8994. **(Appendix 4)**

2009

6. M. Helgesen, S. A. Gevorgyan, F. C. Krebs, and R. A. J. Janssen, Substituted 2,1,3-Benzothiadiazole- And Thiophene-Based Polymers for Solar Cells - Introducing a New Thermocleavable Precursor, *Chem. Mater.*, 2009, **21**, 4669–4675. **(Appendix 5)**

7. F. C. Krebs, S. A. Gevorgyan, and J. Alstrup, A roll-to-roll process to flexible polymer solar cells: model studies, manufacture and operational stability studies, *J.Mater.Chem.*, 2009, **19**, 5442-5451. **(Appendix 6)**

8. F. C. Krebs, S. A. Gevorgyan, B. Gholamkhass, S. Holdcroft, C. Schlenker, M. E. Thompson, B. C. Thompson, D. Olson, D. S. Ginley, S. E. Shaheen, H. N. Alshareef, J. W. Murphy, W. J. Youngblood, N. C. Heston, J. R. Reynolds, S. Jia, D. Laird, S. M. Tuladhar, J. G. A. Dane, P. Atienzar, J. Nelson, J. M. Kroon, M. M. Wienk, R. A. J. Janssen, K. Tvingstedt, F. Zhang, M. Andersson, O. Inganäs, M. Lira-Cantu, R. de Bettignies, S. Guillerez, T. Aernouts, D. Cheyns, L. Lutsen, B. Zimmermann, U. Würfel, M. Niggemann, H. F. Schleiermacher, P. Liska, M. Grätzel, P. Lianos, E. A. Katz, W. Lohwasser, and B. Jannon, A round robin study of flexible large-area roll-to-

roll processed polymer solar cell modules, *Sol.Energy Mater.Sol.Cells*, 2009, **93**, 1968-1977. **(Not Presented in Thesis)**

9. K. Norrman, S. A. Gevorgyan, and F. C. Krebs, Water-Induced Degradation of Polymer Solar Cells Studied by (H2O)-O-18 Labeling, *Acs Applied Materials & Interfaces*, 2009, **1**, 102-112. **(Appendix 8)**
10. S. A. Gevorgyan, and F. C. Krebs, Advanced Processing of New Materials for Extended Operational Lifetime of Polymer Solar Cells, 15, *SVC 52nd Annual Technical Conference*, Santa Clara, CA, 2009 **(Appendix 9)**

11. V. Senkovskyy, R. Tkachov, T. Beryozkina, H. Komber, U. Oertel, M. Horecha, V. Bocharova, M. Stamm, S. A. Gevorgyan, F. C. Krebs, and A. Kiriy, "Hairy" Poly(3-hexylthiophene) Particles Prepared via Surface-Initiated Kumada Catalyst-Transfer Polycondensation, *J. Am. Chem. Soc.*, 2009, **131**, 16445–16453. **(Appendix 1)**

12. T. Tromholt, S. A. Gevorgyan, M. Jørgensen, F. C. Krebs, and K. O. Sylvester-Hvid, Thermocleavable Materials for Polymer Solar Cells with High Open Circuit Voltages - A Comparative Study, *Acs Applied Materials & Interfaces*, 2009, **1**, 2768–2777. **(Appendix 3)**

Book Chapter Contributions

1. S. A. Gevorgyan, and F. C. Krebs, "Photovoltaics Based on Thiophene Polymers: a Short Overview", in book: I. F. Perepichka, D. F. Perepichka (eds.), "Thiophene-Based Materials for Electronics and Photonics", *John Wiley & Sons Ltd*, 2009, ch. 18, 673-693. **(Not Presented in Thesis)**

2. S. A. Gevorgyan, and F. C. Krebs, "Large Scale Production of Efficient and Stable Polymer Solar Cells: From Spin Coating to Roll-to-Roll Processing", in book: D. K. Aswal, J. V. Yakhmi (eds.), "Recent Advances in Molecular and Polymer Devices", *NOVA SCIENCE, New York*, in press. **(Not Presented in Thesis)**

3. S. A. Gevorgyan, R. Søndergaard, and F. C. Krebs, "Introduction"; R. Søndergaard, S. A. Gevorgyan, and F. C. Krebs, "Materials and Processing"; S. A. Gevorgyan, and F. C. Krebs, "Stability and Characterization of Devices", in book: F. C. Krebs (edt.), Materilas, Methods and Manufacturin of Polymer Solar Cells, Bussines Strategies, Company Reviews, Demonstrations and IPR Landscape, submitted. **(Not Presented in Thesis)**

J|A|C|S ARTICLES

Published on Web 10/27/2009

"Hairy" Poly(3-hexylthiophene) Particles Prepared via Surface-Initiated Kumada Catalyst-Transfer Polycondensation

Volodymyr Senkovskyy,[†] Roman Tkachov,[†] Tetyana Beryozkina,[†] Hartmut Komber,[†] Ulrich Oertel,[†] Marta Horecha,[†] Vera Bocharova,[†] Manfred Stamm,[†] Suren A. Gevorgyan,[‡] Frederik C. Krebs,[‡] and Anton Kiriy*,[†]

Leibniz-Institut für Polymerforschung Dresden e.V., Hohe Straβe 6, 01069 Dresden, Germany, and Risø National Laboratory for Sustainable Energy, Technical University of Denmark, Frederiksborgvej 399, DK-4000 Roskilde, Denmark

Received June 15, 2009; E-mail: kiriy@ipfdd.de; senkovskyy@ipfdd.de

Abstract: Herein, we present a new paradigm in the engineering of nanostructured hybrids between conjugated polymer and inorganic materials via a chain-growth surface-initiated Kumada catalyst-transfer polycondensation (SI-KCTP) from particles. Poly(3-hexylthiophene), P3HT, a benchmark material for organic electronics, was selectively grown by SI-KCTP from (nano)particles bearing surface-immobilized Ni catalysts supported by bidentate phosphorus ligands, that resulted in hairy (nano)particles with end-tethered P3HT chains. Densely grafted P3HT chains exhibit strongly altered optical properties compared to the untethered counterparts (red shift and vibronic fine structure in absorption and fluorescence spectra), as a result of efficient planarization and chain-aggregation. These effects are observed in solvents that are normally recognized as good solvents for P3HT (e.g., tetrahydrofurane). We attribute this to strong interchain interactions within densely grafted P3HT chains, which can be tuned by changing the surface curvature (or size) of the supporting particle. The hairy P3HT nanoparticles were successfully applied in bulk heterojunction solar cells.

Introduction

It is well-established that performances of thin-film devices based on π-conjugated polymers (CPs), for example, solar cells, field-effect transistors, and light-emitting diodes, are strongly dependent on the organization of the polymer molecules and their interactions with other constituents in the multicomponent devices.[1] Further progress of organic electronics will require a development of new CPs having not only improved optoelectronic characteristics, but also guidable self-assembly properties.[1] In general, self-assembly is a powerful and cost-efficient approach in the fabrication of complex nanostructured materials. However, it works more predictably in the case of relatively simple, shape-persistent, chemically well-defined building blocks, such as conjugated oligomers or macrocycles.[2] CPs are usually more flexible, larger, and less defined in terms of molecular weight distribution and chemical structure when comparing to their small-molecule counterparts and they exhibit very complex self-assembly behavior. In addition, films of CPs formed from solution rarely give optimally organized structures as prepared, and this can pose problems when they must be delicately organized together with other components, such as in bulk heterojunction solar cells.[1]

We assumed that self-assembly of complex multicomponent functional structures would be subject to a higher degree of control, if relatively large (but still nanoscale), three-dimensional, shape-persistent, and covalently preorganized building blocks were used. We supposed that "hairy" particles, nanoscale objects in which polymer chains are attached by their end points to a particle core and stretched away from it to form spherical brushes, would be such an interesting alternative to conventional linear CPs. In addition, conjugated polyelectrolytes (charged CPs)[3] densely grafted to microsperes would be an attractive approach to sensor applications. The "grafting-to" approach based on a coupling of end-functionalized polymers with complementarily terminated surfaces usually provides rather low grafting densities.[4] This method that has been widely employed

[†] Leibniz-Institut für Polymerforschung Dresden e.V.
[‡] Technical University of Denmark.

(1) (a) Hoppe, H.; Sariciftci, N. S. *J. Mater. Chem.* **2006**, *16*, 45–61. (b) Thompson, B. C.; Fréchet, J. M. J. *Angew. Chem., Int. Ed.* **2008**, *47*, 58–77. (c) Kroon, R.; Lenes, M.; Hummelen, J. C.; Blom, P. W. M.; De Boer, B. *Polym. Rev.* **2008**, *48*, 531–582. (d) Kiriy, N.; Bocharova, V.; Kiriy, A.; Stamm, M.; Krebs, F. C.; Adler, H.-J. *Chem. Mater.* **2004**, *16*, 4765–4771. (e) Kiriy, N.; Kiriy, A.; Bocharova, V.; Stamm, M.; Richter, S.; Plötner, M.; Fischer, W.-J.; Krebs, F. C.; Senkovska, I.; Adler, H.-J. *Chem. Mater.* **2004**, *16*, 4757–4764. (f) Bundgaard, E.; Krebs, F. C. *Sol. Energy Mater. Sol. Cells* **2007**, *91*, 954–985. (g) Boucle, J.; Ravirajan, P.; Nelson, J. *J. Mater. Chem.* **2007**, *17*, 3141–3153. (h) Peet, J.; Senatore, M. L.; Heeger, A. J.; Bazan, G. C. *Adv. Mater.* **2009**, *21*, 1521–1527.

(2) (a) Cavallini, M.; Stoliar, P.; Moulin, J. F.; Surin, M.; Leclere, P.; Lazzaroni, R.; Breiby, D. W.; Andreasen, J. W.; Nielsen, M. M.; Sonar, P.; Grimsdale, A. C.; Müllen, K.; Biscarini, F. *Nano Lett.* **2005**, *5*, 2422–2425. (b) Kiriy, N.; Bocharova, V.; Kiriy, A.; Stamm, M.; Krebs, F. C.; Adler, H.-J. *Chem. Mater.* **2004**, *16*, 4765–4771.

(3) (a) McQuade, D. T.; Pullen, A. E.; Swager, T. M. *Chem. Rev.* **2000**, *100*, 2537–74. (b) Ho, H. A.; Dore, K.; Boissinot, M.; Bergeron, M. G.; Tanguay, R. M.; Boudreau, D.; Leclerc, M. *J. Am. Chem. Soc.* **2005**, *127*, 12673–76. (c) McRae, R. L.; Phillips, R. L.; Kim, I.-B.; Bunz, U. H. F.; Fahrni, C. J. *J. Am. Chem. Soc.* **2008**, *130*, 7851–7853. (d) Ogawa, K.; Chemburu, S.; Lopez, G. P.; Whitten, D. G.; Schanze, K. S. *Langmuir* **2007**, *23*, 4541–4548.

(4) Brittain, W. J.; Minko, S. *J. Polym. Sci., Part A: Polym. Chem.* **2007**, *45*, 3505–3512.

10.1021/ja904885w CCC: $40.75

Scheme 1. Different Ways To Initiate Kumada Polycondensation into Polyalkylthiophenes

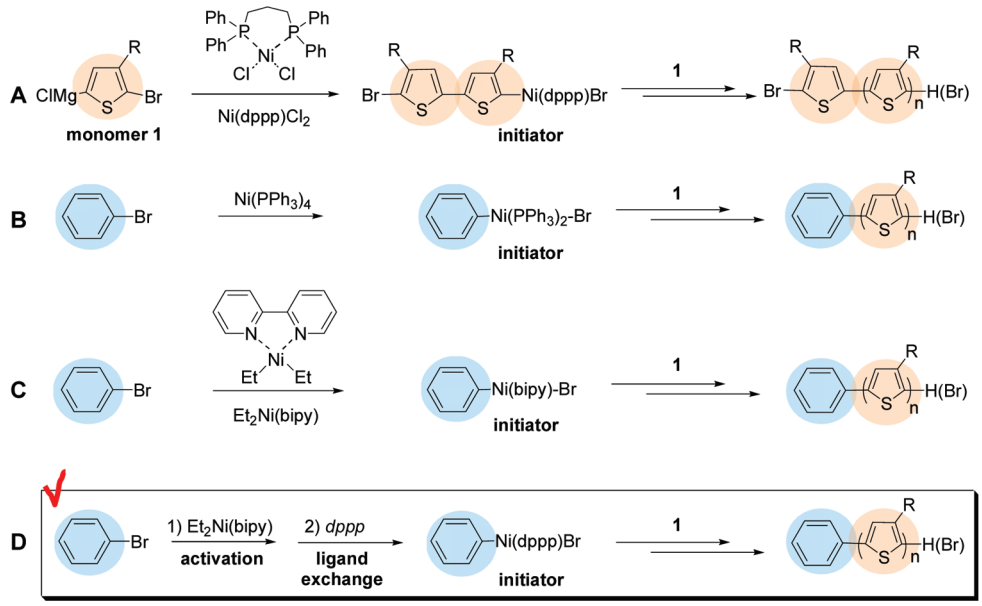

in the modification of particles by nonconjugated polymers has also been exemplified in the grafting of conjugated polymers, for example, by attachment of thiol end-functionalized polyacetylene to gold nanoparticles[5a] or amino-functionalized P3HT to quantum dots.[5b] There are few examples in the literature describing the "reactive-grafting-onto" approach whereby growing CP polymer chains are grafted onto properly functionalized reactive surfaces.[5c] Following this strategy, Schanze et al. performed grafting of polyacetylene that resulted in polymer brushes that were limited to 12 nm thicknesses.[3d]

Surface-initiated polymerization, or the "grafting-from" approach,[6] the method of growing polymer chains selectively from functionalized particles via one-by-one addition of monomers to surface-immobilized initiators, is one of the most powerful synthetic approaches to hairy particles with variable composition and a tunable grafting density. However, to the best of our knowledge, this approach has never been successfully applied for the grafting of conjugated polymers from particles because of a step-growth character of most of synthetic routes to CPs.[7] A few years ago, the groups of McCullough[8] and Yokozawa[9] made the important discovery that Kumada polycondensation into regioregular poly(3-hexythiophene), P3HT, follows a chain-growth mechanism and, therefore, it might become a suitable process for surface-initiated polymerizations. Unfortunately, in its "classical" form, the Kumada polycondensation does not allow surface tethering due to the requirement for a monomer−monomer initiation stage (Scheme 1A). Recently we found a method to prepare a series of Ar-$(PPh_3)_2$-X initiators via an oxidative addition of Ar-X to $Ni(PPh_3)_4$. These initiators were found to efficiently initiate the polymerization of P3HT[10] (Scheme 1B). We also developed surface-initiated Kumada catalyst-transfer polycondensation (SI-KCTP) of P3HT from properly modified planar surfaces.[10−12] However, a direct comparison of the Ph-Ni$(PPh_3)_2$-Br and Ni(dppp)Cl_2 (dppp = $Ph_2P(CH_2)_3PPh_2$) catalysts reveals that the former complex exhibits much poorer polymerization performance than the latter one, as a result of extensive chain-termination and reinitiation reactions. Another problem of the developed method is associated with extensive homocoupling side reactions that take place during the oxidative addition of $Ni(PPh_3)_4$ to aryl halides, especially in the case of *para*-substituted aryl halides or if a number of such groups are located closely to each other. In the present work we found that the latter obstacle almost completely prevents the grafting of P3HT from particles and only ungrafted P3HT is formed instead. Herein we describe a new route to a library of highly efficient surface-immobilized Ni initiators supported by nitrogen- and phosphorus-based *bidentate* ligands that allows for the initiation of polymerization into regioregular P3HT with controlled molecular weight and narrow dispersity. This novel initiating method was successfully applied in selective grafting of regioregular P3HT from submicrometer and nonoscale organosilica particles. Optical and photovoltaic properties of hairy P3HT nonoparticles are also presented.

Results and Discussion

Externally Initiated KCTP. 2,2′-Bipyridyl (bipy)-Supported Initiators. Widely used in Yamamoto polycondensation

(5) (a) Nakashima, H.; Furukawa, K.; Ajito, K.; Kashimura, Y.; Torimitsu, K. *Langmuir* **2005**, *21*, 511–515. (b) Liu, J.; Tanaka, T.; Sivula, K.; Alivisatos, A. P.; Frechet, J. M. J. *J. Am. Chem. Soc.* **2004**, *126*, 6550–52. (c) Odoi, M. Y.; Hammer, N. I.; Sill, K.; Emrick, T.; Barnes, M. D. *J. Am. Chem. Soc.* **2006**, *128*, 3506–3512.

(6) Edmondson, S.; Osborne, V. L.; Huck, W. T. S. *Chem. Soc. Rev.* **2004**, *33*, 14–22.

(7) Iovu, M. C.; Sheina, E. E.; Gil, R. R.; McCullough, R. D. *Macromolecules* **2005**, *38*, 8649–8656.

(8) Miyakoshi, R.; Yokoyama, A.; Yokozawa, T. *J. Am. Chem. Soc.* **2005**, *127*, 17542–17547.

(9) (a) Schlüter, D. *J. Polym. Sci., Part A: Polym. Chem.* **2001**, *39*, 1533. (b) Yamamoto, T. *Macromol. Rapid Commun.* **2002**, *23*, 583.

(10) (a) Senkovskyy, V.; Khanduyeva, N.; Komber, H.; Oertel, U.; Stamm, M.; Kuckling, D.; Kiriy, A. *J. Am. Chem. Soc.* **2007**, *129*, 6626–6632. (b) Khanduyeva, N.; Beryozkina, T.; Senkovskyy, V. N.; Simon, F.; Nitschke, M.; Stamm, M.; Kiriy, A. *Macromolecules* **2008**, *41*, 7383–7389.

(11) (a) Beryozkina, T.; Senkovskyy, V.; Kaul, E.; Kiriy, A. *Macromolecules* **2008**, *41*, 7817–7823. (b) Khanduyeva, N.; Senkovskyy, V.; Beryozkina, T.; Horecha, M.; Stamm, M.; Uhrich, C.; Riede, M.; Leo, K.; Kiriy, A. *J. Am. Chem. Soc.* **2009**, *131*, 153–161. (c) Kiriy, A.; Senkovskyy, V.; Stamm, M. EU patent application number EP 09 005 837.1, filed April 27, 2009.

(12) Surface-initiated Suzuki polycondensation from planar surfaces was also reported: Beryozkina, T.; Boyko, K.; Khanduyeva, N.; Senkovskyy, V.; Horecha, M.; Oertel, U.; Simon, F.; Stamm, M.; Kiriy, A. *Angew. Chem., Int. Ed.* **2009**, *48*, 2695–2698.

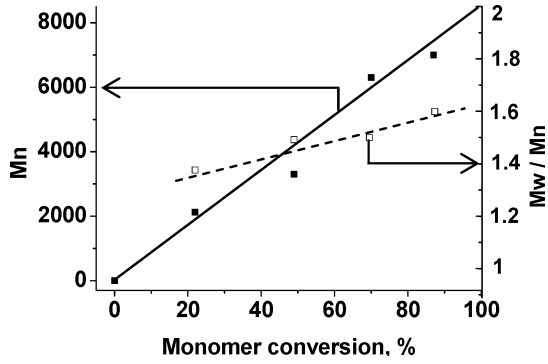

Figure 1. Number-average molecular weight (M_n), calculated molecular weight (M_{ncal}, dotted line), and dispersity (M_w/M_n) as a function of the monomer **1** conversion for the polycondensation initiated by Ph-Ni(bipy)-Br at 50/1 feed ratio. M_{ncal} is calculated by assuming that the polymerization follows a "living" mechanism.

reactions are Ni complexes supported by bipy[9b] that attracted our attention as a potentially viable alternative to phosphorus-containing catalysts.[13] To establish the applicability of bipy as the supporting ligand in KCTP, the polymerization of 2-bromo-5-chloromagnesio-3-hexylthiophene (**1**) was performed in the presence of Ni(bipy)Cl_2 in freshly distilled (under sodium benzophenone ketyl) THF.[14] The polymerization led to highly regioregular head-to-tail (HT) P3HT in a broad range of polymerization temperatures (up to 50 °C). The reaction was found to involve a chain-growth polymerization mechanism, following a gradual growth of the number-average molecular weight (M_n) with polymerization time (Figure S2, SI). Moderate dispersities, $D = M_w/M_n$ (M_w is the weight-average molecular weight and M_n is the number average molecular weight), in the 1.4−1.6 range were achievable when the polycondensation was conducted in freshly distilled THF (SI, Figures S2−S4).

An attractive feature of Ni(bipy)-based chemistry is that various Ar-Ni(bipy)-Br compounds can be obtained in pure form and in high yield by the reaction of diethylbipyridylnickel, Et_2Ni(bipy), with aryl halides.[15,16] A model initiator Ph-Ni(bipy)-Br was prepared from Et_2Ni(bipy), and bromobenzene as a model aryl halide (Scheme 1C). The course of the reaction could be followed easily by a change of the color of the reaction mixture from green (before addition of Ph-Br) to red at the end of the reaction. The reaction course of Ph-Br with Et_2Ni(bipy) was examined using ^{1}H NMR by performing the reaction directly in the NMR tube. Fortunately, the reaction proceeds cleanly and no other products besides Ph-Ni(bipy)-Br were detected in this experiment. As in the case of Ni(bipy)Cl_2, Ph-Ni(bipy)-Br initiated polycondensation of **1** conducted at room temperature in freshly distilled THF affords regioregular HT P3HT and allows moderate control over the molecular weight, MW, and dispersities of about 1.4−1.6 (Figure 1). Careful inspection of the ^{1}H NMR spectrum allows for the identification of the end groups of the P3HT product, as shown in Figure S3. Integration of the spectra shows that the H- and Br-termini (signals at 6.95−6.82 ppm) are present in an excess compared to the Ph-termination (7.59, 7.38, 7.29, Figure S3). This result suggests that besides the "ideal" Ph/H chain-growth product, the reaction mixture also contains rather significant amounts of H/Br-terminated P3HT (>35%), formed presumably due to a chain-termination and reinitiation processes. A comparison of these results with literature data for Ni(dppp)Cl_2-catalyzed polymerizations[7,8] allows for the conclusion that the latter complex significantly outperforms other catalysts for Kumada polycondensation reactions, and therefore, initiators supported by bidentate phosphorus ligands remained an attractive target.

Initiators Supported by Bidentate Phosphorus Ligands. A ligand-exchange strategy was applied to prepare desired Ph-Ni(dppp)-Br and Ph-Ni(dppe)-Br (dppe = $Ph_2P(CH_2)_2PPh_2$) initiators from Ph-Ni(bipy)-Br via its reaction with dppp or dppe ligands to replace bipy by the phosphorus containing ligands (Scheme 1D). The course of the two-step transformation can be monitored by changes of the color of the reaction mixture. Thus, the addition of Et_2Nibipy to Ph-Br is accompanied by a color change from the green to the reddish-brown; the subsequent addition of dppp (or dppe) resulted in a color change of the reaction mixture to orange-yellow. Structures of the formed Ph-Ni(dppp)-Br and Ph-Ni(dppe)-Br complexes were unambiguously proven by ^{1}H, ^{13}C, and ^{31}P NMR analysis data (Figure S4).

The observed nonequivalence of the phosphorus sites is in accordance with literature data for Ph-Ni(dppe)-Cl.[17] The course of both reactions (Ph-Br with Et_2Ni(bipy) and Ph-Ni(bipy)-Br with dppe) was monitored using ^{1}H NMR and ^{31}P NMR by performing the reaction directly in the NMR tube. Fortunately, no side products were detected upon the two-step transformation (Scheme 1D).

An attractive feature of the ligand-exchange method is its universal nature. By using our approach, a library of Ar-Ni(L_2)-X initiators with a tunable reactivity can be prepared within the same synthetic protocol. Variation of the nature of the supporting ligands would be a powerful tool in optimization of the polymerization performance. It has earlier been demonstrated that dppp as supporting ligand significantly outperforms dppe in the preparation of P3ATs,[7,8] whereas dppe is better suited for the preparation of polypyrroles, polyphenylenes,[18] and polythiophenes with oxyethylene side groups.[19]

We found that room temperature polycondensation of **1** initiated by Ph-Ni(dppp)-Br affords regioregular head-to-tail P3HT with a good control of the MW, as seen from the near linear dependence of the number-average molecular weight (M_n) on monomer conversion (Figure 2). The polymerization is less controlled at polymerization degrees (DP) higher than 100 due to limited and MW-dependent solubility of P3HT. High MW P3HT, however, can be obtained performing the polymerization at higher temperatures or by use of other solvents.[20] Importantly, polydispersities of moderate MW P3HT obtained by this method falls into the same range as those achievable by use of Ni(dppp)Cl_2 as catalyst, for example, in the 1.1−1.2 range.[7,8]

(13) Structurally similar Ni-diimine complexes were recently applied as catalysts in the preparation of regioregular P3HT: Sheina, E. E.; Iovu, M. C.; McCullough, R. D. *Polym. Prepr.* **2005**, *46* (2), 1070.
(14) Ni(bipy)-catalyzed polymerizations are sensitive to the solvent (i.e., THF) quality, therefore, freshly distilled THF must be used for obtaining of P3HT with monomodal MW distribution; for further details see SI, Figures S2−S4.
(15) Kiso, Y.; Yamamoto, K.; Tamao, K.; Kumada, M. *J. Am. Chem. Soc.* **1972**, *94*, 4374–4376.
(16) Wilke, G.; Herrmann, G. *Angew. Chem., Int. Ed.* **1966**, *5*, 581–582.
(17) Yamamoto, T.; Kohara, T.; Osakada, K. *Bull. Chem. Soc. Jpn.* **1983**, *56*, 2147–2153.
(18) Miyakoshi, R.; Shimono, K.; Yokoyama, A.; Yokozawa, T. *J. Am. Chem. Soc.* **2006**, *128*, 16012–16013.
(19) Adachi, I.; Miyakoshi, R.; Yokoyama, A.; Yokozawa, T. *Macromolecules* **2006**, *39*, 7793–7795. Yokoyama, A.; Kato, A.; Miyakoshi., R.; Yokozawa, T. *Macromolecules* **2008**, *41*, 7271–7273.
(20) Hiorns, R. C.; de Bettignies, R.; Leroy, J.; Bailly, S.; Firon, M.; Sentein, C.; Khoukh, A.; Preud'homme, H.; Dagron-Lartigau, C. *Adv. Funct. Mater.* **2006**, *16*, 2263–2273.

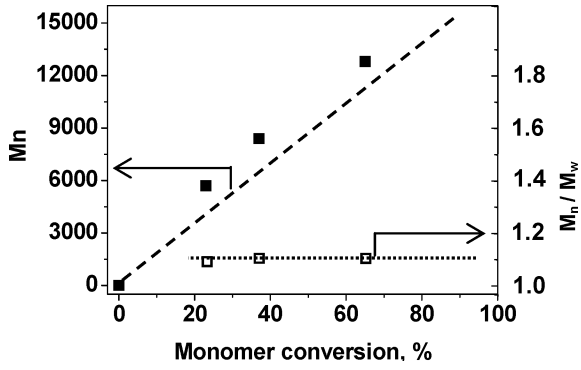

Figure 2. Number-average molecular weight (M_n), calculated molecular weight (M_{ncal}, dotted line), and dispersity (M_w/M_n) as a function of the monomer **1** conversion for the polycondensation initiated by Ph-Ni(dppp)-Br at 100/1 feed ratio. M_{ncal} is calculated by assuming that the polymerization follows a "living" mechanism.

Careful inspection of the ^{1}H NMR spectrum allows for the identification of the end groups of the P3HT product, as shown in Figure S5 in the Supporting Information. Integration of the spectrum reveals that the only Ph/H-terminated P3HT is formed reflecting that the termination and reinitiation side-reactions are negligible. We found that Ph-Ni(dppe)-Br also induces the chain-growth polycondensation of **1**, resulting in Ph-terminated P3HT (Figure S6) with somewhat higher dispersities of ~1.3.

Supporting Particles. Submicrometer organosilica spheres were prepared and used in this work as convenient model particles for development of the SI-KCTP since (i) near monodisperse silica spheres of controlled size and surface chemistry are easily available by a Stöber method;[21a] (ii) relatively large size and high density of the particles facilitate separation of surface-grafted materials from ungrafted ones by a simple centrifugation procedure; (iii) silica particles can be selectively etched under mild conditions without destruction of attached polymers, and therefore, the grafted polymers can be released from the support for further analysis; and (iv) submicrometer particles possess enough surface area to enable the collection of sufficient quantities of degrafted polymers for analysis from a single conventional laboratory-scale experiment. This is in stark contrast to the case when planar surfaces are used as supports.

Monodisperse, ~460 nm in the diameter, silica-core organosilica-shell particles were prepared by a modified Stöber method[21b] via sequential sol−gel hydrolysis of tetramethyl orthosilicates (TMOS) and [2-(4-bromo-phenyl)-ethyl]-triethoxisilane (**2**) under controlled conditions (Scheme 2A). Organosilane **2** obtained by a standard hydrosililation of 4-bromostyrene by triethoxisilane in the presence of chloroplatinic acid catalyst, was used in the particles synthesis to introduce bromophenyl surface-functionality which is necessary for the immobilization of Ni catalysts. According to thermogravimetric analysis, TGA (Figure 3c, black curve), the resulting particles contain ~10% of organosilane residues.

Grafting from Organosilica Particles. Attempting SI-KCTP with PPh_3-Supported Initiators. An approach based on the use of a $Ni(PPh_3)_4$ initiator served as the starting point in our trials to grow P3HT from the 460 nm organosilica particles. To immobilize the Ni catalyst, suspensions of the organosilica particles in anhydrous and degassed THF or toluene were mixed with $Ni(PPh_3)_4$ solutions in the same solvents under argon at room temperature for a period from 2 to 24 h. Prior to the polymerization, thus-treated particles were either purified from unreacted $Ni(PPh_3)_4$ and byproduct by repeated redispersion/centrifugation cycles or used in the grafting experiments without purification. Grafting of P3HT was attempted by the addition of **1** followed by stirring overnight. After quenching of the polymerization mixture with 5 N HCl, the particles were carefully purified from any ungrafted materials by redispersion in various solvents followed by centrifugation. Virtually no conversion of the monomer was observed in experiments that used particles purified after the catalyst immobilization step. When this purification step was omitted, all of the monomer was consumed in the formation of ungrafted P3HT. In all experiments the recovered particles were almost colorless, which is a good indication that the grafting process has failed. This was confirmed when analyzing using TGA showed no grafting of P3HT to the particles. These results suggested that the failure of the polymer grafting originated from unsuccessful immobilization of the $Ni(PPh_3)_4$ catalyst and from early chain terminations.

Attempting SI-KCTP with bipy-Suppported Initiators. To develop |-Si-$(CH_2)_2$-C_6H_4-Ni(bipy)-Br initiating sites, the 460 nm organosilica particles were treated with $Et_2Ni(bipy)$ followed by careful purification from physiosorbed Ni compounds by several centrifugation/redispersion cycles using anhydrous and degassed THF in an argon atmosphere. To perform SI-KCTP, monomer **1** was injected into the dispersion of the activated particles and the mixture was stirred at room temperature for several hours. After quenching of the reaction with 5 N HCl, the resulting particles were carefully separated from any ungrafted polymers, catalyst, and byproducts by several centrifugation/redispersion cycles using water, methanol, and hot chloroform. Unfortunately, only a marginal grafting of P3HT onto the particles was observed and a large amount of monomer **1** was consumed in the formation of ungrafted P3HT. Although the resulting particles exhibited a color inherent to low MW P3HTs (i.e., yellow in chloroform, reddish-brown in a solid state), the amount of the grafted material was so low that a quantitative evaluation of it using degrafting experiments or TGA was unsuccessful.

High-Performance SI-KCTP with dppp- and dppe-Supported Initiators. To develop |-Si-$(CH_2)_2$-C_6H_4-Ni(dppp)-Br or |-Si-$(CH_2)_2$-C_6H_4-Ni(dppe)-Br initiating sites, the organosilica particles were treated with $Et_2Ni(bipy)$ followed by the addition of an excess of the dppp or dppe ligands (Scheme 2B). Prior to the grafting it was found necessary to carefully purify the particles from physiosorbed Ni compounds by several centrifugation/redispersion cycles using anhydrous and degassed THF and CH_2Cl_2 in an argon atmosphere. It is important to note that CH_2Cl_2 is much better solvent than THF for many Ni complexes and thus its use in the purification procedure is desired. However, CH_2Cl_2 treatments can be only applied to relatively stable Ar-Ni(dppp)-Br and Ar-Ni(dppe)-Br complexes and not in the case of easily decomposable Ar-Ni(bipy)-Br.

To perform SI-KCTP, monomer **1** was added into the dispersion of the activated particles, and the polymerizations were performed at room temperature. After the polymerization, the resulting composite particles, further designated as μ-P3HT particles, were carefully separated from any ungrafted polymers, catalyst, and byproducts. A typical purification procedure included several centrifugation/redispersion cycles using the following solvents and additives in the following sequence: 5 N HCl, water, aqueous hydrosine hydrate, water, methanol, and hot chloroform. The latter centrifugation/redispersion cycles were repeated until the supernatant solutions after the centrifu-

Scheme 2. Preparation of Organosilica Particles via a Modified Stöber Method; Immobilization of Ni-Catalyst and SI-KCTP of **1** from the Modified Particles To Form Hairy P3HT Particles

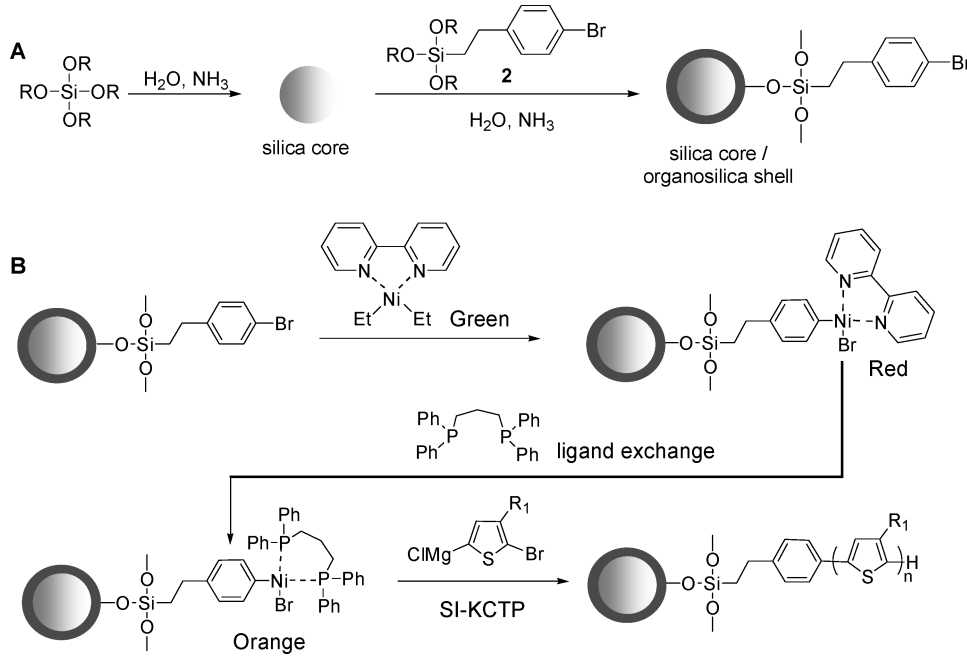

gation procedure remained colorless. Typically, much less than 10% of unbound P3HT was formed in SI-KCTP supported by dppp and dppe ligands reflecting a good selectivity of the grafting-from the nanoparticles.

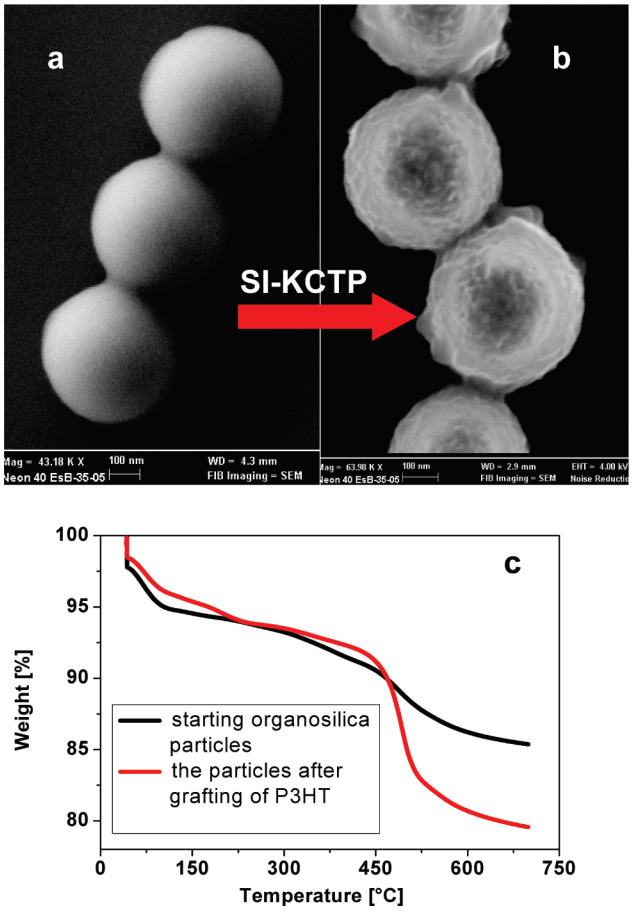

Figure 3. SEM images of the 460 nm organosilica particles before (a) and after (b) modification with P3HT via SI-KCTP of **1**. (c) TGA traces of the particles: starting organosilica particles, black curve; the particles with P3HT shell, red curve.

A significantly lower selectivity of the bipy-based SI-KCTP compared to the case of dppp- and dppe-based SI-KCTPs may not solely be explained by a difference in the polymerization performances for the parent Ph-Ni(bipy)-Br and Ph-Ni(dppp)-Br initiators (compare Figures 1 and 2). Most likely, problems with bipy-based SI-KCTP originate from a relatively low stability of the |-Si-$(CH_2)_2$-C_6H_4-Ni(bipy)-Br initiator sites on the particle surface that easily decompose forming poorly soluble compounds. The later Ni compounds cannot be efficiently removed from the particles (they are not soluble in THF, whereas CH_2Cl_2 cannot be applied since this decomposes the remaining |-Si-$(CH_2)_2$-C_6H_4-Ni(bipy)-Br sites), and after the addition of the monomer **1**, the polymerization proceeds predominantly in the bulk solution. Luckily, the Ar-Ni(dppp)-Br and Ar-Ni(dppe)-Br complexes are stable in many solvents and in the presence of water and oxygen. Thus, to cleanly perform the SI-KCTP process, the dppp or dppe ligands must be added as early as possible to the particles treated with Et_2Ni(bipy) to stabilize the initiating sites. Even if some quantities of Ni-containing byproduct were formed upon the two-step activation, they can be easily washed away by "strong" solvents, like CH_2Cl_2.

The prepared hairy particles having a 460 nm organosilica core and P3HT shells (μ-P3HT particles) were extensively characterized. SEM measurements reveal that SI-KCTP induces a significant increase of the particles surface roughness and increase of their diameter from 460 nm for unmodified particles (Figure 3a) up to 498 nm for the μ-P3HT particles (Figure 3b). According to TGA (Figure 3c), the μ-P3HT particles loose ~13% of their weight in the temperature interval from 450 to 550 °C in an oxygen atmosphere that is a typical decomposition behavior of P3ATs. For the given particle size and densities of the components, the observed weight loss corresponds to the thicknesses of the P3HT shell, h, of about 20 nm (Table 1).

Table 1. Characterization Data for the Hairy Particles Obtained by the dppp-Supported SI-KCTP

sample name	core diameter, nm	shell thickness, nm	DP of grafts	TGA data, weight loss at 450−550 °C, %	UV−vis, nm	emission in THF, nm
μ-P3HT	460	2.0[a]	~250[b]	1.3	518, 555, 620[c]	573, 670, 730[c]
μ-P3DDT	460	2.5[a]	ND	1.7	465, 533, 580, 630[c]	551, 601, 665
nano-P3HT	4	6.5[d]	24[d,e]	95.7	450[c] (517, 550, 598)[f]	560

[a] Calculated from TGA data. [b] Calculated from GPC data for the degrafted polymer. [c] Measured in THF. [d] DLS data. [e] Calculated from ^{1}H NMR data; ND, not determined. [f] Measured in dry state.

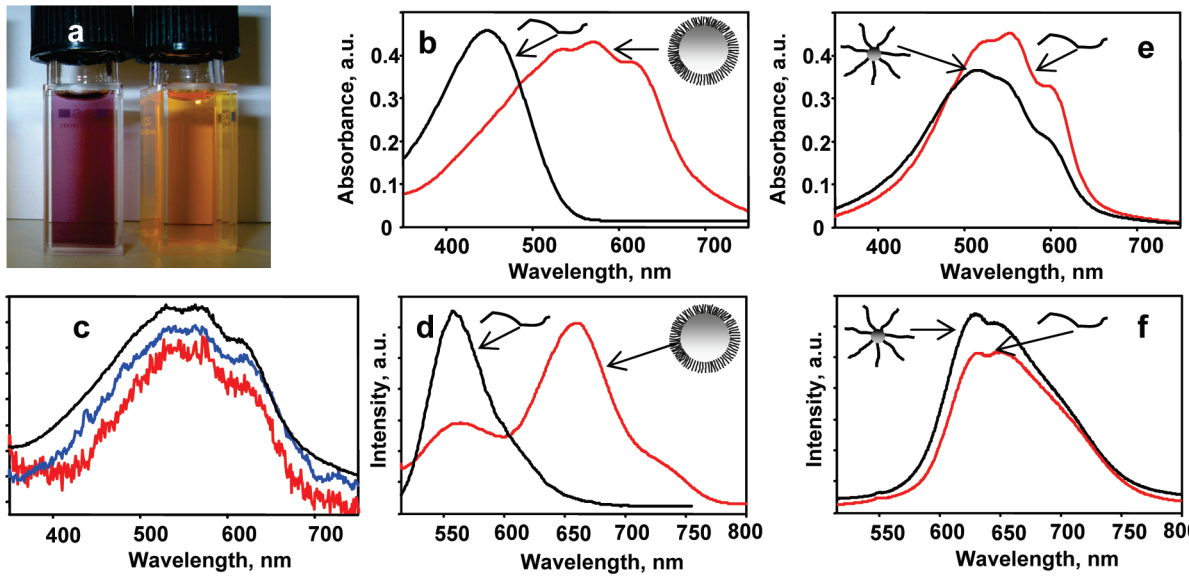

Figure 4. (a) Photograph of the dispersion of the μ-P3HT particles in THF (left-hand cuvette) and of the solution in THF of P3HT detached from the μ-P3HT particles (right-hand cuvette). UV−vis (b,c) and fluorescence (d) spectra of the dispersion of the μ-P3HT particles in THF (red lines in b and d) and of the solution in THF of P3HT detached from the μ-P3HT particles (black lines in b and d). (c) Concentration-independent normalized UV−vis spectra of the dispersions of the μ-P3HT particles in THF: 0.1 mg/mL (black curve); 0.02 mg/mL (blue curve); 0.004 mg/mL (red curve). UV−vis (e) and fluorescence (f) spectra of thermally annealed (150 °C, 5 min) films of the *nano*-P3HT particles (black lines in e and f) and of linear P3HT with M_n = 8000 and M_w = 13300 g/mol (red lines in e and f).

For analytical purposes, grafted P3HT chains were detached from the silica core of the μ-P3HT particles by dissolution of the latter in an aqueous hydrofluoric acid (HF). The mass fraction of the released polymer relative to the mass of the sample before the HF-treatment was found to be ~11% that agrees well with the TGA data. NMR analysis reveals a high head-to-tail regioregularity of P3HT (Figure S7). The detached P3HT exhibits a bimodal GPC trace with M_n = 43000 g/mol and M_w = 112000 g/mol (Figure S8). Most likely, the bimodal MW distribution originates from incomplete cleavage of Si−O and Si−C bonds caused by a poor compatibility of hydrophobic P3HT and aqueous HF. This assumption follows from a substantially increased fraction of the lower MW P3HT, when the HF-treatment was performed twice. Thus, we suggest that the lower MW peak corresponds to individual P3HT grafts with a per-graft DP of ~250, whereas the higher MW peak relates to incompletely disintegrated fragments of the particles, that is, to aggregates with a few-chains of P3HT.[22]

From these data, a reduced tethered density, Σ, an important parameter showing to what extent the conformation of the tethered polymer deviates from its unperturbed conformation in solution, can be estimated.[4] Because of the rather low surface curvature of the supporting particle (the core diameter is 460 nm and the contour length of the grafted chains is less than 100 nm), the following equation for planar brushes was applied: $\Sigma = \sigma\pi R_g^2$, where σ is a grafting density determined as the number of grafted chains per surface unit and R_g is the radius of gyration of P3HT with M_w = 42000 g/mol.[4] The calculated value for the reduced tethered density, Σ, based on the experimental data for the grafting density of P3HT chains (0.28 chains/nm^2) gives a value of 148 which correspond to a "true brush" regime of quite densely grafted and strongly stretched chains (Figures S9 and S10). As a result of the high grafting density, the hairy P3HT particles display much higher colloidal stability than the parent unmodified particles.

It is also interesting to note that the photophysical properties of the chains tethered to the μ-P3HT particles differ significantly from those for P3HT detached from the particles. Thus, we found that P3HT degrafted from the 460 nm particles exhibit optical properties usual for P3HT (orange color of the THF solution with λ_{max} = 450 nm and λ_{em} = 560 nm, Figure 4b,d, black lines). In sharp contrast, the dispersion of the μ-P3HT in THF that has a violet color and strongly red-shifted and structured absorption and fluorescent spectra (absorption: λ_{max} = 518, 555, 620 nm; fluorescence: λ_{em} = 573, 670, 730 nm, Figure 4b,d, red lines). These spectral features reflect a significant planarization of the conjugated backbone and interchain aggregation resulting in efficient delocalization of the

(21) (a) Stöber, W.; Fink, A.; Bohn, E. *J. Colloid Interface Sci.* **1968**, *26*, 62–69. (b) Nozawa, K.; Gailhanou, H.; Raison, L.; Panizza, P.; Ushiki, H.; Sellier, E.; Delville, J. P.; Delville, M. H. *Langmuir* **2005**, *21*, 1516–1523.

(22) The GPC trace with M_w = 112000 g/mol cannot correspond to liner P3HT because of solubility arguments: liner P3HTs with M_w > 50000 g/mol are not soluble in THF.

Scheme 3. Schematics Illustrating that at Constant Grafting Density and Chain Length, Chains Grafted to Supporting Particles with Low Surface Curvature Approach Each Other Closely throughout the Whole Chain Length[a]

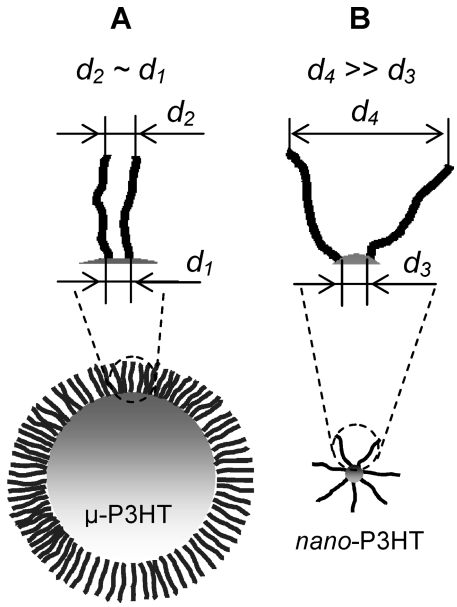

[a] This facilitates chain-stretching and aggregation ($d_2 \sim d_1$, A), whereas at high surface curvature the tethered chains are close to each other close to the grafting points but quickly become separated as one moves away from the grafting point ($d_4 \gg d_3$, B).

π-conjugated electrons (Scheme 3A).[23] It is noteworthy that the shape of the absorption spectra and the position of the absorption maxima remain constant even at very low concentrations of the μ-P3HT particles in THF down to the sensitivity limit of the spectrophotometer, demonstrating that the observed planarization and aggregation of P3HT chains occur at a single-particle level and are not caused by the interparticle aggregation (Figure 4c).[24]

The observed effects can be attributed to the fact that P3HT chains within the densely grafted brush layer are brought closely to each other throughout the whole length ($d_2 \sim d_1$, Scheme 3A) that induces their stretching and facilitates planarization and aggregation even in normally good solvents.

To demonstrate generality of the developed SI-KCTP method, poly(3-dodecylthiophene), P3DDT, was also grafted from 460 nm organosilica particles using the procedure of the preparation of the μ-P3HT particles. SEM measurements reveal that SI-KCTP induces the increase of the particles diameter from 460 up to 515 nm (Figure S10) that corresponds to the shell thickness of about 25 nm (Table 1). The resulting μ-P3DDT particles exhibit optical properties similar to the properties of μ-P3HT. Synthetic and characterization details are given in Supporting Information (Figures S11−13).

To further examine the idea that the optical properties are a function of a macromolecular architecture, the grafting of P3HT from *nanoscale* organosilica particles was performed and the properties of the resulting hairy P3HT nanoparticles were investigated. Due to a high surface curvature of such small-sized particles it is expected that the chain density will decay steeply toward a periphery of the shell ($d_4 \gg d_3$, Scheme 3B), so that even at very high grafting densities (nearby the particle surface) the effects originating from the chain-overcrowding are unlikely here.[25]

Organosilica nanoparticles were obtained via a sol−gel hydrolysis of silane **2** in water-in-oil miniemulsion. After extensive purification from surfactant, the resulting particles were readily soluble in common organic solvents. GPC gave "an apparent" molecular weight of the nanoparticles of about $M_n = 2500$ g/mol against linear polystyrene (PS) standards. Because of a highly compact structure of the nanoparticles and their higher than PS density, the real molar mass of the nanoparticles is assumed to be higher. Dynamic light scattering (DLS) measurements revealed the hydrodynamic radius of the nanoparticles in THF of about 4 nm. Based on these data, we anticipate that each organosilica nanoparticle contains on the order of few tens of residues of the silane **2**.

Grafting of P3HT was performed using the above-described protocol that implies the treatment of the nanoparticles with $Et_2Ni(bipy)$ and dppp followed by addition of **1** at monomer-to-initiator ratio of ∼37/1 (Figures S12−S14). According to TGA, the resulting product, further designated as *nano*-P3HT particles, is P3HT containing 4.3% of noncombustible material, presumably of silica (Figure S12). It has a monomodal GPC trace with $M_n = 35000$ g/mol and $M_w = 75000$ g/mol, as determined by GPC using PS standards or $M_n = 49100$ g/mol and $M_w = 60500$ g/mol, using a light scattering detector. Because of the limited and MW-dependent solubility of P3HT,[26] such a high MW could not be provided by *room temperature* polymerization neither using Ph-Ni(dppp)-Br catalyst (that limits DP) nor with $Ni(dppp)Cl_2$ that does not have end-capping groups. In the grafting experiment, the formation of the high MW P3HT was possible due to a simultaneous growth of a number of P3HT grafts from the multifunctional initiator. A per-graft DP of ∼24 corresponding to $M_n \sim 4000$ g/mol can be deduced from ^{1}H NMR data by integration of main signals and signals from end-groups (Figure S13) that is close to the theoretical per-graft DP value of ∼26 given by the monomer-to-initiator ratio of ∼37/1 and the monomer conversion of ∼70% in this grafting experiment. The hydrodynamic radius determined by DLS of the *nano*-P3HT particles in THF of about 8.5 nm corresponds to the length of 24 thiophene repeat units that fits NMR data (Figure S13). Division of the overall DP of the *nano*-P3HT particles equal to ∼296 (49100/166) on the pregraft DP of 24 gives an approximate number-averaged amount of the P3HT chains attached to the organosilica core of ∼12. The *nano*-P3HT particles exhibit good film-forming properties and an excellent solubility in THF of up to 25−30 g/L at room temperature without signs of aggregation, for example, gelation, precipitation, or change of color (native P3HT is orange in solution when fully dissolved). The aggregation of the *nano*-P3HT particles in THF and xylene was compared with those for linear P3HT samples with different molecular weights.[27] It was found that the *nano*-P3HT particles are much less prone to aggregation when compared to linear P3HT of much lower MW

(23) Magnani, L.; Rumbles, G. I. D.; Samuel, W.; Murray, K.; Moratti, S. C.; Holmes, A. B.; Friend, R. H. *Synth. Met.* **1997**, *84*, 899–900.
(24) Brustolin, F.; Goldoni, F.; Meijer, E. W.; Sommerdijk, N. A. J. M. *Macromolecules* **2002**, *35*, 1054–1059. Kiriy, N.; Jähne, E.; Adler, H.-J.; Schneider, M.; Kiriy, A.; Gorodyska, G.; Minko, S.; Jehnichen, D.; Simon, P.; Fokin, A. A.; Stamm, M. *Nano Lett.* **2003**, *3*, 707–712.
(25) Voudouris, P.; Choi, J.; Dong, H.; Bockstaller, M. R.; Matyjaszewski, K.; Fytas, G. *Macromolecules* **2009**, *42*, 2721–2728.
(26) Zen, A.; Pflaum, J.; Hirschmann, S.; Zhuang, W.; Jaiser, F.; Asawapirom, U.; Rabe, J. P.; Scherf, U.; Neher, D. *Adv. Funct. Mater.* **2004**, *14*, 757–764.
(27) Koppe, M.; Brabec, C. J.; Heiml, S.; Schausberger, A.; Duffy, W.; Heeney, M.; McCulloch, I. *Macromolecules* **2009**, *42*, 4661–4666.

(as determined by GPC) of $M_n = 8000$ and $M_w = 13300$ g/mol. The aggregation behavior and solubility of the *nano*-P3HT particles are very similar to those of linear P3HT with $M_n = 6600$ and $M_w = 8800$ g/mol, that is, to the properties of the sample whose DP approaches the per-graft DP of the *nano*-P3HT particles. A much higher solubility of the *nano*-P3HT particles than that of linear P3HT samples corroborates with a branched nature of the prepared product. It might be tentatively concluded that in contrast to linear P3HTs, the overall MW for branched P3HTs samples is a much less important factor for determining the aggregation behavior, but the contour length of the grafts and the diameter of the *nano*-P3HT particles are crucial parameters here.

The optical properties of the *nano*-P3HT particles in THF and chloroform solutions are very similar to ones for linear untethered P3HT (not shown). This reflects that no overcrowding effects (similar to ones observed in the μ-P3HT particles, Scheme 3A) occur if P3HT chains are attached to the core of a very high surface curvature (Scheme 3B). The absorption of a thermally annealed (150 °C, 5 min) film of the *nano*-P3HT particles is significantly blue-shifted and less intense compared to the absorption of the film with the same thickness made from linear P3HT sample with $M_n = 8000$ and $M_w = 13300$ g/mol (*nano*-P3HT particles, black line in Figure 4e: $\lambda_{max} = 517$ nm, shoulders at 550 and 598 nm; linear P3HT, red line in Figure 4e: $\lambda_{max} = 554$ nm, a shoulder at 602 nm). Such spectral characteristics can be ascribed either to low regioregularitiy (both the shape of the spectrum and the position of the peak are remarkably similar to that for earlier reported P3HT with a low, 86% regioregularity),[28] or to relatively low DP of P3HT. Because ^{1}H NMR reveals rather high HT regioregularity of 97% for the *nano*-P3HT particles (Figure S13), the former explanation can be declined. Thus, we suggest that the prepared product is, in fact, a star-like polymer in which few tens of highly regioregular P3HT arms with an average per-graft DP of ~24 emanate from the cross-linked organosilica core.

Photovoltaic Properties of the *nano*-P3HT Particles. A significant dependence of photovoltaic (PV) performance on both regioregularity[28] of P3HT and on its MW[29] was previously reported, however, the influence of the architecture of P3HTs was not investigated. In the present work we did not intend to establish a comprehensive architecture−property relationship but rather aimed at verifying whether the architecture of P3HT is also a factor able to affect the PV performance. Another motivation to test the PV properties of the *nano*-P3HT particles was to determine if the inclusion of the silica nanoparticles and the preparative procedure had any adverse effects on PV performance. The *nano*-P3HT particles in a combination with PCBM showed a reasonably good PV performance for relatively large area devices with an active area of 1 cm^2 (PCE = 1.8−2.3%, $I_{sc} = 5.5$−6.8 mA cm^{-2}; $V_{oc} = 0.60$−0.62 V; FF = 55−58%; Figure 5 and S14).

Although the PV performance of the *nano*-P3HT particles is lower than for the best reported P3HT-PCBM devices, the observed performance for the *nano*-P3HT particles when employed in a bulk heterojunction with PCBM is similar to what is obtained with linear P3HT with a rather high molecular weight

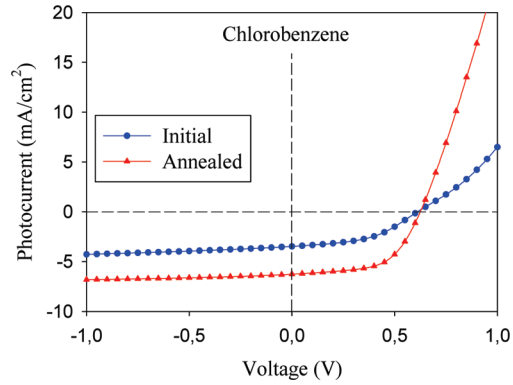

Figure 5. IV curves of Glass/ITO/PEDOT/PSS/*nano*-P3HT particles/PCBM/Al device before (blue circles) and after (red triangle) thermal annealing (130 °C for 5 min).

($M_w = 36\,600$ g/mol) for relatively large active area devices of 1 cm^2.[30] On the other hand, it is even somewhat better than the performance of previously reported small-area devices that utilized relatively low molecular weight P3HTs of $M_w < 13000$ g/mol.[20,29] This result demonstrates that the developed SI-KCTP procedure, at least, does not affect the optoelectronic properties of P3ATs. Although more studies are necessary to comprehensively establish the influence of the polymer architecture on the PV performance, it becomes clear that the molecular weight of linear P3HT constituents of branched P3HT structures must be subjected to further optimization in order to enhance the PV performance.

The fact that at this point we did not obtain clear-cut benefits in PV performance with the *nano*-P3HT particles compared to the benchmark P3HT/PCBM-based devices is not forcibly disappointing because the P3HT/PCBM-based devices are already largely optimized with their performance approaching the theoretical limit for this particular blend. We, therefore, believe that a possible impact of the covalent preorganization would be much more pronounced with systems that exhibit much less self-organization propensity into desired ordered ensembles, such as low bandgap polymers.[1] On the other hand, the particles synthesized in this work (i.e., having the submicrometer or nanometer cores) are obviously not optimal in their size. The larger of them being too large to exhibit acceptable film-forming properties and the smaller ones being too small to show properties substantially deviating from the properties of conventional linear P3HT. From these considerations, the hairy particles with the core size of 20−50 nm would be more attractive for PV applications and they will be a target for further research. Third, we strongly believe that the SI-KCTP strategy presented herein will be applicable for preparation of much more complex and otherwise inaccessible systems comprising, for example, several kinds of conjugated polymers grown from the core. We envisage possibilities for tuning of light-adsorption, charge-transport, or self-assembly properties of the hairy particles using our approach: (i) by a variation of the core nature, size, and shape; (ii) via involvement of other monomers in SI-KCTP to form random, gradient, block copolymer or mixed polymer shells; and (iii) by a proper chain-termination for positioning of additional functionality (e.g., dyes or binding groups) into the periphery of the nanoparticle shell. Recent reports on the preparation of various all-conjugated block

(28) Woo, C. H.; Thompson, B. C.; Kim, B. J.; Toney, M.; Fréchet, J. M. J. *J. Am. Chem. Soc.* **2008**, *130*, 16324–16329.
(29) (a) Schilinsky, P.; Asawapirom, U.; Scherf, U.; Biele, M.; Brabec, C. J. *Chem. Mater.* **2005**, *17*, 2175–2180. (b) Ma, W.; Kim, J. Y.; Lee, K.; Heeger, A. J. *Macromol. Rapid Commun.* **2007**, *28*, 1776–1780.
(30) Krebs, F. C.; Gevorgyan, S. A.; Alstrup, J. *J. Mater. Chem.* **2009**, *19*, 3899–3908.

copolymers via a chain-extension strategy[31] and advanced procedures for selective end-functionalization of polythiophenes[32] complement our SI-KCTP process well and makes the above-listed tasks a valiant cause.

Conclusions

We demonstrated a new strategy for the preparation of (nano)structured conjugated polymer hybrids, that in this work was exemplified by the synthesis of hairy poly(3-alkylthiophene) particles. In particular, poly(3-alkylthiophenes) were selectively grown via a quasi-living surface-initiated Kumada catalyst-transfer polycondensation (SI-KCTP) reaction from particles bearing surface-immobilized Ni catalysts supported by bidentate phosphorus ligands. This resulted in hairy particles with end-tethered P3HT chains. Densely grafted P3HT within the μ-P3HT particles exhibits strongly altered optical properties as compared to the untethered counterparts or to P3HT grafted onto small nanoparticles with a high surface curvature. We attribute this to strong interchain interactions within the densely grafted P3HT chains, which can be tuned by changing of the surface curvature (or size) of the supporting particle. The hairy P3HT nanoparticles were successfully applied in bulk heterojunction solar cells. We believe that the developed SI-KCTP approach can be extended for the preparation of much more complex materials in which many kinds of functional constituents are covalently preorganized.

Acknowledgment. The authors acknowledge the financial support of the Leibniz-Institut für Polymerforschung Dresden e.V. and the Deutsche Forschungsgemeinschaft (KI-1094/3-1). This work was further supported by the Danish Strategic Research Council (DSF 2104-05-0052 and 2104-07-0022) and by EUDP (j. nr. 64009-0050). The authors acknowledge Petra Treppe and Albena Lederer for making GPC measurements.

Supporting Information Available: Materials and equipment data; experimental procedures: synthesis of Ph-Ni(bipy)-Br, Ph-Ni(dppp)-Br, and Ph-Ni(dppe)-Br; model experiments of externally initiated KCTPs; synthesis of organosilane particles; preparation of μ-P3HT, μ-P3DDT, and *nano*-P3HT particles; characterization data of obtained products: NMR, UV−vis, fluorescence spectra, TGA, GPC data; preparation and characterization of solar cell. This material is available free of charge via the Internet at http://pubs.acs.org.

JA904885W

(31) Yokoyama, A.; Kato, A.; Miyakoshi, R.; Yokozawa, T. *Macromolecules* **2008**, *41*, 7271–7273. (a) Miyakoshi, R.; Yokoyama, A.; Yokozawa, T. *Chem. Lett.* **2008**, *37*, 1022–1023.
(32) Liu, J.; McCullough, R. D. *Macromolecules* **2002**, *35*, 9882–9889.

4386 *Chem. Mater.* **2008,** *20,* 4386–4390

Bulk Heterojunctions Based on Native Polythiophene

Suren A. Gevorgyan and Frederik C. Krebs*

Risø National Laboratory for Sustainable Energy, Technical University of Denmark, Frederiksborgvej 399, DK-4000 Roskilde, Denmark

Received February 13, 2008. Revised Manuscript Received May 6, 2008

Three different bulk heterojunctions were prepared by solution processing from the same precursor film. The procedure employs standard film-forming processing methods from solution whereby bulk heterojunctions of poly-(3-(2-methylhexan-2-yl)-oxy-carbonyldithiophene) (P3MHOCT) and the fullerene derivatives [60]PCBM or [70]PCBM were prepared. The films were subjected to temperatures of 200 °C whereby P3MHOCT is converted to the more rigid and insoluble poly-3-carboxydithiophene (P3CT); films subjected to a temperature of 310 °C lead to decarboxylation of P3CT giving native unsubstituted polythiophene (PT). The same precursor film prepared by standard solution processing thus gave access to three chemically different bulk heterojunctions that were studied in terms of performance and stability. The device with a bulk heterojunction of PT/[70]PCBM and an active area of 3 cm^2 showed the best efficiency of 1.5% (1000 W m^{-2}, AM1.5G, 70 °C) as well as a slow decay of the performance over 500 h of continuous illumination in a nitrogen atmosphere (330 W m^{-2}, AM1.5G, 25 °C).

Introduction

Plastic photovoltaics[1–4] present an alternative to conventional solar cells that are typically based on inorganic materials such as silicon. They offer new possibilities in terms of processing conditions, processing speed, and cost. The fabrication of the photovoltaic devices is envisaged to be entirely using low temperature solution-based roll-to-roll processing on flexible substrates. This is in stark contrast to solar cells based on inorganic materials that typically involve rigid substrates, high temperatures, and by comparison slow processing. The polymer solar cells remain inferior to the inorganic cells in terms of both efficiency and stability, but significant and consistent advances have been documented during the past decade, and today the state of the art offers power conversion efficiencies (PCEs) of around 5% for single junctions[5,6] and 6.5% for stacked tandem cells,[7] stabilities under accelerated conditions for thousands of hours,[8,9] morphological stability,[10] and processing on a scale of up to 0.1 m^2.[11] While most focus has been on the power conversion efficiency, the issues of stability, operational lifetime, and processing are gaining attention, and it should be emphasized that the combination of high efficiency, long lifetime, and large area processing has not been achieved for the same material currently. To meet this challenge of unification, the delicate interplay between many parameters such as processing, morphology, carrier transport, photochemistry, and chemistry at interfaces needs to be controlled. The current state of the art is well exemplified with bulk heterojunctions based on the conjugated polymer poly-3-hexylthiophene (P3HT) and a soluble fullerene derivative (PCBM).[5,6] The formation of devices with high power conversion efficiency is achieved through careful control of the processing conditions where the choice of solvent and

* Corresponding author. E-mail: frederik.krebs@risoe.dk.

(1) (a) Brabec, C. J.; Sariciftci, N. S.; Hummelen, J. C. *Adv. Funct. Mater.* **2001**, *11*, 15–26. (b) Spanggaard, H.; Krebs, F. C. *Sol. Energy Mater. Sol. Cells* **2004**, *83*, 125–146. (c) Coakley, K. M.; McGehee, M. D. *Chem. Mater.* **2004**, *16*, 4533–4542. (d) Hoppe, H.; Sariciftci, N. S. *J. Mater. Res.* **2004**, *19*, 1924–1945. (e) Günes, S.; Neugebauer, H.; Sariciftci, N. S. *Chem. Rev.* **2007**, *107*, 1324–1338.

(2) (a) Winder, C.; Sariciftci, N. S. *J. Mater. Chem.* **2004**, *14*, 1077–1086. (b) Bundgaard, E.; Krebs, F. C. *Sol. Energy Mater. Sol. Cells* **2007**, *91*, 954–985.

(3) (a) Thompson, B. C.; Fréchet, J. M. J. *Angew. Chem., Int. Ed.* **2008**, *47*, 58–77. (b) Hoppe, H.; Sariciftci, N. S. *J. Mater. Chem.* **2006**, *16*, 45–61. (c) Yang, X.; Loos, J. *Macromolecules* **2007**, *40*, 1353–1362.

(4) Jørgensen, M.; Norrman, K.; Krebs, F. C. *Sol. Energy Mater. Sol. Cells* **2008**, *92*, 686–714.

(5) Li, G.; Shrotriya, V.; Huang, J.; Yao, Y.; Moriarty, T.; Emery, K.; Yang, Y. *Nat. Mater.* **2005**, *4*, 864–868.

(6) Ma, W.; Yang, C.; Gong, X.; Lee, K.; Heeger, A. J. *Adv. Funct. Mater.* **2005**, *15*, 1617–1622.

(7) Kim, J. Y.; Lee, K.; Coates, N. E.; Moses, D.; Nguyen, T.-Q.; Dante, M.; Heeger, A. J. *Science* **2007**, *317*, 222–225.

(8) (a) Krebs, F. C.; Spanggaard, H. *Chem. Mater.* **2005**, *17*, 5235–5237. (b) Krebs, F. C.; Norrman, K. *Prog. Photovolt.: Res. Appl.* **2007**, *15*, 697–712. (c) Bjerring, M.; Nielsen, J. S.; Siu, A.; Nielsen, N. C.; Krebs, F. C. *Sol. Energy Mater. Sol. Cells* **2008**, *92*, 772–784. (d) Katz, E. A.; Gevorgyan, S.; Orynbayev, M. S.; Krebs, F. C. *Eur. Phys. J.: Appl. Phys.* **2007**, *36*, 307–311. (e) Hauch, J. A.; Schilinsky, P.; Choulis, S. A.; Childers, R.; Biele, M.; Brabec, C. J. *Sol. Energy Mater. Sol. Cells* **2008**, *92*, 727–731.

(9) Yang, X.; Loos, J.; Veenstra, S. C.; Verhees, W. J. H.; Wienk, M. M.; Kroon, J. M.; Michels, M. A. J.; Janssen, R. A. J. *Nano Lett.* **2005**, *5*, 579–583.

(10) (a) Bertho, S.; Janssen, G.; Cleij, T.; Conings, B.; Moons, W.; Gadisa, A.; D'Haen, J.; Goovaerts, E.; Lutsen, L.; Manca, J.; Vanderzande, D. *Sol. Energy Mater. Sol. Cells* **2008**, *92*, 753–760. (b) Bertho, S.; Haeldermans, I.; Swinnen, A.; Moons, W.; Martens, T.; Lutsen, L.; Vanderzande, D.; Manca, J.; Senes, A.; Bonfiglio, A. *Sol. Energy Mater. Sol. Cells* **2007**, *91*, 385–389. (c) Thompson, B. C.; Kim, B. J.; Kavulak, D. F.; Sivula, K.; Mauldin, C.; Fréchet, J. M. J. *Macromolecules* **2007**, *40*, 7425–7428. (d) Sivula, K.; Luscombe, C. K.; Thompson, B. C.; Fréchet, J. M. J. *J. Am. Chem. Soc.* **2006**, *128*, 13988–13989.

(11) (a) Krebs, F. C.; Spanggaard, H.; Kjær, T.; Biancardo, M.; Alstrup, J. *Mater. Sci. Eng., B* **2007**, *138*, 106–111. (b) Krebs, F. C.; Alstrup, J.; Spangaard, H.; Larsen, K.; Kold, E. *Sol. Energy Mater. Sol. Cells* **2004**, *83*, 293–300. (c) Lungenschmied, C.; Dennler, G.; Neugebauer, H.; Sariciftci, N. S.; Glatthaar, M.; Meyer, T.; Meyer, A. *Sol. Energy Mater. Sol. Cells* **2007**, *91*, 379–384.

10.1021/cm800431s CCC: $40.75
Published on Web 06/14/2008

the rate of evaporation during film formation play a very influential role.[5,6] After the device film has been formed, thermal annealing can be employed to further increase the PCE.[5,6] It should however be emphasized that the use of solvent and/or thermal annealing does not generally apply to all materials as a means of improving device performance. Processing from solution requires that the materials are made soluble, and this is normally achieved by attaching solubilizing side chains such as alkyl groups onto the conjugated polymer backbone. Once the film is formed, there is in principle no longer any need for the solubilizing side chains that make up a significant proportion of the active material. In the case of P3HT, the hexyl groups account for ~50% of the material weight and are passive in terms of light harvesting and charge transport. Furthermore, the side chains make the material soft and allow for diffusion of small molecules and constituents.[8b,12] The softness that alkyl groups purvey has been linked to the instability of plastic photovoltaics, and more rigid systems generally give devices with a better stability.[8] From this point of view, it is of some interest to prepare bulk heterojunctions via solution processing where the final device film does not have solubilizing side chains. From a fundamental point of view, a bulk heterojunction between native polythiophene and a soluble fullerene derivative such as [60]PCBM or [70]PCBM represents a challenge that cannot be met using known procedures as native (unsubstituted) polythiophene is an insoluble and intractable material.

In this work, we present an efficient procedure for the preparation of bulk heterojunctions based on solution processing of the device film and subsequent chemical conversions of the device film through thermal processing. Bulk heterojunctions of native polythiophene are presented.

Experimental Section

Regiorandom poly-(3-(2-methylhex-2-yl)-oxy-carbonyldithiophene) (P3MHOCT) was prepared as described in the literature.[13] The polymer had the following properties: $M_n = 11\,624$ g mol^{-1}, $M_w = 28\,266$ g mol^{-1}, $M_p = 27\,505$ g mol^{-1}, PD = 2.564. [60]PCBM and [70]PCBM were obtained from Solenne and had a purity of 99%. Glass substrates with pre-etched 100 nm thick layer of ITO and a sheet resistivity of 8−12 Ω □$^{-1}$ purchased from LumTec were cleaned by consecutive ultrasonication in isopropanol and distilled water for 10 min each followed by drying immediately prior to use. A layer of PEDOT:PSS purchased from Aldrich as a 1.3 wt % aqueous solution was spin-coated on top of ITO at a rotational speed of 2800 rpm, and the slides were annealed at 160 °C for 5 min. Subsequently, the samples were transported into the glovebox and an active layer of a mixture containing P3MHOCT and [60]PCBM or [70]PCBM (25 mg/mL in dichlorobenzene) was spin-coated onto the PEDOT:PSS covered glass–ITO substrates. The samples were then annealed at the different temperatures chosen in the range between room temperature and 310 °C. The annealing time was kept at 30 s for the temperatures up to 250 °C and at 10 s for temperatures above 250 °C. Longer annealing times lowered the V_{oc}. The aluminum metal electrode was evaporated on top after the thermal annealing to complete the devices. The devices had an active area of 3 cm^2 and were tested for photovoltaic performance and stability. The photovoltaic performance was tested under a solar simulator where the irradiance and emission spectrum were checked carefully using an optical spectrum analyzer in conjunction with a precision radiometer from Eppley Laboratories. The spectrum during characterization of the solar cell efficiency was AM1.5G with an incident light power of 1000 W m^{-2}. The solar simulator is Class AAA from 400−800 nm, over the area of the cell and for the duration of the experiment. The stability measurements were performed in a stainless steel chamber with quartz windows and controlled atmosphere.[14] The atmosphere consisted of nitrogen with an oxygen content of <1 ppm and a humidity of 0% relative. The oxygen and humidity level was monitored continuously.

Results and Discussion

The current state of the art in plastic photovoltaics is represented by the bulk heterojunction that comprises a mixture between a conjugated polymer material such as P3HT and a soluble fullerene material such as [60]PCBM or [70]PCBM (Scheme 1).[5,6] The active layer in the devices reported has been prepared almost exclusively by the spin-coating technique whereby a solution containing the active components is applied to a rapidly rotating substrate. The spin-coating technique excellently allows for the reproducible formation of very even films with a well-defined thickness and a smooth surface. The thickness essentially only depends on the viscosity of the coating solution and of the angular speed of the substrate. However, the as-formed film rarely gives the best devices, and additional post preparation treatments need to be performed such as slow drying of the film or thermal annealing whereby the structure and the morphology of the film are altered.[5,6] The most efficient devices require a well-ordered state with a phase segregation at the scale of the exciton diffusion length (~10 nm scale). The chemistry in the film does not change as a function of the various post treatment and annealing steps that have been reported. In the case of bulk heterojunctions based on P3HT and [60]PCBM, the nanomorphology is quite stable at room temperature and at slightly elevated temperatures.[9] High temperatures can lead to rapid changes in the morphology for bulk heterojunctions.[15] This is the effect that is efficiently explored to improve the performance of these devices. To achieve thermal stability at higher temperatures, there is a necessity for processing methods that offer advantages of higher thermal and morphological stability[16] without any compromise of the processing ease and ideally also without decrease in device performance.

One way to increase thermal stability is by increasing the glass transition temperature of the material through increasing the rigidity of the molecules, but this is normally associated with adverse changes in materials properties. It is thus difficult to envisage an efficient solution to the problem that relies solely on physical transformations (i.e., thermal annealing), and a chemical methodology whereby the

(12) Norrman, K.; Krebs, F. C. *Sol. Energy Mater. Sol. Cells* **2006**, *90*, 213–227.
(13) Liu, J. S.; Kadnikova, E. N.; Liu, Y. X.; McGehee, M. D.; Fréchet, J. M. J. *J. Am. Chem. Soc.* **2004**, *126*, 9486–9487.
(14) Gevorgyan, S. A.; Jørgensen, M.; Krebs, F. C. *Sol. Energy Mater. Sol. Cells* **2008**, *92*, 736–745.
(15) Peumans, P.; Uchida, S.; Forrest, S. R. *Nature* **2003**, *425*, 158–162.
(16) Andreasen, J. W.; Jørgensen, M.; Krebs, F. C. *Macromolecules* **2007**, *40*, 7758–7762.

Scheme 1. Chemical Transformation of P3MHOCT to P3CT at ~200 °C and Further Transformation to PT at ~300 °C[a]

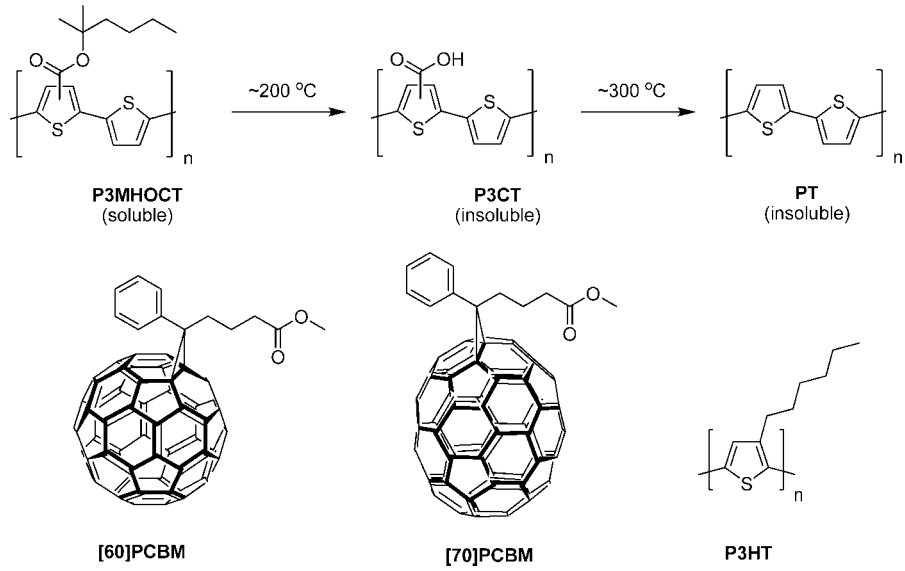

[a] The soluble fullerene derivatives employed in this work are shown in the lower part of the scheme along with the conjugated polymer P3HT.

chemistry of the material is altered during the process is needed. The polymer material P3MHOCT developed by the group of J. M. J. Fréchet was shown to convert to P3CT at temperatures of ~200 °C through elimination of 2-methylhexene.[13] It was later shown by ^{13}C labeling studies and solid-state NMR that P3CT could be further converted to PT at temperatures of ~300 °C by decarboxylation.[17] P3MHOCT is readily soluble in common organic solvents and is easily processed into thin films on its own or as mixtures with fullerene molecules prototypical of bulk heterojunctions. The advantage of bulk heterojunctions based on P3MHOCT and [60]PCBM or [70]PCBM is thus that they can be characterized as photovoltaic devices or processed to bulk heterojunctions of P3CT or PT and the aforementioned fullerenes by simple heating for a brief period of time (seconds to minutes) to the specific temperature where the chemical transformation takes place. In this work, we simply explored these three different bulk heterojunctions (P3MHOCT, P3CT, and PT) for each of the fullerene derivatives [60]PCBM or [70]PCBM. For that reason, the samples with a freshly spin-coated active layer containing P3MHOCT were annealed correspondingly at temperatures from 190 to 270 °C for about 30 s to obtain P3CT, more than 300 °C (technically limited by 310 °C) for about 10 s to obtain PT. For P3MHOCT itself, the devices were just left at room temperature to dry or were heated to annealing temperatures below the cleavage temperature. During the annealing, it was possible to visually see the color change of the sample from red to orange (conversion from P3MHOCT to P3CT) and then from orange to purple-red (conversion from P3CT to PT). The brief periods of heating time involved here possibly do not give rise to full chemical conversion of the device film, and it is reasonable to assume that the films are composite mixtures representative of the chemistry that is accessible at the given processing temperatures. Figure 1 shows the results of UV−vis analysis of P3MHOCT and

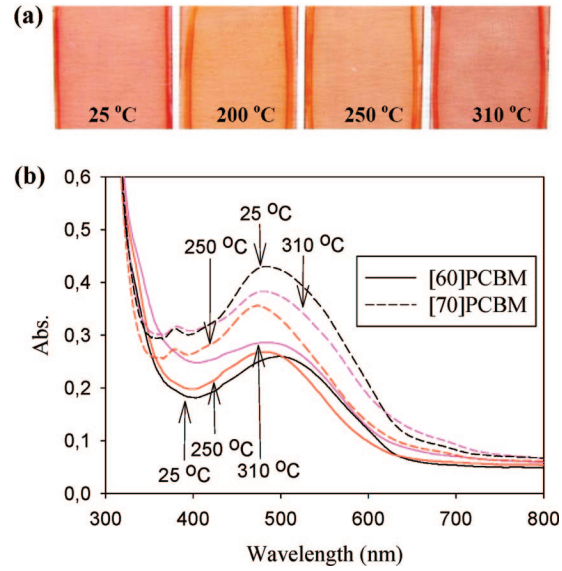

Figure 1. (a) A photograph showing the appearance of films based on [70]PCBM when heated to different temperatures. (b) UV−vis spectra of films based on P3MHOCT and [60]PCBM or [70]PCBM mixtures spin-coated on glass slides and annealed at three different temperatures (25, 250, and 310 °C). Vertical axes correspond to the absorption of the films as measured in transmission geometry neglecting the reflection losses.

[60]PCBM or [70]PCBM mixtures spin-coated on glass slides and annealed at different temperatures.

The measurements confirm a significant change of the absorption coefficient at different temperatures. Also, a slight shift of the peaks (at 500 nm) toward longer wavelengths can be seen when the samples were heated up to 310 °C. Figure 2 shows the plot of the efficiency of the cells versus annealing temperature.

The vertical lines separate regions that correspond to different polymers. The decrease of the efficiency in the first region was mostly due to the open circuit voltage of the cells being rather sensitive to thermal stresses (complete sets of *IV*-curves and graphs of V_{oc}, I_{sc}, and FF are provided in the Supporting Information). From the graph, it is clear that

(17) Bjerring, M.; Nielsen, J. S.; Nielsen, N. C.; Krebs, F. C. *Macromolecules* **2007**, *40*, 6012–6013.

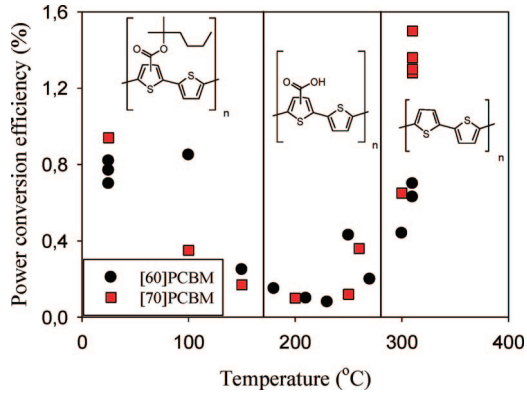

Figure 2. Efficiency versus annealing temperature for the cells with P3MHOCT polymer and [60]PCBM (●) or [70]PCBM (red ■) mixture measured under 1000 W m^{-2}, AM1.5G, 70 °C conditions. The vertical lines show the temperatures at which the thermocleavage becomes significant upon increasing the temperature according to the TGA analysis reported in ref 14. The conversion is irreversible. The molecular structures for the polymers in the different temperature ranges are shown.

the performance was poorer for annealing in the temperature range where P3CT forms and best in the temperature where PT forms. The best efficiency of 1.5% (under 1 sun) could be achieved for a device with PT and [70]PCBM. SEM analysis of the surface of active layer for the same type of cells carried out after peeling off the aluminum electrode confirms (Figure 3) the formation of well-defined bulk heterojunction structure of the compound. The power conversion efficiency of the bulk heterojunctions in the as-formed films was generally observed to be in the range of 0.7−0.9% and was found to decrease as the device film was annealed in the range of temperatures below the transformation of P3MHOCT to P3CT. A broad minimum is then reached as the first cleavage temperature is reached, and the devices based on P3CT were all the poorest performing in terms of power conversion efficiency where the typical power conversion efficiency was in the range of 0.1−0.4%. When reaching the temperatures of the second transformation from P3CT to PT, a dramatic increase in power conversion efficiency was observed from the low value of 0.1−0.4% up to 0.6% in the case of [60]PCBM and as high as 1.5% in the case of [70]PCBM. [70]PCBM devices showed the largest improvement, which may be linked not only to morphology but also to better light harvesting properties of [70]PCBM as compared to [60]PCBM. It should, however, be noted that devices based on [60]PCBM and [70]PCBM generally gave the same result at processing temperatures below 300 °C. One possible explanation of the decrease in performance at annealing temperatures below 190−210 °C could be that the morphology changes and that the fullerene component grows to form large crystallites. The nanomorphology plays a crucial role in the performance of polymer solar cells, and any change in morphology toward larger aggregates or crystallites could account for this.[10,18] It is, however, not very likely seen in the light of the morphology that we observe in the SEM images (examples are shown in Figure 3). Films treated in the temperature range of 25−250 °C show a completely homogeneous nature with no observable phase separation. Films heated to 310 °C do show distinct phase separation and represent traditional bulk heterojunctions of PT and the fullerene. If the performance decrease was due to changes in morphology and the formation of large fullerene crystallites, we would have expected this to be conserved in

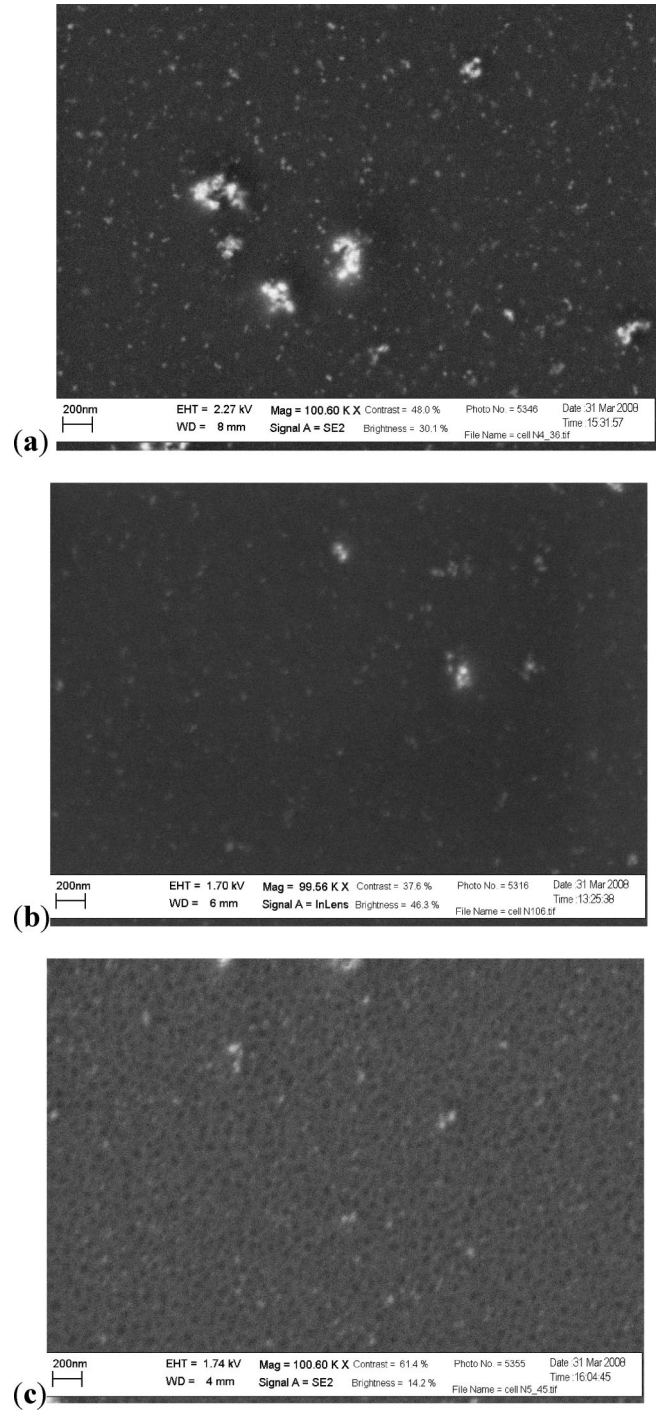

Figure 3. SEM images of the surfaces of films based on P3MHOCT and [60]PCBM compound treated at (a) room temperature, (b) 200 °C, and (c) 310 °C.

the rigid polymer matrix that both P3CT and PT comprise.[16] We further attempted photoluminescence quenching experiments as this is a good method to probe the intimacy of the polymer–fullerene mixture. We observe a moderate photoluminescence for P3MHOCT that is completely quenched when mixed with [60]PCBM as established using spin-coated films

(18) (a) Douhéret, O.; Swinnen, A.; Bertho, S.; Haeldermans, I.; D'Haen, J.; D'Olieslaeger, M.; Vanderzande, D.; Manca, J. V. *Prog. Photovolt.: Res. Appl.* **2007**, *15*, 713–726. (b) Yang, X.; van Duren, J. K. J.; Janssen, R. A. J.; Michels, M. A. J.; Loos, J. *Macromolecules* **2004**, *37*, 2151–2158.
(19) Hummelen, J. C.; Knight, B. W.; LePeq, F.; Wudl, F.; Yao, J.; Wilkins, C. L. *J. Org. Chem.* **1995**, *60*, 532–538.

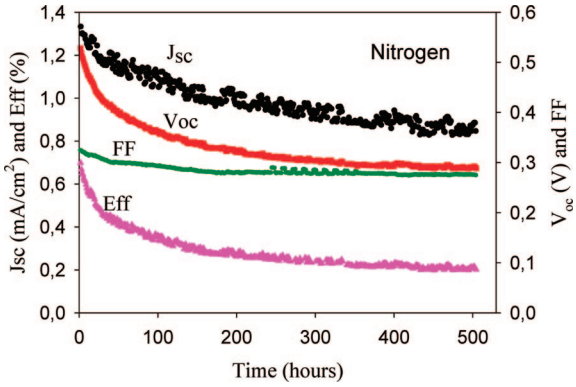

Figure 4. Variation of PV parameters of ITO/PEDOT:PSS/PT:[70]PCBM/Al device kept in nitrogen atmosphere under 1/3 sun irradiation for 500 h (330 W m^{-2}, AM1.5G, nitrogen, 0% relative humidity, 25 °C).

on glass substrates employing front face illumination (see Supporting Information). Unfortunately, the pure films of P3CT and PT and their mixtures with [60]PCBM did not show any photoluminescence, and it was thus difficult to draw any further conclusions from these studies. While this is subject to further study, we can offer two possible explanations currently. First, slight changes in the optical properties may account for some of the degradation in performance (the effect of this is expected to be minor if present). The second and more likely explanation is that the performance of the three different devices based on respectively P3MHOCT, P3CT, PT, and [60]PCBM exhibits typical performances in the ranges of 0.7−0.8%, 0.1−0.2%, and 0.6−0.7%. For the three different devices based on respectively P3MHOCT, P3CT, PT, and [70]PCBM, typical performances in the ranges of 0.9%, 0.1%, and 1.3−1.5% are observed. At the intermediate temperatures, cleavage may take place to a small extent as evidenced from the weight loss during TGA experiments.[17] We thus propose that the observed changes in performance with temperature represent a complex interplay between morphological changes and changes in the chemistry of the film.

In addition to the morphological and chemical changes that take place during the heating steps, the diffusion and partitioning of PCBM into the polymer matrix may play an important role. One possibility is, for instance, that the solubility of PCBM in the polymer matrix decreases as the material is cleaved, thus promoting phase separation. In terms of thermal stability of the materials employed, we assume that they are stable with respect to the temperatures and the duration of the thermal treatments employed. The polymer is quite stable thermally as shown earlier,[17] and fullerenes are very thermally stable materials and allow for sublimation at temperatures of up to 400 °C in their pure state, while the derivatives such as PCBM sustain temperatures of ∼180 °C in refluxing dichlorobenzene for 7 h during the preparation.

In addition, lifetime measurements were carried out for different devices, and the cells with PT showed the most stable performance. Figure 4 shows the change of photovoltaic parameters versus time for devices based on PT and [70]PCBM kept in nitrogen atmosphere at 0% relative humidity with an incident power of 330 W m^{-2}. The short circuit current density stayed above 50% of the initial value for more than 500 h and the fill factor showed almost no decay, while the open circuit voltage decreased significantly during the decay process, which was the major cause of the rather fast initial decay of efficiency.

The results confirm that the V_{oc} of these types of devices is rather sensitive toward stresses applied to the cells. Further investigation of the devices is needed to reveal the reason of poor performance of V_{oc}. We believe that if one could improve the stability of V_{oc}, then this type of device could certainly challenge the commonly used traditional organic materials, such as P3HT and others.

Conclusions

We have shown that a simple bulk heterojunction precursor film can be prepared by solution processing compatible with the state of the art procedures and how it can be processed into chemically different bulk heterojunctions through a simple thermal treatment. While there was no difference in the processing conditions, there was a slightly lower performance in terms of the power conversion efficiency than the current state of the art, while there was a relative increase in performance as the processing temperature was increased, and efficiencies up to 1.5% could be achieved for bulk heterojunctions based on native polythiophene and [70]PCBM under simulated sunlight (1000 W m^{-2}, AM1.5G, 70 °C). The photocurrents of the devices showed quite stable performance in time and were studied for more then 500 h where an initial fast decay was observed followed by a long steady period where the performance remained constant. While the power conversion efficiency obtained in this work for native polythiophene is a modest 1.5% for a large area device (3 cm^2) as compared to the state of the art that gives more than twice as much, it should be borne in mind that the current state of the art did not reach the high efficiencies to begin with. In the prototypical case of P3HT/PCBM, the high efficiencies were arrived at through a massive and directed research effort over the past few years involving a detailed understanding of the relationship between film-forming process and device function. It is not unlikely that the processing of device films via thermocleavability can be extended to other polymer systems and that the processes can be developed along the same lines as has taken place for the P3HT/PCBM system such that more efficient and stable devices can be obtained. We believe that a better understanding of the complex interplay between morphological changes and the chemistry of the film as a function of temperature could lead to significant improvements in both device performance and operational stability.

Acknowledgment. This work was supported by the Danish Strategic Research Council (DSF 2104-05-0052 and 2104-07-0022).

Supporting Information Available: Experimental details of device preparation and device characterization, *IV*-curves, plots of V_{oc}, I_{sc}, and FF as a function of temperature, and photoluminescence data (PDF). This material is available free of charge via the Internet at http://pubs.acs.org.

CM800431S

Supporting information

Bulk heterojunctions based on native polythiophene

*Suren A. Gevorgyan and Frederik C. Krebs**

National Laboratory for Sustainable Energy, Technical University of Denmark, Frederiksborgvej 399, DK-4000 Roskilde, Denmark.

E-mail: frederik.krebs@risoe.dk

Device preparation

Poly-(3-(2-methylhex-2-yl)-oxy-carbonyldithiophene) (P3MHOCT) and PCBM ([60] or [70]) were accurately weighed and dissolved in Dichlorobenzene. The prepared solution was stirred on the hotplate at 50 ^{o}C inside the glove box for one day and was then filtered through a 1µm filter and spin coated with rotational speed of 800 rpm on top of freshly spincoated and annealed (120 ^{o}C, 15 min) PEDOT:PSS. Right after the spin coating the samples were cleaved on the hotplate at certain temperatures (from room temperature to 310 ^{o}C) and transported to the vacuum chamber for Al evaporation.

Solar simulation and calibration

Described on the website:

www.risoe.dk/solarcells under the heading "Instrumentation" at the listing "Sun simulator performance (according to ASTM)".

The full link is:

http://www.risoe.dk/Research/sustainable_energy/new_energy_technologies/projects/solar_energy/~/media/risoe_dk/research/solar_cells/documents/khs_routine_test.ashx

Device Characterisation

After removing the samples from the evaporator conducting aluminium tape was applied to the cell electrodes and connections were made using alligator clips to the source measuring device. The cells were then illuminated using calibrated sun simulators and IV-curves were measured with a Keithley 2400 using PC control. Figure S1 and S2 present some of the IV-curves taken for the cells cleaved at different temperatures, while Figures S3 – S6 present the key PV parameters, such as I_{sc},

V_{oc}, FF and Efficiency extracted from the IV-curves during the measurements. The complete set of IV-curves for the different devices are shown in figures S7-S12.

IV-curves

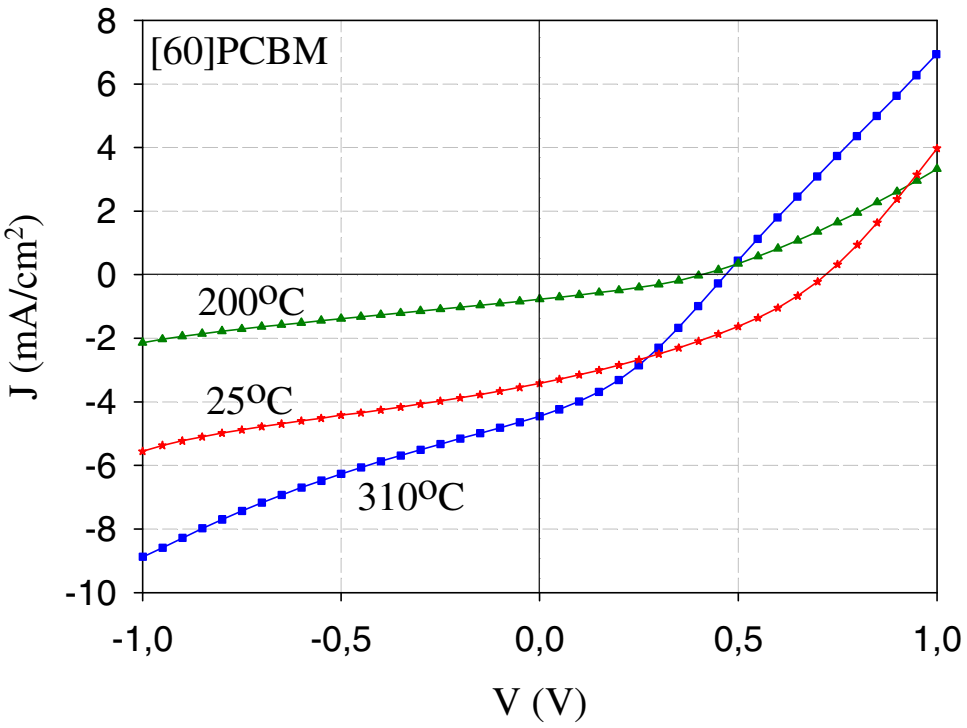

Figure S1. IV curves for a devices with the same configuration cleaved at different temperatures. The devices had the following configuration: Glass/ITO/PEDOT:PSS/Polymer:PCBM[60]/Al (1000 W m^{-2}, AM1.5G, 70 ºC).

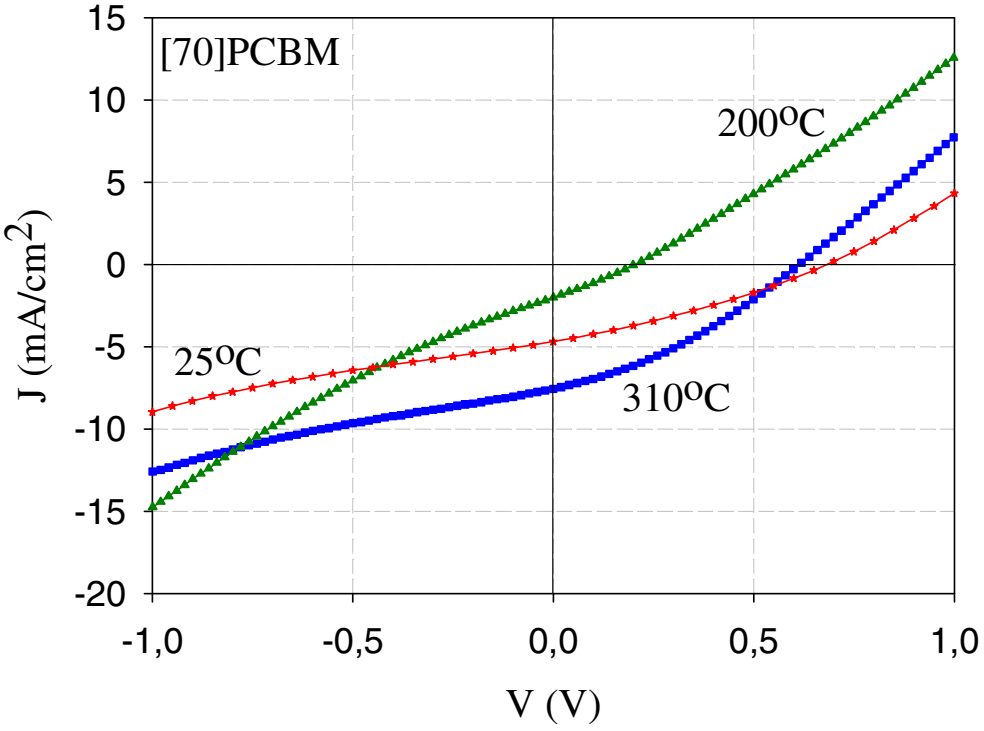

Figure S2. IV curves for devices with the same configuration cleaved at different temperatures. The devices had the following configuration: Glass/ITO/PEDOT:PSS/Polymer:PCBM[70]/Al (1000 W m^{-2}, AM1.5G, 70 ^{o}C).

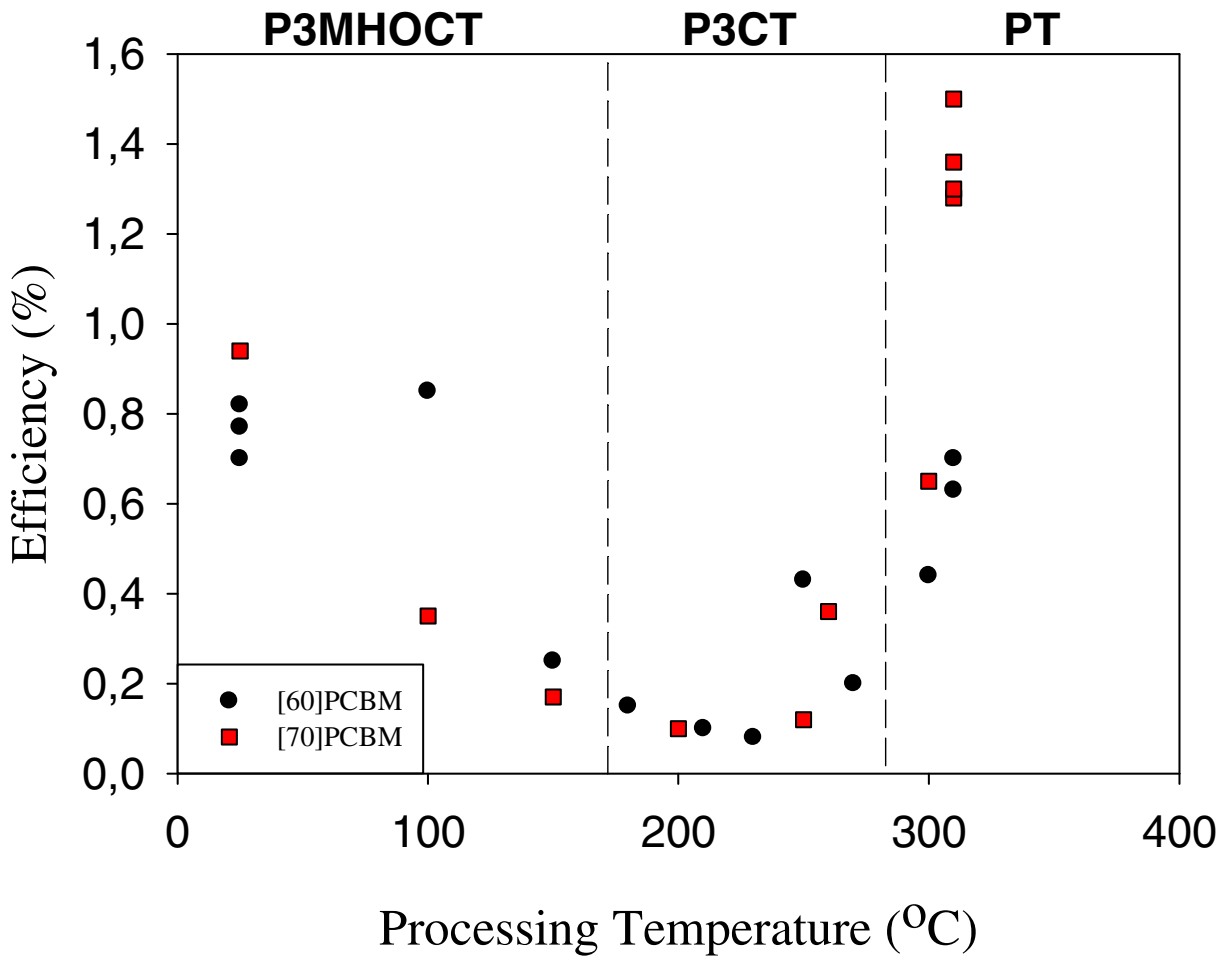

Figure S3. Efficiency versus annealing temperature for the cells with P3MHOCT polymer and [60]PCBM (black circles) or [70]PCBM (red squares) mixture measured under 1000 Wm^{-2}, AM1.5G, 70 °C conditions. The vertical lines show the temperatures at which the thermocleavage causes conversion of polymer to different chemical configuration.

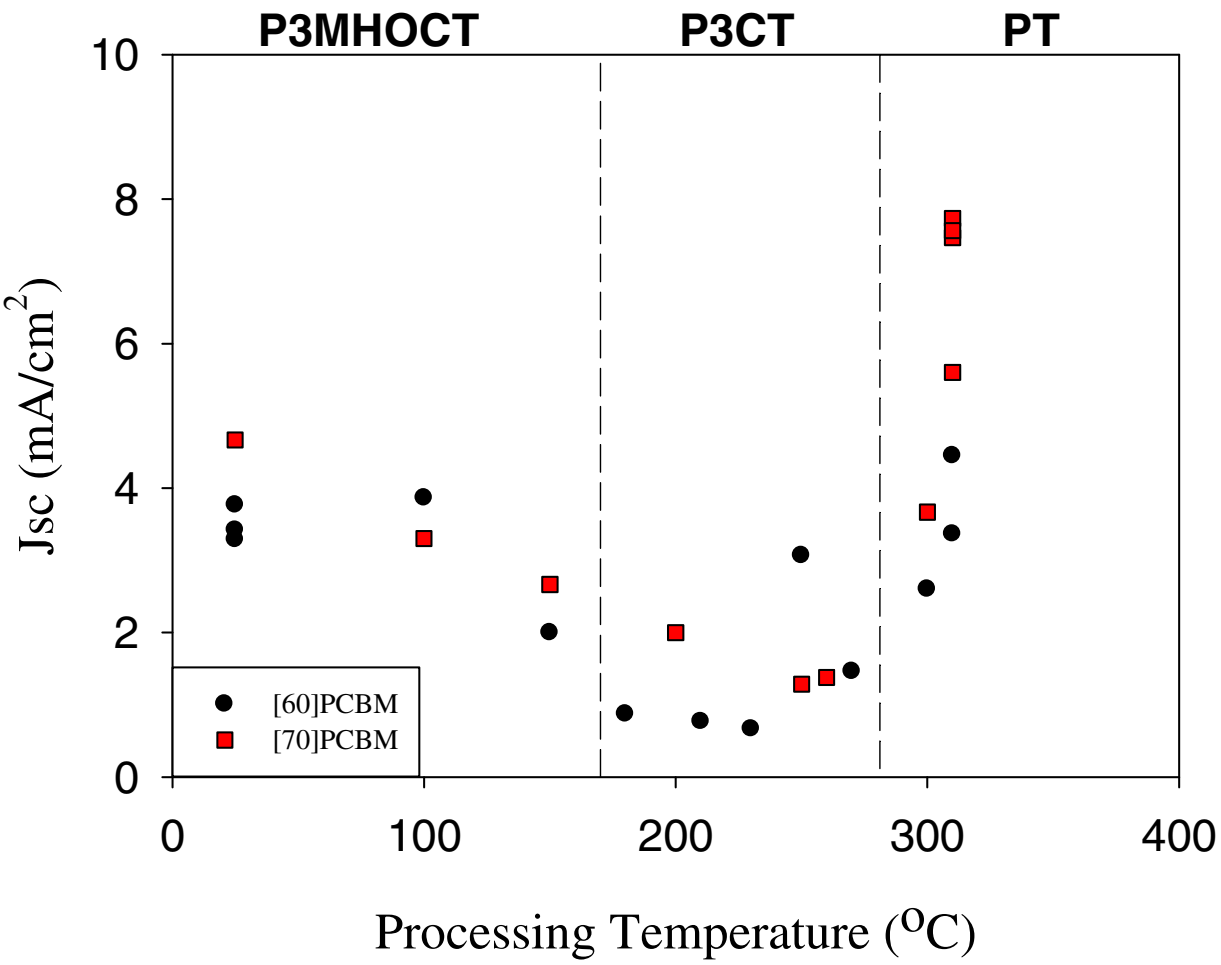

Figure S4. Jsc short circuit current density versus annealing temperature for the cells with P3MHOCT polymer and [60]PCBM (black circles) or [70]PCBM (red squares) mixture measured under 1000 Wm^{-2}, AM1.5G, 70 ^{o}C conditions. The vertical lines show the temperatures at which the thermocleavage causes conversion of polymer to a different chemical configuration.

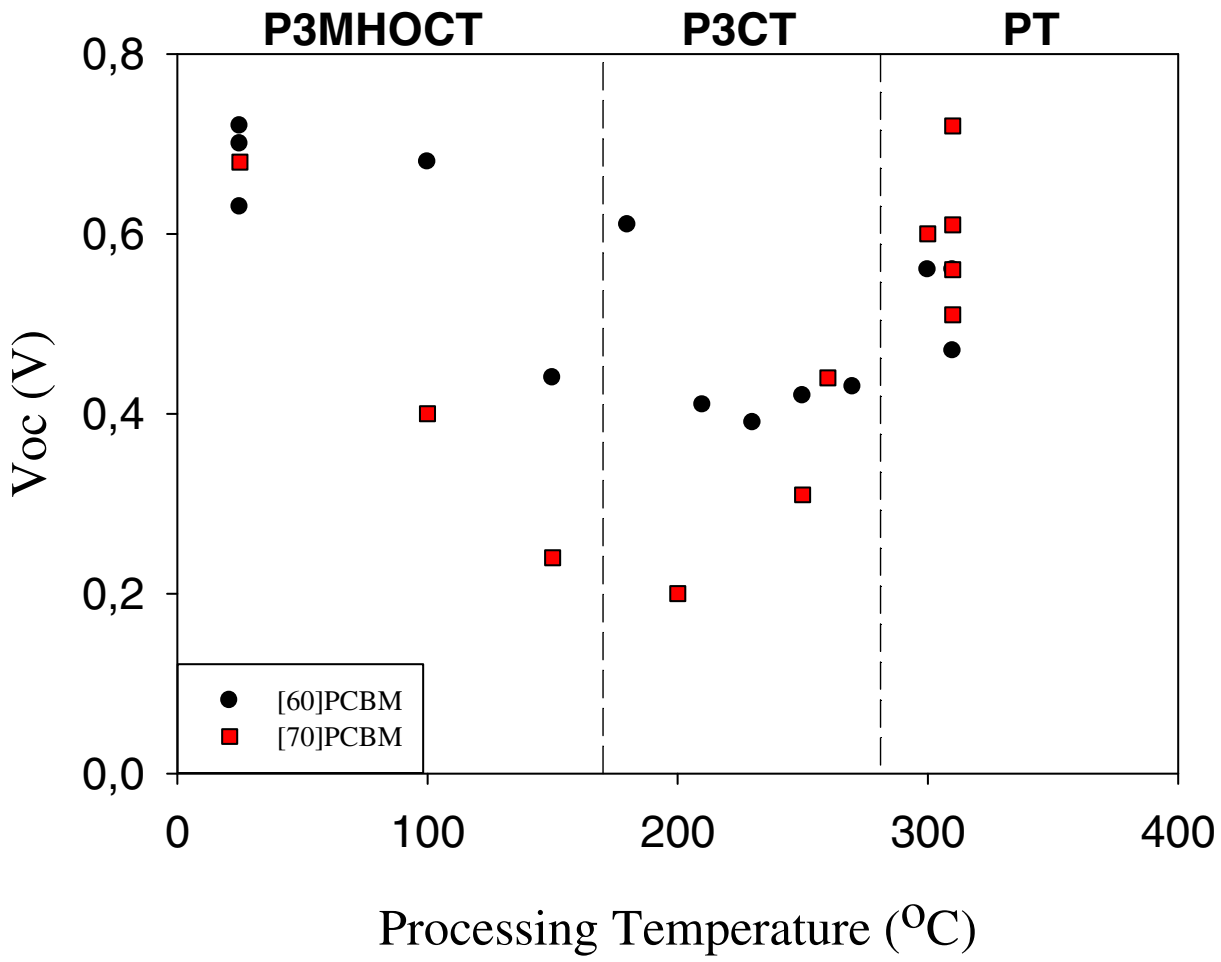

Figure S5. Voc open circuit voltage versus annealing temperature for the cells with P3MHOCT polymer and [60]PCBM (black circles) or [70]PCBM (red squares) mixture measured under 1000 Wm^{-2}, AM1.5G, 70 °C conditions. The vertical lines show the temperatures at which the thermocleavage causes conversion of polymer to a different chemical configuration.

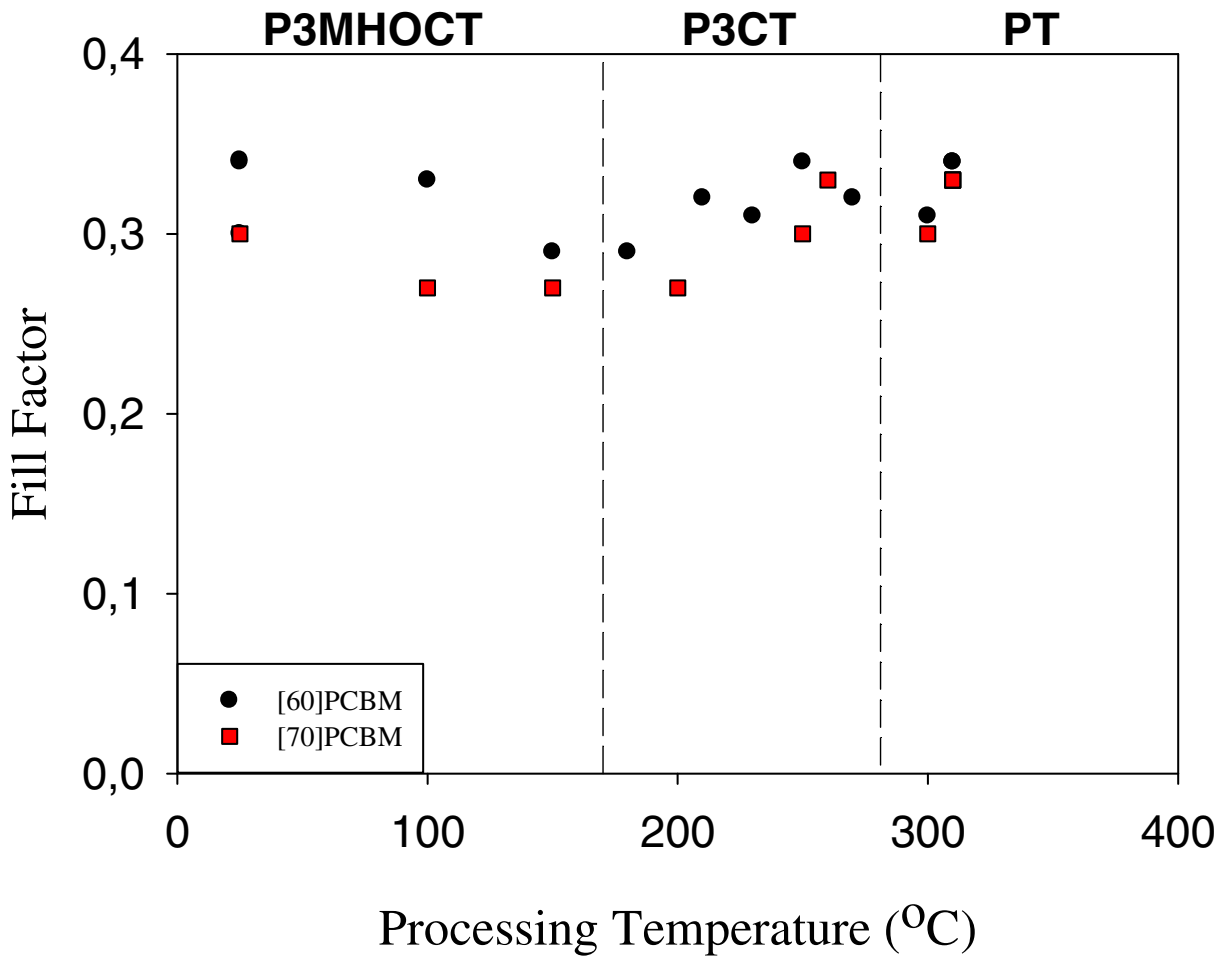

Figure S6. FF fill factor versus annealing temperature for the cells with P3MHOCT polymer and [60]PCBM (black circles) or [70]PCBM (red squares) mixture measured under 1000 Wm^{-2}, AM1.5G, 70 °C conditions. The vertical lines show the temperatures at which the thermocleavage causes conversion of polymer to a different chemical configuration.

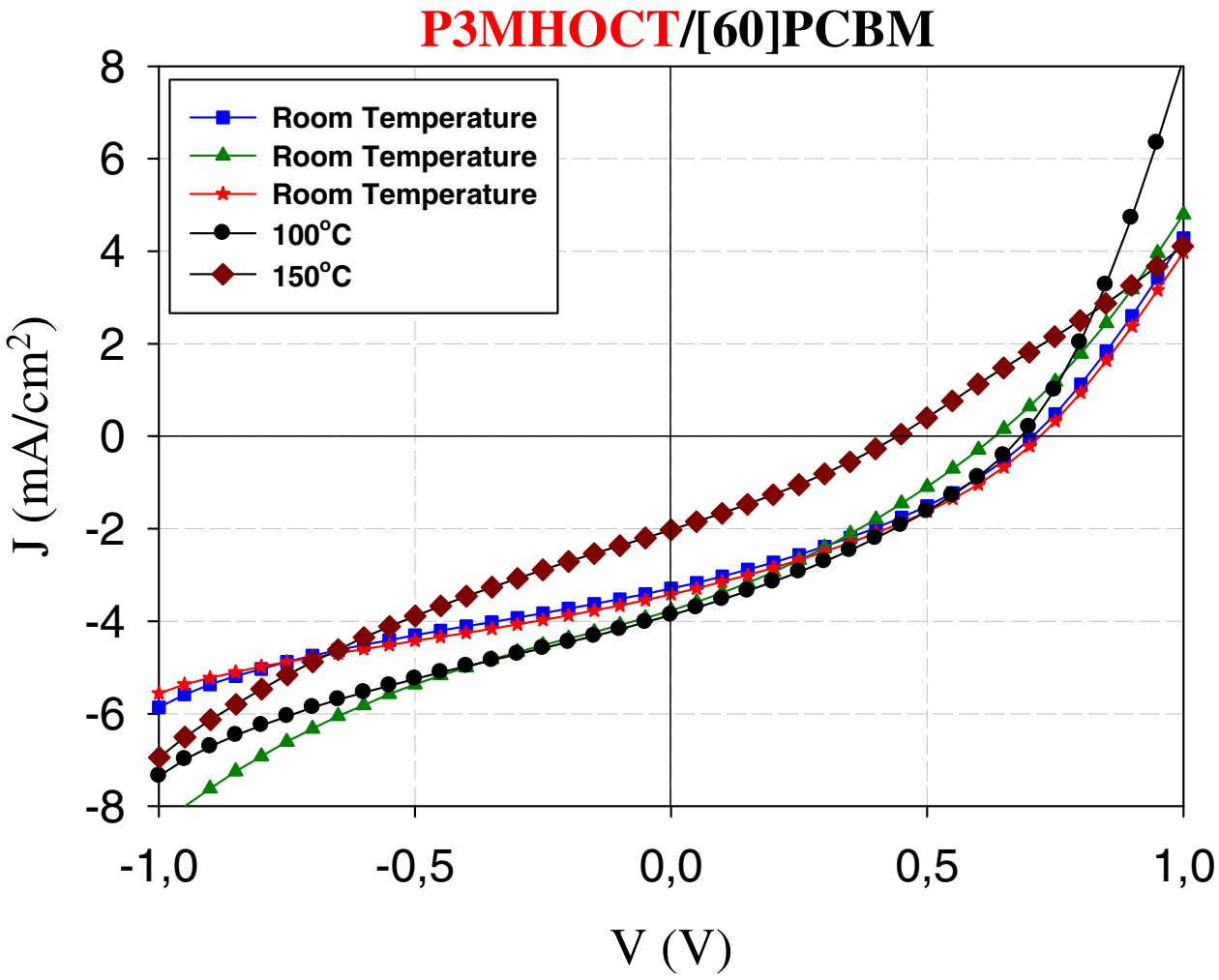

Figure S7. IV curves for devices with the same configuration cleaved at different temperatures. The devices had the following configuration: Glass/ITO/PEDOT:PSS/P3MHOCT:PCBM[60]/Al (1000 W m^{-2}, AM1.5G, 70 ^{o}C).

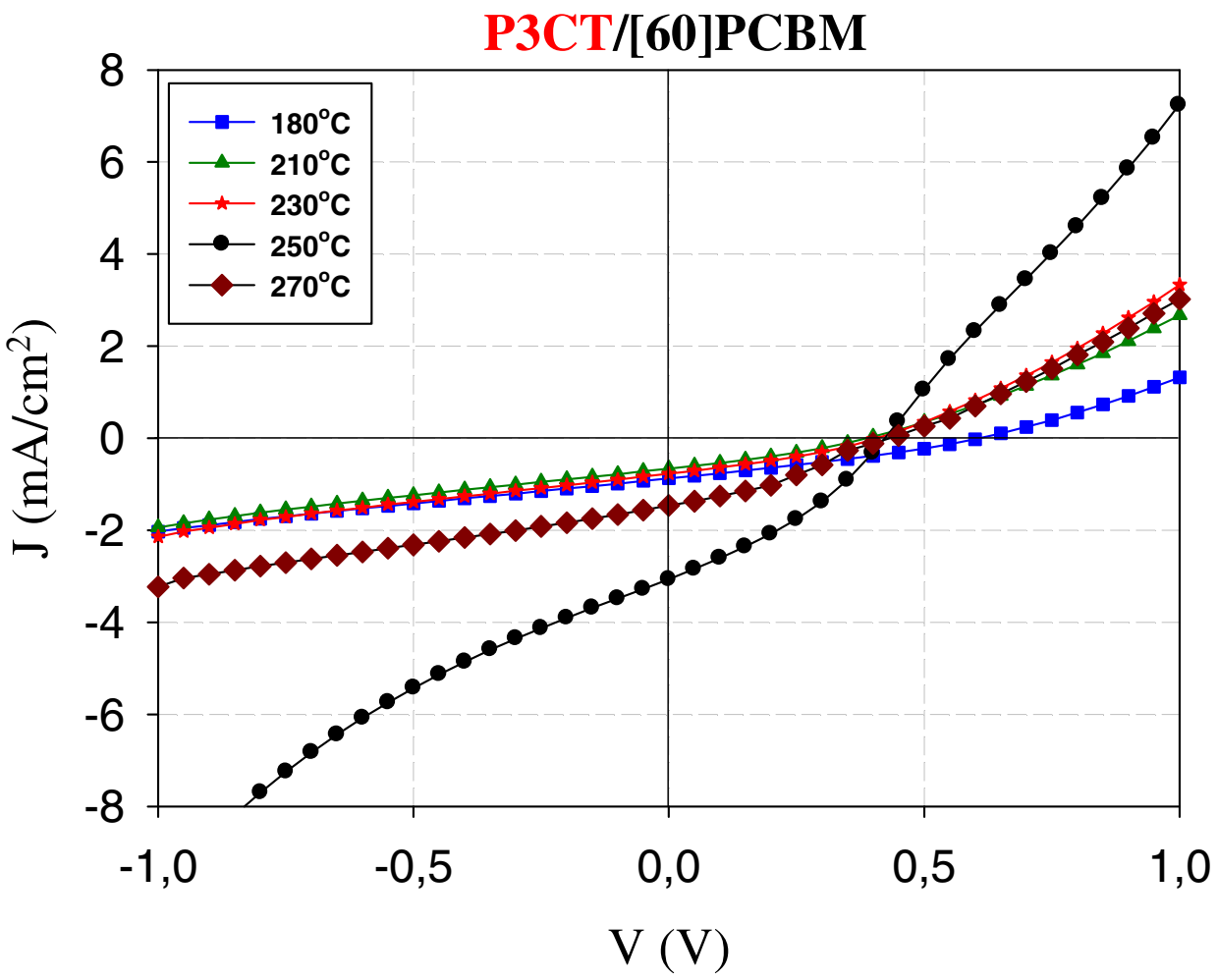

Figure S8. IV curves for devices with the same configuration cleaved at different temperatures. The devices had the following configuration: Glass/ITO/PEDOT:PSS/P3CT:PCBM[60]/Al (1000 W m^{-2}, AM1.5G, 70 °C).

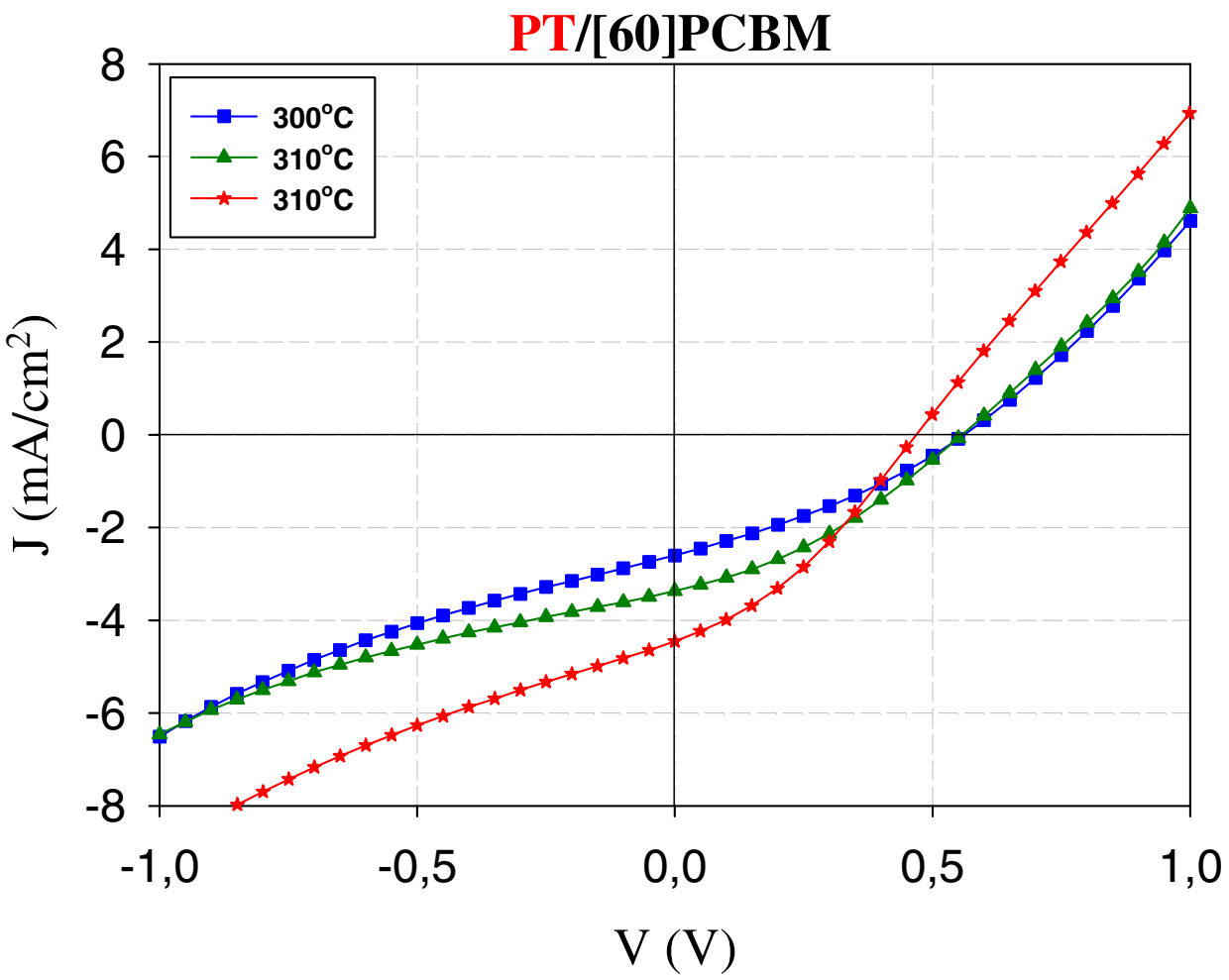

Figure S9. IV curves for devices with the same configuration cleaved at different temperatures. The devices had the following configuration: Glass/ITO/PEDOT:PSS/PT:PCBM[60]/Al (1000 W m^{-2}, AM1.5G, 70 ^{o}C).

Figure 3.

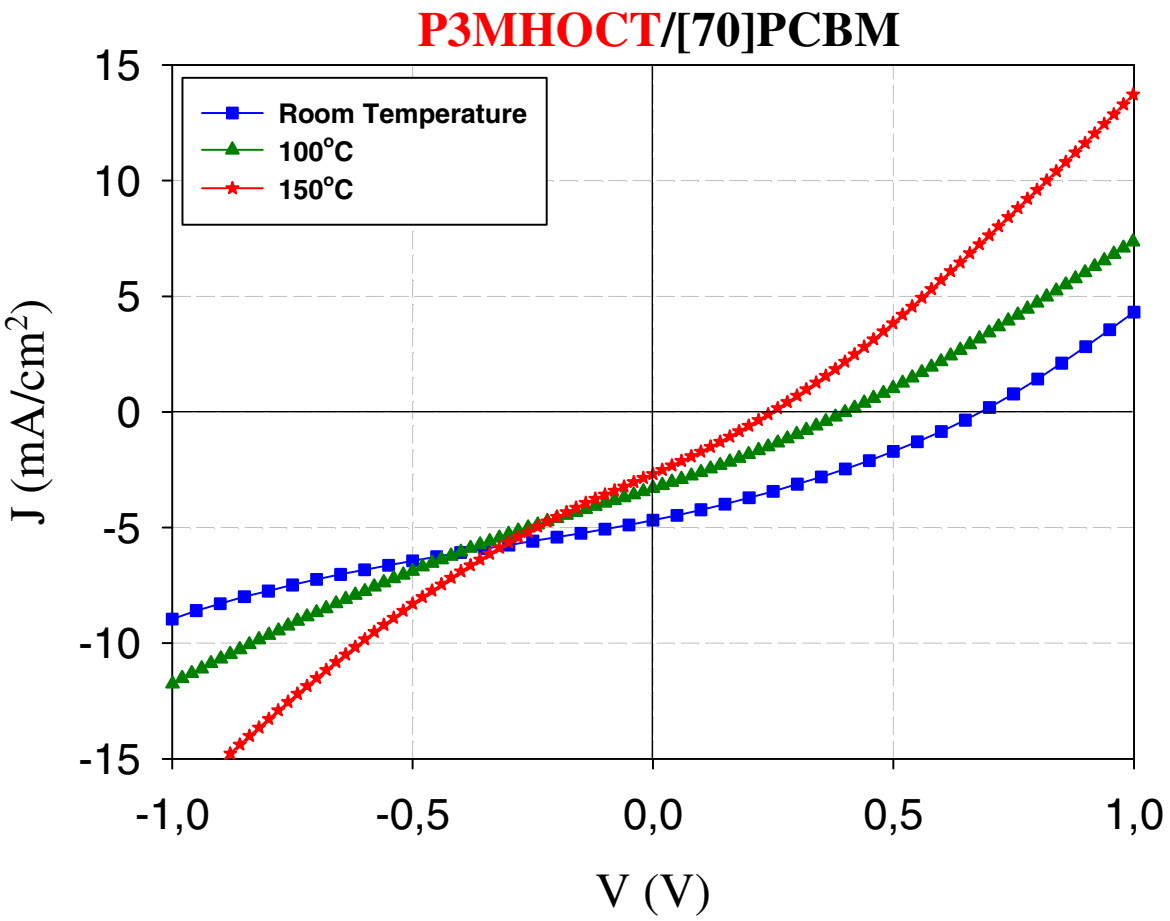

Figure S10. IV curves for devices with the same configuration cleaved at different temperatures. The devices had the following configuration: Glass/ITO/PEDOT:PSS/P3MHOCT:PCBM[70]/Al (1000 W m^{-2}, AM1.5G, 70 °C).

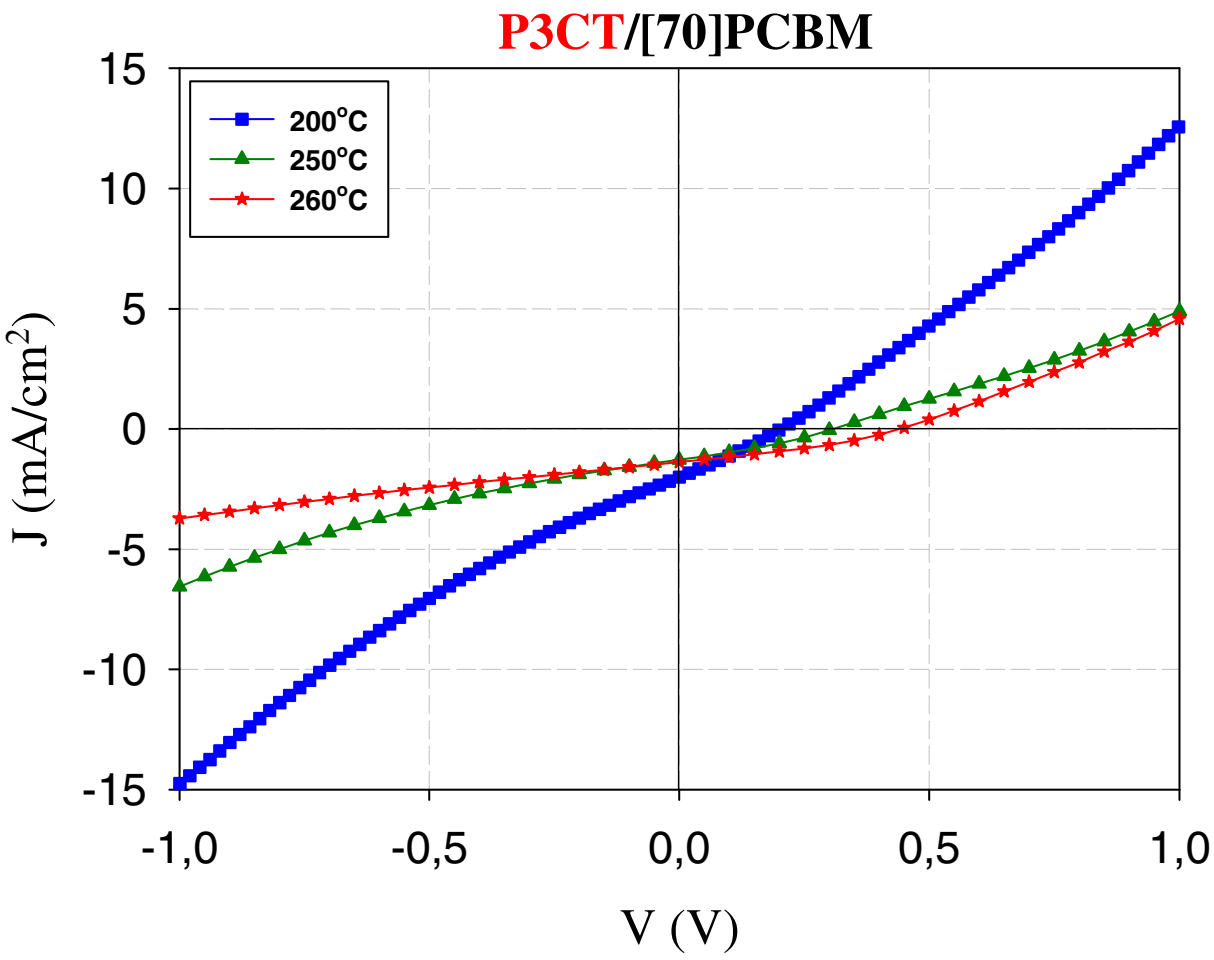

Figure S11. IV curves for devices with the same configuration cleaved at different temperatures. The devices had the following configuration: Glass/ITO/PEDOT:PSS/P3CT:PCBM[70]/Al (1000 W m^{-2}, AM1.5G, 70 ^{o}C).

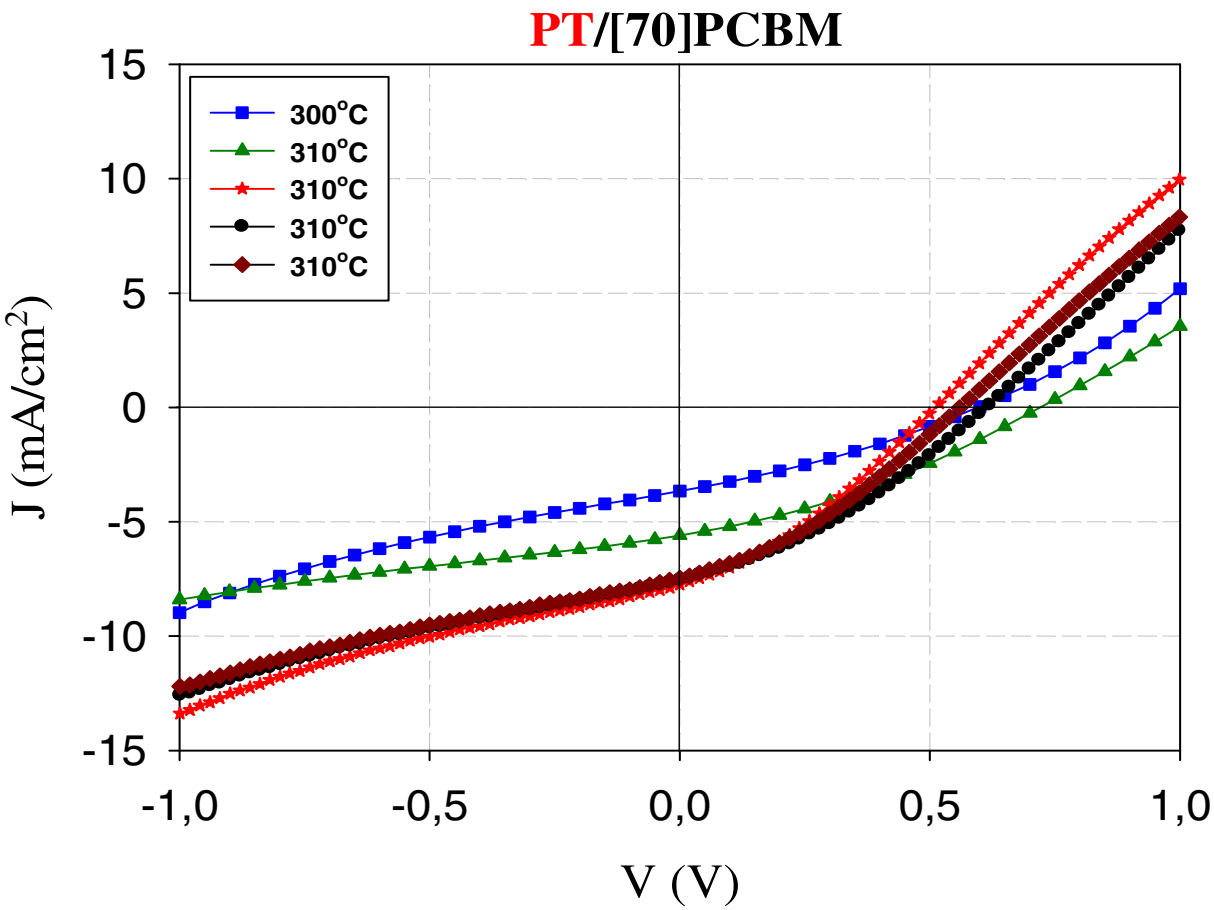

Figure S12. IV curves for devices with the same configuration cleaved at different temperatures. The devices had the following configuration: Glass/ITO/PEDOT:PSS/PT:PCBM[70]/Al (1000 W m^{-2}, AM1.5G, 70 ^{o}C).

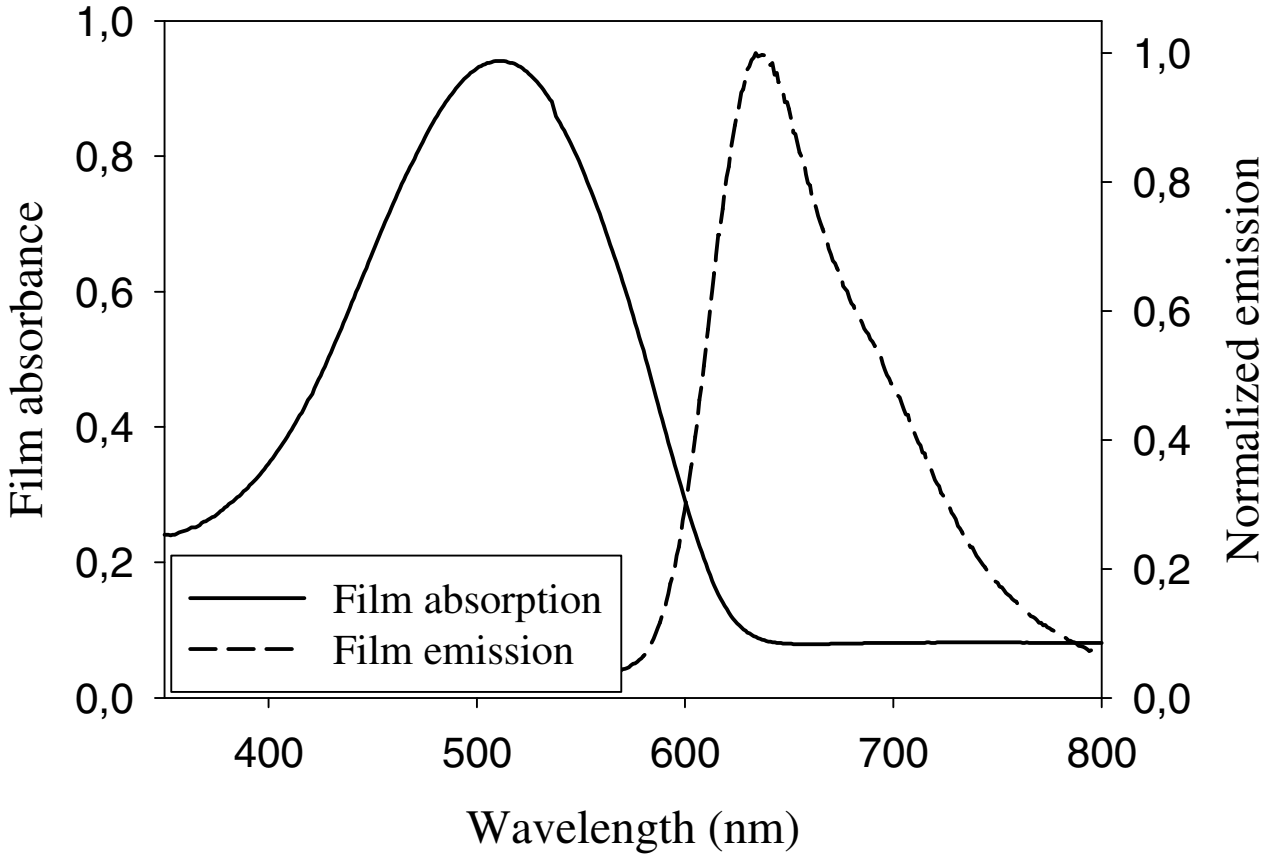

Figure S13. Absroption and emission scan for a film of P3MHOCT on a glass substrate. The absorption data were obtained in a transmission geometry and the emission data were obtained using front face illumination of the film using detection at 90 ^{o} to the incident beam. The polarizer was set to 90 ^{o} to eliminate reflected light in the detector. The emission wavelength was set to 480 nm. In the case of P3MHOCT-PCBM (1:1, w/w) the emission was completely quenched (not shown).

Stability measurements

In order to test the devices for stability, long term lifetime measurements were carried out in indoor conditions. For that purpose the samples were placed in a special atmospheric chamber,[S1] which allows to control the atmosphere surrounding the cells. Nitrogen was introduced into the chamber

and the samples were illuminated through the windows of the chamber (intensity of the illumination was aproximately 1/3 sun or 330W/cm^2). IV curves of the cells were periodicaly measured (aproximately each 5 min.) for more then 500 hours and the PV parameters such as I_{sc}, V_{oc} and FF were extracted from the curves using a special software writen by Visual Basic. The devices were kept under short circuit conditions. Figure S14 presents a combination of IV-curves measured for the same device at different stages of degradation.

Devices annealed at different temperatures performed differently. Figure S15 shows the decay of devices cleaved at two different temperatures (250^{o}C and 310^{o}C)

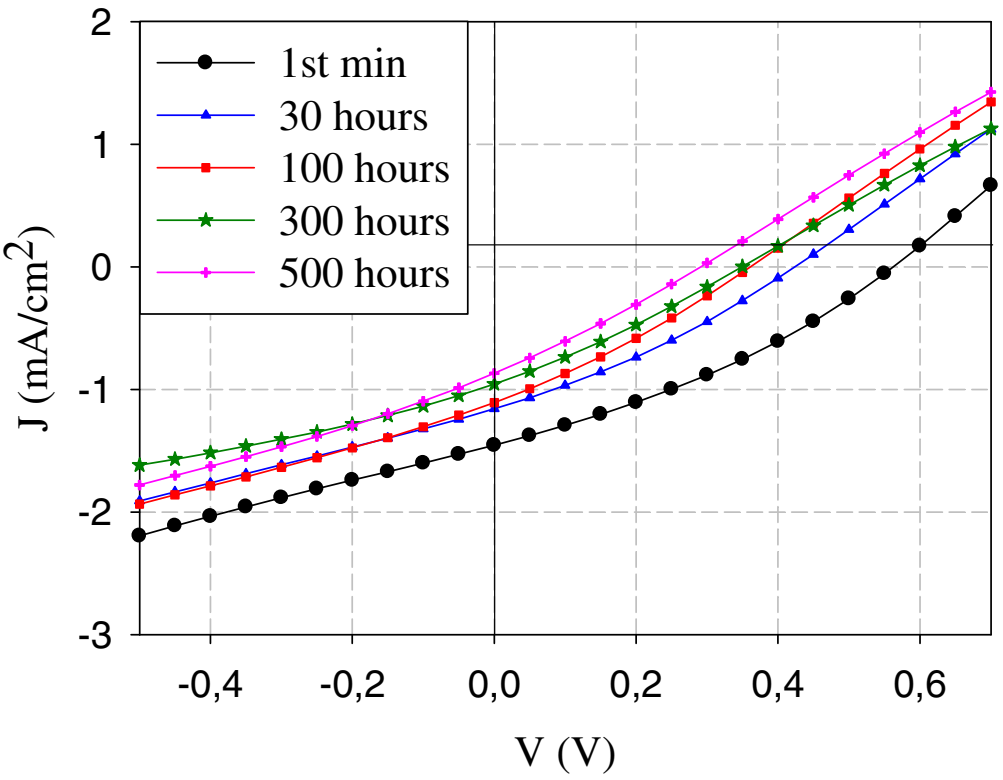

Figure S14. The evolution of IV-curves along the decay process in nitrogen for device with configuration Glass/ITO/PEDOT:PSS/PT:PCBM[70]/Al (330 W m^{-2}, AM1.5G, nitrogen, 0% relative humidity, 25 ^{o}C).

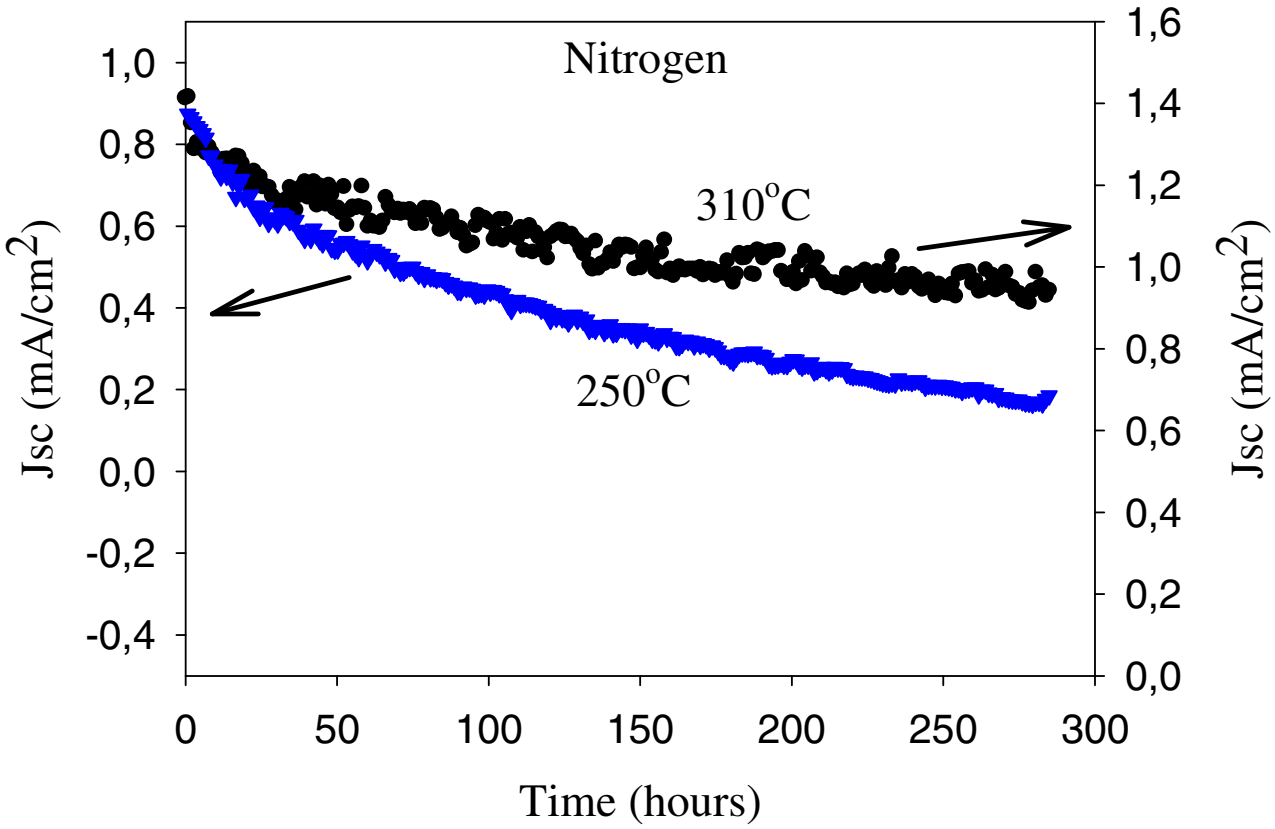

Figure S15. Decay of J_{sc} for devices Glass/ITO/PEDOT:PSS/Polymer:PCBM[70]/Al cleaved at two different temperatures (330 W m^{-2}, AM1.5G, nitrogen, 0% relative humidity, 25 °C).

References

S1) Gevorgyan, S. A.; Jørgensen, M.; Krebs, F. C. *Sol. Energy Mater. Sol. Cells*, **2008**, *92*, 736-745.

ARTICLE

Thermocleavable Materials for Polymer Solar Cells with High Open Circuit Voltage—A Comparative Study

Thomas Tromholt, Suren A. Gevorgyan, Mikkel Jørgensen, Frederik C. Krebs, and Kristian O. Sylvester-Hvid*

Risø National Laboratory for Sustainable Energy, Technical University of Denmark, Frederiksborgvej 399, DK-4000 Roskilde, Denmark

ABSTRACT The search for polymer solar cells giving a high open circuit voltage was conducted through a comparative study of four types of bulk-heterojunction solar cells employing different photoactive layers. As electron donors the thermo-cleavable polymer poly-(3-(2-methylhexyloxycarbonyl)dithiophene) (P3MHOCT) and unsubstituted polythiophene (PT) were used, the latter of which results from thermo cleaving the former at 310 °C. As reference, P3HT solar cells were built in parallel. As electron acceptors, either PCBM or bis-[60]PCBM were used. In excess of 300 solar cells were produced under as identical conditions as possible, varying only the material combination of the photo active layer. It was observed that on replacing PCBM with bis[60]PCBM, the open circuit voltage on average increased by 100 mV for P3MHOCT and 200 mV for PT solar cells. Open circuit voltages approaching 1 V were observed for the PT:bis[60]PCBM solar cells and a maximum conversion efficiency of 1.3% was obtained for solar cells with P3MHOCT:PCBM as the photoactive material. For the reference solar cells maximum efficiencies of 2.1 and 2.4% were achieved for P3HT:PCBM and P3HT:bis[60]PCBM, respectively. Despite special measures taken in terms of substrate design and device processing, a substantial spread in the photovoltaic properties was generally observed. This spread could not be correlated with the optical properties of the solar cells, the thickness of the photo active layer or the electrode deposition conditions of the aluminum top electrode.

KEYWORDS: thermocleavable polymers • high open circuit voltage • P3MHOCT • PT • bis-PCBM

INTRODUCTION

The efficiency optimization of polymer solar cells (1–5) involves detailed studies of the material properties (i.e., band gap, charge carrier mobility, absorption cross-section), the interplay between the material and film forming process, the film morphology dependence on processing (i.e., solvents, drying speed, printing, or coating method) as well as post film formation processes (i.e., solvent annealing, thermal annealing). The search for better suited photoactive materials is therefore challenging and there is no single litmus test for determining if a newly synthesized material will yield improved performance in a given solar cell geometry. An approach normally taken is to make the best of a given set of materials through optimizing deposition techniques, layer sequences, thicknesses, and device architecture in general. In regard to the latter, the use of tandem structures has proven a viable approach to overcome the limitations of using photoactive materials with a limited spectral overlap with the solar spectrum. However, from a processing point of view, the formation of structures with multiple photoactive layers, as well as optical spacer and blocking layers by solution processing has not yet been solved in a satisfactory manner. The obvious problem lies in protecting the first solution processed layer from being redissolved while processing of subsequent layers. The general lack of so-called orthogonal solvent systems for the deposition of different photoactive materials has led to the development of methods that typically employ an oxide, a metal or a PEDOT:PSS layer as the separation layer. For a review of these methods we refer to refs 6 and 7. However, none of these methods seem viable in terms of large-scale roll-to-roll processing, because insertion of inorganic and insoluble separation layers often requires special processing measures, e.g., vacuum deposition.

Photoactive polymers with solubilizing side chains that can be chemically modified or entirely removed by a thermal treatment, that is thermocleavable polymers, may be one way to overcome the problems outlined above. Thermocleavable polymers therefore are highly relevant in the context of polymer-based tandem solar cells, and recently some progress has been made with such materials (8, 9). One such promising candidate is the electron donating polymer poly-(3-(2-methylhexan-2-yl)-oxy-carbonyldithiophene) (P3MHOCT) as reported by Fréchet et al. (10), and later found to allow for fabrication of polymer solar cells with good stability, even under ambient conditions (11–15). Through ^{13}C isotopic labeling coupled with solid-state NMR studies P3MHOCT was found to be cleaved thermally in two subsequent steps as shown in Scheme 1 (16). First, P3MHOCT (pristine or blended with an electron accepting material) undergoes a de-esterfication at 210 °C to yield poly-3-carboxydithiophene (P3CT), which is then decarboxylated at ~300 °C to yield the unsubstituted (or native) poly thiophene (PT). Films of both P3CT and PT are insoluble in organic solvents and thus

* Corresponding author. E-mail: kosh@risoe.dtu.dk.
Received for review August 5, 2009 and accepted November 9, 2009
DOI: 10.1021/am900518r

Scheme 1. Chemical Transitions Involved in the Thermal Cleaving of P3MHOCT to P3CT and Further from P3CT to PT

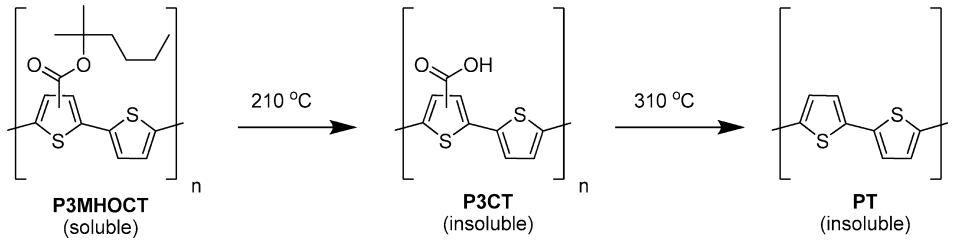

Scheme 2. (A) Layout of the ITO pattern of 50 mm × 50 mm Float Glass Substrates Employed (along the edges of the substrate are all together 16 contact pads, four of which are contacted with the round ITO area available to the solar cells); (B) Evaporation Mask Defining the Four Solar Cells Placed Centrosymmetrically on the Substrate, Each with an Area of 2 cm²

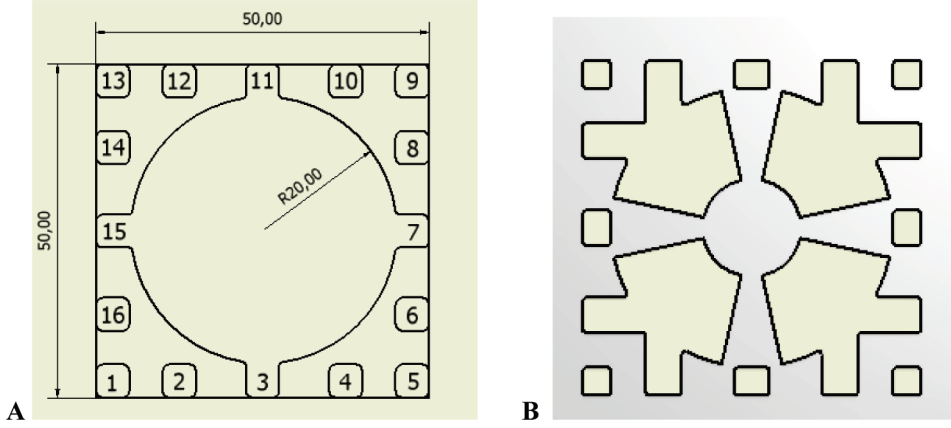

are ideally suited for device structures with multiple photoactive layers as demonstrated, for example, for tandem cells (8). In terms of solar cell efficiency, none of the three materials perform in the range as typical for P3HT, although in the case of PT (in combination with $PC_{70}BM$), bulk-heterojunction solar cells with efficiencies approaching 1.5% have been demonstrated (17).

In this investigation, we extend previous work on the optimization of solar cells based on P3MHOCT and PT and the electron acceptor $PC_{60}BM$ (henceforth referred to as PCBM). Specifically, we investigate the impact on solar cell performance when substituting PCBM with the corresponding bis-adduct (bis-PCBM) as recently used in P3HT solar cells (18). According to cyclic voltammetry (CV), the LUMO of bis-PCBM should be shifted approximately 0.1 eV up in energy relative to the LUMO for PCBM (18). Hence, solar cells with photoactive layers of P3MHOCT:bis-PCBM and PT:bis-PCBM hold the potential for improved performance by virtue of a higher open circuit voltage (V_{oc}). This naturally assumes that neither blend mobilities nor morphology are negatively affected by replacing PCBM with bis-PCBM, as well as the absorption characteristic of the solar cell. To elucidate this, we here present a comparative study of solar cells produced with the P3MHOCT:PCBM, PT:PCBM, P3MHOCT:bis-PCBM and PT:bis-PCBM composites.

Solar cells based on poly(3-hexyl-thiophene) (P3HT) have been found to exhibit a large spread in their photovoltaic properties and efficiency as demonstrated in a study where ~360 identical P3HT:PCBM cells were produced and a statistical analysis performed (19). Even for small area solar cells produced on the same small substrate, a substantial spread in efficiency was observed. When taking this to an industrial process scale, a similar spread was observed for printed solar cells employing the same type of materials (20). In the present comparative study, we consider a large number of solar cells produced under identical conditions, changing only the photoactive composite material. On the basis of the experiences obtained in ref 19, further measures in terms of substrate design are taken in an attempt to decrease the variability of the electrical properties of solar cells.

EXPERIMENTAL SECTION

Device Layout. Photovoltaic devices were prepared on 50 mm by 50 mm patterned ITO (~140 nm) substrates as provided by Luminescence Technology with a thickness of 0.7 mm and a nominal surface resistance of 5−15 Ω/□. The typical surface resistance was about 12 Ω/□. The ITO pattern as shown in Scheme 2A consists of 16 contact pads positioned symmetrically along the substrate edges and a round area with radius of 20 mm centered on the substrate. Four of the contact pads (number 3, 7, 11, and 15) are part of the round ITO area, the latter of which is intended as a general region where any number of solar cells can be positioned, depending on the contacting scheme. The substrate was designed specifically with spin-coating in mind and thus allows solar cells to be positioned and contacted in a centro-symmetric fashion within the round ITO area. Also, the round uninterrupted ITO area allows for a uniform and uninterrupted solution flow during spin-coating procedure, regardless of how the solar cells are laid out on the substrate.

Here we have chosen a device layout with four 2 cm^2 cells laid out centrosymmetrically on the substrate with symmetric and redundant contact structures. The layout is illustrated by the mask used for electrode deposition as shown in Scheme 2B. Hence, under ideal spin-coating conditions (substrate centered on spin chuck and solution deposition centered on substrate) in terms of process geometry, the four cells see identical process conditions. Further, the four solar cells have been positioned such as to maximize the radial distance to the center in order to minimize the radial width of the solar cells while maintaining an area of 2 cm^2. Note that in order to minimize the influence of the radial dependence of the film thickness, in principle, the solar cells should be laid out in as narrow a band as possible.

Device Preparation. The solar cells were prepared according to the following general procedure: Sonication for 10 min in isopropanol and then in demineralized water followed by blow drying. The substrates were flooded with cold (ca. 5 °C) Poly(3,4-ethylenedioxythiophene)-poly(styrenesulfonate) (PEDOT:PSS, 1.3 wt % in H_2O) as supplied from Aldrich and spun at 2800 rpm for 1 min, after which PEDOT:PSS was removed manually from the contact pads. Immediately before PEDOT:PSS spin coating, each substrate was washed with water while spinning at 2800 rpm. Annealing for 1 min at 150 °C was done on a hot plate after which the substrates were transferred to a N_2 glovebox environment (O_2 and H_2O below 0.1 ppm) where the substrates subsequently were annealed for further 5 min at 150 °C on a hot plate. A 0.5 mL blend solution was spin coated using a procedure where the substrate was first spun at 3000 rpm for 30 s, during which the substrate was washed with 0.5 mL *o*-dichlorobenzene, followed by spinning at 800 rpm afterward. The substrates were generally spun until they appeared dry (ca. 4 min) after which the photoactive layer was removed from the contract structure. The resulting films generally appeared very homogeneous always covering the entire substrate, i.e., the P3MHOCT:acceptor solution exhibits very good wetting and flow properties and thus is well-suited for spin coating.

PT devices were obtained by thermally cleaving the P3MHOCT devices on a hot plate at 310 °C in the glovebox right after spin coating. The chemical transition from P3MHOCT to PT is accompanied by two color changes upon heating; first the film changes color from purple to yellow as a characteristic of P3CT formation. Upon further heating, the film again turns purple signifying the formation of PT. The substrates were removed from the hot plate as quickly as possible after the second color change was completed. Note that the color change always evolved as a seeded process. Hence, the devices were always placed on the same place on the same hot plate. Because of the small nonuniformity of the heating of the hot plate the thermal cleaving (i.e., color change) could therefore be made to initiate from the same location on nearly all devices. The thermal cleaving was defined to be complete when the entire film had undergone the last color change.

The above production steps were always performed on a batch of six substrates (24 solar cells) of which three were processed with polymer:PCBM blend and the remaining three with polymer:bis-PCBM blend. Care was taken to minimize the variation of production parameters during the processing of a batch, which typically took about 6 h (characterization included). Immediately following the film-processing (and thermal cleaving for PT devices), all six substrates of the given batch were transferred to an external vacuum chamber where approximately 100 nm Al was deposited at a base pressure of $\sim 2 \times 10^{-6}$ Torr within ~1−2 min, while rotating the substrate holder.

Electrical characterization of the entire batch of solar cells followed immediately thereafter under ambient conditions.

All together 8 batches were processed for the purposes of this study: In batches 1−4,the polymer was PT and these batches are termed PT1 to PT4. In batches 5−8, the uncleaved polymer P3MHOCT was employed and these are termed P3MHOCT1 to P3MHOCT4. Care was also taken not to change any experimental conditions between processing of different batches.

An additional four batches of solar cells (one for each blend combination) were prepared for the purpose of correlating spectral features of the UV−vis spectra of the solar cells with the thickness of the photoactive layer. Each batch consisted of 7 substrates prepared in the same way as described above, but with the blend spin-coating speed and time chosen differently for each substrate (i.e., 300, 400, 500, 600, 800, 1000, or 1200 rpm). The same material combination was used for the entire batch of 7 solar cell substrates. After recording the UV−vis absorption spectra for these additional 28 substrates, each substrate was analyzed by AFM to estimate the thickness of the photoactive layer. This was done by recording step profiles obtained from scanning across a scratch in the film multiple times. For the two batches with PT solar cells, regions where only the blend layer occurred on the substrate (corner regions outside the ITO pattern) were scratched and analyzed. For the P3MHOCT solar cells, regions between the solar-cell pixels were subject to AFM analysis. In this case, double step profiles could always be located, yielding both a PEDOT:PSS and blend layer thickness. In both cases, an average of two AFM step scans were performed per substrate.

For reference, an additional four batches of P3HT:PCBM and P3HT:bis-PCBM solar cells (batches named P3HT1 to P3HT4) with three substrates of each were prepared according to the procedure described above. Following electrode deposition, however, the P3HT based solar cells were thermally annealed at 140 °C for 5 min in the glovebox and subsequently taken out for immediate characterization.

Preparation of Photo Active Solutions. Poly-(3-(2-methylhexan-2-yl)-oxy-carbonyldithiophene) (P3MHOCT) as previously synthesized for a study of large scale production of solar cells was used here (M_n = 11 300, M_w = 36 900, M_p = 29 800, PD = 3.3) (20). PCBM (99%, Lot: 08.01.08) and bis-PCBM (99.9% Lot: 31.01.08 as well as Lot: 15.07.08) both obtained from Solenne BV were used as received. All blend solutions were made from 20 mg of P3MHOCT plus 20 mg of PCBM (or bis-PCBM) per 1 mL of anhydrous *o*-dichlorobenzene, and were stirred overnight at ~40 °C, after which they were filtered cold through 0.45 μm filters. Typically, 20 mL solution was prepared such that all batches could be processed from the same solution. Solutions were always kept stirring at ~40 °C and all handling of the solutions was restricted to the glovebox environment and also deposited at this temperature.

For the P3HT solar cells a blend solution consisting of 10 mg/mL P3HT (Rieke Metals, Lot: BS16−24) and 10 mg/mL PCBM (99% Lot: 29.06.09) or bis-PCBM (99.5% Lot: 11.12.08) in chlorobenzene was used. The solution was stirred at ca. 40 °C overnight, after which it was brought to room temperature and was ready to use. Because of the relativity low concentrations, no filtering was required. The solution was kept under inert atmosphere at constant stirring and deposited at room temperature.

Electrical and Optical Device Characterization. The dark and illuminated IV characteristics of the four solar cells on each substrate were recorded using a substrate holder contacting the contact pads 1−16 (see Scheme 2A) simultaneously. A computer program was employed to automatically switch the relays in a Keithley 2700 multimeter/data acquisition system connecting each solar cell in turn to a Keithley 2400 sourcemeter in a two-wire measurement configuration. The solar cells were contacted in a redundant and symmetric fashion that is, for solar cell 1 contacting the cathode was done on pad 15 and 3, whereas the anode was contacted on pad 16 and 2. For cell 2, the cathode was contacted on pad 3 and 7 and the anode on pad 4 and 6 and vice versa for solar cell 3 and 4. First $I-V$ curves for illuminated devices were recorded between −1 and 1 V, and then $I-V$ curves between −2 and 2 V were recorded in the dark.

The conditions of the characterization under simulated sunlight were KHS 575 using a solar simulator from Steuernagel Lichttechnik operating at 1000 W m^{-2}, AM1.5G. The spectrum of the solar simulator was checked using an optical spectrum analyzer made for measuring irradiance, and its intensity was calibrated bolometrically using a precision spectral pyranometer from Eppley Laboratories. During measurements, the incident light intensity was monitored continuously using a CM4 high-temperature pyranometer from Kipp & Zonen.

IPCE measurements were performed using a homemade LED -based illumination system with 18 different wavelengths in the 400−1000 nm range.

UV−vis absorption spectra of the solar cells were recorded in a reflection geometry employing an Avantes CCD UV−vis spectrometer (range 150 to 1100 nm), a Halogen/Deuterium light source (AVA-AVALIGHT-DH) and a seven-furcated (AVA-FCR-7UV200) fiber optics reflection probe with an adjustable collimating lens.

These measurements were performed in an automated setup handling up to 12 substrates at a time, and hence 44 solar cells on 11 substrates were recorded in a single run employing a freshly evaporated Al mirror as reference. Contrary to the automated procedure used in ref 21. the reflection probe used here is within 1−2 cm of the substrate, which renders geometrical corrections less critical. The absorption measurement probed a circular spot with a diameter of ~3 mm and all solar cells were probed at exactly the same position.

RESULTS AND DISCUSSION

General Trends in Photovoltaic Key Values. Figures 1A−3A show scatter plots of J_{sc}, V_{oc}, and FF versus the power conversion efficiency (η) as measured for PT:PCBM and PT:bis-PCBM solar cells in batches PT[1−4]. In Figures 1B−3B, the corresponding results are shown for P3MHOCT:PCBM and P3MHOCT:bis-PCBM solar cells in batches P3MHOCT[1−4]. All data points relating to PT and P3MHOCT are shown with circles in Figure 1−3. Filled symbols designate PCBM and empty symbols bis-PCBM. The batch numbering is indicated by different colors, i.e., black, red, green, and gray designate batches 1−4, respectively.

For reference, the same type of data is shown in Figures 1−3 for the P3HT:PCBM and P3HT:bis-PCBM solar cells made in batches P3HT[1−4]. This data is shown with stars (filled for PCBM and empty for bis-PCBM) and the same color coding as used for PT and P3MHOCT. Note that the same P3HT data are shown in both A and B figures. The corresponding average values, standard deviations and extreme values of η, J_{sc}, V_{oc}, and FF are compiled in Tables 1 and 2.

From Figure 1, it is seen that P3MHOCT solar cells generally give larger J_{sc} than the corresponding PT solar cells and that this is generally also reflected in η. Comparing with the P3HT reference solar cells on average half the value of J_{sc} can be achieved with P3MHOCT as generally also reflected by the efficiencies.

In terms of V_{oc}, from Figure 2 and Table , the performance of P3MHOCT:PCBM cells appears comparable to that of PT:PCBM cells. With bis-PCBM however, on average V_{oc} is ~100 mV larger for PT than for P3MHOCT cells. Despite the considerable spread in V_{oc} it is noteworthy that several PT:bis-PCBM solar cells (from different batches) have a V_{oc} approaching 1 V, which is unprecedented considering that their efficiency is in the range of 0.6%. In other studies

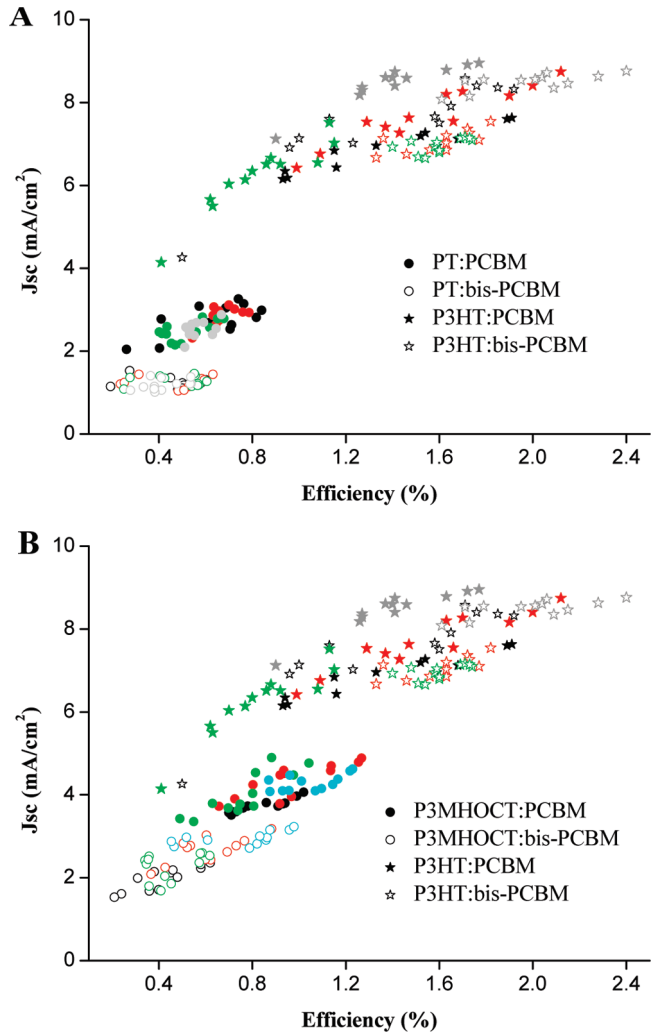

FIGURE 1. Short circuit current density (J_{sc}) as a function of the power conversion efficiency (η) for different production batches 1 to 4 of (A) PT:PCBM and PT:bis-PCBM and (B) P3MHOCT:PCBM and P3MHOCT:bis-PCBM solar cells. Batch numbers are shown with different colors. Results obtained with PCBM are shown with filled symbols, whereas results obtained for bis-PCBM are shown with open symbols. The corresponding results obtained for P3HT:PCBM and P3HT:bis-PCBM (same color coding) solar cells are shown for reference.

where a V_{oc} approaching 1 V was observed, the corresponding efficiency is much lower (22). Compared to P3HT, both PT and P3MHOCT solar cells on average yield higher V_{oc} for both PCBM and bis-PCBM.

In terms of the FF, on average PT:bis-PCBM cells perform much better than the P3MHOCT:bis-PCBM solar cells, as seen from Figure 3 and Table 2. For PT:PCBM and P3MHOCT:PCBM however, on average both the V_{oc} and FF are comparable. On average, the FF for all solar cells employing PCBM are in the same range as seen from Table 1. However, for solar cells employing bis-PCBM, on average PT cells give higher FF than for P3HT cells, which again give higher FF than observed for P3MHOCT cells.

Overall, the P3MHOCT solar cells have higher efficiencies than the PT cells, the performance difference being most outspoken for PCBM, and entirely due to higher J_{sc} values for the P3MHOCT solar cells. In terms of efficiency, both PT and P3MHOCT are inferior compared to P3HT. This is

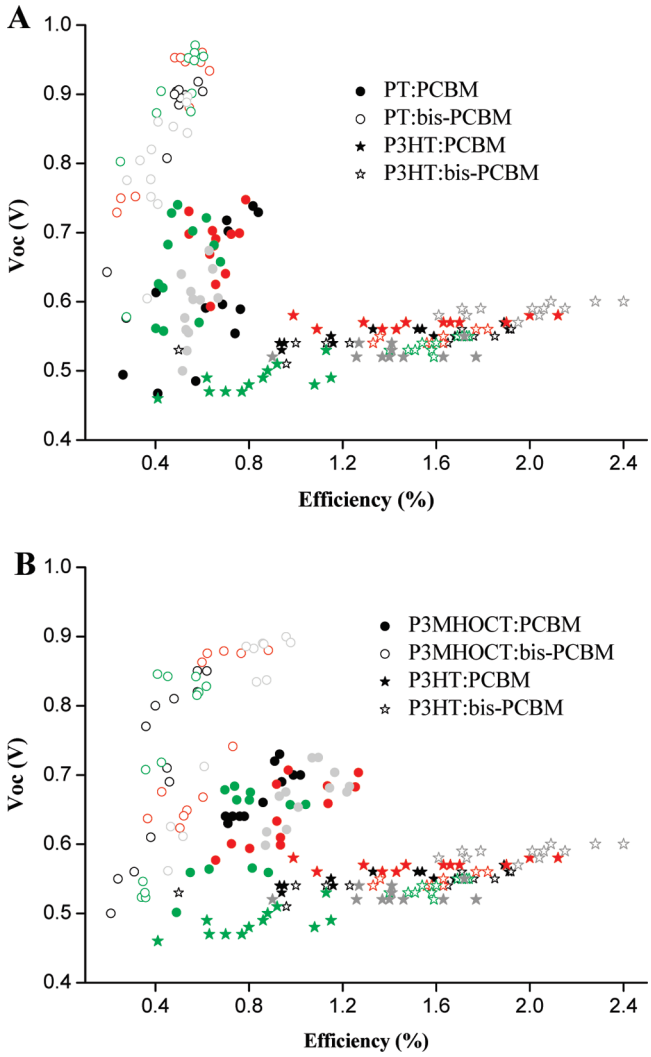

FIGURE 2. Open circuit voltage (V_{oc}) as a function of the power conversion efficiency (η) for different production batches 1 to 4 of (A) PT:PCBM and PT:bis-PCBM and (B) P3MHOCT:PCBM and P3MHOCT:bis-PCBM solar cells. Batch numbers are shown with different colors. Results obtained with PCBM are shown with filled symbols, whereas results obtained for bis-PCBM are shown with open symbols. The corresponding results obtained for P3HT:PCBM and P3HT:bis-PCBM (same color coding) solar cells are shown for reference.

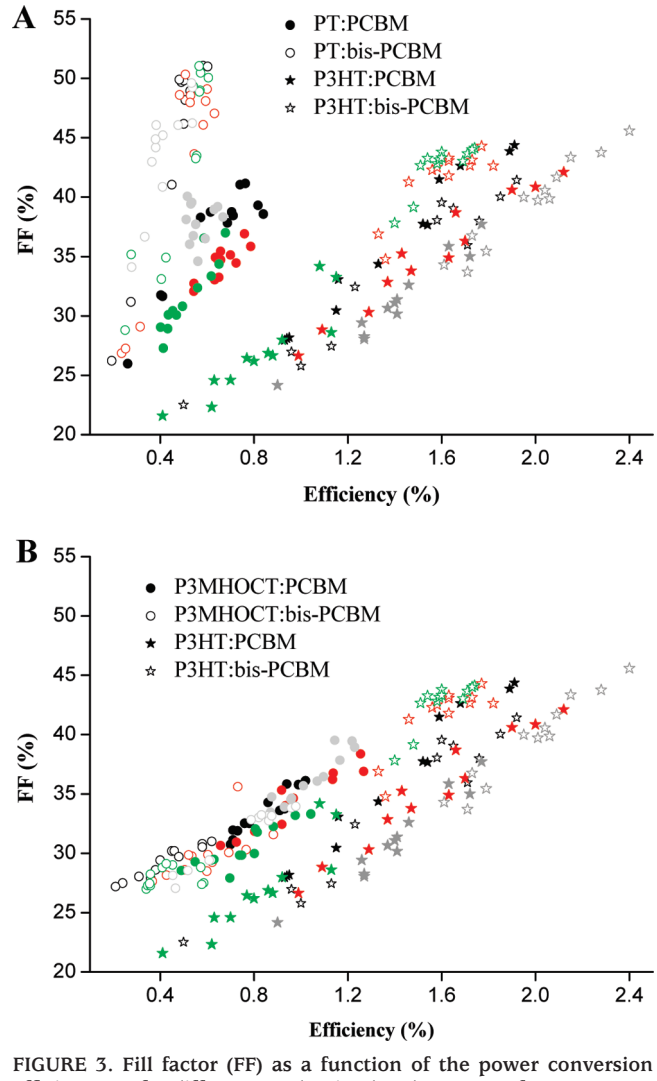

FIGURE 3. Fill factor (FF) as a function of the power conversion efficiency (η) for different production batches 1 to 4 of: (A) PT:PCBM and PT:bis-PCBM and (B) P3MHOCT:PCBM and P3MHOCT:bis-PCBM solar cells. Batch numbers are shown with different colors. Results obtained with PCBM are shown with filled symbols whereas results obtained for bis-PCBM are shown with open symbols. The corresponding results obtained for P3HT:PCBM and P3HT:bis-PCBM (same color coding) solar cells are shown for reference.

mainly due to the significantly larger photo currents of the P3HT solar cells as clearly seen from Figure 1.

When comparing the performance of PCBM and bis-PCBM solar cells, from Figures 1− and Tables 1 and 2, it is found that PCBM is the better choice of acceptor material for PT and P3MHOCT, mainly by virtue of higher J_{sc} values. Even the higher V_{oc} obtained for PT:bis-PCBM cannot compensate the decrease in J_{sc} when replacing bis-PCBM with PCBM. Conversely, for P3HT solar cells bis-PCBM is the better choice of acceptor material due to increased J_{sc} and FF, as seen from Table 1 and 2.

The best material combination in this study is P3MHOCT:PCBM with a peak and average efficiency of 1.3 and 0.9%, respectively. However, this is still clearly below the efficiencies obtained for the reference P3HT solar cells, which for PCBM yields peak and average efficiencies of 2.12 and 1.29% and for bis-PCBM yield 2.40 and 1.65%, respectively. In terms of V_{oc} 1 V has been approached by a peak value of 0.97 V as measured for some PT:bis-PCBM solar cells.

The scatter plot data representation in Figure 1−3 reveals how η correlates with J_{sc}, V_{oc}, and FF. In general terms Figure 3 shows that for all solar cells there is a linear correlation between η and FF. From Figure 2 the picture for V_{oc} seems less clear for PT and P3MHOCT solar cells whereas for P3HT cells there is a clear linear correlation between V_{oc} and η. Figure 1 shows clear correlations between η and J_{sc} for both P3MHOCT and P3HT solar cells.

These correlations indicate which photovoltaic parameters influence the device efficiency by virtue of variations in the processing parameters which are beyond our control. For example, Figure 1B shows that the fluctuation in some experimental condition may influence J_{sc} in the P3MHOCT:bis-PCBM case, such that if J_{sc} is large for a given solar cell then also η becomes large. Conversely, from Figure 1A is seen that in case of PT:bis-PCBM the J_{sc} is virtually un-

Table 1. Average, Standard Deviation, and Maximum and Minimum Key PV Values As Obtained for PT, P3MHOCT, and P3HT Solar Cells Employing PCBM as the Acceptor Material

	η (%)			V_{oc} (V)			J_{sc} (mA/cm^2)			FF (%)		
	PT	P3MHOCT	P3HT	PT	P3MHOCT	P3HT	PT	P3MHOCT	P3HT	PT	P3MHOCT	P3HT
avg	0.59	0.90	1.29	0.63	0.65	0.53	2.65	4.09	7.31	35.22	33.64	32.22
std	0.12	0.19	0.40	0.08	0.05	0.04	0.31	0.42	1.07	3.75	2.9	5.94
max	0.84	1.27	2.12	0.75	0.73	0.58	3.26	4.90	8.95	41.16	39.53	44.38
min	0.26	0.49	0.41	0.47	0.50	0.46	2.04	3.36	4.14	25.98	27.90	21.57

Table 2. Average, Standard Deviation, Maximum and Minimum Key PV Values As Obtained for PT, P3MHOCT, and P3HT Solar Cells Employing bis-PCBM as the Acceptor Material

	η (%)			V_{oc} (V)			J_{sc} (mA/cm^2)			FF (%)		
	PT	P3MHOCT	P3HT	PT	P3MHOCT	P3HT	PT	P3MHOCT	P3HT	PT	P3MHOCT	P3HT
avg	0.46	0.56	1.65	0.86	0.74	0.55	1.23	2.47	7.50	43.61	29.71	39.40
std	0.12	0.20	0.33	0.11	0.13	0.02	0.13	0.46	0.85	7.57	2.18	5.27
max	0.63	0.98	2.40	0.97	0.90	0.60	1.53	3.23	8.76	51.07	35.61	45.57
min	0.19	0.21	0.50	0.58	0.50	0.51	1.01	1.53	4.26	26.22	26.98	22.49

changed under these same process conditions and corresponding unintended parameter variations. In the latter case the spread in η comes about mainly through a correlation between η and FF as seen in Figure 3A.

Performance of the Best Solar Cells. Figure 4 shows the $I-V$ curves for the best performing solar cells under illumination for each material combination employed. To a large extent, these $I-V$ curves are representative of the well-performing solar cells in all the production batches and Figure 4 is therefore used for a general discussion.

Figure 4 underscores two trends seen for PT and P3MHOCT in Figures 1−3; first, that on substituting PCBM with bis-PCBM, V_{oc} increases but with a significant sacrifice in J_{sc} (about a factor of 2), and second, that cleaving P3MHOCT to PT also reduces J_{sc} (again by a factor two). A lowering in J_{sc} could arise from decreased driving force for the initial charge separation, increased bulk-recombination (decreased mobilities and/or unfavorable morphology), decreased light harvesting in the photoactive layer, or the introduction of an electrical barrier. The fact that the $I-V$ curves in Figure 4 display nearly the same slope under reverse bias may point to that bulk-recombination alone is not responsible for the

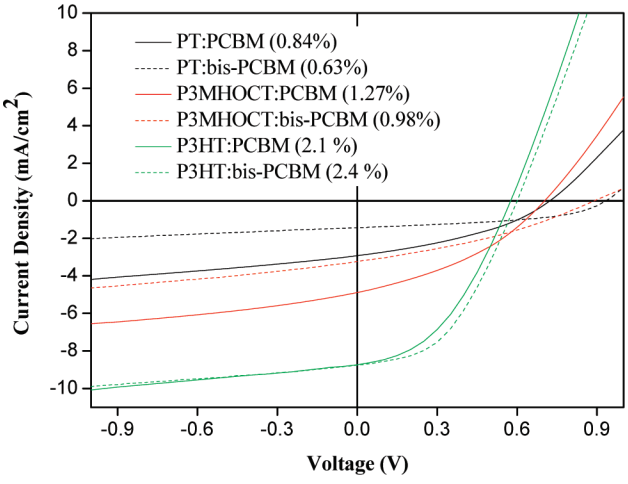

FIGURE 4. $I-V$ curves for the best solar cells obtained for PT and P3MHOCT under illumination. For reference is shown the corresponding curves obtained for P3HT.

lowing of J_{sc} on replacing PCBM with bis-PCBM and on cleaving P3MHOCT to PT. Admittedly, the solar cells should be characterized under much larger reverse bias conditions for this statement to be firm. We refrained from this, however, because we observed bubble formation in the films when going to −2 V under illumination.

The introduction of an electrical barrier on cleaving P3MHOCT to PT or by replacing PCBM with bis-PCBM can also be ruled out because inflection points were never observed in the $I-V$ curves (12, 23–25). In fact, when going from P3MHOCT:PCBM to PT:PCBM and from PT:PCBM to PT:bis-PCBM, the FF increases. Hence, the reduced J_{sc} must come about either by diminished light harvesting or decreased driving force for initial charge separation.

Substituting PCBM with bis-PCBM for the P3HT reference solar cells only leads to a small increase in V_{oc} and FF, and hardly any change in J_{sc}. The $I-V$ curves for the P3HT solar cells can be taken as a measure of what happens when shifting the acceptor LUMO energy (ε_a^L) up by ∼ 0.1 eV (PCBM → bis-PCBM) while keeping the driving force for initial charge separation constant. That is to say, the energy difference between the donor and acceptor LUMO ($\varepsilon_d^L - \varepsilon_a^L$) is such (∼ 0.7 eV or more) that changing ε_a^L by 0.1 eV will not affect the overall driving force for charge separation in the P3HT case. Therefore, J_{sc} is unchanged as seen from Figure 4, but a small increase in V_{oc} and FF results. From Tables 1 and 2, we confirm that this is also in line with the average performance numbers. Note that this is in contradiction with the original paper introducing P3HT:bis-PCBM solar cells, where a ∼0.2 V increase in V_{oc} was ascribed to the substitution of PCBM with bis-PCBM (18). For P3MHOCT and PT, an increase in V_{oc} in the range of 0.2 V can also be observed as seen from Figure 4. From the average numbers in Table 1 and 2, the increase in V_{oc} amounts to ∼0.1 and ∼0.2 V for P3MHOCT and PT, respectively. In the latter case, an increase of 0.2 V cannot simply be rationalized in terms of HOMO LUMO energies, and a more complex mechanism must be at work.

Going from P3HT over P3MHOCT to PT, the optical band gap is largely unchanged as confirmed in Figure S1 of the

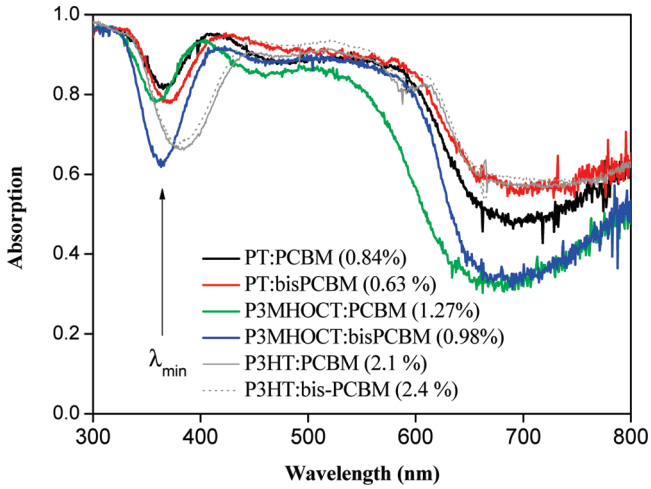

FIGURE 5. UV−vis absorption spectra recorded for the best performing PT and P3MHOCT solar cells. The approximate position of λ_{min} is indicated by an arrow. The corresponding results are shown for the best performing P3HT solar cells.

Supporting Information, whereas the donor HOMO level (ε_d^H) is shifted substantially downward, at least in the case of P3MHOCT (26). From preliminary CV experiments on identically prepared films of P3HT:PCBM, P3MHOCT:PCBM, and PT:PCBM (see Figure S2 in the Supporting Information), an ~600 meV shift of the first oxidation potential is observed on going from P3HT to P3MHOCT. The corresponding decrease in $\varepsilon_d^L-\varepsilon_a^L$ for P3MHOCT:PCBM compared to P3HT:PCBM therefore implies a decrease in J_{sc} in the former case. Because for P3MHOCT:PCBM ε_d^L and ε_a^L are quite close in energy, J_{sc} becomes susceptible to even small changes in ε_a^L as, for example, induced by substituting PCBM by bis-PCBM. This might explain why J_{sc} is abruptly halved on replacing PCBM with bis-PCBM in case of P3MHOCT, but not in the case of P3HT. For PT the CV results (see Figure S2 in the Supporting Information) are less conclusive and thus we can not rationalize the decrease in J_{sc} on going from P3MHOCT to PT based on the HOMO LUMO energies. Experimentally, however, this decrease could be ascribed to the thermal treatment leading to PT. Indeed we made the general observation that prolonged heating during the cleaving step only leads to a lowering of the efficiency for the PT solar cells, and consequently this step was kept as short as possible. In practice, this amounts to a few seconds, and within this time we cannot trace any sign of decomposition of either PEDOT:PSS or the PCBM/bis-PCBM as inquired by UV−vis spectroscopy, AFM, thermogravimetric analysis, and differential scanning calorimetry (see Figures S3−S6 in the Supporting Information). However, from AFM measurements performed on P3MHOCT:PCBM films before and after thermal cleaving (see Figure S7 in the Supporting Information), it is seen that both the interface roughness and domain size changes. To assess if this morphology change gives rise to changes in charge carrier mobilities, we attempted to derive hole mobilities from FET devices prepared from P3MHOCT and PT. However, because of pronounced contact resistances, these preliminary results were not conclusive.

In Figure 5, the UV−vis absorption spectra as measured for the best performing solar cells are shown. Again, these may be taken as representatives for the remaining set of solar cells in the respective production batches. Note that these spectra are recorded for the entire solar cell in reflection geometry and thus are very sensitive films imperfections and opaqueness. The absorption spectra cannot be used to assess the light harvesting potential (in terms of an upper limit to the photo current) of the photoactive layer itself. Nonetheless, by comparisons of the spectra in Figure 5, it may still be loosely argued that the differences in J_{sc} (Table 1 and 2) seen for different material combinations, most likely is not of an optical origin as the spectra appear rather similar. This is seen on comparing the absorption spectra for the PT:bis-PCBM and P3HT:bis-PCBM solar cells. Apart from the 300−400 nm range, these spectra are nearly identical and yet, on average, J_{sc} is six times larger in the P3HT case. Also, the fact that the spectrum for P3MHOCT:PCBM in Figure 5 cuts off at shorter wavelengths than for the remaining three material combinations, contradicts that P3MHOCT:PCBM solar cells display the largest values of J_{sc} among the P3MHOCT and PT solar cells.

The absorption spectra in Figure 5 do not reflect the trends seen for the Incident Photo to Current Conversion Efficiency (IPCE) as measured for the different material combinations (see Figure S8 in the Supporting Information). This again supports the assumption that it is not the light-harvesting properties of the materials per se that give rise to reduced J_{sc} on replacing PCBM with bis-PCBM or when cleaving P3MHOCT to PT.

An important characteristic is the minimum between 300 and 400 nm, the position of which is indicated in Figure 5 and designated as λ_{min}. As previously shown for P3HT:PCBM solar cells, a linear correlation between the thickness of the photoactive layer and the position of a certain distinct minimum in the UV−vis absorption spectrum of the entire solar cell can be established (21). Because the first absorption minimum in Figure 5 is very sensitive to changes in the photoactive layer thickness, it is possible to correlate thickness and λ_{min} in a similar fashion as done in ref 21.

Hence in Figure 6, the average position of λ_{min} versus the average thickness of the photoactive layer is shown for solar cells in the four extra batches where the spin-coating speed was varied (a batch each for PT:PCBM, PT:bis-PCBM, P3MHOCT:PCBM, and P3MHOCT:bis-PCBM). Clearly, four linear correlations between λ_{min} and the thickness of the photoactive layer have been obtained, and the parameters corresponding to the best linear fit of the data are shown in Figure 6.

Spread of the Photovoltaic Data. Figures 1−3 reveal a notable spread in the measured $I-V$ data. In terms of η, the standard deviation obtained for P3MHOCT cells is almost twice the standard deviation calculated for PT cells. This is due to a larger spread in J_{sc} for P3MHOCT than for PT cells. However, for the P3HT solar cells, the spread in η is larger than for both PT and P3MHOCT by virtue of a substantial spread in J_{sc} and/or FF.

Figure 2 shows a substantial spread in V_{oc} for the PT and P3MHOCT solar cells compared to the P3HT reference solar

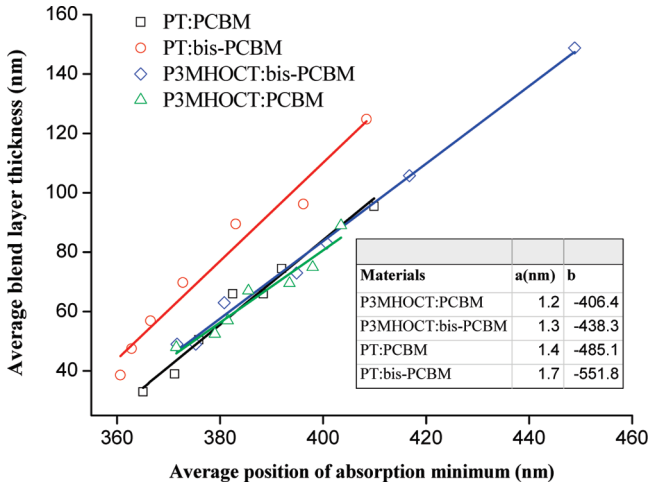

FIGURE 6. Average blend layer thickness as measured by AFM as a function of the average position of λ_{min} for PT and P3MHOCT solar cells. Also shown are the best linear fit of the data for the four types of solar cells described the relation $d = a + b\lambda_{min}$. The values of a and b as obtained for the different material combinations are shown in the inset table.

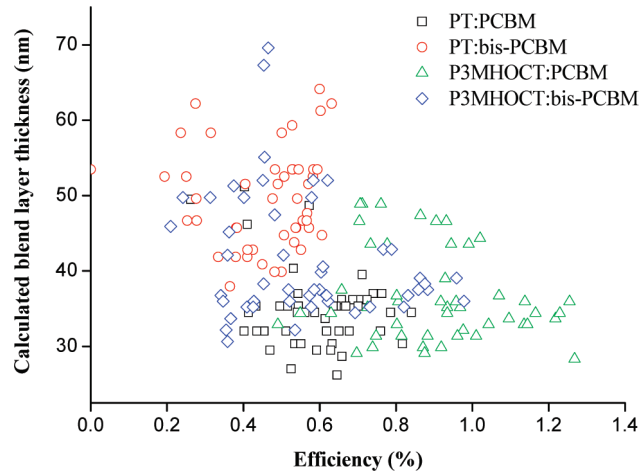

FIGURE 7. Thickness of the active layer for all PT:PCBM, PT:bis-PCBM, P3MHOCT:PCBM, and P3MHOCT:bis-PCBM solar cells as a function of their efficiency. The thickness is derived from λ_{min} as obtained from the UV−vis absorption spectrum of each cell.

cells which display a quite small spread in V_{oc}. Most notably is the large spread for the PT:bis-PCBM and P3MHOCT:bis-PCBM solar cells as also confirmed by Tables 1 and 2. From Figure 3 and Tables 1 and 2, a comparable spread in FF is seen for PT:PCBM and P3MHOCT solar cells. The PT:bis-PCBM solar cells display the largest spread in FF, even larger than that of the P3HT solar cells. It should be noted that the relatively low values obtained for FF in this study generally can be ascribed to the substrate layout which was designed mainly with reproducibility in mind. Improved FF values can be achieved by employing smaller active areas and/or Au busses on the substrate prior to processing. However, we have refrained from this to avoid areas on the substrate with wetting properties different from ITO, as this may affect the film uniformity.

It is noteworthy that the PT:bis-PCBM solar cells with an average efficiency of 0.46% display the smallest spread in J_{sc} but the largest spread in FF as seen from Table 2. Among all solar cells, the PT cells also display the smallest spread in efficiency. Considering their manufacturing process, a priori a larger spread in η could have been expected because PT cells are subject to a thermal cleaving step, inherently difficult to perform in a strictly reproducible way. However, the opposite trend is observed, and in fact η is less reproducible for the P3MHOCT, and in particular P3HT solar cells.

From the scatter plots in Figure 1−3 clustering of data points belonging to the same production (i.e., data points of same color) batch is not observed. Thus, whatever influential production parameters are causing spread in the $I-V$ data, the fluctuations in these parameters occur also while processing substrates belonging to the same evaporation batch. Hence, the batchwise spread is not due to variations in the Al deposition conditions.

The spread in the $I-V$ data may also be considered at the substrate level, i.e., the variability of the $I-V$ data for solar cells on the same substrate. In principle, the four solar cells on a substrate are subject to exactly the same process conditions, and by virtue of the substrate design all four solar cells also experience identical electrical surroundings. The substratewise spread can therefore only be ascribed to nonuniformity of the different thin-film layers and/or intrinsic morphology/interface nonuniformities. The substratewise (or residual) spread can be assessed by carefully inspecting the scatter plots in Figures 1−3, where it is seen that the 12 symbols of a given color only occasionally appear in groups of four.

To assess if the spread in the $I-V$ data in Figures 1−3 (including the residual spread) is linked to variations of the photoactive layer thickness, this thickness was calculated for all solar cells based on their absorption spectra. This was done using λ_{min} and the linear relations given in the inset in Figure 6 for PT and P3MHOCT. Knowing the thickness of the photoactive layer of each solar cell, the IV data may then be investigated for correlations with respect to the thickness. Hence, in Figure 7, a scatter plot of the calculated thickness versus efficiency is shown for all the PT and P3HMOCT solar cells. No correlation between η and the layer thickness of the photoactive layer is seen for any of the material combinations investigated. Similar scatter plots of the photoactive layer thickness versus J_{sc}, V_{oc}, and FF (not shown) were scrutinized and no correlations found either. Also for the reference P3HT solar cells where the spread is quite substantial, no correlation between η and blend layer thickness was found (see Figure S9 in the Supporting Information). To this end, it should be emphasized that a significant effort was made to ensure that for all material combinations uniform films could be accomplished repeatedly. In fact, the particular choice of P3HT blend formulation and spin-coating conditions was made in order to obtain as uniform films as possible and not in order to optimize device efficiency. Therefore, chlorobenzene was used for the processing of the P3HT solar cells and not o-dichlorobenzene, because in the latter case highly uniform films could not be accomplished.

The solar cells have very uniform films and to a large extent the measured absorption spectrum (always probed at the same location but for a limited area of the solar cell)

can be taken as representative of the whole cell. Hence, the spread in the IV data for solar cells produced under seemingly identical conditions is neither of optical origin nor coupled to variations in the blend layer thickness.

In terms of the substrate-wise spread in the IV data, the only remaining possible causes of it can be variations of the local film morphology and/or interfaces properties, both of which only impact the electrical properties of the solar cells. The fact that the solar cells of this study feature an active area ~38 times larger than that used in ref (19) (ten P3HT:PCBM solar cells 5.3 mm^2 each on a substrate) apparently does not decrease the spread in the IV data by virtue of averaging local variations out. Also, the fact that we use an ITO pattern on the substrate that allows for an uninterrupted blend flow while spin coating, contrary to the structured ITO used in ref (19), seems not to diminish the spread in the IV data. Hence, the active area and ITO patterning are not decisive in terms of the spread in the IV data as sometimes speculated.

Film Morphology. To further pursue the question of why solar cells from the same process batch, or even from the same substrate, can display so different solar cell performance, we conducted several AFM measurements for P3MHOCT and PT solar cells with good and poor efficiencies from the same batch. Figure S10 shows an example of such AFM measurements for P3MHOCT:PCBM and PT:PCBM solar cells, from which it is clear that no significant roughness or morphology features characterize good or poor device performance. We should stress that such measurements by nature are not representative since only a restricted region on a limited number of devices are probed in practice, and because the region probed lies between the solar cells (inside the ITO area) where no Al contact has been deposited.

CONCLUSION

By a comparative study of solar cells employing the thermo-cleavable polymer P3MHOCT and its cleaved end product PT it was shown that V_{oc} can increase significantly when substituting PCBM with bis-PCBM. In the case of PT:bis-PCBM, V_{oc} approaching 1 V was obtained for several solar cells which is unprecedented considering their efficiencies being in the 0.6% range. However, this substitution of acceptor material involves a sacrifice in J_{sc} which amounts to a factor two, and overall the optimal material combination remains P3MHOCT:PCBM with a peak efficiency of 1.3%. Based on the IV data for cells under illumination, the photovoltaic behavior of solar cells with the different material combinations to some extent could be rationalized in terms of simple considerations of HOMO and LUMO energy levels. However, the rather large increase in V_{oc} for PT and P3MHOCT upon substituting PCBM with bis-PCBM, and as *not* seen for the corresponding P3HT solar cells, can not be rationalized in such simple terms. Despite the effort and special measures taken in terms of substrate design, characterization and process standardization, a significant scatter in the photovoltaic key parameters was generally observed. The smallest spread in the photovoltaic efficiency was observed for PT solar cells which however also featured the lowest efficiencies. The largest spread was clearly seen for the P3HT reference solar cells which however gave rise to highest photovoltaic efficiencies.

Generally, a residual spread in the IV data for solar cells on the same substrate was observed. Combined with the absence of correlations between the photovoltaic parameters and the thickness of the photoactive layer indicates that at least one possible cause of the variability for the IV data should not be ascribed to the unintended variation of the processing parameters as the inevitabe part of the manual making (lab scale) of polymer solar cells.

Acknowledgment. This work was supported by the Danish Strategic Research Council (DSF 2104-05-0052 and 2104-07-0022). We would like to thank Torben Kjær and Jan Asltrup for technical assistance, Noemi Rozlosnik for assisting with the AFM measurements and Ole Hammerich for assisting with the CV measurements.

Supporting Information Available: Transmission spectra of the blend materials subject to different process conditions, Cyclic voltammogram for P3HT:PCBM, P3MHOCT:PCBM and PT:PCBM as measured on ITO glass, Transmission spectra for PEDOT:PSS on ITO glass subject to different process conditions, AFM images of PEDOT:PSS before and after annealing at 310 °C, Transmission spectra for PCBM and bis-PCBM on float glass before and after an annealing at 310 °C, TGA and DSC for PCBM and bis-PCBM, AFM images of P3MHOCT:PCBM and PT:PCBM on float glass, IPCE measurements for all the material combinations investigated and scatter plot of the thickness of the active layer for all P3HT based solar cells versus their efficiency (PDF). This material is available free of charge via the Internet at http://pubs.acs.org.

REFERENCES AND NOTES

(1) Hoppe, H.; Sariciftci, N. S. *J. Mater. Chem.* **2006**, *16*, 45–61.
(2) Günes, S.; Neugebauer, H.; Sariciftci, N. S. *Chem. Rev.* **2007**, *107*, 1324–1338.
(3) Bundgaard, E.; Krebs, F. C. *Sol. Energy Mater. Sol. Cells* **2007**, *91*, 954–985.
(4) Jørgensen, M.; Norrman, K.; Krebs, F. C. *Sol. Energy Mater. Sol. Cells* **2008**, *92*, 686–714.
(5) Thompson, B. C.; Fréchet, J. M. J. *Angew. Chem., Int. Ed.* **2008**, *47*, 58–77.
(6) Hadipour, A.; de Boer, B.; Blom, P. W. M. *Adv. Funct. Mater.* **2008**, *18*, 169–181.
(7) Ameri, T.; Dennler, G.; Lungenschmied, C.; Brabec, C. J. *Energ. Environ. Sci.* **2009**, *2*, 347–363.
(8) Hagemann, O.; Bjerring, M.; Nielsen, N. C.; Krebs, F. C. *Sol. Energy Mater. Sol. Cells* **2008**, *92*, 1327–1335.
(9) Han, X.; Chen, X.; Holdcroft, S. *Adv. Mater.* **2007**, *19*, 1697–1702.
(10) Liu, J. S.; Kadnikova, E. N.; Liu, Y. X.; McGehee, M. D.; Fréchet, J. M. J. *J. Am. Chem. Soc.* **2004**, *126*, 9486–9487.
(11) Krebs, F. C.; Spanggaard, H. *Chem. Mater.* **2005**, *17*, 5235–5237.
(12) Krebs, F. C.; Norrman, K. *Prog. Photovoltaics: Res. Appl.* **2007**, *15*, 697–712.
(13) Krebs, F. C. *Sol. Energy Mater. Sol. Cells* **2008**, *92*, 715–726.
(14) Bjerring, M.; Nielsen, J. S.; Siu, A.; Nielsen, N. C.; Krebs, F. C. *Sol. Energy Mater. Sol. Cells* **2008**, *92*, 772–784.
(15) Krebs, F. C.; Thomann, Y.; Thomann, R.; Andreasen, J. W. *Nanotechnology* **2008**, *19*, 424013.
(16) Bjerring, M.; Nielsen, J. S.; Nielsen, N. C.; Krebs, F. C. *Macromolecules* **2007**, *40*, 6012–6013.
(17) Gevorgyan, S. A.; Krebs, F. C. *Chem. Mater.* **2008**, *20*, 4386–4390.
(18) Lenes, M.; Wetzelaer, G.-J. A. H.; Kooistra, F. B.; Veenstra, S. C.; Hummelen, J. C.; Blom, P. W. M. *Adv. Mater.* **2008**, *20*, 2116–2119.

(19) Riede, M. K.; Sylvester-Hvid, K. O.; Glatthaar, M.; Keegan, N.; Ziegler, T.; Zimmermann, B.; Niggemann, M.; Liehr, A. W.; Willeke, G.; Gombert, A. *Prog. Photovoltaics: Res. Appl.* **2008**, *16*, 561–576.
(20) Krebs, F. C.; Jørgensen, M.; Norrman, K.; Hagemann, O.; Alstrup, J.; Nielsen, T.; Fyenbo, J.; Larsen, K.; Kristensen, J. *Sol. Energy Mater. Sol. Cells* **2009**, *93*, 422–441.
(21) Sylvester-Hvid, K. O.; Ziegler, T.; Riede, M. K.; Keegan, N.; Niggemann, M.; Gombert, A. *J. Appl. Phys.* **2007**, *102*, 054502.
(22) Peng, Q.; Park, K.; Lin, T.; Durstock, M.; Dai, L. *J. Phys. Chem. B* **2008**, *112*, 2801–2808.
(23) Glatthaar, M.; Riede, M.; Keegan, N.; Sylvester-Hvid, K. O.; Zimmermann, B.; Niggemann, M.; Hinsch, A.; Gombert, A. *Sol. Energy Mater. Sol. Cells* **2008**, *91*, 390–393.
(24) Vogel, M.; Doka, S.; Breyer, M.; Lux-Steiner, C.; Fostiropoulos, K. *Appl. Phys. Lett.* **2006**, *89*, 163501.
(25) Zhang, S. T.; Zhou, Y. C.; Zhao, J. M.; Zhan, Y. Q.; Wang, Z. J.; Wu, Y.; Ding, X. M.; Hou, X. Y. *Appl. Phys. Lett.* **2006**, *89*, 043502.
(26) Murphy, A. R.; Liu, J.; Luscombe, C.; Kavulak, D.; Frechet, J. M. J.; Kline, R. J.; McGehee, M. *Chem. Mater.* **2005**, *17*, 4892–4899.

AM900518R

Thermocleavable Low Band Gap Polymers and Solar Cells Therefrom with Remarkable Stability toward Oxygen

Martin H. Petersen, Suren A. Gevorgyan, and Frederik C. Krebs*

Risø National Laboratory for Sustainable Energy, Technical University of Denmark, P.O. Box 49, DK-4000 Roskilde, Denmark

Received August 26, 2008; Revised Manuscript Received October 10, 2008

ABSTRACT: Thermocleavable esters of low band gap monomers and polymers based on diphenyldithienylthienopyrazine were prepared by incorporating carboxylic acid functionalities into the system. A series of different ester groups were prepared and the temperature of elimination of the ester group was studied. The lowest temperatures of elimination obtained were in the range 220−240 °C for tertiary esters giving the free acid. The highest temperatures of elimination were found for primary esters that also lead to decomposition of the molecule. Only the tertiary esters offer a good degree of control over the chemistry in the thermocleaved product. The photovoltaic performance of the polymers prepared was tested under simulated sunlight (1000 W m^{-2}, AM1.5G, 72 °C) and the best power conversion efficiency that could be reached for devices with an active area of 3 cm^2 was up to 0.4% in an ITO/PEDOT/polymer−PCBM/aluminum device geometry. The best performing polymer material was subjected to lifetime studies in four different atmospheres (dry nitrogen, dry oxygen, humid nitrogen and the ambient atmosphere). The best stability was observed in nitrogen while the devices showed nearly the same degree of stability in dry oxygen. In both the ambient atmosphere and the humid nitrogen atmospheres the devices degraded quickly. Finally the stability was compared with two other polymer systems that are known to give stable devices, poly(3-hexylthiophene) (P3HT) and native polythiophene (PT) obtained from the thermocleavable poly(3-(2-methylhexyloxycarbonyl)dithiophene) (P3MHOCT). The performance of the materials reported here was inferior to the performance of P3HT and PT in terms of power conversion efficiency (PCE). The photovoltaic parameters as studied under continuous illumination were however much more stable than those of the reference compounds.

Introduction

The processing requirements of functional materials and polymers are key to the successful application in active devices such as polymer solar cells.[1] In addition to processing there is, in the context of polymer solar cells, increasing focus on preparation of efficient materials with low optical band gaps[1b] and materials that give stable devices. Polymer solar cell devices most often rely on a thin multilayer structure with exact requirements of the nanomorphology of the individual layers. One of the advantages of the technology is that the individual layers can be prepared by solution processing thus gaining considerably in the potential speed, simplicity and lowered cost. However, the formation of multilayer structures based on organic materials such as polymers require that the deposition of subsequent layers does not affect the previously deposited layers. In practical terms this poses a major challenge and has only been solved with some success by following one of three possible strategies or a combination thereof.

(1) Orthogonal solvents for different layers.

(2) Cross-linking after film formation.

(3) Removal of solubilizing groups by thermocleavage.

The use of orthogonal solvents is the simplest and most facile approach. While it is not generic, in the sense that one may encounter combinations of materials for which no orthogonal solvents can be devised, it is commonly employed either intentionally or because there are no other alternatives with the materials at hand. A good example is the use of a PEDOT:PSS layer spincoated from polar solvents such as water followed by another layer spincoated from an organic solvent such as dichlorobenzene.[2] Cross-linking has been employed only rarely as the possibility for cross-linkage has to be engineered into the material. One of the best known examples involved the use of solubilizing sidechains containing an oxetane group that can be cross-linked by a ring opening polymerization.[3] The last approach involving solubilizing groups that can be removed after the film is prepared is the most appealing from the solar cell point of view since all the advantages of solution processing are available up until the film has been produced. After the film has been prepared the side chains take up a considerable part of the volume of the film and are passive in terms of carrier transport and light absorption. There are obvious challenges in controlling the purity, structure and morphology of the film material after the removal of the solubilizing groups but it is reasonable to assume that these can be overcome. The most

Table 1. List of TGA Data for 6a−m, 8b−d, 8i−l

compound	ester elimination (°C)	weight loss (%) calculated	found
6a	410[a]	23.7	36
6b	333	26.7	25
6c	325	31.8	34
6d	332	26.7	25
6e	360[a]	21.1	22
6f[b]		22.4	
6g	326[a]	20.1	17
6h	300[a]	22.9	15
6i	266	27.8	18
6j	225	26.7	26
6k	197	20.1	18
6l	246	19.7	10
6m[b]		22.4	
8b	329	24.0	25
8c	325	28.9	28
8d	325	24.0	24
8i	254	25.6	15
8j	225	24.0	21
8k	206	18.0	8
8l	*c*	17.6	6

[a] Molecule decomposes at first inflection. [b] Insufficient TGA data. [c] Broad derivative peak with no maximum (see Supporting Information).

* Corresponding author. E-mail: frederik.krebs@risoe.dk.

10.1021/ma801932a CCC: $40.75
Published on Web 11/07/2008

Table 2. Photovoltaic Parameters of the Materials Reported with and without Thermocleavage[a]

polymer	J_{sc} (mA/cm^2)	V_{oc} (V)	FF	PCE (%)	cleaving temp (°C)[b]	solubility in DCB
8b	1.52	0.14	0.25	0.05	25	easy to dissolve
	0.41	0.16	0.26	0.017	310	
8c	2.1	0.4	0.29	0.25	25	hard to dissolve
	0.36	0.14	0.27	0.013	310	
8d	2.55	0.41	0.29	0.3	25	easy to dissolve
	0.24	0.08	0.26	0.005	310	
8j	2.4	0.46	0.36	0.4	25	easy to dissolve
	1.94	0.4	0.33	0.25	230	

[a] The devices had a glass/ITO/PEDOT:PSS/polymer:PCBM/Al geometry and the performance was recorded immediately after preparation in the ambient atmosphere (1000 W m^{-2}, AM1.5G, 72 ± °C, humidity 30 ± 5% rh). [b] The duration of cleaving at 230 °C was 1 min and at 310 °C was 10 min.

Scheme 1. Synthesis of the Dithienylthienopyrazines 6a−m and the Polymers 8b−d, 8i−l with Thermocleavable Benzoate Esters Substituted on the Pyrazine Ring[a]

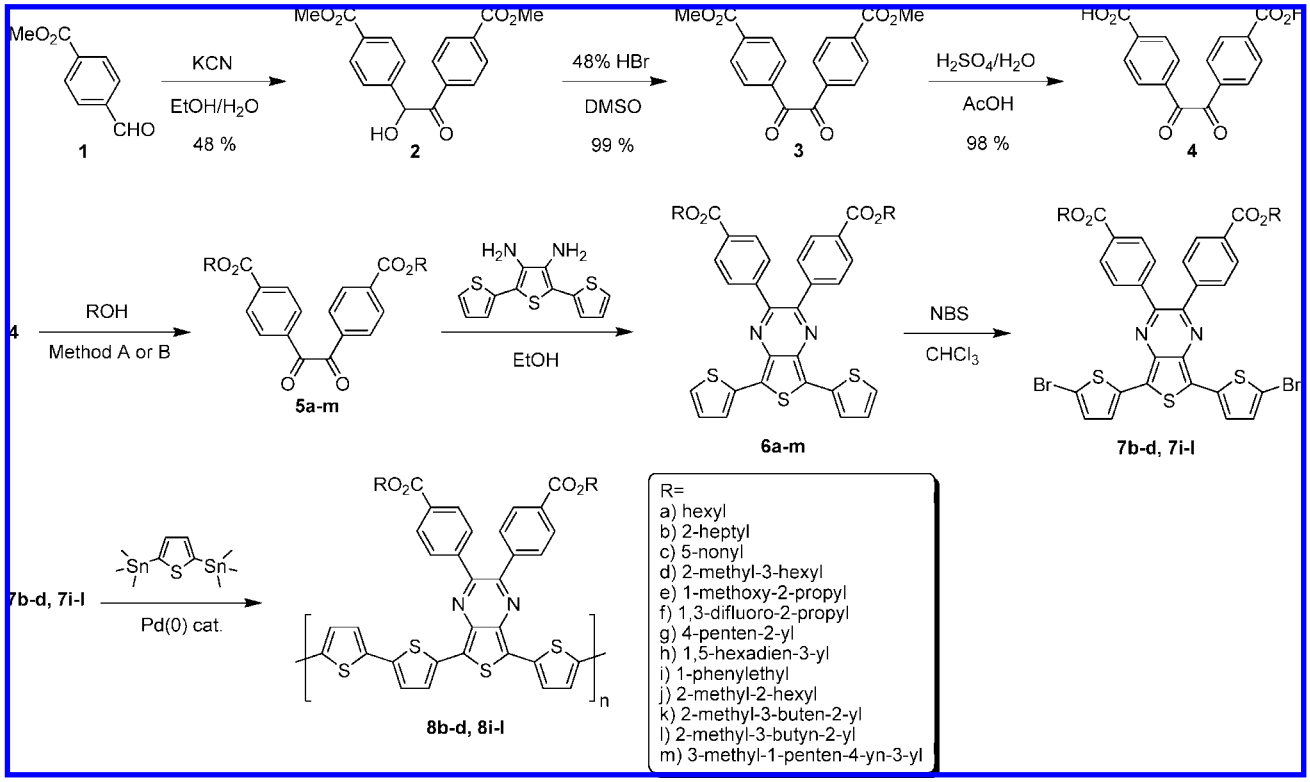

[a] Method A: 1,1′-carbonyldiimidazole, pyridine. Method B: DMAP, Sc(OTf)$_3$, *N,N*′-diisopropylcarbodiimide.

recent developments are the thermocleavable ester groups[4] and the dithiocarbamate precursor route.[5] The thermocleavable ester groups have been explored in the context of polymer solar cells giving stable operation,[6] stable nanostructures[7] and multilayer tandem cells.[8] The use of thermocleavable materials offer several advantages. Most importantly the side chains that constitute a significant proportion of the final film are alleviated and ideally the final film comprises only the active component. Furthermore, in the case of carboxylic esters attached to thiophenes the processing offer removal of the esters at lower temperatures and the acid groups at higher temperatures allowing for multistep processing.[4b] One aim is to achieve as low a temperature of elimination of the ester group as possible and the purpose of this work was to establish this in the context of choice of ester alcohol, mode of preparation of the ester using the monomers for model studies, extending this to the polymers, evaluate these materials in solar cells and finally to establish their stability performance when subjected to different conditions comprising both inert, ambient and model atmospheres presenting either water or oxygen on their own.

Experimental Section

4,4′-Bis(methyloxycarbonyl)benzoin (2). Methyl 4-formylbenzoate (**1**) (50 g, 305 mmol, 1 equiv) was stirred in 99% ethanol (150 mL) and water (50 mL). Potassium cyanide (6 g, 92.1 mmol, 0.3 equiv) was added, and the reaction mixture was stirred at room temperature for 15 min. The product was filtered, washed with water (3 × 200 mL) and dried at 70 °C in vacuum. Yield: 48 g (48%), light yellow solid. M_p = 140−141 °C. ^{1}H NMR (DMSO): δ = 8.09 (d, 2H, J = 8.6 Hz), 8.00 (d, 2H, J = 8.6 Hz), 7.90 (d, 2H, J = 8.3 Hz), 7.55 (d, 2H, J = 8.3 Hz), 6.46 (s, 1H), 6.15 (s, 1H), 3.84 (s, 3H), 3.80 (s, 3H). ^{13}C NMR (DMSO): δ = 199.0, 166.4, 165.9, 145.0, 138.8, 133.7, 129.7, 129.7, 129.6, 129.5, 127.9, 76.2, 52.9, 52.5.

4,4′-Bis(methyloxycarbonyl)benzil (3). To a stirred solution of **2** (74 g, 225 mmol) in DMSO (510 mL) was added slowly 105 mL 48% aqueous hydrobromic acid. The solution was heated to 55 °C for 24 h after which 500 mL water was added and the product was filtered, washed with water (3 × 200 mL) and dried at 70 °C in vacuum. Yield: 72.5 g (99%), yellow solid. M_p = 197−198 °C. ^{1}H NMR ($CDCl_3$): δ = 8.19 (d, 4H, J = 7.5 Hz), 8.06 (d, 4H, J = 7.5 Hz), 3.97 (s, 6H). ^{13}C NMR ($CDCl_3$): δ = 192.9, 165.8, 135.7, 135.5, 130.1, 129.9, 52.7.

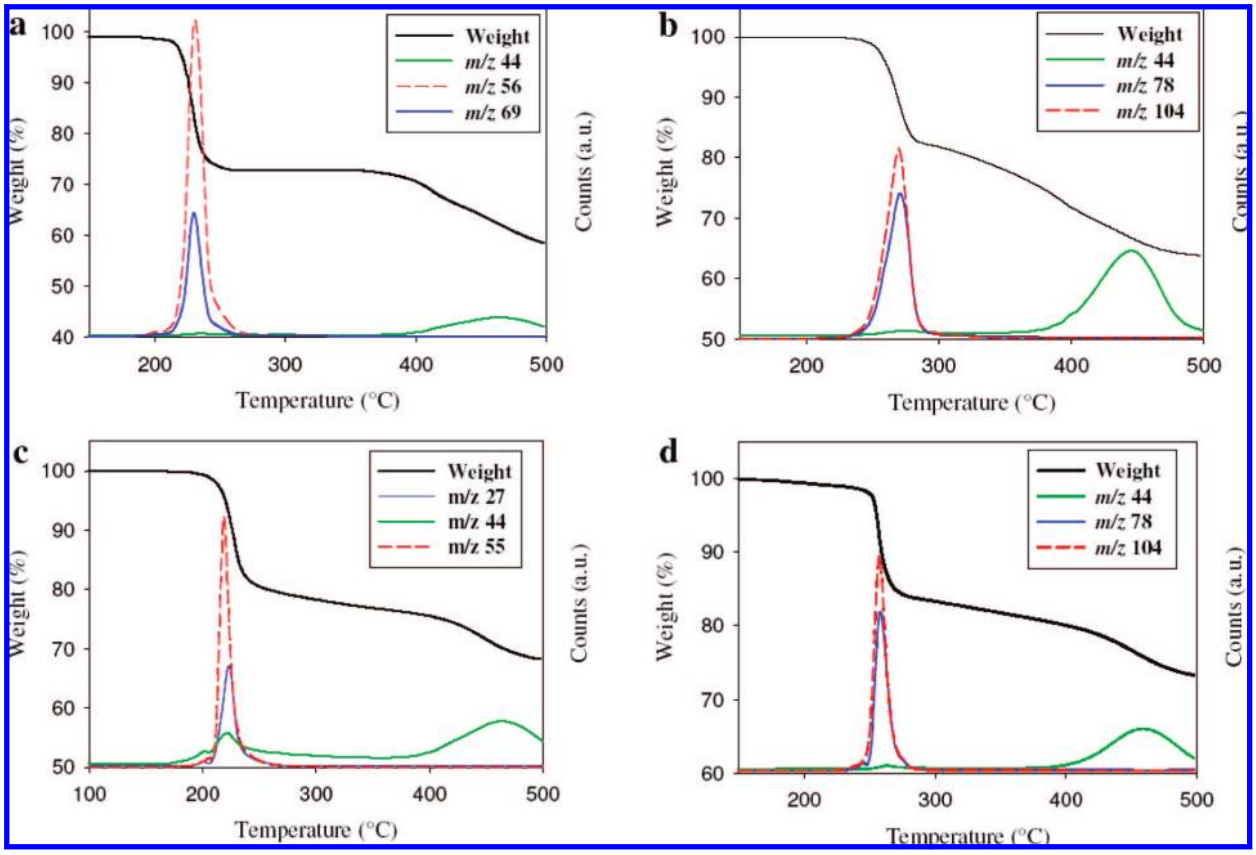

Figure 1. (a) TGA−MS of **6j**, (b) TGA−MS of **6i**, (c) TGA−MS of **8j**, and (d) TGA−MS of **8i**. The first inflection accounts for the ester elimination and the second weight loss around 400−500 °C is decomposition. The red and blue curves correspond to loss of alkenes and the green curves corresponds to loss of carbon dioxide.

4,4′-Bis(hydroxycarbonyl)benzil (4). 3 (5 g, 15.3 mmol) was mixed in acetic acid (350 mL) and a 4:1 H_2SO_4/H_2O solution (175 mL). The reaction mixture was heated to reflux and stirred for 10 h after which 250 mL water was added and the mixture was cooled on ice. After cooling the product was filtered, washed with water (3 × 20 mL) and dried at 70 °C in vacuum. Yield: 4.5 g (98%), pale yellow solid. M_p > 300 °C. ^{1}H NMR (DMSO): δ = 13.54 (s, 2H), 8.15 (d, 4H, J = 7.0 Hz), 8.08 (d, 4H, J = 7.0 Hz). ^{13}C NMR (DMSO): δ = 193.8, 166.8, 136.9, 135.5, 130.5, 130.5.

General Procedure for the Preparation of Primary and Secondary Diesters (Method A). *4,4′-Bis(hexyloxycarbonyl)benzil (***5a***).* **4** (500 mg, 1.68 mmol, 1 equiv) and 1,1′-carbonyldiimidazole (557 mg, 3.44 mmol, 2.05 equiv) were mixed in dry pyridine (5 mL) and stirred at 50 °C under argon for 1 h. 1-Hexanol (439 μL, 3.52 mmol, 2.1 equiv) was added and the reaction mixture was heated to reflux for 10 h. After TLC showed reaction completion the pyridine was evaporated in vacuum. The residue was added saturated $NaHCO_3$ (30 mL) and extracted with ether (3 × 30 mL). The combined organic phase was dried ($MgSO_4$), filtered and concentrated in vacuum. Dry column chromatography (silica gel 15−40 μm, eluted with EtOAc/Heptane, gradient 1−5% EtOAc) afforded **5a**. Yield: 625 mg (80%), yellow solid. M_p = 140−141 °C. ^{1}H NMR ($CDCl_3$): δ = 8.18 (d, 4H, J = 8.5 Hz), 8.05 (d, 4H, J = 8.5 Hz), 4.36 (t, 4H, J = 6.7 Hz), 1.83−1.74 (m, 4H), 1.49−1.39 (m, 4H), 1.39−1.29 (m, 8H), 0.95−0.86 (m, 6H). ^{13}C NMR ($CDCl_3$): δ = 192.9, 165.4, 135.9, 135.7, 130.1, 129.8, 65.9, 31.4, 28.6, 25.6, 22.5, 13.9. HRMS-FAB: *m/z* calcd for $C_{28}H_{35}O_6$ $[M + H]^+$, 467.2434; found, 467.2430.

General Procedure for the Preparation of Tertiary Diesters (Method B). *4,4′-Bis(2-methylhexan-2-yloxycarbonyl)benzil (***5j***).* A suspension of **4** (300 mg, 1.01 mmol, 1 equiv), DMAP (258 mg, 2.11 mmol, 2.1 equiv), scandium triflate (49.5 mg, 0,101 mmol, 0.1 equiv) and 2-methyl-2-hexanol (302 μL, 2.11 mmol, 2.1 equiv) in dry methylene chloride (5 mL) was stirred at room temperature under argon for 30 min. *N*,*N*′-Diisopropylcarbodiimide (331 μL, 2.11 mmol, 2.1 equiv) was added and the reaction mixture was heated to reflux and stirred for 24 h. The reaction mixture was concentrated on celite in vacuum. Dry column chromatography (silica gel 15−40 μm, eluted with EtOAc/Heptane, gradient 1−5% EtOAc) afforded **5j**. Yield: 388 mg (78%), yellow oil. ^{1}H NMR ($CDCl_3$): δ = 8.08 (d, 4H, J = 8.5 Hz), 7.99 (d, 4H, J = 8.5 Hz), 1.92−1.80 (m, 4H), 1.55 (s, 12H), 1.42−1.25 (m, 8H), 0.94−0.82 (m, 6H). ^{13}C NMR ($CDCl_3$): δ = 193.1, 164.2, 137.5, 135.5, 129.9, 129.6, 84.4, 40.6, 26.1, 26.0, 22.9, 13.9. HRMS-FAB: *m/z* calcd for $C_{30}H_{39}O_6$ $[M + H]^+$, 495.2747; found, 495.2735.

General Procedure for the Condensation. *Bis(2-methylhexan-2-yl) 4,4′-(5,7-Di(thiophen-2-yl)thieno-[3,4-b]pyrazine-2,3-diyl)dibenzoate (***6j***).* **5j** (567 mg, 1.15 mmol, 1 equiv), [2,2′;5′,2″]terthiophene-3′,4′-diamine hydrochloride (397 mg, 1.26 mmol, 1.1 equiv) and triethylamine (3.44 mmol, 0.480 mL, 3 equiv) was mixed in 99% ethanol (20 mL). The reaction mixture was heated to reflux and stirred for 15 h. After the reaction was complete the mixture was cooled on ice followed by filtration of the product. The product was washed with 99% ethanol (3 × 5 mL) and dried at 50 °C in vacuum.Yield: 730 mg (86%), dark purple solid. M_p = 197−198 °C. ^{1}H NMR ($CDCl_3$): δ = 7.97 (d, 4H, J = 8.3 Hz), 7.67−7.60 (m, 6H), 7.40 (dd, 2H, J = 5.1, 1.0 Hz), 7.11 (dd, 2H, J = 5.1, 3.7 Hz), 1.96−1.86 (m, 4H), 1.60 (s, 12H), 1.44−1.34 (m, 8H), 0.94 (t, 6H, J = 6.9, 6.9 Hz). ^{13}C NMR ($CDCl_3$): δ = 165.0, 151.3, 142.6, 137.3, 134.5, 132.4, 129.8, 129.3, 127.3, 126.9, 125.6, 124.9, 83.7, 40.8, 26.2, 26.1, 23.0, 14.0. HRMS-FAB: *m/z* calcd for $C_{42}H_{44}N_2O_4S_3$ $[M + H]^+$, 736.2463; found, 736.2466.

General Procedure for the NBS Bromination. *Bis(2-methylhexan-2-yl) 4,4′-(5,7-Bis(5-bromothiophen-2-yl)thieno[3,4-b]pyrazine-2,3-diyl)dibenzoate (***7j***).* **6j** (1 g, 1.36 mmol, 1 equiv) was dissolved in dry chloroform (70 mL). Then NBS (483 mg, 2.71 mmol, 2 equiv) was added slowly and the reaction mixture was stirred at room temperature in the dark for 20 min. After completed reaction

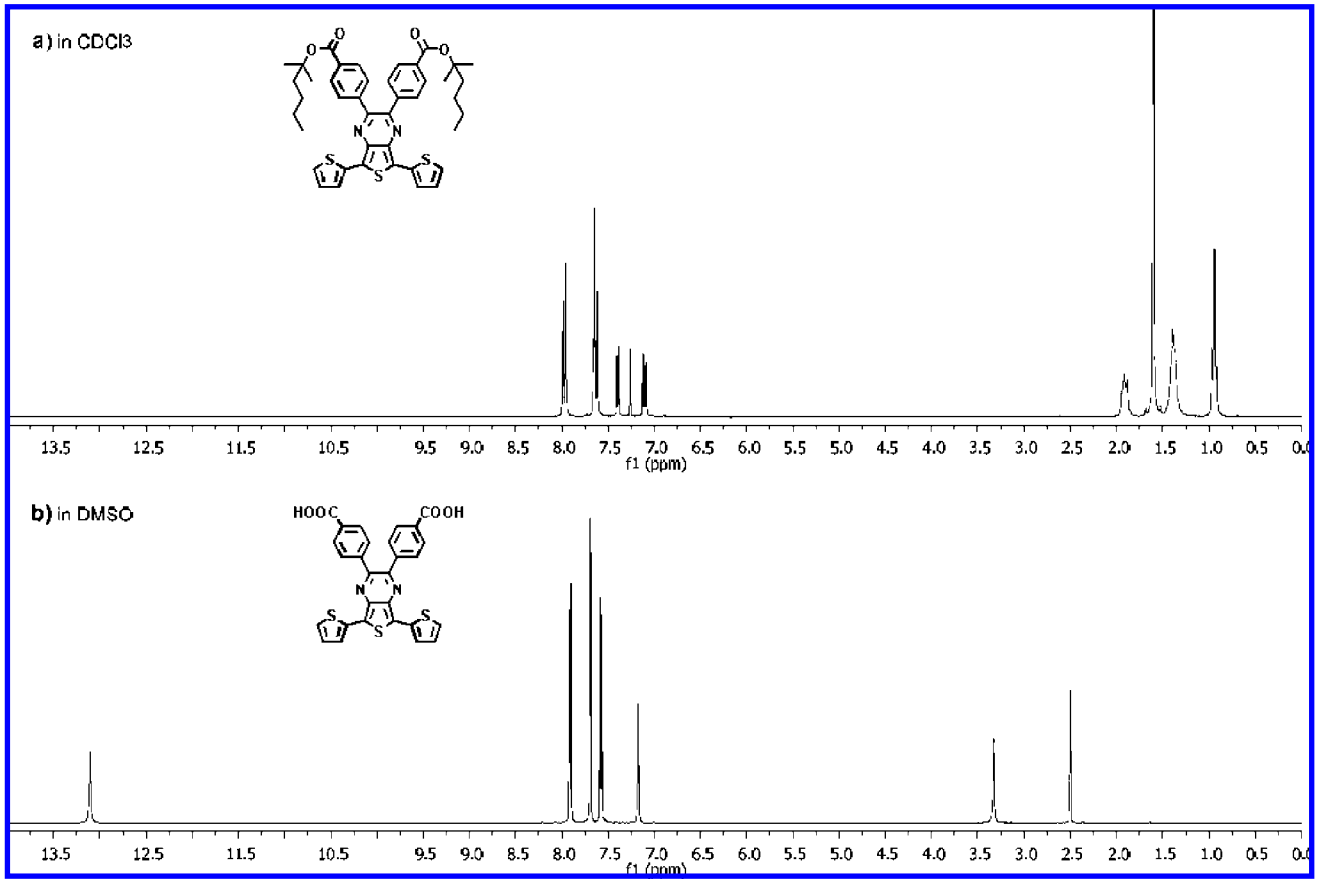

Figure 2. ^{1}H NMR spectra of **6j** (a) from before and after (b) heating to 233 °C for 30 min under argon.

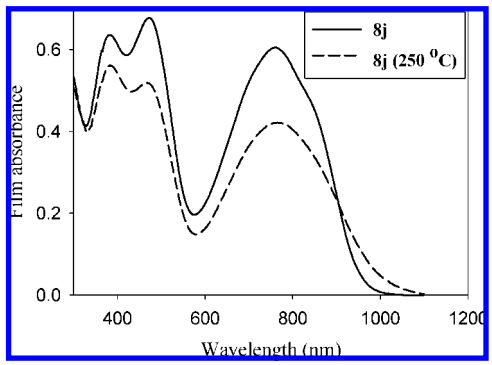

Figure 3. UV−vis for a spincoated film of **8j** on a glass substrate as measured in a transmission geometry. The spectrum for the thermocleaved film is also shown (heated to 250 °C for 1 min).

the mixture was washed with water (3 × 50 mL), dried ($MgSO_4$), filtered and concentrated in vacuum affording **7j**. Yield: 1.13 g (93%), dark purple solid. M_p = 185−186 °C.

^{1}H NMR ($CDCl_3$): δ = 7.98 (d, J = 8.4 Hz, 4H), 7.58 (d, J = 8.4 Hz, 4H), 7.22 (d, J = 4.0 Hz, 2H), 7.01 (d, J = 4.0 Hz, 2H), 1.97−1.87 (m, 4H), 1.61 (s, 12H), 1.46−1.33 (m, 8H), 0.94 (t, J = 7.0 Hz, 6H). ^{13}C NMR ($CDCl_3$): δ = 165.1, 152.0, 142.1, 137.3, 135.6, 132.7, 129.9, 129.8, 129.3, 124.8, 124.3, 115.1, 83.8, 40.8, 26.2, 26.1, 23.0, 14.0.

General Procedure for the Stille Coupling Polymerization. *Poly{bis(2-methylhexan-2-yl) 4,4′-(5-(2,2′-bithiophen-5-yl)-7-(thiophen-2-yl)thieno[3,4-b]pyrazine-2,3-diyl)dibenzoate} (8j).* **7j** (200 mg, 0.22 mmol, 1 equiv), 2,5-bis(trimethylstannyl)thiophene (92 mg, 0.22 mmol, 1 equiv), Pd_2dba_3 (20 mg, 0.022 mmol, 0.1 equiv) and tri(o-tolyl)phosphine (54 mg, 0.18 mmol, 0.8 equiv) was dissolved in dry toluene (50 mL). The reaction mixture was heated to reflux for 24 h under argon. Then the mixture was poured into 150 mL methanol and the polymer was allowed to precipitate. Finally the polymer **8j** was filtered and purified by Soxhlet extraction with MeOH,hexane and $CHCl_3$. Yield: 169 mg (92%), dark green solid. ^{1}H NMR (CD_2Cl_2): δ = 8.18−6.37 (m, 14H), 2.30−0.45 (m, 30H). SEC ($CHCl_3$): M_w = 39429, M_n = 20410, M_p = 17839, and PD = 1.932.

Thermal Analysis. The sample holders were carefully weighed and the samples introduced followed by drying for 24 h at 50 °C in vacuum. The thermogravimetric analysis was then carried out using heating rate of 10 °C min^{-1}. The carrier gas used was argon and the exhaust gases were passed through a mass spectrometer allowing for the simultaneous acquisition of mass data. A series of masses relevant to the degradation process were specifically followed such as CO_2, alkyl chain fragments and fluorine when relevant (see Supporting Information for each material).

Solar Cell Preparation. Glass substrates with pre-etched 100 nm thick layer of ITO and a sheet resistivity of 8−12 Ω square^{-1} purchased from LumTec were cleaned by consecutive ultrasonication in isopropanol and distilled water for 10 min each followed by drying immediately prior to use. A layer of PEDOT:PSS purchased from Aldrich as a 1.3 wt % aqueous solution was spin coated on top of ITO at a rotational speed of 2800 rpm and the slides were annealed at 160 °C for 5 min. Subsequently, the samples were transported into a glovebox and the active layer was applied as a blend of the polymer and [60]PCBM in a 1:1 ratio (20 mg mL^{-1} in dichlorobenzene) by spin coating onto the glass/ITO/PEDOT:PSS substrates. The samples were then dried at room temperature (25 °C) or heated to the desired cleaving temperature (see Tables 1 and 2). An aluminum metal electrode was evaporated on top after the thermal annealing to complete the devices. The devices had an active area of 3 cm^2 and were tested for photovoltaic performance and stability.

Device Characterization. The photovoltaic performance was tested under a solar simulator (KHS575) where the irradiance and emission spectrum were observed using an optical spectrum

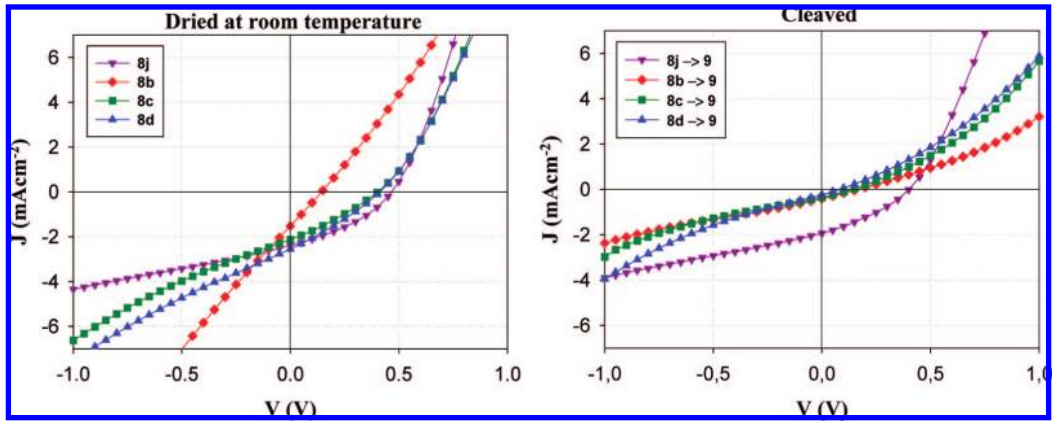

Figure 4. IV-curves for the different polymers uncleaved (left) and cleaved (right). The polymers **8b**, **8c**, and **8d** were cleaved at 310 °C for 10 min and the polymer **8j** was cleaved at 230 °C for 1 min.

Table 3. Summary of the Ranges of Performance Obtained for All Polymers (8b, 8c, 8d and 8j) in Pristine and Thermocleaved Form (1000 W m^{-2}, AM1.5G, 72 ± °C, Humidity 30 ± 5% rh)

J_{sc} (mA cm^{-2})	V_{oc} (V)	FF	PCE (%)	cleaving temp (°C)
1.52−2.55	0.14−0.46	0.25−0.36	0.05−0.4	25
0.24−1.94	0.08−0.4	0.26−0.33	0.005−0.25	230−310

Scheme 2. Thermocleavage of the the Polymer Materials 8b, 8c, 8d, or 8j All Lead to the Same Polymer Material 9

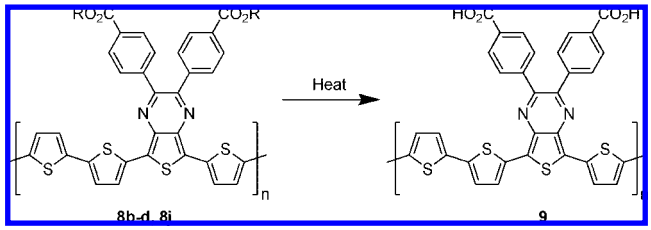

analyzer in conjunction with a precision radiometer from Eppley Laboratories. The spectrum during characterization of the solar cell efficiency was AM1.5G with an incident light power of 1000 W m^{-2}. The solar simulator is Class AAA from 400−800 nm, over the area of the cell and for the duration of the experiment. No corrections for mismatch were performed.

Stability Measurements. The stability measurements were performed in a stainless steel chamber[6f] with quartz windows and controlled atmosphere. Four different atmospheric conditions were applied to the chambers by continuously introducing the following gas mixtures: (1) nitrogen atmosphere 99.999% (oxygen <2 ppm, humidity <2 ppm); (2) dry oxygen atmosphere 99.5% (humidity <2 ppm); (3) ambient atmosphere (20 ± 5% relative humidity); (4) humid nitrogen 99.999% (oxygen <2 ppm, 95 ± 5% relative humidity). The main impurity in the 99.5% pure oxygen is nitrogen. The temperature during all experiments was 30 ± 2 °C and the incident light intensity was 330 W m^{-2}. The setup is automated and employ IV-measurements at intervals of 10 min using a Keithley 2400 through a switch matrix based on a Keithley 7705 contained in a Keithley 2700.[6f]

Results and Discussion

Synthesis. The synthetic steps involved in the preparation of the dithienylthienopyrazines with thermocleavable esters are outlined in Scheme 1. The benzils **5a**−**m** were made by a four step synthetic sequence employing a standard benzoin condensation of methyl 4-formylbenzoate (**1**) and potassium cyanide. The reaction was very fast and no heating was required. The insoluble benzoin **2** was oxidized using 48% aqueous hydrobromic acid in dimethyl sulfoxide[9] affording the benzil **3** that was then hydrolyzed in an aqueous acid to give the diacid **4**. The esterifications of the primary and secondary esters **5a**−**i** employed 1,1′-carbonyldiimidazole as the acylating agent (method A). Tertiary esters are notoriously difficult to synthesize and a series of techniques were attempted. Transformation of **4** into the diacid chloride followed by direct reaction with the tertiary alcohols (2-methyl-2-hexanol, 2-methyl-3-buten-2-ol, 2-methyl-3-butyn-2-ol, 3-methyl-1-penten-4-yn-3-ol) or by adding freshly precipitated AgCN[10] was ineffective. Other acylating agents such as 2,2′-dipyridyl disulfide/PPh$_3$,[11] 2-chloro-1-methylpyridinium iodide[12] and 2-chloro-3,5-dinitropyridine[4a] all failed. The latter method has proven useful for monoesterification albeit in low yield that makes its use impractical for diesterification. A procedure reported by Zhao et al.[13] turned out to work efficiently. The method employs a catalytic amount of scandium triflate in combination with *N*,*N*′-diisopropylcarbodiimide and DMAP (method B). Very good yields of the tertiary diesters **5j**−**m** (78−81%) were obtained. Finally, the diphenyldithienyl thienopyrazines **6a**−**m** were prepared by a known procedure[14] where the benzils **5a**−**m** were condensed with [2,2′;5′,2″]terthiophene-3′,4′-diamine.[15] The polymers of **6b**−**d** and **6i**−**l** were also made. Activation of the monomers was done by a NBS bromination and was followed by a Stille coupling polymerization with 2,5-bis(trimethylstannyl)thiophene giving **8b**−**d** and **8i**−**l**.

Thermal Behavior. The relative stability of the dithienylthienopyrazines with thermocleavable benzoate esters substituted on the pyrazine ring, **6a**−**m**, was investigated by thermogravimetric analysis (TGA) and thermogravimetric analysis in conjunction with mass spectrometry of the carrier gas (TGA−MS) in the temperature range 50−500 °C (Table 1). The thermogravimetric data in table 1 are consistent with earlier pyrolysis studies of esters.[16] As expected elimination of an alkene from the tertiary diesters **6j**−**l** take place at lower temperatures than the secondary diesters **6b**−**i**. The primary diester **6a** eliminated with decomposition at a significantly higher temperature. The presence of an inductively (σ bond) electron withdrawing β substituent on the alcohol is known to slow down the rate of ester pyrolysis.[17] **6e** eliminate at 360 °C which is 35 °C higher than the elimination temperature of **6c** that bears a β alkyl substituent.

A double bond substituent at the β carbon can reduce the elimination temperature moderately as observed by comparing **6g** with **6b** and **6d**. **6h** eliminates hexatriene at around 300 °C which is approximately 25 °C lower compared to **6c**. We ascribe this to an activation of the adjacent C$_\beta$−H bond that assist the elimination. The double bond substituents apparently contribute to other reactions (weight losses) at the higher temperatures as **6g** and **6h** decompose at the elimination temperatures. Furthermore, we observed that **6e**, **6h**, and **6m** showed a slight weight

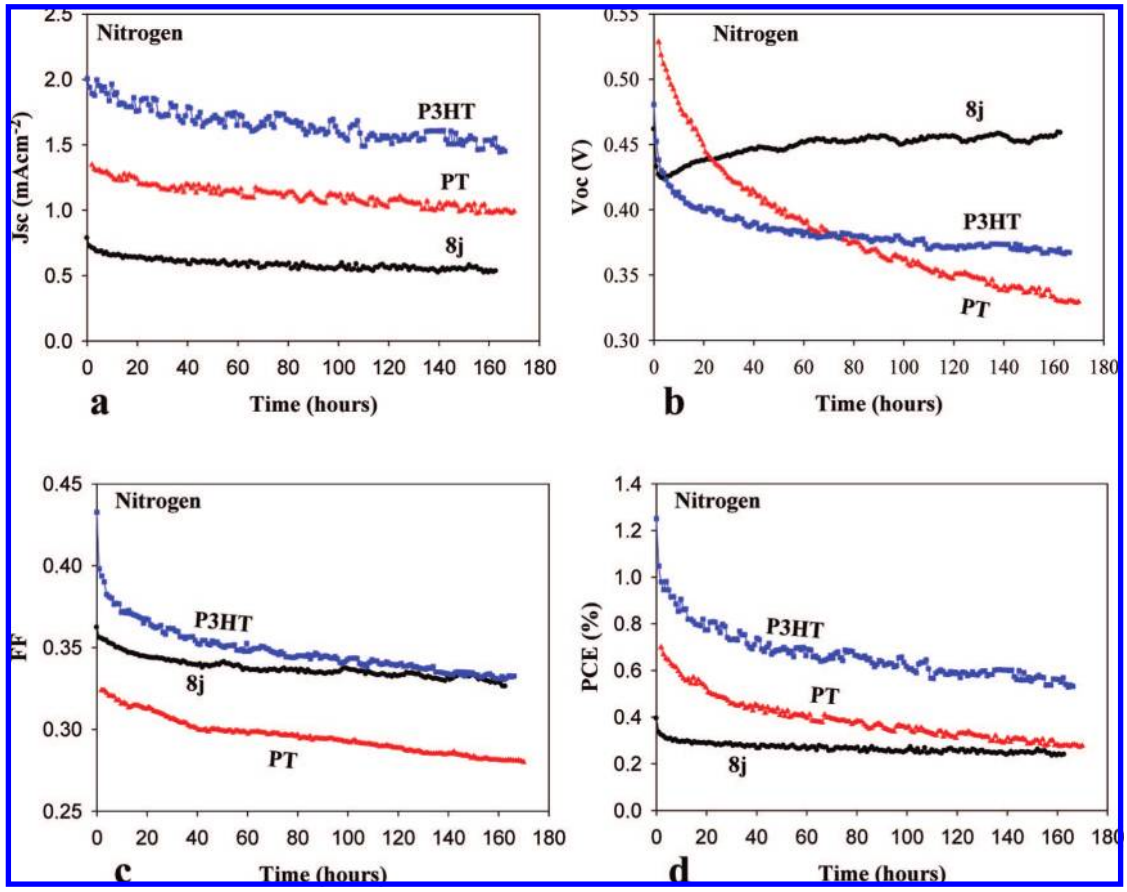

Figure 5. Comparison of the decay of the photovoltaic parameters for P3HT, PT, and **8j** polymers with a Glass/ITO/PEDOT:PSS/polymer:PCBM/Al device geometry in a nitrogen atmosphere (330 W m^{-2}, 30 °C, oxygen <2 ppm, water <2 ppm).

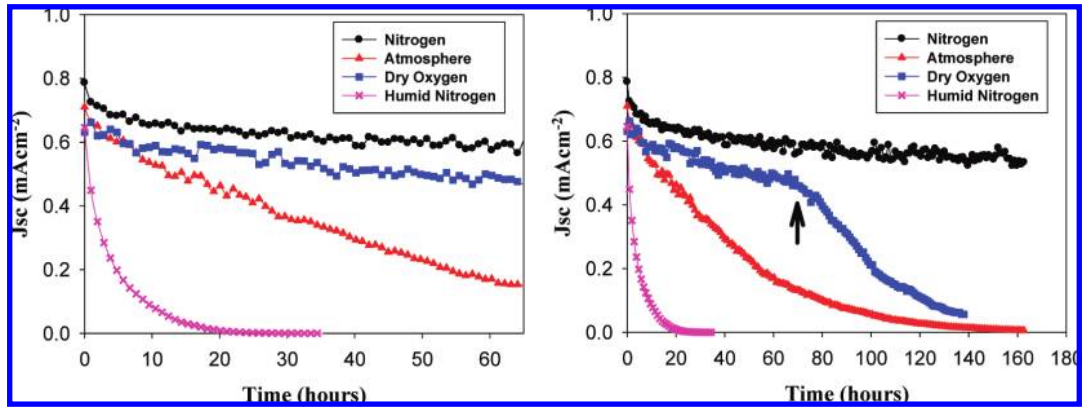

Figure 6. Decay of devices with configuration Glass/ITO/PEDOT:PSS/**8j**:PCBM/Al under conditions of: pure nitrogen atmosphere 99.999% (oxygen <2 ppm, humidity <2 ppm), dry oxygen atmosphere 99.5% (humidity <2 ppm), ambient atmosphere (20 ± 5% relative humidity), humid nitrogen 99.999% (oxygen <2 ppm, 95 ± 5% relative humidity). The temperature was 30 ± 2 °C and the incident light intensity was 330 W m^{-2} (left). The same experiment was repeated for a longer period of time while introducing ambient atmosphere after 70 h (see arrow) thus reducing the oxygen level by a factor of 5 and increasing the humidity by a factor of 10^5 whereupon rapid degradation sets in thereafter (right).

loss at low temperatures. We found no identifiable mass peaks corresponding to the solvent and also rule out the possibility for solvent loss as the samples were dried prior to analysis in a vacuum oven at 50 °C for 24 h. It is possible that these materials are subject to chemical reactions in the solid state (ie. a Cope reaction for **6h** and **6m** or elimination of methanol for **6e**). We currently have no explanation for these observations other then it being an elimination reaction or an electrocyclic reaction followed by an elimination reaction giving fragments that we did not observe in our mass spectra. **6i** has a 1-phenylethyl ester where the π bonded substituent contributes to the activation of the adjacent C_β−H. It has a simple TGA curve where the first inflection is responsible for the elimination of styrene (Figure 1). The phenyl substituent decrease the temperature for the first weight loss even further compared to **6g** and **6h.**

The tertiary diesters **6j**−**l** eliminate in the temperature range 197−246 °C. **6k** eliminates at a lower temperature compared to **6j** which may arise from the double bond activation as described above. **6l** eliminate 14 °C higher compared to **6j** and we conclude that a triple bond is not as activating as the double bond in this position (α carbon). The observed weight loss for the compounds **6g**, **6h**, **6i**, **6k**, and **6l** all show weight loss at the first inflection which is significantly lower than the calculated

value. Since all these fragments have multiple unsaturations after the elimination we ascribe this to polymerization reactions of these materials in the matrix of the material or to cross-linking. Analysis of the materials after the first weight loss by NMR was used to establish whether the ester could be used efficiently as a solubilizing group that can be removed quantitatively by a simple thermal treatment (Figure 2). NMR analysis after heating compound **6a**−**m** at the temperature of the first weight loss for 15 min. under argon showed that compounds **6a**, **6e**−**h**, **6m** could not be used for the preparation of the diacid. While the esters may eliminate liberating an alkene the materials also decompose at the given temperature. The ^{1}H NMR spectra of **6j** from before and after the pyrolysis clearly shows that the diester has been transformed into the diacid (Figure 2). Spectrum b in Figure 3 shows no aliphatic protons and the protons from the carboxylic acid appear at 13.08 ppm. From the TGA−MS data it was possible to track evolution of various small molecules and fragments as a function of the temperature. As expected the signals for the observed fragments peak in the same temperature range as the weight losses. The mass signals that we focused on were carbon dioxide and fragments for even and uneven alkenes. As shown earlier[4b] for tertiary esters of polythiophene several weight loss mechanisms may be observed and the advantage of studying the monomer was that the effects of the polymer matrix on the weight loss mechanisms were possibly eliminated.

The primary ester showed loss of both alkene and carbon dioxide starting at around 300 °C peaking at around 400 °C. For the secondary alkyl esters two loss mechanisms could be distinguished as elimination of the ester at the lower temperature (around 300 °C) and loss of carbon dioxide at a higher temperature (425 °C). The weight loss of the secondary alkyl esters corresponded well with the calculated loss while some decarboxylation was evident from a small mass peak of carbon dioxide during the first loss peak. The secondary esters with unsaturations, branching, fluorine and methoxy substituents showed more complex weight loss curves. It would seem that the only useful materials in this series are the simple secondary and tertiary esters. In terms of achieving a lower temperature for the thermocleavage this limits the choice to simple tertiary esters. The only secondary ester that works well is the ester with a phenyl group α to the alcohol and no other unsaturations. As discussed above the simplest secondary alcohol with an α-phenyl group gives styrene upon elimination and this gave an incomplete weight loss. While successfully achieving a lower temperature of elimination this alone does not grant usefulness. The elimination reaction also has to complete the weight loss and the polymer material that is the end product should be insoluble.

Polymers. The polymerization of the monomer materials was achieved through selective bromination of **6b**−**d** and **6i**−**l** using NBS to give **7b**−**d** and **7i**−**l**. These monomers were then polymerized by Stille cross coupling using bis(2,5-trimethylstannyl)thiophene. This gave the polymers **8b**−**d** and **8i**−**l** in good yield. The polymer materials had a low band gap as expected. A major requirement for processing into thin films is that the polymer materials are soluble in organic solvents. While the thermal behavior could be studied for all the polymers, not all of them had a good solubility. The molecular weights for the materials were in the 40000−70000 g mol^{-1} range and the polydispersity was around 2 as expected (see Supporting Information). The only polymers that were readily soluble, could be analyzed, processed into thin films and showed a useful thermal behavior were thus **8b**, **8c**, **8d**, and **8j**.

Only **8j** could be cleaved at an acceptably low temperature. The UV−vis spectrum of a film of **8j** spincoated from chlorobenzene is shown in figure 3. A film absorbance of 1 was easily reached with a very good film quality. The color of the film is olive green and the band gap of **8j** in the film was estimated from the crossing point of the tangent on the absorption edges[18] and was 950 nm or 1.3 eV. The observed band gap is as expected from earlier studies on the same polymer backbone[14] and similar polymers.[19] Upon thermocleavage of the film by heating it at 250 °C for 1 min a color change is observed whereby the film changes to a more brown color. The associated changes in the absorption spectrum are a less intense absorption and a smaller band gap with a band gap of 1010 nm or 1.2 eV. There may be several explanations for the lower absorption intensity.

First, the associated change in film thickness and dielectric constant may lead to changes in the reflection phenomena that also contribute to the intensities in the observed absorption spectrum for a solid film in a transmission geometry. Second, the intensity of absorption quite often decreases as the band gap is lowered. After the short thermal treatment the film maintained the optical quality and was completely insoluble in organic solvents.

Photovoltaic Performance. All of the polymer materials presented in Scheme 1 were intended for use in solar cell devices. Some of the polymer materials however were not very soluble and did not process well into films and the photovoltaic performance obtained for these were either not possible to establish or very poor. Consequently only **8b**, **8c**, **8d**, and **8j** were studied in solar cells. The devices were prepared in duplicate and were after spincoating of the active layer either processed directly into a solar cell by evaporation of the aluminum electrode or subjected to a thermal treatment at the temperature of thermocleavage immediately before evaporation of the aluminum electrode. The results obtained are shown in table 2.

A general observation was that the devices performed significantly worse after thermocleavage as indicated by a decrease in voltage and current. Some examples of IV-curves for uncleaved and cleaved devices are shown in figure 4 (see also Supporting Information). The best performing material was **8j**, which show a decreased performance upon thermocleavage, but maintained a significant performance. We chose to repeat the preparation of devices based on all polymers and obtained results in the ranges outlined in table 3.

It should be noted that polymer solar cells based on thermocleavable materials present additional complexity in terms of processing as compared to materials such as P3HT. In the case of P3HT heating of the device film leads to crystallization and changes in the morphology of the device film that significantly influences the device performance. In the case of thermocleavable materials these effects also take place, but in addition, the chemistry of the device film change and as the chemistry changes so do the processes relating to crystallization and changes in morphology. This has been observed in the case of P3MHOCT where the chemistry of the device film can be processed into three distinct forms starting from the same device film.[4b,20] This allowed for the preparation of devices with a PCE of up to 1.5%.[20]

This implies that not only the temperature of thermal annealing and the duration but also the speed of heating becomes influential. In the case of the polymers presented here the polymer esters (**8b**, **8c**, **8d**, or **8j**) are all chemically different materials. Heating them to the temperature of thermocleavage gives, in principle, the same product as polymer **9** (Scheme 2). The difference in device performance is thus not related to the molecule but rather how the final device film was obtained. Thus the same material can present different levels of performance depending on how it was processed. The chemistry of the sidechains may influence the morphology before thermocleav-

age, and if the process of thermocleavage is faster than the changes in morphology upon heating, this may also allow for the preparation of different final film morphologies. It has been shown that the morphology is stable in the final thermocleaved form when using a temperature of thermocleavage[7] below T_g and the kinetics of the film formation in such a case is important. A final issue is the completion of the thermocleavage in the final film. It is likely that thermocleavage under a given set of conditions lead only to a partially cleaved film that then present chemistry corresponding to both the uncleaved and cleaved material to varying degrees.[20] In the experiments performed here the films were completely cleaved and a detailed study of varying the degree of thermocleavage warrants further study.

In Figure 4, the performance of some of the devices are shown as IV-curves in the cleaved and uncleaved state. The drastic decrease of the performance for polymers **8b**, **8c** and **8d** is probably due to high cleaving temperature (310 °C) and long cleaving time (10 min), while thermocleavage of **8j** resulted in very little decrease of performance. In the case of earlier reported cleaving of P3MHOCT the performance dropped around 10-fold when cleaved to P3CT and then improved 15-fold when cleaved further to PT.[20]

Stability Studies. We chose to subject the best performing material **8j** to detailed stability studies. Polymer solar cells are inherently unstable under intense illumination and will degrade through a large number of coexisting paths. Some of the paths involve reactants such as water and oxygen from the atmosphere that will dominate the course of degradation if allowed to access the active layer during operation. Their efficient removal efficiently eliminates the associated degradation processes, and other slower processes become readily observable (ie. morphological changes, interlayer diffusion, reactions at interfaces, photochemistry). To get an overview of the stability of the **8j** in relation to other known polymers and as a function of atmospheric reactants we performed two studies. One comparative study in an inert atmosphere and a study where devices were subjected to different atmospheres during continuous (uninterrupted) illumination.

Figure 5 shows the degradation of devices prepared in the same manner employing respectively P3HT, PT, and **8j**. The performance of **8j** is inferior to both P3HT and PT while the photovoltaic parameters are much more stable in time. The P3HT device was annealed at 150 °C for 5 min after evaporation of the aluminum electrode. PT devices were prepared by heating P3MHOCT−PCBM films to 310 °C before evaporation of the aluminum electrode. The decay in the photovoltaic parameters were not affected significantly by the thermocleavage at 230 °C and the stability of **8j** is thus concluded to be very good without cleavage while there are processing advantages of thermocleaved **8j**. Cleaving **8j** at a higher temperature (310 °C) reduced the photovoltaic performance drastically and the decay of V_{oc} and FF was much faster.

When subjecting **8j** devices to four different atmospheres to establish the inherent stability in nitrogen and the effect of water and oxygen taken separately and finally in combination in the real atmosphere it was found that oxygen had little effect on the stability as shown in Figure 6. The interesting finding was that the presence of pure oxygen at high concentration (i.e., five times more than in the ambient atmosphere) does not seem to speed up degradation significantly and we would rate **8j** as stable toward oxygen under illumination. Humidity however was found to profoundly influence the stability leading to rapid degradation that is complete within less than 20 h whereas the absence of water leads to moderately stable operation.

Conclusion

In conclusion, the application of esters as solubilizing groups that allow for removal by a simple thermal treatment is limited to simple secondary and tertiary esters where the alcohol is saturated in order to ensure that the alkene that is eliminated is removed efficiently without undesired side reactions. The lowest temperatures of elimination were found to be achieved when employing tertiary esters as expected. In contrast to the systems where the ester reside on a thiophene ring we found that no decarboxylation takes place prior to decomposition, and it is thus not possible to access the native system without the carboxylic acid groups by a thermal treatment. We showed that a monomer relevant to low band gap polymer systems could be prepared with solubilizing groups that allow for removal by a thermal treatment of around 200−225 °C. We further prepared the polymer materials from the monomers and found that only the polymers with secondary and tertiary esters are useful and the solubility requirements make the choice of side chain functionality limited. The band gaps of the materials were in the 1.2−1.3 eV range and the operational stability was found to be very good compared to model materials such as P3HT and PT. In addition polymer solar cells in a glass/ITO/PEDOT:PSS/polymer:PCBM/Al were found to be very stable toward oxygen during operation. In pure oxygen the device decay was similar to inert conditions. This is in stark contrast to conjugated materials containing vinylene bonds that are very sensitive toward oxygen. The devices decayed rapidly in the presence of water (with and without oxygen present) and removal of water from this type of device gives devices with stability that exceeds hundreds of hours.

Acknowledgment. This work was supported by the Danish Strategic Research Council (DSF 2104-05-0052 and 2104-07-0022).

Supporting Information Available: Text giving general procedures and characterization data (including structural diagrams) and figures showing TGA and TGA−MS data, NMR spectra, IPCE curves for **8j**, and plots of the photovoltaic response as a function of incident light intensity. This material is available free of charge via the Internet at http://pubs.acs.org.

References and Notes

(1) (a) Günes, S.; Neugebauer, H.; Sariciftci, N. S. *Chem. Rev.* **2007**, *107*, 1324–1338. (b) Bundgaard, E.; Krebs, F. C. *Sol. Energy Mater. Sol. Cells* **2007**, *91*, 954–985. (c) Thompson, B. C.; Fréchet, J. M. J. *Angew. Chem. Int. Ed.* **2008**, *47*, 58–77.

(2) Hadipour, A.; de Boer, B.; Wildeman, J.; Kooistra, F. B.; Hummelen, J. C.; Turbiez, M. G. R.; Wienk, M. M.; Janssen, R. A. J.; Blom, P. W. M. *Adv. Funct. Mater.* **2006**, *16*, 1897–1903.

(3) (a) Barche, J.; Janietz, S.; Ahles, M.; Schmechel, R.; von Seggern, H. *Chem. Mater.* **2004**, *16*, 4286–4291. (b) Müller, C. D.; Falcou, A.; Reckefuss, N.; Rojahn, M.; Wiederhirn, V.; Rudati, P.; Frohne, H.; Nuyken, O.; Becker, H.; Meerholz, K. *Nature* **2003**, *421*, 829–833.

(4) (a) Liu, J. S.; Kadnikova, E. N.; Liu, Y. X.; McGehee, M. D.; Fréchet, J. M. J. *J. Am. Chem. Soc.* **2004**, *126*, 9486–9487. (b) Bjerring, M.; Nielsen, J. S.; Nielsen, N. C.; Krebs, F. C. *Macromolecules* **2007**, *40*, 6012–6013.

(5) (a) Nguyen, L. H.; Günes, S.; Neugebauer, H.; Sariciftci, N. S.; Banishoeib, F.; Henckens, A.; Cleij, T.; Lutsen, L.; Vanderzande, D. *Sol. Energy Mater. Sol. Cells* **2006**, *90*, 2815–2828. (b) Banishoeib, F.; Adriaensens, P.; Berson, S.; Guillerez, S.; Douheret, O.; Manca, J.; Fourier, S.; Cleij, T. J.; Lutsen, L.; Vanderzande, D. *Sol. Energy Mater. Sol. Cells* **2007**, *91*, 1026–1034. (c) Banishoeib, F.; Henckens, A.; Fourier, S.; Vanhooyland, G.; Breselge, M.; Manca, J.; Cleij, T. J.; Lutsen, L.; Vanderzande, D.; Nguyen, L. H.; Neugebauer, H.; Sariciftci, N. S. *Thin Solid Films* **2008**, *516*, 3978–3988.

(6) (a) Krebs, F. C.; Spanggaard, H. *Chem. Mater.* **2005**, *17*, 5235–5237. (b) Krebs, F. C.; Norrman, K. *Prog. Photovolt. Res. Appl.* **2007**, *15*, 697–712. (c) Bjerring, M.; Nielsen, J. S.; Siu, A.; Nielsen, N. C.; Krebs, F. C. *Sol. Energ. Mater. Sol. Cells* **2008**, *92*, 772–784. (d) Krebs, F. C. *Sol. Energ. Mater. Sol. Cells* **2008**, *92*, 715–726. (e) Jørgensen,

M.; Norrman, K.; Krebs, F. C. *Sol. Energ. Mater. Sol. Cells* **2008**, *92*, 686–714. (f) Gevorgyan, S. A.; Jørgensen, M.; Krebs, F. C. *Sol. Energ. Mater. Sol. Cells* **2008**, *92*, 736–745.

(7) Andreasen, J. W.; Jørgensen, M.; Krebs, F. C. *Macromolecules* **2007**, *40*, 7758–7762.

(8) Hagemann, O.; Bjerring, M.; Nielsen, N. C.; Krebs, F. C. *Sol. Energ. Mater. Sol. Cells* **2008**, *92*, 1327–1335.

(9) Floyd, M. B.; Du, M. T.; Fabio, P. F.; Jacob, L. A.; Johnson, B. D. *J. Org. Chem.* **1985**, *50*, 5022–5027.

(10) Takimoto, S.; Inanaga, J.; Katsuki, T.; Yamaguchi, M. *Bull. Chem. Soc. Jpn.* **1976**, *49*, 2335.

(11) Mukaiyama, T.; Matsueda, R.; Suzuki, M. *Tetrahedron Lett.* **1970**, 1901–1904.

(12) Mukaiyama, T.; Usui, M.; Shimada, E.; Saigo, K. *Chem. Lett.* **1975**, 1045–1048.

(13) Zhao, H.; Pendri, A.; Greenwald, R. B. *J. Org. Chem.* **1998**, *63*, 7559–7562.

(14) Petersen, M. H.; Hagemann, O.; Nielsen, K. T.; Jørgensen, M.; Krebs, F. C. *Sol. Energy Mater. Sol. Cells* **2007**, *91*, 996–1009.

(15) Mangeney, C.; Lacroix, J.-C.; Chane-Ching, K. I.; Jouini, M.; Villain, F.; Ammar, S.; Jouini, N.; Lacaze, P.-C. *Chem. Eur. J.* **2001**, *7*, 5029–5040.

(16) Houtman, J. P. W.; van Steenis, J.; Heartjes, P. M. *Recl. Trav. Chim.* **1946**, *65*, 781.

(17) Chuchani, G.; Martín, I.; Hernández, J. A.; Rotinov, A.; Fraile, G. *J. Phys. Chem.* **1980**, *84*, 944–948.

(18) Bundgaard, E.; Krebs, F. C. *Macromolecules* **2006**, *39*, 2823–2831.

(19) (a) Campos, L. M.; Toncheva, A.; Günes, S.; Sonmez, G.; Neugebauer, H.; Sariciftci, N. S.; Wudl, F. *Chem. Mater.* **2005**, *17*, 4031–4033. (b) Wienk, M. M.; Turbiez, M. G. R.; Struijk, M. P.; Fonrodona, M.; Janssen, R.A. J. *Appl. Phys. Lett.* **2006**, *88*, 153511.

(20) Gevorgyan, S. A.; Krebs, F. C. *Chem. Mater.* **2008**, *20*, 4386–4390.

MA801932A

CHEMISTRY OF MATERIALS
Article

Chem. Mater. **2009,** *21,* 4669–4675 4669
DOI:10.1021/cm901937d

Substituted 2,1,3-Benzothiadiazole- And Thiophene-Based Polymers for Solar Cells − Introducing a New Thermocleavable Precursor

Martin Helgesen,*,† Suren A. Gevorgyan,† Frederik C. Krebs,† and René A. J. Janssen‡

†*Risø National Laboratory for Sustainable Energy, Technical University of Denmark, Frederiksborgvej 399, DK-4000 Roskilde, Denmark, and* ‡*Molecular Materials and Nanosystems, Departments of Applied Physics and Chemical Engineering & Chemistry, Eindhoven University of Technology, PO Box 513, 5600 MB Eindhoven, The Netherlands*

Received July 1, 2009. Revised Manuscript Received August 25, 2009

Alkoxysubstituted and unsubstituted 2,1,3-benzothiadiazoles were prepared and copolymerized with substituted and unsubstituted thiophenes using both Stille and Yamamoto cross-coupling reactions. One class of the materials bore thermally labile ester groups. The materials were all found to have a reduced band gap in the range of 1.69−1.75 eV and were explored in polymer photovoltaic devices as mixtures with the soluble fullerene PCBM. High open circuit voltages of up to 0.93 V and power conversion efficiencies (PCE) of up to 2.22% was observed for materials without the thermally labile groups. The thermocleavable materials have the advantage that they are insoluble after a thermal treatment, enabling a larger degree of processing freedom when preparing multilayer devices and they provide a better operational stability for the devices. So far the process of thermocleavage has led to poorer device performance than for the soluble precursor polymers; however, we found processing conditions that lead to a higher performance for the thermocleaved product, where open circuit voltages of up to 0.9 V could be obtained with power conversion efficiencies of up to 0.42%, representing a doubling as compared to the soluble precursor polymer.

Introduction

Encouraging progress has been made over the past few years in the field of photovoltaic solar cells using organic materials. Especially conjugated polymers are an attractive alternative to the traditional silicon-based solar cells because they are strong absorbers of visible light and can be deposited onto flexible substrates over large areas using wet-processing techniques such as spin-coating, printing, or roll-to-roll coating.[1−14] Compared to silicon-based solar cells, polymer photovoltaics are inferior when it comes to power conversion efficiency and stability. However, they offer low production cost, low thermal budget, and a very high speed of processing, which makes them competitive in certain applications. Many reviews and special issues on the topic of polymer solar cells have been published during the past 5 years[3,15−38] and the definitions are quite broad spanning all polymer

*Corresponding author.

(1) Dennler, G.; Lungenschmied, C.; Neugebauer, H.; Sariciftci, N. S.; Labouret, A. *J. Mater. Res.* **2005**, *20*(12), 3224–3233.
(2) Blankenburg, L.; Schultheis, K.; Schache, H.; Sensfuss, S.; Schrodner, M. *Sol. Energy Mater.* **2009**, *93*(4), 476–483.
(3) Krebs, F. C. *Sol. Energy Mater.* **2009**, *93*(4), 394–412.
(4) Krebs, F. C.; Jorgensen, M.; Norrman, K.; Hagemann, O.; Alstrup, J.; Nielsen, T. D.; Fyenbo, J.; Larsen, K.; Kristensen, J. *Sol. Energy Mater.* **2009**, *93*(4), 422–441.
(5) Krebs, F. C. *Sol. Energy Mater.* **2009**, *93*(4), 465–475.
(6) Krebs, F. C.; Alstrup, J.; Spanggaard, H.; Larsen, K.; Kold, E. *Sol. Energy Mater.* **2004**, *83*(2−3), 293–300.
(7) Krebs, F. C.; Spanggaard, H.; Kjaer, T.; Biancardo, M.; Alstrup, J. *Mater. Sci. Eng., B* **2007**, *138*(2), 106–111.
(8) Krebs, F. C. *Sol. Energy Mater.* **2009**, *93*, 1636–1641.
(9) Krebs, F. C. *Org. Electron.* **2009**, *10*, 761–768.
(10) Krebs, F. C.; Gevorgyan, S. A.; Alstrup, J. *J. Mater. Chem.* **2009**, *19*, 5442–5451.
(11) Lungenschmied, C.; Dennler, G.; Neugebauer, H.; Sariciftci, S. N.; Glatthaar, M.; Meyer, T.; Meyer, A. *Sol. Energy Mater.* **2007**, *91* (5), 379–384.
(12) Niggemann, M.; Zimmermann, B.; Haschke, J.; Glatthaar, M.; Gombert, A. *Thin Solid Films* **2008**, *516*(20), 7181–7187.
(13) Tipnis, R.; Bernkopf, J.; Jia, S.; Krieg, J.; Li, S.; Storch, M.; Laird, D. *Sol. Energy Mater.* **2009**, *93*(4), 442–446.
(14) Zimmermann, B.; Glatthaar, M.; Niggemann, M.; Riede, M. K.; Hinsch, A.; Gombert, A. *Sol. Energy Mater.* **2007**, *91*(5), 374–378.
(15) Brabec, C. J.; Hauch, J. A.; Schilinsky, P.; Waldauf, C. *Mrs Bulletin* **2005**, *30*(1), 50–52.
(16) Brabec, C. J.; Durrant, J. R. *MRS Bull.* **2008**, *33*(7), 670–675.
(17) Bundgaard, E.; Krebs, F. C. *Sol. Energy Mater.* **2007**, *91*(11), 954–985.
(18) Chen, L. M.; Hong, Z. R.; Li, G.; Yang, Y. *Adv. Mater.* **2009**, *21* (14−15), 1434–1449.
(19) Coakley, K. M.; McGehee, M. D. *Chem. Mater.* **2004**, *16*, 4533–4542.
(20) Coakley, K. M.; Liu, Y. X.; Goh, C.; McGehee, M. D. *Mrs Bulletin* **2005**, *30*, 37–40.
(21) Dennler, G.; Scharber, M. C.; Brabec, C. *J. Adv. Mater.* **2009**, *21* (13), 1323–1338.
(22) Günes, S.; Neugebauer, H.; Sariciftci, N. S. *Chem. Rev.* **2007**, *107* (4), 1324–1338.
(23) Günes, S.; Sariciftci, N. S. *Inorg. Chim. Acta* **2008**, *361*(3), 581–588.
(24) Hoppe, H.; Sariciftci, N. S. *J. Mater. Res.* **2004**, *19*(7), 1924–1945.
(25) Janssen, R. A. J.; Hummelen, J. C.; Saricifti, N. S. *Mrs Bulletin* **2005**, *30*(1), 33–36.
(26) Jørgensen, M.; Norrman, K.; Krebs, F. C. *Sol. Energy Mater.* **2008**, *92*(7), 686–714.
(27) Kippelen, B.; Bredas, J. L. *Energy Environ. Sci.* **2009**, *2*(3), 251–261.
(28) Krebs, F. C. Sol. Energy Mater. **2004**, *83* (2−3) 125−322.
(29) Krebs, F. C. *Refocus* **2005**, *6*(3), 38–39.
(30) Kroon, R.; Lenes, M.; Hummelen, J. C.; Blom, P. W. M.; de Boer, B. *Polym. Rev.* **2008**, *48*(3), 531–582.
(31) Lloyd, M. T.; Anthony, J. E.; Malliaras, G. G. *Mater. Today* **2007**, *10*, 34–41.
(32) Mayer, A. C.; Scully, S. R.; Hardin, B. E.; Rowell, M. W.; McGehee, M. D. *Mater. Today* **2007**, *10*(11), 28–33.

Published on Web 09/16/2009

solar cells, polymer-fullerene solar cells, small molecule, and hybrid solar cells. Polymer-fullerene solar cells based on composites of an electron-donating conjugated polymer and an electron-accepting fullerene have proven to be the most successful so far with power conversion efficiencies exceeding 6%.[39,40] In addition to the power conversion efficiency, there is, in the context of polymer solar cells, increasing focus on preparation of efficient materials with low optical band gaps and materials that give stable devices. Because the photon flux reaching the surface of the earth from the sun has a maximum of approximately 1.8 eV (700 nm) state-of-the-art materials for polymer solar cells like poly(3-hexylthiophene) (P3HT) is only able to harvest up to ∼22% of the available solar photons.[17,30] Therefore, by decreasing the band gap of the active material it is possible to harvest a larger amount of the solar photons and thereby increase the power conversion efficiency. In terms of stability and operational lifetime polymer solar cells generally perform poorly. However, it has been demonstrated that polymer solar cells based on a blend of poly-3-(2-methylhexan-2-yl)-oxy-carbonylbithiophene (P3MHOCT) and PCBM can provide very stable behavior after thermal elimination of the solubilizing ester groups,[41−47] whereas the thermocleavage step was observed to lead to a decrease in performance.[41,42,47,48] It was found that the carboxy groups residing on the backbone after thermocleavage of the ester group could be removed by an even higher thermal treatment[49] and this could then give devices with a higher performance than the devices that had not been thermocleaved.[42] The softness provided by the solubilizing groups is related to the instability of polymer solar cells, and more rigid systems generally give devices with a better stability.[44,50,51] Furthermore, typical nonconjugated solubilizing groups reduce the density of chromophores in the polymer and do not contribute to light harvesting and charge transport. The motivation for preparing materials with thermocleavable side chains are multifold and can be summarized as the possibility to prepare materials with a higher density of chromophores leading to device films with a better operational stability and a higher level of permissible processing conditions due to the insolubility of thermocleaved films in all solvents. This has been explored with success in tandem solar cells based on thermocleavable materials.[52] It should, however, be stressed that these advantages should not come at the expense of the power conversion efficiency for the devices. So far, this has not been the case and there is an urgent need to uncover the processing conditions that are required to get high performance for devices based on thermocleavable materials.

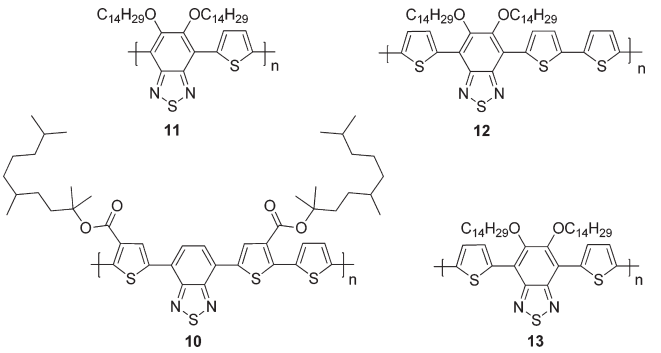

Figure 1. Low band gap polymers based on 2,1,3-benzothiadiazole and thiophene units.

Herein, we report the synthesis of four new low band gap polymers and their photovoltaic performance in blends with [6,6]-phenyl C_{61} butyric acid methyl ester (PCBM). Three of the polymers (**11**−**13**) are based on 2,1,3-benzothiadiazole, bearing solubilizing alkoxy side chains at the 5- and 6-position, alternating with thiophene units along the chain (Figure 1). The fourth polymer (**10**) is based on 2,1,3-benzothiadiazole alternating with three thiophene units along the chain. In addition, a branched alkyl chain is attached to the polymer backbone through a labile ester bond to the thiophene segment. When heated, this bond breaks, eliminating a volatile alkene and leaving the polymer component more rigid (Figure 2). The thermal treatment can be viewed as a way of performing an in situ chemical reaction, thereby allowing for the alteration of both physical and chemical properties such as solubility, hardness, hydrogen bonding, chromophore density, and ionicity after the active layer has been deposited.[42]

Experimental section

Synthetic procedures for synthesis of monomers and polymers according to Schemes 1−3 and their characterization data

(33) Rand, B. P.; Genoe, J.; Heremans, P.; Poortmans, J. *Prog. Photovoltaics* **2007**, *15*(8), 659–676.
(34) Shaheen, S. E.; Ginley, D. S.; Jabbour, G. E. *MRS Bull.* **2005**, *30*(1), 10–19.
(35) Shaheen, S. E.; Ginley, D. S.; Jabbour, G. E. MRS Bull. **2005**, *30* (Special Issue 1), 10−52.
(36) Spanggaard, H.; Krebs, F. C. *Sol. Energy Mater.* **2004**, *83*(2−3), 125–146.
(37) Thompson, B. C.; Frechet, J. M. J. *Angew. Chem., Int. Ed.* **2008**, *47* (1), 58–77.
(38) Winder, C.; Sariciftci, N. S. *J. Mater. Chem.* **2004**, *14*(7), 1077–1086.
(39) Kim, J. Y.; Lee, K.; Coates, N. E.; Moses, D.; Nguyen, T. Q.; Dante, M.; Heeger, A. J. *Science* **2007**, *317*(5835), 222–225.
(40) Park, S. H.; Roy, A.; Beaupre, S.; Cho, S.; Coates, N.; Moon, J. S.; Moses, D.; Leclerc, M.; Lee, K.; Heeger, A. J. *Nat. Photonics* **2009**, *3*(5), 297–302.
(41) Bjerring, M.; Nielsen, J. S.; Siu, A.; Nielsen, N. C.; Krebs, F. C. *Sol. Energy Mater.* **2008**, *92*(7), 772–784.
(42) Gevorgyan, S. A.; Krebs, F. C. *Chem. Mater.* **2008**, *20*(13), 4386–4390.
(43) Krebs, F. C.; Spanggaard, H. *Chem. Mater.* **2005**, *17*(21), 5235–5237.
(44) Krebs, F. C.; Norrman, K. *Prog. Photovoltaics* **2007**, *15*(8), 697–712.
(45) Krebs, F. C. *Sol. Energy Mater.* **2008**, *92*(7), 715–726.
(46) Krebs, F. C.; Thomann, Y.; Thomann, R.; Andreasen, J. W. *Nanotechnology* **2008**, *19*(42), 424013.
(47) Krebs, F. C. *Design and Applications of Polymer Solar Cells with Lifetimes Longer Than 10000 h*; Kafafi, Z. H., Lane, P. A., Eds.; SPIE: San Diego, CA, 2005; pp 59380Y−593811.
(48) Petersen, M. H.; Gevorgyan, S. A.; Krebs, F. C. *Macromolecules* **2008**, *41*(23), 8986–8994.
(49) Bjerring, M.; Nielsen, J. S.; Nielsen, N. C.; Krebs, F. C. *Macromolecules* **2007**, *40*(16), 6012–6013.
(50) Norrman, K.; Alstrup, J.; Jorgensen, M.; Lira-Cantu, M.; Larsen, N. B.; Krebs, F. C. *Proceedings of Organic Photovoltaics VII*; SPIE: Bellingham, WA, 2006; Vol. *6334*, pp U100−U111.
(51) Norrman, K.; Krebs, F. C. *Sol. Energy Mater.* **2006**, *90*(2), 213–227.
(52) Hagemann, O.; Bjerring, M.; Nielsen, N. C.; Krebs, F. C. *Sol. Energy Mater.* **2008**, *92*(11), 1327–1335.

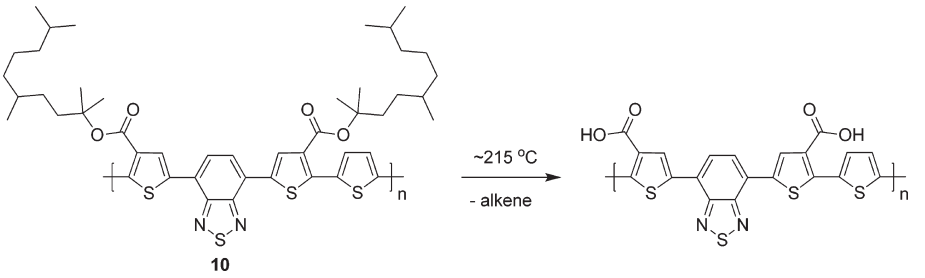

Figure 2. Thermocleavable ester groups attached to the polymer backbone of **10**. After a thermal treatment around 215 °C, the solubilizing groups are eliminated.

Scheme 1. Synthetic Steps Involved in the Preparation of the Monomers 4 and 6

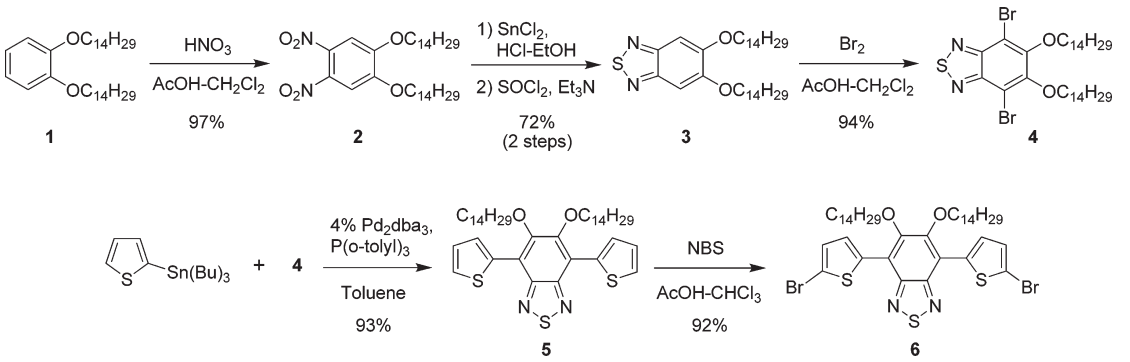

Scheme 2. Synthetic Steps Involved in the Preparation of the Thermocleavable Polymer 10; R = 2,5,9-Trimethyl-2-decanyl

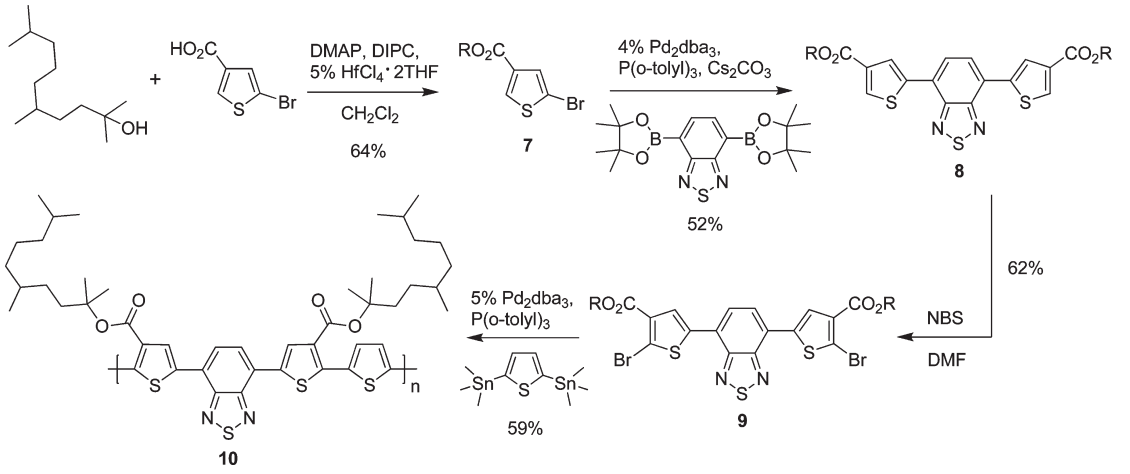

(including ^{1}H NMR and ^{13}C NMR) are described in detail in the Supporting Information, together with general experimental details.

Polymer Solar Cell Fabrication and Analysis. Photovoltaic devices were made by spin coating PEDOT:PSS (Clevios P, VP Al4083) onto precleaned, patterned indium tin oxide (ITO) substrates (14 Ω per square) (Naranjo Substrates). The active layer was deposited by spin coating a blend of the polymer and [60]PCBM dissolved in chlorobenzene (20−30 mg/mL). The counter electrode of LiF (1 nm) and aluminum (100 nm) was deposited by vacuum evaporation at $2-3 \times 10^{-7}$ mbar. The active area of the cells was 0.091−0.162 cm^2 and the active layer thickness was determined with a Dektak surface profiler. $J-V$ characteristics were measured under 100 mW/cm^2 white light from a tungsten-halogen lamp filtered by a Schott GG385 UV filter and a Hoya LB120 daylight filter, using a Keithley 2400 source meter. The spectral response (SR) was measured under operating conditions using bias light from a 532 nm solid state laser (Edmund Optics). Monochromatic light from a 50 W tungsten halogen lamp (Philips focusline) in combination with monochromator (Oriel, Cornerstone 130) was modulated with a mechanical chopper. The response was recorded as the voltage over a 50 Ω resistance, using a lock-in amplifier (Stanford research Systems SR830). A calibrated Si cell was used as reference. The device was kept behind a quartz window in a nitrogen filled container. Short circuit currents under AM1.5 conditions were obtained from the spectral response and convolution with the solar spectrum (J_{sc}(SR)). The value of J_{sc}(SR) was used with V_{oc} and FF from the 100 mW/cm^2 white light $J-V$ characteristics to estimate the power conversion efficiency η.

Results and Discussion

Approaches to Thermal Processing of Conjugated Polymers. Traditionally conjugated materials were prepared by a thermocleavable route whereby a soluble nonconjugated

Scheme 3. Synthetic Steps Involved in the Preparation of the Polymers 11, 12, and 13

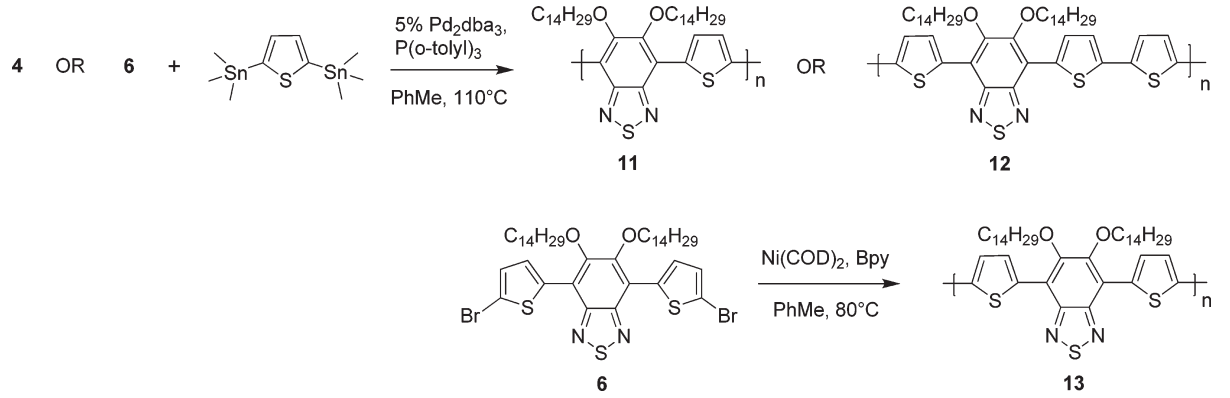

precursor was heated to provide the insoluble conjugated polymer film. Examples of this include the Wessling route to PPV[53−56] and the Durham routes to polyacetylene.[57−59] These were then replaced by efficient routes to soluble conjugated materials and it is only recently that requirements for better operational stability and processing freedom has spawned new research in this area. Generally, two approaches have been followed. The precursor route where the conjugation in the polymer film is formed upon thermocleavage after formation of a film based on the precursor polymer.[60−64] The other approach is the thermocleavable side chain route where the conjugated backbone is already present in the polymer film during formation but where the side chains are removed upon the thermal treatment to give the unsubstituted conjugated polymer backbone.[41−48,52,65−69] Common to both approaches is that the final film is insoluble and the chromophore density is high. The main difference is that the thermocleavable side chain film is functional as a photovoltaic device before being thermocleaved.

Synthesis. The synthetic steps involved in the preparation of the monomers **4** and **6** are outlined in Scheme 1. 1,2-Bis(tetradecyloxy)benzene (**1**) were prepared by a standard alkylation of catechol with 1-bromotetradecane in DMF at 100 °C.[70] Electrophilic aromatic nitration of **1** affords the substituted *o*-dinitrobenzene (**2**).[71] Reduction of the nitro groups with tin(II) chloride[72] gives the diamine as its hydrochloride salt which has to be used directly because of its unstable nature. Treatment of the diamine with thionyl chloride affords **3**, which is brominated with molecular bromine to give monomer **4** in excellent yield.[73] Stille coupling of **4** with 2-tributylstannylthiophene gives **5** as a yellow solid that is highly fluorescent in solution. Finally, NBS bromination of **5** gives monomer **6**.

The synthetic steps involved in the preparation of the thermocleavable polymer **10** are outlined in Scheme 2. A slightly modified procedure, reported in our earlier work[48] for the synthesis of tertiary esters, was used to prepare **7**. The esterification employs a catalytic amount of hafnium(IV) chloride tetrahydrofuran complex (1:2) in combination with *N,N′*-diisopropylcarbodiimide and DMAP. Suzuki cross-coupling of **7** with the boronic ester 4,7-bis(4,4,5,5-tetramethyl-1,3,2-dioxaborolan-2-yl)benzo-[*c*][1,2,5]thiadiazole affords **8** which is NBS brominated to give monomer **9**. Finally copolymerisation of **9** via Stille coupling with 2,5-bis(trimethylstannyl)thiophene affords the thermocleavable polymer **10** as a dark purple-brown solid.

Using the same conditions as for **9**, copolymerisation of **4** and **6** via Stille coupling with 2,5-bis(trimethylstannyl)-thiophene gives polymer **11** and **12** as dark purple solids (Scheme 3). Yamamoto coupling of **6**, using bis(1,5-cyclooctadiene)nickel(0) ($Ni(COD)_2$) and bipyridine (Bpy)

(53) Gagnon, D. R.; Capistran, J. D.; Karasz, F. E.; Lenz, R. W.; Antoun, S. *Polymer* **1987**, *28*(4), 567–573.
(54) Garay, R. O.; Mayer, B.; Karasz, F. E.; Lenz, R. W. *J. Polym. Sci., Part A: Polym. Chem.* **1995**, *33*(3), 525–531.
(55) Lenz, R. W.; Han, C. C.; Stengersmith, J.; Karasz, F. E. *J. Polym. Sci., Part A: Polym. Chem.* **1988**, *26*(12), 3241–3249.
(56) Wessling, R. A. *J. Polym. Sci., Polym. Symp.* **1985**, No. 72, 55–66.
(57) Bott, D. C.; Brown, C. S.; Chai, C. K.; Walker, N. S.; Feast, W. J.; Foot, P. J. S.; Calvert, P. D.; Billingham, N. C.; Friend, R. H. *Synth. Met.* **1986**, *14*(4), 245–269.
(58) Feast, W. J.; Winter, J. N. *J. Chem. Soc., Chem. Commun.* **1985**, No. 4, 202–203.
(59) Furlani, A.; Napoletano, C.; Russo, M. V.; Feast, W. J. *Polym. Bull.* **1986**, *16*(4), 311–317.
(60) Banishoeib, F.; Adriaensens, P.; Berson, S.; Guillerez, S.; Douheret, O.; Manca, J.; Fourier, S.; Cleij, T. J.; Lutsen, L.; Vanderzande, D. *Sol. Energy Mater.* **2007**, *91*(11), 1026–1034.
(61) Banishoeib, F.; Henckens, A.; Fourier, S.; Vanhooyland, G.; Breselge, M.; Manca, J.; Cleij, T. J.; Lutsen, L.; Vanderzande, D.; Nguyen, L. H.; Neugebauer, H.; Sariciftci, N. S. *Thin Solid Films* **2008**, *516*(12), 3978–3988.
(62) Girotto, C.; Cheyns, D.; Aernouts, T.; Banishoeib, F.; Lutsen, L.; Cleij, T. J.; Vanderzande, D.; Genoe, J.; Poortman, J.; Heremans, P. *Org, Electron,* **2008**, *9*(5), 740–746.
(63) Henckens, A.; Colladet, K.; Fourier, S.; Cleij, T. J.; Lutsen, L.; Gelan, J.; Vanderzande, D. *Macromolecules* **2005**, *38*(1), 19–26.
(64) Nguyen, L. H.; Gunes, S.; Neugebauer, H.; Sariciftci, N. S.; Banishoeib, F.; Henckens, A.; Cleij, T.; Lutsen, L.; Vanderzande, D. *Sol. Energy Mater.* **2006**, *90*(17), 2815–2828.
(65) Gordon, T. J.; Yu, J. F.; Yang, C.; Holdcroft, S. *Chem. Mater.* **2007**, *19*(9), 2155–2161.
(66) Gordon, T. J.; Vamvounis, G.; Holdcroft, S. *Adv. Mater.* **2008**, *20* (13), 2486–2490.
(67) Han, X.; Chen, X. W.; Holdcroft, S. *Adv. Mater.* **2007**, *19*(13), 1697–1702.
(68) Liu, J. S.; Kadnikova, E. N.; Liu, Y. X.; McGehee, M. D.; Frechet, J. M. J. *J. Am. Chem. Soc.* **2004**, *126*(31), 9486–9487.
(69) Yu, J. F.; Holdcroft, S. *Macromolecules* **2000**, *33*(14), 5073–5079.
(70) Zhang, D.; Tessier, C. A.; Youngs, W. J. *Chem. Mater.* **1999**, *11* (11), 3050–3057.
(71) Sessler, J. L.; Callaway, W. B.; Dudek, S. P.; Date, R. W.; Bruce, D. W. *Inorg. Chem.* **2004**, *43*(21), 6650–6653.
(72) Far, A. R.; Shivanyuk, A.; Rebek, J. *J. Am. Chem. Soc.* **2002**, *124* (12), 2854–2855.
(73) Bouffard, J.; Swager, T. M. *Macromolecules* **2008**, *41*(15), 5559–5562.

Table 1. GPC and Spectroscopic Data for Polymers 10−13

	solution					film		
polymer	M_w (g/mol)	PDI	λ_{max} (nm)	λ_{onset} (nm)	E_g (eV)	λ_{max} (nm)	λ_{onset} (nm)	E_g (eV)
10	173000	2.6	525	633	1.96	593,[a] 570[b]	732	1.69
11	16600	1.7	563	643	1.93	654	711	1.74
12	26000	2.9	570	687	1.80	644	707	1.75
13	7100	1.7	543	639	1.94	592	715	1.73

[a] 25 °C. [b] Heated at 250 °C for 1 min.

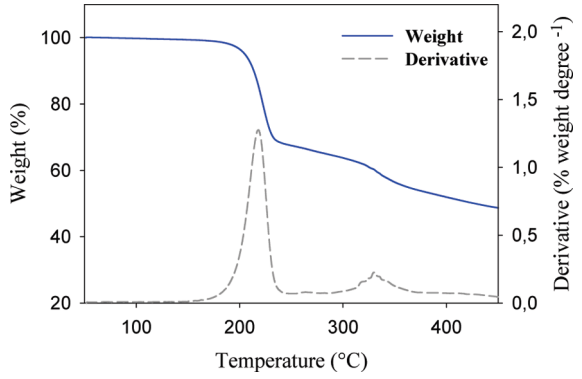

Figure 3. Thermogravimetric data for **10** in the temperature range 50−500 °C. The theoretical weight loss for the elimination process around 215 °C is 44%, whereas the observed value is ~31%. A second minor weight loss (~8%) is observed around 330 °C. The data were recorded at 10 °C min^{-1} under an argon atmosphere.

gives polymer **13** in 20% yield (Scheme 3) with a molecular weight (M_w) of 7100 g/mol and a polydispersity (PDI) of 1.7. The low yield was caused by the fact that a large portion of the polymer formed was insoluble and could not be isolated by Soxhlet extraction. For the same reason, a low yield of **12** was isolated (28%) but with a higher molecular weight (M_w = 26 000 g/mol, PDI = 2.9). On the contrary Polymer **10** and **11** were isolated in good yields and are very soluble in organic solvents such as chloroform and toluene at room temperature. The large variation in molecular weight between **10** and **11** could be explained by the difference in coupling groups, bromothiophene-stannylthiophene versus bromobenzothiadiazole-stannylthiophene.

Thermal Behavior. The sample holders were carefully weighed and the samples introduced. Thermogravimetric analysis (TGA) was then carried out using heating rate of 10 °C min^{-1}. TGA of **10** in the temperature range 50−500 °C indicates that the ester bond starts to break around 200 °C (Figure 3). The second loss peak at ~330 °C corresponds to loss of CO_2.[48,49]

Optical Properties. The absorption spectra for polymer **10**−**13** in chloroform solution are shown in Figure 4a and Figure 5. The optical band gaps, defined by the onset of absorption, are rather similar ranging from 1.8 to 1.96 eV (Table 1). **12** exhibits a lower optical band gap in solution due to partial aggregation of the polymer in solution. The difference in absorption maxima (λ_{max}) is relatively small but **10** is blue-shifted compared to polymers **11**−**13** (Table 1), indicating a more twisted backbone because of the branched ester side chains. The film absorption spectra for polymers **10**−**13** are shown in Figures 4b and

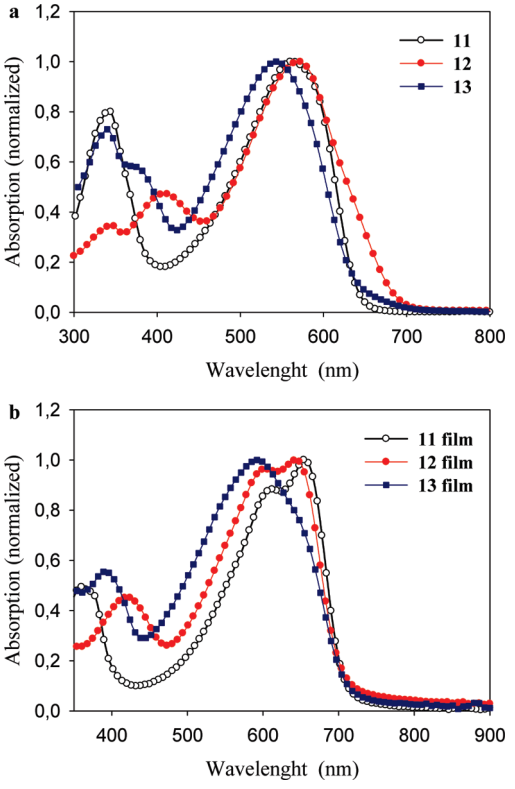

Figure 4. UV−vis absorption spectra of polymers **11**−**13** in (a) chloroform solution and (b) thin film.

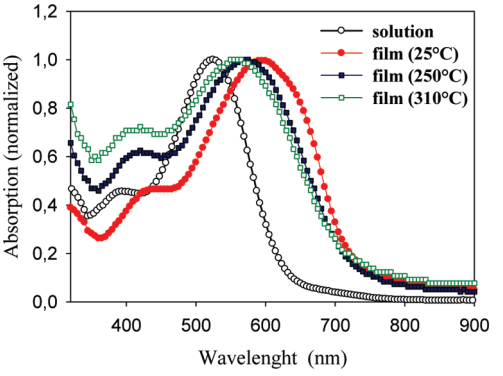

Figure 5. UV−vis absorption spectra of **10** in chloroform solution and in thin film before and after thermocleavage.

5. Again, the optical band gaps are very similar ranging from 1.69 to 1.75 eV (Table 1). The polymers have absorption maxima ranging from 525 to 570 nm in chloroform, and these are red-shifted further to 592−654 nm when in a solid film (Table 1), indicating significant interchain association in the solid state. In addition polymers **11** and **12** show vibronic fine structure

Table 2. Photovoltaic Performance of Devices Based on Blends of Polymer and PCBM

polymer	thermal treatment[a] (°C)	layer thickness (nm)	V_{oc} (V)	J_{sc}(SR) (mA/cm^2)	FF	η (%)
10		92	0.75	1.07[b]	0.26	0.21
10	200	92	0.90	0.72[b]	0.37	0.24
10	285	78	0.90	1.36	0.34	0.42
11		63	0.93	5.18	0.46	2.22
12		80	0.61	6.21	0.47	1.78
13		65	0.76	2.56	0.32	0.62

[a] Heated for 20−30 s. [b] Unestimated.

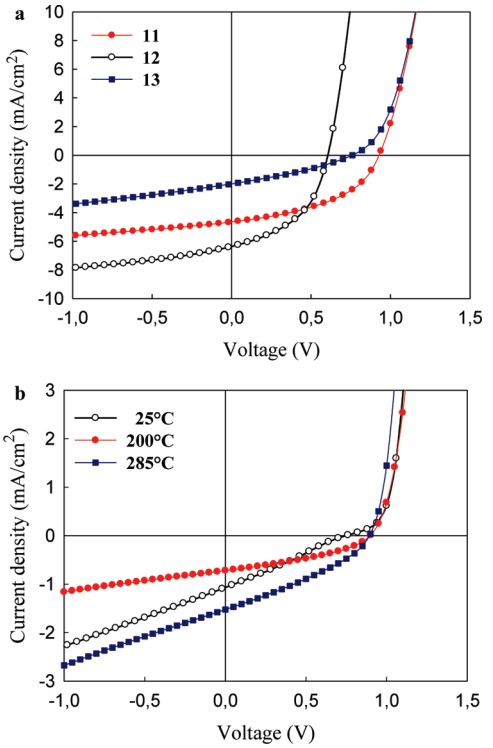

Figure 6. (a) $J-V$ characteristics of the **11**:PCBM, **12**:PCBM and **13**:PCBM solar cells measured under 100 mW/cm^2 white light; (b) $J-V$ characteristics of solar cells based on **10** and PCBM measured under 100 mW/cm^2 white light before and after a thermal treatment.

at 625 nm in the solid state. A weak vibronic transition may also account for the observed shoulder of **13** (Figure 4b). With regard to the thermocleavable polymer **10**, a blue shift of the absorption maxima is observed when the film is heated at 250 °C for 1 min (Figure 5), but no clear color change is observed. Only a minor blue shift in the absorption maxima is observed when the film is heated at 310 °C for 1 min compared to heating at 250 °C. After the thermal treatment, the film was completely insoluble.

Photovoltaic Performance. Bulk heterojunction solar cells were fabricated on an indium tin oxide (ITO) covered glass substrate, using conventional device architecture. A thin layer of poly(3,4-ethylenedioxythiophene)−poly-(styrenesulfonate) (PEDOT-PSS) was spin coated on top of the ITO coating followed by spin coating of the active layer. The active layer contained a blend of the respective polymer and [60]PCBM. After spin coating of the active layer the devices were either processed directly into a solar cell by evaporation of LiF (1 nm) and aluminum (100 nm) as back electrode or subjected to a

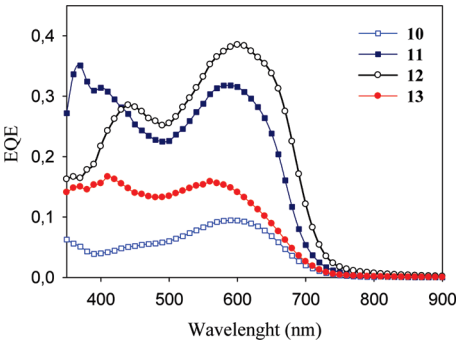

Figure 7. EQE spectra of polymer:PCBM solar cells. **10** were thermocleaved at 285 °C.

thermal treatment at the temperature of thermocleavage immediately before evaporation of the back electrode. The most efficient devices comprised a polymer/PCBM ratio of 1:2 spin-coated from chlorobenzene with a polymer concentration of 7.5 mg/mL. The optimal layer thickness was around 60−80 nm.

The obtained current−voltage curves are presented in figure 6 which shows the current−voltage characteristics of the **10**:PCBM, **11**:PCBM, **12**:PCBM and **13**:PCBM solar cells measured under 100 mW/cm^2 white light. The devices based on **11**, with only one thiophene unit alternating with benzothiadiazole, and PCBM showed power conversion efficiencies of up to 2.22% (Table 2). The devices had high open-circuit voltages (V_{oc}) of 0.93 V, moderate fill factors (FF) of 0.46 and current densities (J_{sc}) of 5.18 mA/cm^2. The external quantum efficiency (EQE) for **11**:PCBM is higher than 23% in the wavelength range between 350 and 650 nm, and the maximum was found to be 35% around 370 nm where PCBM also absorbs (Figure 7). Polymer **12**:PCBM gives an EQE higher than 22% in the range between 400 and 680 nm with a maximum of 39% at around 600 nm. Compared to **11**:PCBM, the EQE is enhanced by up to 10% in the range 450−720 nm, which gives a current density of 6.21 mA/cm^2. The devices based on **12**:PCBM performed slightly poorer due to a lower V_{oc} of typically 0.61 V, which resulted in power conversion efficiencies of up to 1.78%. Solar cells based on polymer **13**:PCBM gave significantly lower EQE with quantum efficiencies around 10−15% in the range of 350−650 nm, giving current densities of 2.56 mA/cm^2. Together with a typical V_{oc} of 0.76 V and low fill factors of 0.32, power conversion efficiencies of up to 0.62% were obtained. The lower performance of **13** compared to **11** and **12** could be due to the different polymerization procedure where excess of

nickel(0) was used instead of a catalytic amount of palladium employed in the Stille coupling. The devices based on the thermocleavable polymer **10** and PCBM showed the lowest power conversion efficiencies of up to 0.42% (Table 2). Without thermal treatment of **10**:PCBM devices a typical V_{oc} of 0.75 V was obtained. Upon heating the device to 200 °C the V_{oc} increases to 0.90 V and resides there when annealing at 285 °C. The FF increased from 0.26 to 0.37 after thermal treatment at 200 °C and then drops a bit upon heating the device at 285 °C. The current density first drops after thermal treatment and then increases again when heating at 285 °C. The EQE of **10**:PCBM (cleaved at 285 °C) is relatively low with quantum efficiencies of about 5−10% in the range 350−670 nm (figure 7) giving it an estimated current density of 1.36 mA/cm^2. A general observation was that the devices based on **10**:PCBM performed better after thermocleavage due to an increase in mainly the current and fill factor. $J-V$ curves for uncleaved and cleaved **10**:PCBM devices are shown in figure 6b. Despite the lower efficiency of polymer **10** compared to the polymers **11-13** the thermocleavable polymer **10** does show promising results with increased performance after thermocleavage. In the majority of cases where thermocleavable materials have been employed in polymer solar cells, a drop in performance has been observed when thermocleaving the polymer and only one previous case has demonstrated an advantage of thermocleavage in terms of performance.[42] The lower performance of polymer **10** compared to the polymers **11**−**13** can be an effect of the more electron-attracting ester groups situated on thiophene (**10**) compared to the electron-donating alkoxy groups on benzothiadiazole (**11**−**13**).

Conclusion

In conclusion, four new low band gap polymers have been synthesized. They are based on 2,1,3-benzothiadiazole alternating with thiophene units along the chain, bearing solubilizing chains on either benzothiadiazole (**11**−**13**) or thiophene (**10**). The solubilizing chain on **10** is attached to the polymer backbone through a labile ester bond which is thermocleavable around 215 °C. When heated, this bond breaks, eliminating a volatile alkene and leaving the polymer component more rigid. The four polymers optical properties and photovoltaic performance in blends with PCBM have been investigated. In chloroform solution, the polymers had very similar optical band gaps ranging from 1.8 to 1.96 eV. The optical band gaps are lowered to 1.69−1.75 eV in thin film (Table 1), indicating significant interchain association in the solid state. Furthermore polymer **11** and **12** showed vibronic fine structure centered at 625 nm in the solid state. The best performing polymer in a bulk heterojunction solar cell was **11** with J_{sc} = 5.18 mA/cm^2, V_{oc} = 0.93 V, FF = 0.46, and η = 2.22%. Devices based on **10**:PCBM performed better after thermocleavage because of an increase in mainly current and fill factor giving power conversion efficiencies up to 0.42%.

Acknowledgment. This work was supported by the Danish Strategic Research Council (DSF 2104-05-0052 and 2104-07-0022).

Supporting Information Available: General procedures and characterization data including NMR spectra; experimental procedures for the synthesis of the monomers and polymers according to Schemes 1, 2, and 3. This material is available free of charge via the Internet at http://pubs.acs.org.

PAPER www.rsc.org/materials | Journal of Materials Chemistry

A roll-to-roll process to flexible polymer solar cells: model studies, manufacture and operational stability studies†‡

Frederik C. Krebs,* Suren A. Gevorgyan and Jan Alstrup

Received 23rd December 2008, Accepted 2nd April 2009
First published as an Advance Article on the web 6th May 2009
DOI: 10.1039/b823001c

An inverted polymer solar cell geometry comprising a total of five layers was optimized using laboratory scale cells and the operational stability was studied under model atmospheres. The device geometry was substrate-ITO-ZnO-(active layer)-PEDOT:PSS-silver with P3HT-PCBM as the active layer. The inverted devices were compared to model devices with a normal geometry where the order of the layers was substrate-ITO-PEDOT:PSS-(active layer)-aluminium. In both cases illumination was through the substrate which requires that it is transparent. Both device types were optimized to a power conversion efficiency of 2.7% (1000 W m^{-2}, AM1.5G, 72 ± 2 °C). The devices were operated under illumination while being subjected to different atmospheres to identify the dominant modes of degradation. Dry nitrogen (99.999%), dry oxygen (99.5%), humid nitrogen (90 ± 5% relative humidity) and ambient atmosphere (20% oxygen, 20 ± 5% relative humidity) were employed and both device types were found to be stable in a nitrogen atmosphere during the test period of 200 hours. The devices with a normal geometry where an aluminium electrode is employed gave stable operation in dry oxygen but did not give stable device operation in the presence of humidity. The inverted devices behaved oppositely where the less reactive silver electrode gave stable operation in the presence of humidity but poor stability in the presence of oxygen. The inverted model device was then used to develop a new process giving access to fully roll-to-roll (R2R) processed polymer solar cells entirely by solution processing starting from a polyethyleneterephthalate (PET) substrate with a layer of indium-tin-oxide (ITO). All processing was performed in air without vacuum coating steps and modules comprising eight serially connected cells gave power conversion efficiencies as high as 2.1% for the full module with 120 cm^2 active area (AM1.5G, 393 W m^{-2}) and up to 2.3% for modules with 4.8 cm^2 active area (AM1.5G, 1000 W m^{-2}).

Introduction

The polymer solar cell[1–5] relies on a thin active layer sandwiched between two electrodes where at least one of them is transparent or semitransparent allowing light to access the active area. In the best performing devices charge carriers are formed throughout the bulk of the active layer and the directional flow of oppositely charged carriers is granted through judicious choice of electrodes that selectively allows for transport of the preferred carrier. The state-of-the-art is well represented by a mixture of poly(3-hexylthiophene) and [60]PCBM as the active layer.[2]

The geometry of the typical polymer solar cell device is shown in Fig. 1 as the normal geometry and employs frontface illumination. The choice of the normal geometry is mostly historical and has not been developed rationally but has rather evolved from the contemporary understanding and the means available. Traditionally devices have been prepared on glass substrates with ITO as the transparent conductor and later developments include transparent hole transporting layers that operate well with ITO as the anode. As a consequence the electron accepting electrode was typically a metal with a low work function (*e.g.* aluminium or calcium) that has sometimes been employed in conjunction with an electron transporting layer (or tunnel barrier) such as LiF.[6] In order to form a good contact between the active layer and a low work function metal this type of electrode has been prepared exclusively using physical vapour deposition techniques (*i.e.* by evaporating the metal onto the active layer). The realisation of the normal geometry has been refined and high performing devices can be prepared. In the context of operational stability[4] and large scale solution processing[5] without vacuum coating steps the normal geometry is far from ideal and other device geometries are worth pursuing. Some of the different possibilities are outlined in Fig. 1. The construction of the multilayered polymer solar cell structure is assumed to start with the substrate and one has a choice of whether light should be entering the active layer of the device through the substrate (*i.e.* through the substrate and all the layers processed before the active layer is applied) or whether light should enter the active layer through the back electrode (*i.e.* through all the layers processed after the active layer is applied). It should be emphasized that there might be other possibilities of

Risø National Laboratory for Sustainable Energy, Technical University of Denmark, Frederiksborgvej 399, DK-4000 Roskilde, Denmark. E-mail: frederik.krebs@risoe.dk

† This paper is part of a *Journal of Materials Chemistry* theme issue on solar cells. Guest editors: Michael Grätzel and René Janssen.

‡ Electronic supplementary information (ESI) available: Decay of the Open Circuit Voltage V_{oc}, Short Circuit Current Density J_{sc}, Fill Factor FF and power conversion efficiency PCE of the model devices under different conditions. See DOI: 10.1039/b823001c

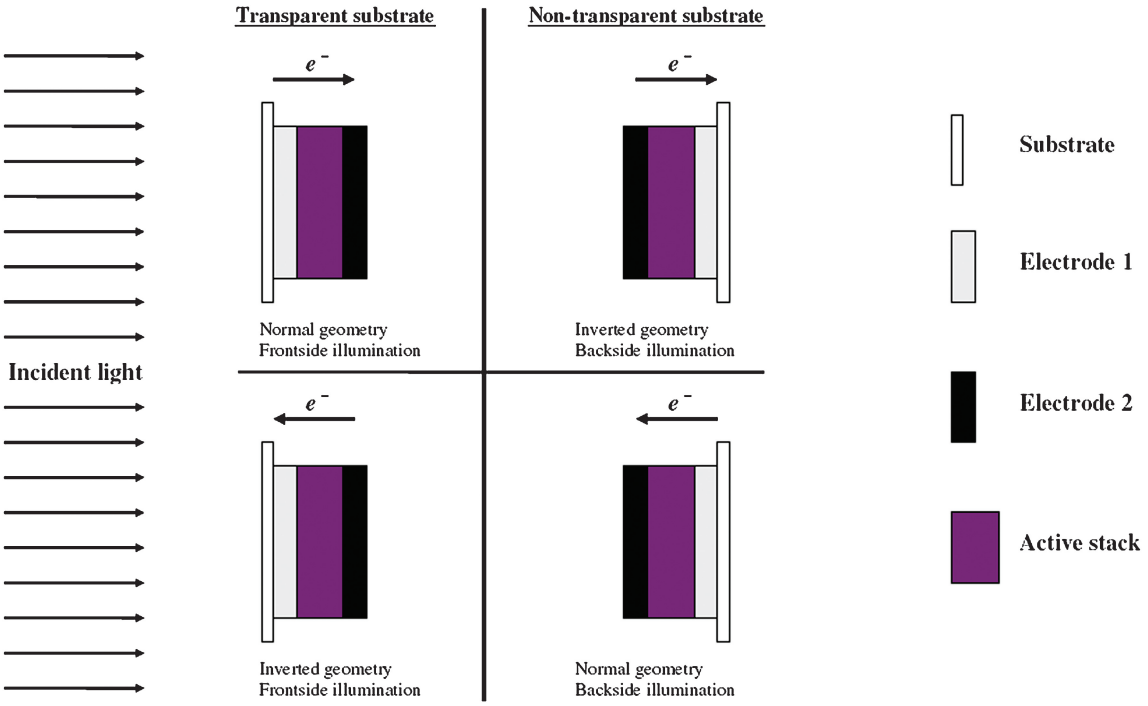

Fig. 1 An illustration of the four possible device geometries for multilayer polymer solar cells assuming charge transport in a direction perpendicular to the substrate surface. Frontface illumination requires that the substrate is transparent whereas backside illumination does not forcibly require this. Illumination is assumed to take place from one preferred side. Bifacial illumination is possible and requires transparency of both electrodes (not shown in this diagram). The hole flow is in a direction opposite to the electron flow.

device fabrication where a part of or the entire solar cell structure is transferred after the multilayer structure (or part of it) has been prepared. There are however no reported examples of this approach. The traditional manner in which polymer solar cell devices are prepared has introduced severe limitations and it would seem that a typical laboratory report would have great difficulty in finding new approaches that differ significantly from ITO on rigid glass, evaporated electrodes and spincoating. There have been a few recent reports that deviate convincingly from the traditional methods with success in both achieving a similar performance[7] and even alleviating the use of ITO.[8,9] ITO is currently viewed as a material that has proven useful for the development of polymer and organic solar cells while it does not share a commercially viable future with polymer solar cells. One of the unmet challenges that has limited the possibilities that have been explored is that there are very few available transparent conductors. Aside from using a material that is inherently transparent in the visible region (*e.g.* ITO, AZO) composite electrodes have been developed where a non-transparent metallic grid is used in conjunction with semitransparent electrode material[9] that will not allow for efficient charge collection on its own (*e.g.* a silver grid used in conjunction with PEDOT:PSS). The inverted geometry has been explored with success in two generically different instances. The most explored is the one that falls closest to the normal geometry where frontface illumination and ITO substrates are still used but the flow of charge has been inverted by addition of a selective electron transport layer on top of ITO. This allows for collecting holes at the back electrode and from an operational point of view more stable devices can be prepared because no reactive electrode materials need to be involved. The second approach, known as the "ITO free wrap through" approach, was reported by Zimmermann *et al.*[8] This truly novel approach avoids the use of both ITO and any metal back electrode. It would be classified as an inverted geometry that employs backside illumination according to Fig. 1. The purpose of all these developments is to establish a process that allows for transfer of the laboratory polymer solar cells to a large scale processed industrial polymer solar cell product and this has proven far easier said then done. There are few examples of preparation of large area polymer solar cells[10] and even fewer examples of polymer solar cells produced on a reasonable scale (*i.e.* more than 100 individual devices and more than a square metre of active area).[11]

In this report we demonstrate the development of an inverted device that for laboratory devices is brought to the same level of performance as devices in a normal geometry. We subsequently demonstrate how some of the problems with operational stability for the devices with a normal geometry can be solved through stability studies using model atmospheres. We finally transfer the process to a full R2R process entirely using solution processing on a flexible plastic substrate using slot-die coating and screen printing. We obtain a performance for the R2R processed modules that is acceptably close to the performance obtained for the laboratory cells in terms of both power conversion efficiency and operational stability.

Results and discussion

The device types explored in this work are illustrated in Fig. 2. The normal device geometry comprises four layers on the

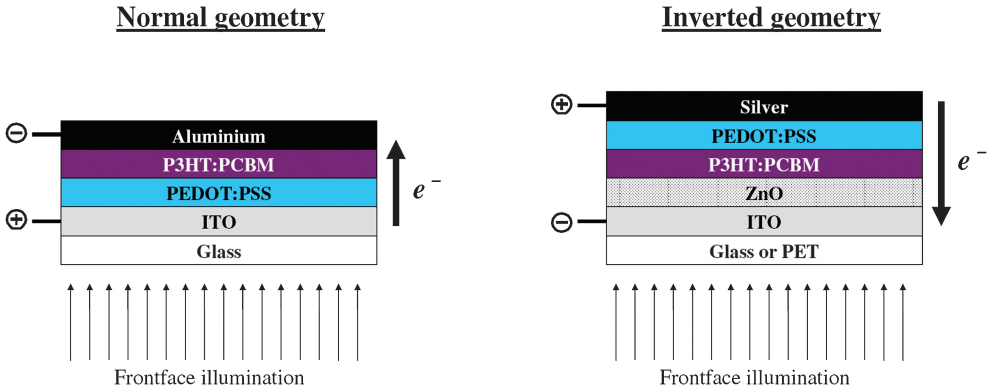

Fig. 2 The Normal geometry employed for the model devices (left) comprise spincoated PEDOT:PSS and P3HT-PCBM layers and evaporated aluminium. The inverted geometry employed for both model devices and fully R2R coated modules (right). The model devices employed spincoated ZnO, P3HT-PCBM and PEDOT:PSS and evaporated silver whereas the fully R2R coated modules employed slot-die coated ZnO, P3HT-PCBM and PEDOT:PSS with the silver electrode being applied using screen printing (slot-die coating would also have been possible).

substrate where the inverted device type has five layers to enable selective transport of electrons to ITO and holes to the metal electrode.

The use of the inverted geometry enables the use of silver as the hole collecting electrode. While the work function of silver is similar to that of aluminium and does not qualify as a metal with a high work function the advantage of using silver as the metal electrode is that printable silver formulations are commercially available making solution processing of the silver electrode a possibility. The power conversion efficiency that can be reached for devices based on P3HT and PCBM has been reported in the range of 3.5–5%.[12] The short circuit current density (I_{sc}) that can be reached is practically limited to be around 11 mA cm^{-2} and the open circuit voltage (V_{oc}) obtained with an aluminium cathode is in the range of 0.5–0.6 V (the use of LiF or calcium may improve this number slightly).

The remaining possibility for improving performance is through maximizing the fill factor. High fill factors in excess of 60% are possible and naturally yield high performance. These high fill factors are however difficult to achieve when employing large area devices and poorly conducting contacts. In order to make a fair comparison we prepared model devices with an active area of 1 cm^2 and dimensions expected to approach those of an upscaled version of the final device on flexible substrates. The reference devices in the normal geometry gave the expected short circuit current and open circuit voltage. The power conversion efficiency was 2.7%. The fill factor was up to 52% which is lower than commonly observed for high performing devices and we ascribe this to the thick active layer in the device (due to the high concentrations of the compounds used in the active blend). The inverted device was optimized to perform as well as the device with normal geometry when employing an evaporated aluminium electrode. *IV*-curves for devices with the normal and inverted geometry are shown in Fig. 3 and Table 1.

The next step was to develop an R2R compatible process for preparing the inverted devices employing solution processed silver electrodes on flexible substrates. A previous study demonstrating production of several thousand polymer solar cell modules prepared entirely by screen printing techniques[11] presented a well established process for patterning the ITO. This

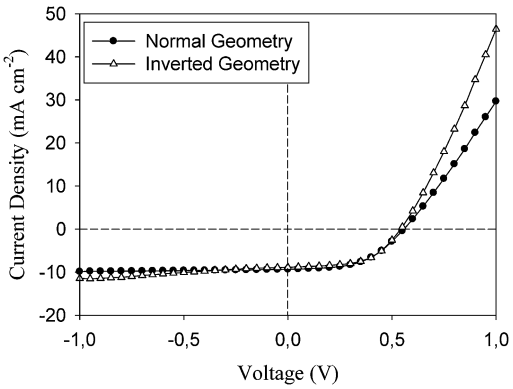

Fig. 3 A comparison of *IV*-curves for devices with a normal geometry (glass/ITO/PEDOT:PSS/P3HT-PCBM/aluminium) and an inverted geometry (glass/ITO/ZnO/P3HT-PCBM/PEDOT:PSS/silver). Both devices were prepared by spincoating the layers and evaporating the back electrodes.

Table 1 Performance of the model cells shown in Fig. 3. The measurement conditions were 1000 W m^{-2}, AM1.5G, 72 ± 2 °C

Module	V_{oc}/V	I_{sc}/mA cm^{-2}	FF (%)	PCE (%)
Normal geometry (evaporated Al) [a]	0.56	9.30	52	2.70
Inverted geometry (evaporated Ag) [a]	0.54	8.85	56	2.67

[a] The active area was 1 cm^2.

involves the screen printing and UV-hardening an etch resist on an ITO-covered PET material in a full R2R process followed by etching using aqueous copper chloride, stripping the etch resist using sodium hydroxide, washing the substrate using demineralised water and drying in a full R2R process (shown as steps 1 and 2 in Fig. 4).

The next challenge was to coat the zinc oxide in an R2R process and this was achieved by development of an ink for slot-die coating that is stable in the atmosphere until the layer has been dried.[11,13,14] Slot-die coating proceeded smoothly by

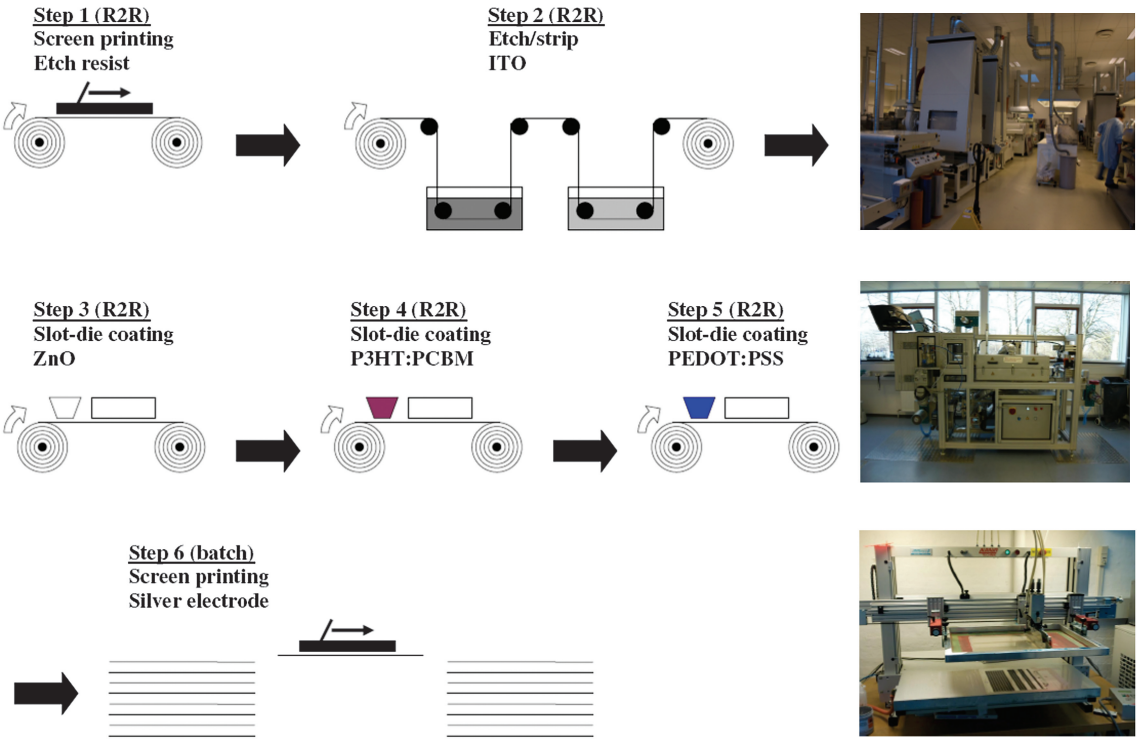

Fig. 4 An illustration of the process and the six different processing steps employed during fabrication of the R2R coated modules.

employing a modified slot-die coating technique described earlier.[14] The ITO pattern is shown in Fig. 5 and the ZnO was coated as 9 mm wide stripes coated on top of the ITO with an offset of 1 mm to the right (as shown in Fig. 5) to allow for contact between the printed silver and the ITO in the serial connection. The active layer was subsequently coated on top of the ITO–ZnO again with an offset of 1 mm to the right with respect to the ZnO. Coating of the P3HT:PCBM mixture proceeded smoothly with good wetting behaviour. Finally the PEDOT:PSS layer was slot-die coated on top of the active layer offset by 1 mm to the right to avoid contact with ITO and ZnO. The wetting of P3HT:PCBM by PEDOT:PSS is not very good and the use of corona treatment is not possible since this destroys the surface of the active layer and thereby device function is impaired. To solve this problem it was useful to mix isopropanol into the PEDOT:PSS and also wet the active layer with isopropanol immediately before the slot-die coating head. Coating proceeded smoothly in this manner. These coating steps are shown in Fig. 4 as steps 3, 4 and 5.

To complete the device the silver back electrode was screen printed on top of the active layer in step 6 as shown in Fig. 4. The overlap between the silver grid lines and the ITO is nominally 6 mm giving an active area for a 25 cm long stripe of 15 cm^2. While printing of the final silver electrode could easily have been performed in a full R2R process it was performed in-house on a manual screen printer after having cut the continuous roll into sheets. This was done to minimize the time between coating the PEDOT:PSS layer and completing the device.

After having dried the silver electrode the 1, 2, 3 and 8 stripe modules were cut into individual modules and either characterised without encapsulation or after back lamination with a simple PET foil using an acrylic adhesive suitable for cold lamination.

The performance of the individual lines was quite close to the model device in terms of voltage and current while the fill factor was quite poor as shown in Fig. 6. The data have been summarized in Table 2. The serial connection of the cells was additive in terms of voltage as expected and each stripe gave 0.47–0.50 V and 100–120 mA whether on its own or connected in series (values as high as 160 mA were observed). In terms of performance it was found that the devices were limited by extraction problems when operating under full sunlight. By decreasing the incident light intensity higher performances were reached and a PCE of more than 2% on the active area and 1% on the module was achieved as shown in Fig. 7. This is still significantly below the performance of the model cells and this was tested by decreasing the active area thus giving a PCE of 2.33% (1000 W m^{-2}, AM1.5G, 72 °C) which is sufficiently close to the model devices to be acceptable (Fig. 7).

The use of the silver grid served several purposes. Firstly it reduces the amount of silver needed and secondly it made the devices more flexible with less delamination problems. A third aspect was that the modules became bifacial and thus responding to illumination from both sides. The backface illumination was less efficient than frontface illumination by a factor of around 5. The module efficiency for an 8 stripe serially connected module with a length of 1 cm (nominal active area = 4.8 cm^2) was, as mentioned above, 2.33% with frontface illumination and only 0.43% with backface illumination and performance decreased in terms of a lower voltage and current while the fill factor increased to 49%. While it is most likely that the reduced performance is due to the thick PEDOT:PSS layer one factor which may

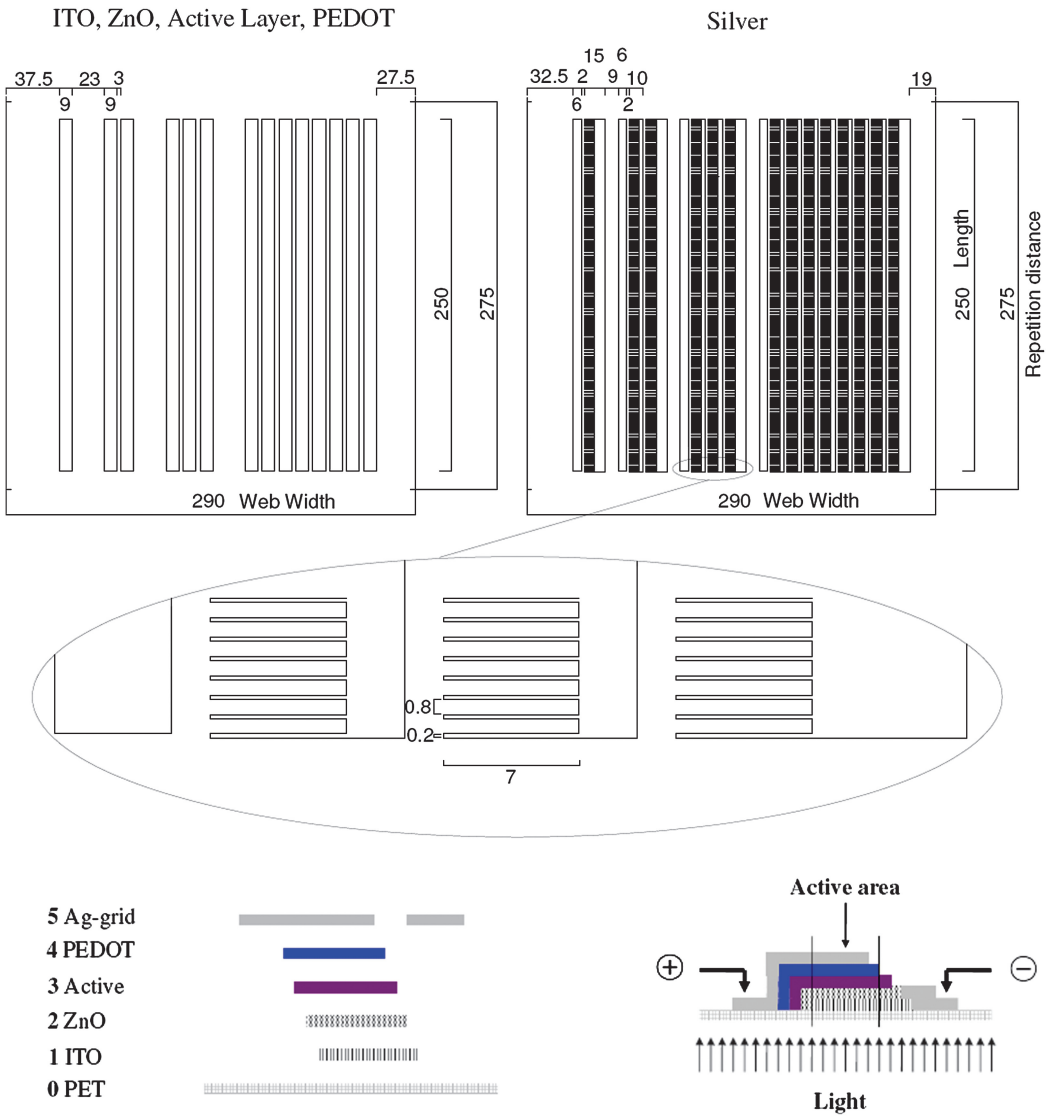

Fig. 5 An illustration of the pattern employed for the R2R processed cells. The ITO pattern is shown (top left). The ZnO, active layer and PEDOT:PSS layers had the same outline but were continuous lines running along the substrate since they were slot-die coated. The silver pattern was screen printed as shown (top right) with a grid pattern over the active area having an aperture loss of 20% (middle). An exploded side view is shown (bottom left) along with a schematic of a one stripe cell emphasizing the overlap of the different layers and their juxtaposition (bottom right).

contribute to the higher fill factor is the photoconductivity of PEDOT:PSS which is illuminated directly when illuminated from the back. For the current devices the thick PEDOT:PSS layer was required for successful device function. It would be a simple matter to reduce the PEDOT:PSS thickness and thus increase transmission of light when illuminating from the backside. Thin PEDOT:PSS layers however led to short circuit which we ascribe to solvent in the silver paste destroying the active layer. A thick PEDOT:PSS layer solved this problem but naturally led to poor transmission from the backside.

In terms of operational stability[4] the electron-collecting electrode is problematic because this implies that the electron carriers travel at high energy levels (LUMO). This is incompatible with operation in the presence of molecular oxygen and water molecules. The hole carriers do not have the same problems associated with transport in the presence of water molecules and molecular oxygen. It should thus in principle be possible to gain stability through an inverted device geometry towards both oxygen and water and to establish this model studies were performed using different atmospheres. The general view of stability of polymer and organic solar cells is that they are an inherently unstable technology with many different degradation processes contributing to the overall decay of the device during operation and in the dark.[4] There are methods to identify and remove (or reduce) the most preponderant mechanisms leaving the less dominant ones. The largest culprits are atmospheric components such as oxygen and water and from the point of view of preparing a functioning device with some level of stability the removal of these by using a suitable barrier material can improve the performance in terms of stability. It is of use to evaluate the stability of the device under four different atmospheric conditions:

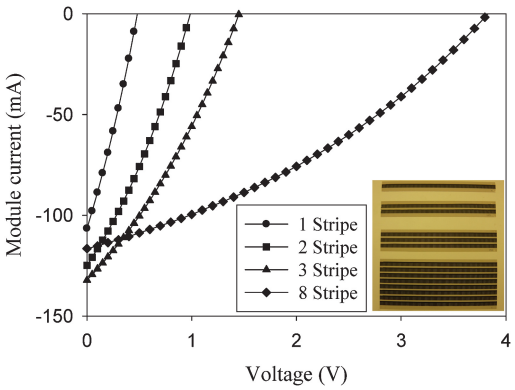

Fig. 6 Typical performance of the individual 1, 2, 3 and 8 stripe modules. The module voltages correspond well to the sum of voltages for the individual cells in the module and the module currents are only slightly affected by the serial connection. The individual modules are shown on the photograph from the backside. The measurement conditions were 1000 W m^{-2}, AM1.5G, 72 ± 2 °C.

1) Nitrogen (water < 1 ppm, oxygen < 1 ppm)
2) Humid nitrogen (water ~90 ± 5% relative humidity, oxygen < 1 ppm)
3) Oxygen (water < 1 ppm, oxygen ~100%)
4) Ambient atmosphere (water ~20 ± 5% relative humidity, oxygen ~20%)

There are many more conditions that could be tested such as varying light intensity, temperature, mechanical flexing, cyclic testing, *etc.* For the purpose of getting a picture of the stability of the device towards the major atmospheric reactants the conditions outlined above are efficiently employed. The normal devices degraded as expected in the presence of humidity[15] but were quite stable in the presence of molecular oxygen (even in pure oxygen). This has been observed earlier for devices based on a low band gap copolymer of thiophene and thienopyrazine.[16] In contrast, devices with a normal geometry based on PPV degrade rapidly in the presence of either water[15] or oxygen.[17] Humidity (water) reacts efficiently with aluminium at unprotected interfaces leading to rapid degradation as shown in Fig. 8 and as summarized in Table 3.

In the inverted device this was then expected to be efficiently solved as silver should not react with water at the metal-organic interface. Good operational stability in the presence of humidity was also observed confirming this hypothesis. However, the device presented poor stability towards oxygen. While it is problematic that we did not achieve stability towards both oxygen and humidity simultaneously it is reassuring that it is possible to make devices that are stable in the presence of oxygen (normal geometry) and in the presence of humidity (inverted geometry). This does hold promise for the possibility of developing a materials and device combination that exhibits stability in the presence of both oxygen and humidity.

It is unfortunate that it was not possible to arrive at a situation with stability towards both oxygen and water simultaneously for the system explored here whereas this had been observed earlier albeit for devices with significantly lower performance.[13,18] One complication is associated with the fact that suppliers of printable silver formulations understandably do not give full chemical detail of their formulations. This however makes it difficult to ascertain whether the observed instability towards oxygen for the devices prepared with silver paste electrodes is due to degradation in the active layers or whether it is the silver paste formulation that is not stable towards oxygen and illumination. This warrants further study. Simple cold back lamination with PET and an acrylic resin as the binder improved the operational stability significantly as shown in Fig. 8. It is interesting that the inverted devices that are based on zinc oxide work well in the absence of oxygen since this has been shown to be problematic earlier in bulk heterojunctions based on PPVs and metal oxide semiconductors including zinc oxide[19] and also for poly-3- carboxydithiophene-ZnO bulk heterojunctions.[13,18] From this point of view dependence on the presence of oxygen for device function was expected. It should however be noted that the charge carrier separation processes in these devices are assumed to take place in the bulk of P3HT and PCBM and that zinc oxide in these devices only work as an electron transport layer. We ascribe the indifference of device function with respect to the presence of molecular oxygen to be due to this fact.

Experimental

Materials employed

Poly(3-hexylthiophene) was prepared according to the McCullough route[20] and was purified by extensive Soxhlet extraction

Table 2 Typical performance of the modules prepared by slot-die coating as shown in Fig. 5, 6 and 7. The nominal active area of each stripe is 15 cm^2. The module performance is also shown corresponding to the total aperture of the printed module including the silver bus. The module areas for the 1, 2, 3 and 8 stripe modules are 57.5, 87.5, 117.5 and 267.5 cm^2, respectively. The measurement conditions were 1000 W m^{-2}, AM1.5G, 72 ± 2 °C unless otherwise stated. The values are for the module unless otherwise stated

Module	*V*/V	*I*/mA	FF (%)	Max. power/mW	Module PCE (%)	Active area PCE (%)
1 stripe	0.48	106.54	28	14.57	0.25	0.97
2 stripe	0.99	124.83	31	38.23	0.44	1.27
3 stripe	1.45	132.18	31	60.44	0.51	1.34
8 stripe	3.83	116.53	34	153.47	0.57	1.28
8 stripe[a]	3.76	159.97	35	213.08	0.79	1.78
8 stripe[a,b]	3.67	76.97	41	117.72	0.88	1.96
8 stripe[a,c]	3.60	60.00	44	97.94	0.93	2.08
8 stripe[a,d]	3.62	6.87	44	11.20	1.04	2.33
8 stripe[a,d,e]	3.09	1.35	49	2.06	0.19	0.43

[a] Laminated. [b] Incident light 500 W m^{-2}. [c] Incident light 393 W m^{-2}. [d] A module with the length reduced to 1 cm (active area 4.8 cm^2) to minimize resistive loss in the silver bus. [e] backface illumination of the device.

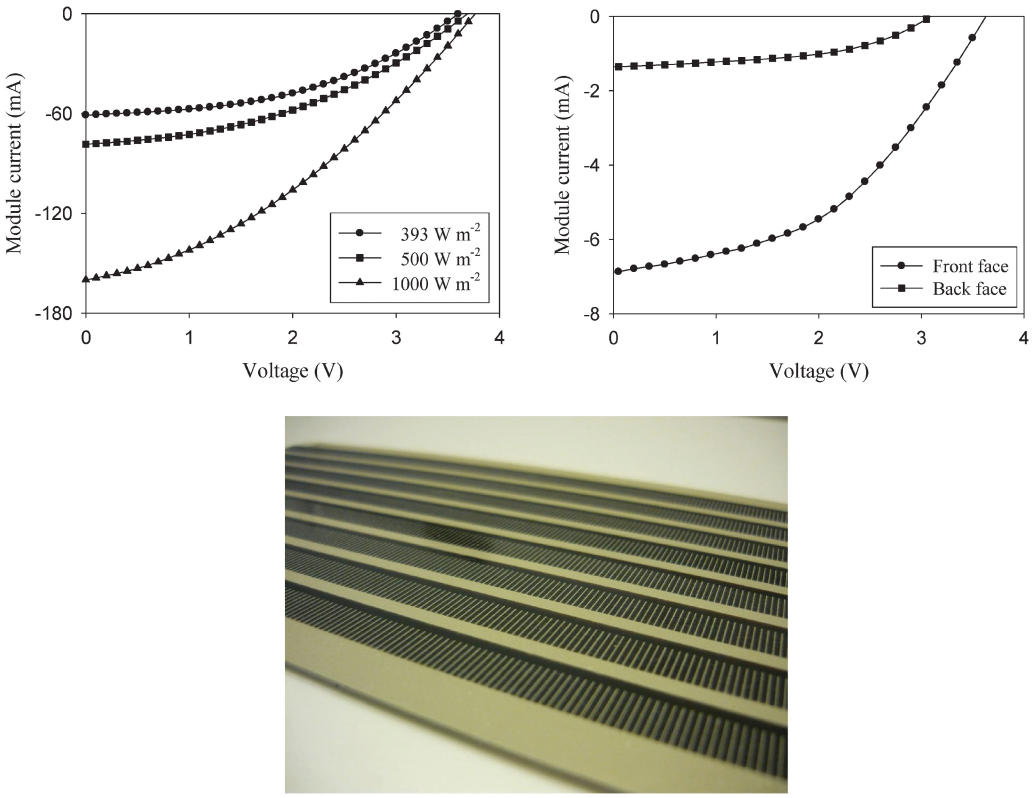

Fig. 7 *IV*-curves for a full 8 stripe module with a nominal active area of 120 cm^2 as a function of incident light intensity (top left) and for an 8 stripe module with a length of 1 cm giving a nominal active area of 4.8 cm^2 (top right). The device is also responsive to light entering the device through the printed silver grid back electrode albeit with lower performance due to the aperture loss from the grid and transmission loss in the PEDOT:PSS (top right). A photograph of the 8 stripe module from the back electrode highlighting the printed silver grid is also shown (bottom). Data are shown in Table 2.

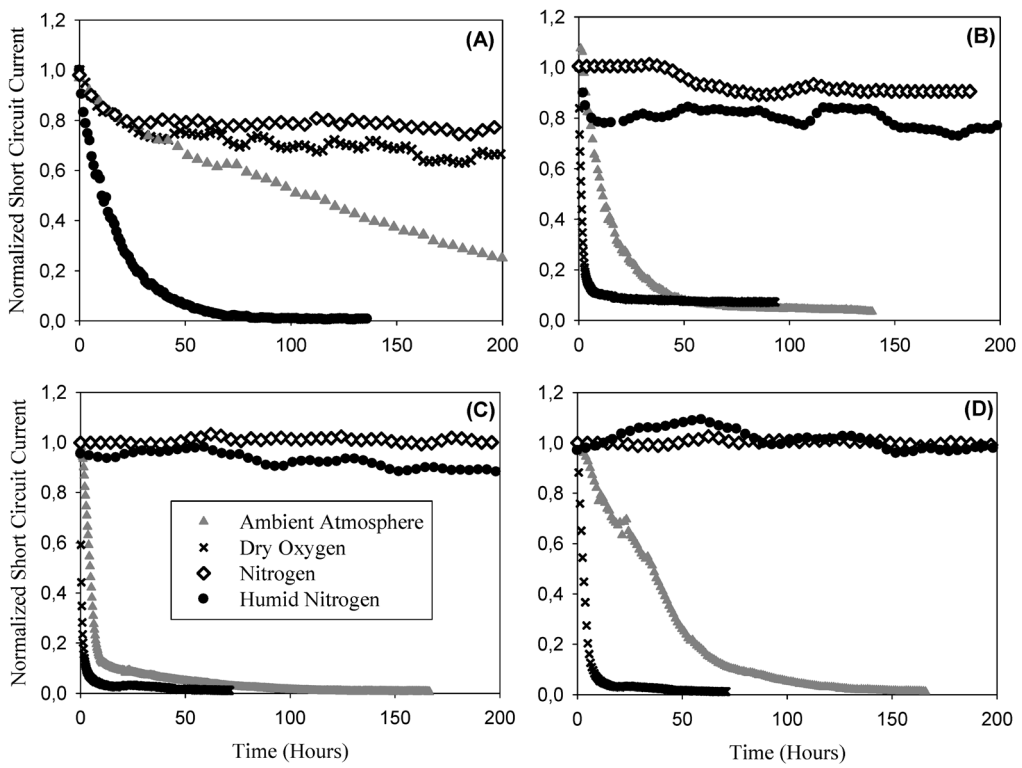

Fig. 8 Curves showing the degradation as a function of illumination time under different atmospheric conditions for device models with normal geometry (A) and inverted geometry (B) and R2R processed inverted devices without encapsulation (C) and with simple encapsulation (D).

Table 3 Stability testing under different atmospheric conditions

Module	N_2	H_2O	O_2	H_2O/O_2
Normal geometry (evaporated Al) [a]	+	—	+	—
Inverted geometry (evaporated Ag) [a]	+	+	—	—
Inverted geometry (solution processed silver paste) [a]	+	+	—	—
Inverted geometry (All R2R processed) [b]	+	+	—	—

[a] The active area was 3 cm^2, the measurement conditions were 330 W m^{-2}, AM1.5G, 40 ± 3 °C. [b] The active area was 4.8 cm^2, the measurement conditions were 330 W m^{-2}, AM1.5G, 40 ± 3 °C.

procedures employing in turn methanol, acetone, hexane and finally chloroform. The product was precipitated from chloroform using methanol. The procedure was repeated twice giving a material with a regioregularity >97% and $M_n = 18\,700$, $M_w = 36\,600$, $M_p = 33\,900$, PD = 1.9. [60]PCBM was purchased from Solenne BV with a purity of 99%. Zinc oxide nanoparticles (ZnO np) were prepared and stabilised with methoxyethoxyacetic acid (MEA) as described earlier.[13] The thermocleavable solvent WS-1 was obtained as described in the literature.[21,22] PEDOT:PSS was purchased as an aqueous dispersion from Aldrich or as a screen printing paste from Agfa (Orgacon EL-P 5010, www.agfa.com). The silver electrode was purchased from Dupont as a screen printing paste (Dupont PV410, www.dupont.com). The substrates for the model devices comprised 25 mm × 50 mm ITO covered glass substrates with a nominal sheet resistance of 5–8 Ohm $square^{-1}$. The flexible substrate was purchased as ITO covered poly(ethylene terephthalate) (PET) (175 μm) in rolls having a roll width of 305 mm and a length of 100 m. The material was used as received from Innovative Specialty Films (ISF, T-MOX). The nominal sheet resistance was 60 Ohm $square^{-1}$. The material was trimmed to a web width of 290 mm and reference holes were punched along the edges. Cold lamination with a mechanical protection layer was carried out on top of the silver back electrodes, using a 25 μm thick Fasson overlaminating polyester material from Avery Dennison.

Model device preparation

Normal geometry. The ITO covered glass slides for the model devices were ultrasonically cleaned in 2-propanol and distilled water for 10 min followed by spincoating an aqueous dispersion of PEDOT:PSS (purchased from Aldrich) at a rotational speed of 2800 rpm. The samples were annealed at 150 °C and transferred into a glovebox (oxygen and water <0.1 ppm), where an active layer of P3HT:PCBM (25 : 22 mg mL^{-1} in *m*-xylene) was spincoated at 800 rpm, followed by drying. Subsequently an aluminium electrode was evaporated on top and the final device was annealed at 150 °C for 5 min.

Inverted geometry. After the same procedure of ultrasonic cleaning the glass/ITO slides were transferred into a glovebox, where a layer of unstabilized ZnO nanoparticles (50 mg mL^{-1} chlorobenzene) was spincoated at a rotational speed of 1000 rpm, which followed by spincoating of the active layer consisting of the same compound used for the normal geometry device and subsequent drying in dichlorobenzene vapour. Finally, a layer of PEDOT:PSS (Agfa 5010) was applied by firstly wetting the surface of the P3HT:PCBM with isopropanol followed by spincoating the PEDOT:PSS solution at 3000 rpm followed by annealing at 130 °C for 5 min and final evaporation of silver. Model devices had an active area of 1 cm^2, while the decay studies were carried out on devices with 3 cm^2 active area.

Coating and printing equipment

The patterning of ITO was performed on a Klemm line at Mekoprint A/S.[11] The slot-die coating was performed on a BC30 basecoater from Solar Coating Machinery (Germany) comprising unwinder, corona treater, edge guide, double faced contact cleaning, antistatic system, coating station, oven and winding station.[14] The manual screen printing was performed on an AT701 from Alraun Technik (Germany). The screens were mounted with a 120 mesh screen for printing the silver paste.

R2R processing

Step 1 (screen printing etch resist). The desired striped pattern of the ITO (Fig. 5) was prepared by printing a UV-curable etch resist in the areas of the ITO pattern on a Klemm line in a full R2R process (Fig. 4). The printing speed was 180 prints h^{-1}. The pattern is shown to the left in Fig. 5 and comprises stripes with a width of 9 mm spaced by 3 mm and a length of 250 mm along the direction of the web. The repetition distance was 275 mm since it is not possible to print continuous lines with a reversing screen printer. The distance of 25 mm between the stripes allowed for a sufficient margin between prints. The processing speed for printing and UV-curing the etch resist was 49.5 m h^{-1}.

Step 2 (etching and stripping). The ITO was subsequently etched using a full R2R etching machine comprising etching baths ($CuCl_2$), stripping baths (NaOH), washing baths (demineralised water) and drying sections (hot air). The etching speed was 40 m h^{-1}. The thickness of the ITO was 80 nm.

Step 3 (slot-die coating of ZnO). ZnO nanoparticles in chlorobenzene solution were stabilized with MEA and mixed with WS-1 followed by evaporation of chlorobenzene and methanol to give ZnO nanoparticles in WS-1. This stock solution was diluted with 4 volumes of *o*-xylene to give the final ink that was microfiltered through a 0.45 micron Teflon filter immediately prior to coating. The concentration of ZnO nanoparticles in the final coating ink was 30 mg mL^{-1}. The typical coating speed was 54 m $hour^{-1}$. The material was dried at temperatures up to 140 °C with a residence time in the oven of around 1 minute. This gave insoluble films of zinc oxide.

Step 4 (slot-die coating of P3HT:PCBM). P3HT was dissolved in dichlorobenzene followed by addition of PCBM. When making up the final ink one volume of chloroform was added giving a final concentration of 22 mg mL^{-1} P3HT and 20 mg mL^{-1} PCBM. The typical coating speed was 24 m h^{-1}. The material was dried at temperatures up to 140 °C with a residence time in the oven of around 2–3 min.

Step 5 (slot-die coating of PEDOT:PSS). PEDOT:PSS was used as a screen printing formulation (Agfa 5010) that was diluted with isopropanol (100 g PEDOT:PSS was mixed with 60 g isopropanol) and shaken vigorously for 1 h. The desired viscosity was around 200 mPa s. The typical coating speed was 12 m h^{-1} and involved wetting of the active layer with isopropanol immediately prior to coating in order to avoid dewetting of the PEDOT:PSS layer prior to drying. The material was dried at temperatures up to 140 °C with a residence time in the oven of around 5 min.

Step 6 (sheet fed screen printing of the silver back electrode). The material was unwound and cut manually into sheets. Registry holes were punched along one of the edges to allow indexing of the silver grid structure on the screen with the coated pattern on the substrate. The silver paste (PV410) was printed using a small laboratory screen printer with a printing speed of 550 mm s^{-1}. The drying was carried out immediately after printing at 140 °C in a hot air oven. The total drying time was 15 min.

Post treatment. The finally processed material was cut into 1 stripe, 2 stripe, 3 stripe and 8 stripe modules that were either used as is or back-laminated using a thin PET based 25 micron foil material. Contacts were applied using alligator clips to the silver bus.

Device and module characterisation

Model devices. When characterising devices with an inverted device geometry care has to be taken to avoid overestimation of the PCE due to a larger effective overlap between electrodes. This is due to the fact that PEDOT:PSS conducts significantly well to allow for harvesting light in areas outside the evaporated silver back electrode. In order to avoid this the devices were illuminated through a shadow mask such that only the active area was illuminated. In order to be consistent the masking was also performed for the devices with a normal geometry.

R2R coated devices. The effective active area for each stripe is typically 250 mm × 6 mm. The width varies a little depending on the alignment and therefore the overlap between the ITO electrode and the PEDOT:PSS-silver back electrode also varies. The nominal active areas, aperture areas and geometric fill factor for the modules were as follows: single stripe modules (15 cm^2, 57.5 cm^2, 26%), two stripe module (30 cm^2, 87.5 cm^2, 34%), three stripe module (45 cm^2, 117.5 cm^2, 38%) and the eight stripe module (120 cm^2, 267.5 cm^2, 45%). The *IV*-characteristics were recorded using a Keithley 2400 sourcemeter. The conditions of the characterization under simulated sunlight were KHS 575 solar simulators from Steuernagel Lichttechnik operating at 1000 W m^{-2}, AM1.5G, 45 ± 5% relative humidity, 72 ± 3 °C. The spectrum of the solar simulator was checked using an optical spectrum analyzer calculated for measuring irradiance. The incident light intensity of the solar simulator was calibrated bolometrically using a precision spectral pyranometer from Eppley Laboratories (www.eppleylab.com). The incident light intensity was monitored continuously during measurements using a CM4 high temperature pyranometer from Kipp & Zonen (www.kippzonen.com).

Stability studies

The devices were mounted using silver epoxy and inserted into atmospheric test chambers as described earlier.[23] After introduction of the devices in the test chamber the chamber was evacuated to a pressure of 10^{-2} mBar and the desired atmosphere was introduced. This evacuation and refilling procedure served to quickly reach the desired levels of humidity and oxygen in the chamber. Light was hereafter admitted to the device and the *IV*-curves were recorded every 5 min during the experiment. The experiments were carried out for 200 h and the illumination of the devices was constant. The temperature of the devices during the stability experiments was 40 ± 3 °C.

Conclusion

Inverted model devices comprising glass/ITO/ZnO/P3HT-PCBM/PEDOT:PSS/silver were optimized to exhibit the same performance as model devices with a normal geometry (glass/ITO/PEDOT:PSS/P3HT-PCBM/aluminium). The active area of the model devices was 1 cm^2 and illumination was through the glass/ITO (frontface). The power conversion efficiency that could be obtained for both devices as tested under ambient conditions was 2.7% (AM1.5G, 1000 W m^{-2}, 72 ± 2 °C, 40 ± 5% relative humidity). The devices were tested in different model atmospheres and the normal device geometry was found to be sensitive to moisture but stable in dry oxygen. This effect is ascribed to interaction with aluminium at the interface between the active layer and the aluminium electrode. In contrast the inverted devices were stable in the presence of humidity but were sensitive to oxygen. The process leading to the inverted model device was subsequently transferred to a full R2R process employing a flexible PET substrate covered with ITO as the source material. The ITO was processed into stripes by screen printing an etch resist, etching away the ITO as desired followed by stripping of the etch resist. Subsequently, a zinc oxide layer, the active layer and a PEDOT:PSS layer were juxtaposed and coated on top of the ITO layer using slot-die coating. Finally the device was completed using a screen printed silver paste. All the device preparation for the R2R processed devices was performed in air without special precaution. Several different modules were explored in the R2R process and single cell modules and serially connected modules comprising 2, 3 and 8 cells in series were explored. The best performance that was obtained for the modules comprising 8 serially connected cells was 1.7% for the active area of the full module that was limited by extraction of carriers. The performance for a small area device where the Ohmic losses had been reduced amounted to 2.3% for an active area of 4.8 cm^2 which is similar to the performance obtained for the model devices.

Acknowledgements

This work was supported by the Danish Strategic Research Council (DSF 2104-05-0052 and 2104-07-0022). We thank Jan Fyenbo at Mekoprint A/S for help during preparation and patterning of the flexible ITO substrate. The method for manufacture of polymer solar cells described in this work is known as ProcessOne.

References

1 C. J. Brabec, N. S. Sariciftci and J. C. Hummelen, *Adv. Funct. Mater.*, 2001, **11**, 15; H. Spanggaard and F. C. Krebs, *Sol. Energy Mater. Sol. Cells*, 2004, **83**, 125–146; K. M. Coakley and M. D. McGehee, *Chem. Mater.*, 2004, **16**, 4533–4542; H. Hoppe and N. S. Sariciftci, *J. Mater. Res.*, 2004, **19**, 1924–1945.

2 H. Hoppe and N. S. Sariciftci, *J. Mater. Chem*, 2006, **16**, 45–61; S. Günes, H. Neugebauer and N. S. Sariciftci, *Chem. Rev.*, 2007, **107**, 1324; B. C. Thompson and J. M. J. Fréchet, *Angew. Chem., Int. Ed.*, 2008, **47**, 58.

3 C. Winder and N. S. Sariciftci, *J. Mater. Chem.*, 2004, **14**, 1077–1086; E. Bundgaard and F. C. Krebs, *Sol. Energy Mater. Sol. Cells*, 2007, **91**, 954–985; R. Kroon, M. Lenes, J. C. Hummelen, P. W. M. Blom and B. de Boer, *Polym. Rev.*, 2008, **48**, 531.

4 M. Jørgensen, K. Norrman and F. C. Krebs, *Sol. Energy Mater. Sol. Cells*, 2008, **92**, 686–714.

5 C. J. Brabec and J. R. Durrant, *MRS Bull.*, 2008, **33**, 670–675; F. C. Krebs, *Sol. Energy Mater. Sol. Cells*, 2009, **93**, 394–412.

6 C. J. Brabec, S. E. Shaheen, C. Winder and N. S. Sariciftci, *Appl. Phys. Lett.*, 2002, **80**, 1288–1290.

7 T. Ameri, G. Dennler, C. Waldauf, P. Denk, K. Forberich, M. C. Scharber, C. J. Brabec and K. Hingerl, *J. Appl. Phys.*, 2008, **103**, 084506; G. Li, C.-W. Chu, V. Schrotriya, J. Huang and Y. Yang, *Appl. Phys. Lett.*, 2006, **88**, 253503.

8 B. Zimmermann, M. Glatthaar, M. Niggemann, M. K. Riede, A. Hinsch and A. Gombert, *Sol. Energy Mater. Sol. Cells*, 2007, **91**, 374–378.

9 T. Aernouts, P. Vanlaeke, W. Geens, J. Poortmans, P. Heremans, S. Borghs, R. Mertens, R. Andriessen and L. Leenders, *Thin Solid Films*, 2004, **451–452**, 22–25; B. Winther-Jensen and F. C. Krebs, *Sol. Energy Mater. Sol. Cells*, 2006, **90**, 123; M. Strange, D. Plackett, M. Kaasgaard and F. C. Krebs, *Sol. Energy Mater. Sol. Cells*, 2008, **92**, 805; J.-Y. Lee, S. T. Connor, Y. Cui and P. Peumans, *Nano Lett.*, 2008, **8**, 689–692.

10 C. Lungenschmied, G. Dennler, H. Neugebauer, N. S. Sariciftci, M. Glatthaar, T. Meyer and A. Meyer, *Sol. Energy Mater. Sol. Cells*, 2007, **91**, 379; F. C. Krebs, J. Alstrup, H. Spangaard, K. Larsen and E. Kold, *Sol. Energy Mater. Sol. Cells*, 2004, **83**, 293–300; F. C. Krebs, H. Spanggaard, T. Kjær, M. Biancardo and J. Alstrup, *Mater. Sci. Eng., B*, 2007, **138**, 106; M. Niggemann, B. Zimmermann, J. Haschke, M. Glatthaar and A. Gombert, *Thin Solid Films*, 2008, **516**, 7181–7187.

11 F. C. Krebs, M. Jørgensen, K. Norrman, O. Hagemann, J. Alstrup, T. D. Nielsen, J. Fyenbo, K. Larsen and J. Kristensen, *Sol. Energy Mater. Sol. Cells*, 2009, **93**, 422–441.

12 M. K. Riede, K. O. Sylvester-Hvid, M. Glatthaar, N. Keegan, T. Ziegler, B. Zimmermann, M. Niggemann, A. W. Liehr, G. Willeke and A. Gombert, *Progr. Photovolt.: Res. Appl.*, 2008, **16**, 561; W. Ma, C. Yang, X. Gong, K. Lee and A. J. Heeger, *Adv. Funct. Mater.*, 2005, **15**, 1617–1622; G. Li, V. Shrotriya, J. S. Huang, Y. Yao, T. Moriarty, K. Emery and Y. Yang, *Nat. Mater.*, 2005, **4**, 864.

13 F. C. Krebs, Y. Thomann, R. Thomann and J. W. Andreasen, *Nanotechnology*, 2008, **19**, 424013.

14 F. C. Krebs, *Sol. Energy Mater. Sol. Cells*, 2009, **93**, 465–475.

15 K. Norrman, S. A. Gevorgyan and F. C. Krebs, *ACS Appl. Mater. Interfaces*, 2009, **1**, 102–112.

16 M. H. Petersen, S. A. Gevorgyan and F. C. Krebs, *Macromolecules*, 2008, **41**, 8986–8994.

17 T. Jeranko, H. Tributsch, N. S. Sariciftci and J. C. Hummelen, *Sol. Energy Mater. Sol. Cells*, 2004, **83**, 247; F. C. Krebs, J. E. Carlé, N. Cruys-Bagger, M. Andersen, M. R. Lilliedal, M. A. Hammond and S. Hvidt, *Sol. Energy Mater. Sol. Cells*, 2005, **86**, 499; K. Kawano, R. Pacios, D. Poplavskyy, J. Nelson, D. D. C. Bradley and J. R. Durrant, *Sol. Energy Mater. Sol. Cells*, 2006, **90**, 3520; K. Norrman and F. C. Krebs, *Sol. Energy Mater. Sol. Cells*, 2006, **90**, 213; K. Norrman, J. Alstrup, M. Jørgensen and F. C. Krebs, *Surf. Interface Anal.*, 2006, **38**, 1302–1310.

18 F. C. Krebs, *Sol. Energy Mater. Sol. Cells*, 2008, **92**, 715.

19 M. Lira-Cantu and F. C. Krebs, *Sol. Energy Mater. Sol. Cells*, 2006, **90**, 2076; M. Lira-Cantu, K. Norrman, J. W. Andreasen and F. C. Krebs, *Chem. Mater.*, 2006, **18**, 5684–5690; M. Lira-Cantu, K. Norrman, J. W. Andreasen, N. Casan-Pastor and F. C. Krebs, *J. Electrochem. Soc.*, 2007, **154**, B508–B513.

20 R. D. McCullough, R. D. Lowe, M. Jayaraman and D. L. Anderson, *J. Org. Chem.*, 1993, **58**, 904–912.

21 F. C. Krebs and M. Jørgensen, *WO Pat.*, 2007118850 A1.

22 M. Jørgensen, O. Hagemann, J. Alstrup and F. C. Krebs, *Sol. Energy Mater. Sol. Cells*, 2009, **93**, 413.

23 S. A. Gevorgyan, M. Jørgensen and F. C. Krebs, *Sol. Energy Mater. Sol. Cells*, 2008, **92**, 736.

Available online at www.sciencedirect.com
ScienceDirect
Solar Energy Materials & Solar Cells 92 (2008) 736–745
Solar Energy Materials and Solar Cells
www.elsevier.com/locate/solmat

A setup for studying stability and degradation of polymer solar cells

Suren A. Gevorgyan, Mikkel Jørgensen, Frederik C. Krebs*

National Laboratory for Sustainable Energy, Technical University of Denmark, Frederiksborgvej 399, DK-4000 Roskilde, Denmark

Received 13 November 2007; received in revised form 14 February 2008; accepted 14 February 2008

Abstract

A detailed description of a setup for studying ageing of polymer devices is presented. The system offers individual control of the environmental factors (oxygen, humidity, atmosphere, temperature and light intensity) causing the degradation of organic devices. The system was developed for accurate control of the conditions and data collection of photovoltaic (PV) parameters for organic solar cells during long-term testing. The atmosphere chamber can operate under vacuum conditions without temperature control. It is designed for operation at an internal gas pressure of around 1 atm. It is further equipped for isotopic labeling experiments of the internal atmosphere ($^{18}O_2$ and $H_2{}^{18}O$) such that degradation mechanisms can be studied using TOF-SIMS as a chemical probe. Experiments on both "accelerated" (by applying thermal stress to the devices) and "long-term" lifetime measurements of traditional organic bulk heterojunction solar cell devices have been realized while controlling the environmental conditions. As an example of use of the setup we determined the acceleration factor for standard bulk heterojunction devices based on ITO/PEDOT:PSS/P3HT-[60]PCBM/Al when operated under an ambient atmosphere and under an inert atmosphere at temperatures of 25, 43, 63 and 83 °C. Different values for the acceleration factor were found depending on the atmosphere used and further our results suggest that the acceleration factor may change in time as different degradation mechanisms may dominate at different times during the device life.

Keywords: Stability; Degradation; Accelerated testing; Multiple processes; Setup; Instrumentation

1. Introduction

The field of polymer solar cells is still in a state of rapid development and has been reviewed several times [1–8]. The efficiency has reached 5% for simple bulk heterojunction cells [9,10] and 6.5% for tandem cells [11], while theoretical predictions suggest that it should be possible to obtain 10% [12,13]. The short operational stability and lifetime still remain one of the key issues of polymer PVs [14]. Significant improvement of stability and increase of lifetimes up to scales that could comply with industrial standards are essential requirements for further progress and commercialization of organic solar cell devices.

The ageing phenomenon in the organic solar cells occurs due to the combined influence of environmental factors, such as light, temperature, oxygen, humidity and intrinsic factors such as the constituents of the device. A number of scenarios have been proposed to describe the degradation processes [15–26] mainly using TOF-SIMS [20–26]. As yet, however, there is no general rule as to what mechanisms take place for any given device disposition and each case must still be studied in detail and while some basic mechanisms have been identified the overall scheme still remains unclear. In order to produce devices with good stability, it is necessary to thoroughly understand the decay mechanisms taking place in the cells. The effect of each of the aforementioned environmental components must be understood and mapped in order to prevent or sufficiently slow down the processes that they result in. Therefore, it is essential to develop an efficient procedure for accurate stability measurements of organic solar cell devices, while controlling all the affecting parameters individually. Methods, standards and equipment for studying inorganic solar cells were developed in the mid-1980s along with standardized measurement procedures of power conversion efficiency through a massive series of publications and standards [27–37] that later have been adapted for power

*Corresponding author. Tel.: +45 46 77 47 99.
E-mail address: Frederik.krebs@risoe.dk (F.C. Krebs).

0927-0248/$ - see front matter © 2008 Elsevier B.V. All rights reserved.
doi:10.1016/j.solmat.2008.02.008

conversion efficiency measurements of organic solar cells [38–40]. From this point of view one may ask why there is any need for a description of an apparatus for doing essentially the same with the exception that the solar cell is a polymer or an organic-based device. To answer this question we point to the fact that polymer and organic PVs differ from the inorganic technologies in the way they break down as detailed in this issue [14]. Inorganic solar cells are nearly all intrinsically stable from a chemical point of view and the materials will withstand illumination under intense sunlight in the ambient atmosphere indefinitely. Organic and polymer materials do not have this ability and will degrade over time. From this point of view the degradation of PV devices based on inorganic and organic materials share only some of the mechanisms associated with degradation (i.e. mechanical, encapsulant, electrical connections) but they do not share the internal instability of the material that organics have. As a result organic solar cells require special techniques for studying degradation and stability [14,20–26].

Standard test conditions have been proposed for accurate indoor determination of the power conversion efficiency of organic solar cell devices [38–40], which allow for an evaluation of the cells in a comparable manner. However, it is technically complicated to characterize the cells within a longer period, if the lifetimes extend far beyond a month. One of the proposed partial solutions is long-term out-door testing of the cells under real sun [41] which includes the effect of nighttime and different weather conditions. As such this gives essential information on how the solar cell would perform under real conditions. In our case the aim is to correlate the observed degradation to the well-defined conditions of the experiment (light intensity, atmosphere, etc.) and from this point of view the demand for reliable weather conditions in the particular region are too extreme and in-door measurements using accelerated conditions are best suited. Accelerated lifetime measurements have been reported [42,43] and simply involve the application of a certain stress to the cells that accelerates the decay processes inside the device. The prediction of an operational lifetime under normal conditions can ideally be predicted from the accelerated data and the acceleration factor assuming that it is constant. The acceleration factor may vary depending on the type of the material and conditions.

In this article we describe a setup that allows for controlled and accurate long-term stability measurements of organic PV devices. This easy-to-use setup consists of an atmospheric chamber (AC) (manufactured at the National Laboratory for Sustainable Energy) and apparatus for recording the decay of PV parameters. A full description of the AC that allows for creating specific environmental conditions during the testing process is given. A few words are devoted to installation of samples inside the chamber and realization of periodic lifetime measurements under certain ambient conditions. Additionally, to demonstrate the use of the apparatus we compare results of both accelerated and normal lifetime measurements for traditional polymer bulk heterojunction solar cells maintained under ambient or inert environmental conditions using the AC setup. The rates of degradation for the devices maintained under different conditions were used to estimate acceleration factors and the results are discussed.

2. Experimental

2.1. Description of the experimental setup

The general experimental setup is shown in Fig. 1. Up to two devices under investigation are placed in an AC beneath the sun simulator and connected to a source measure unit (SMU) through a multiplexing system (*vide supra*) to obtain diode characteristics at intervals. The intensity of the flux from the sun simulator is measured using a precision pyranometer (Eppley Laboratories) in conjunction with irradiance measurements using an optical spectrum analyzer (AvaSpec 2048 from Avantes) to ensure that the conditions approach AM1.5G. The solar simulator is Class AAA with the exception of the wavelength range 700–800 nm where it is Class AAB with respect to non-uniformity, temporal instability and spectral match. It is not possible to fit the pyranometer inside the chamber and therefore Hamamatsu S1133 KG5 filtered photodiodes were employed inside the chamber (see our website www.risoe.dk/solarcells for a routine solar simulator calibration). We have not corrected for mismatch in the data reported as the purpose is not accurate determination of the device efficiency but rather the relative degradation of the performance. It is however possible with the setup presented here and the standard method that has been

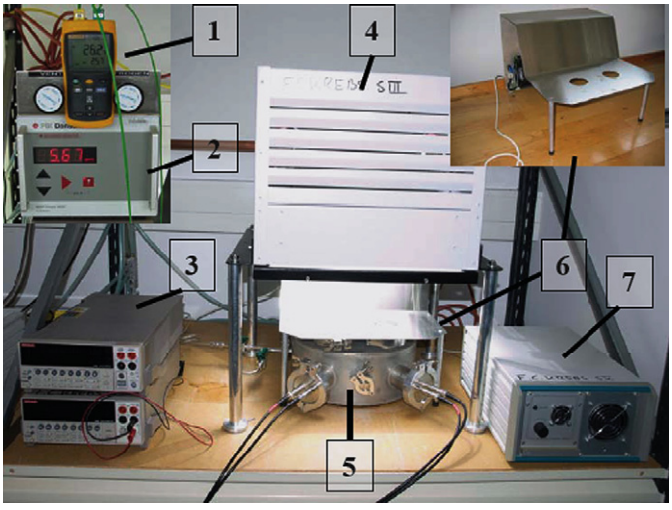

Fig. 1. *IV* testing setup: digital thermometer—to monitor the data of the thermocouples (1), O_2 Analyzer MAP Check 9000 (PBI Dansensor) (2), Keithley 2400 Sourcemeter and Keithley 2000 Multimeter—to transfer the *IV* data to PC (3), solar simulator (KHS Solar Constant 575) (4), atmospheric chamber (5), metal screen—to protect the chamber from overheating (also shown as an inset in the upper right corner) (6), power supply for solar simulator (7).

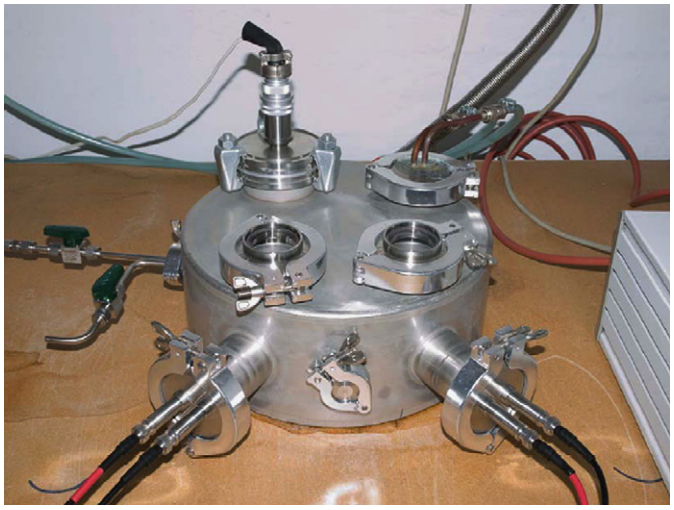

Fig. 2. General view of the atmospheric chamber (AC).

described in the literature [39,40]. A picture of the AC is shown in Fig. 2, and as a technical drawing in Fig. 3. The chamber is constructed as a closed steel cylinder with two access ports (flanges 6) for solar cell devices and corresponding viewports (Figs. 3 and 5)—quartz windows [44] mounted on the top. These windows have less than 10% absorbance in the wavelength range from 250 to 2600 nm and less than 50% up to 3400 nm. During measurements the chamber can be evacuated to remove any oxygen or water via flange (7) connected to an oil-free scroll-pump (vacuum: 10^{-2} mbar) or a turbomolecular pump (vacuum: $<10^{-6}$ mbar). Devices can also be measured in a controlled atmosphere e.g. nitrogen. This atmosphere (N_2 from a gas cylinder) is admitted through another flange (8). The ambient air is replaced by placing the entire chamber in a nitrogen-filled glove-box. If ambient or artificial atmosphere is present in the chamber inside fans are used to even out any temperature variations.

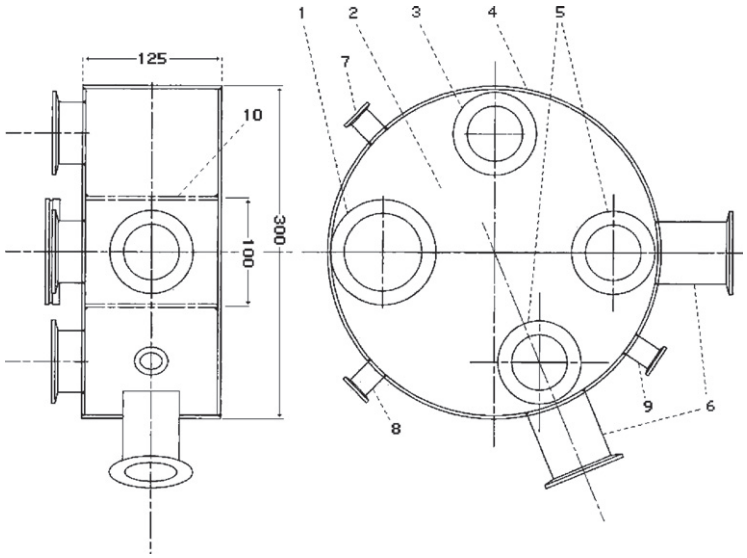

Item	Qty.	Description	Material	Purpose
1	1	DN63LF Flange	Stainless Steel	To introduce fans for circulation
2	1	Top Plate (thickness 3*)	Stainless Steel	-
3	1	KF50 Flange	Stainless Steel	To introduce cooling pipeline
4	1	Chamber Frame (thickness 3*)	Stainless Steel	-
5	2	KF50 Flange	Stainless Steel	Viewports for light exposure
6	2	KF50 Flange	Stainless Steel	To place testing samples
7	1	KF16 Flange	Stainless Steel	For Vacuum Pump and humidity sensor
8	1	KF16 Flange	Stainless Steel	To pump inert gases
9	1	KF16 Flange	Stainless Steel	To introduce thermocouples
10	1	Ring of central cylindrical cavity	Stainless Steel	-

*all dimensions are in mm

Fig. 3. Sketch of the atmospheric chamber: the side (left) and the top (right) views. All geometrical dimensions are in mm. Table below describes details of different components.

These fans are mounted through a large flange (1) shown in detail in Fig. 4a. The temperature affects both the performance and the lifetime of the devices so it must be controlled. This is achieved through active cooling with a cooling fluid circulating through copper pipes as shown in Fig. 4b. Some of the heat from the sun simulator can also be deflected using a metal screen so that light is only allowed through apertures over the windows in the chamber (upper right-hand inset in Fig. 1). External cooling fans are mounted on the backside of the screen so they can cool the chamber with the surrounding atmosphere. The parameters of temperature, pressure, oxygen and water content are measured using gauges and sensors. The temperature is measured with two thermocouples (type K) that go in through a flange (9). One is placed on a spring fixed on the bottom of the chamber directly under the device to be tested and another has thermal contact with the circulating atmosphere. The thermocouples are connected to an external multimeter (Fig. 1(1)) for read-out. A humidity sensor (Gallatec, CVC 2/5 humidity/temperature sensor) (Figs. 5 and 6) can be connected to the chamber using the flange for the vacuum pump, or via a T-shaped connector junction. In the latter case vacuum can be applied to the system while the humidity is measured. Another future possibility is to add a humidifier to the system to control the humidity over a range. The oxygen concentration inside the chamber is monitored using an O_2 analyzer (MAP Check 9000, PBI Dansensor) that is mounted on flange 8.

The solar cell devices are mounted on a sample holder that ensures the correct placement and orientation beneath the windows in the AC. A close-up is seen in Fig. 5. The sample holder consists of two copper rods with BNC connectors, one longer than the other, that are connected to the device using thermosetting silver epoxy paste. This holder is then mounted on the vacuum flange with electrical feed throughs and connected to the SMU on the outside.

2.2. Sample illumination

The AC, with the samples, is illuminated using the solar simulator. Inside the chamber the intensity is reduced

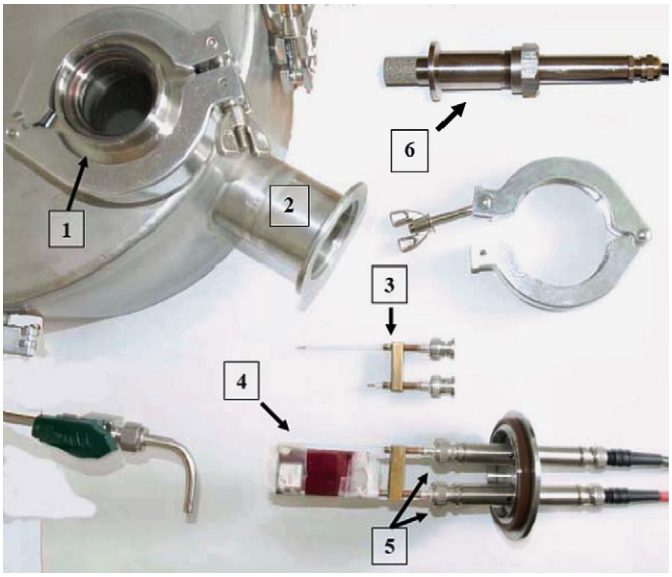

Fig. 5. Viewport for exposing the sample to light (1), KF flange for introducing the samples (2), holder with BNC connections for fixing the samples (3), tested solar cell (4), cell with holder fixed on the flange through BNC connections (5) and humidity sensor with high-grade steel housing (Gallatec) (6).

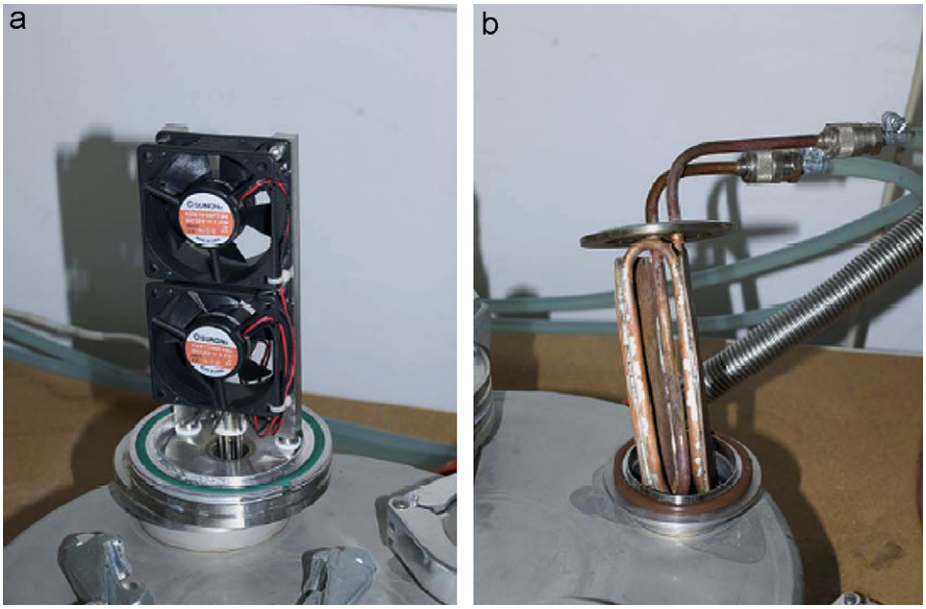

Fig. 4. System for circulation with two fans fixed on the flange (a) and the cooling copper pipe welded on the flange (b).

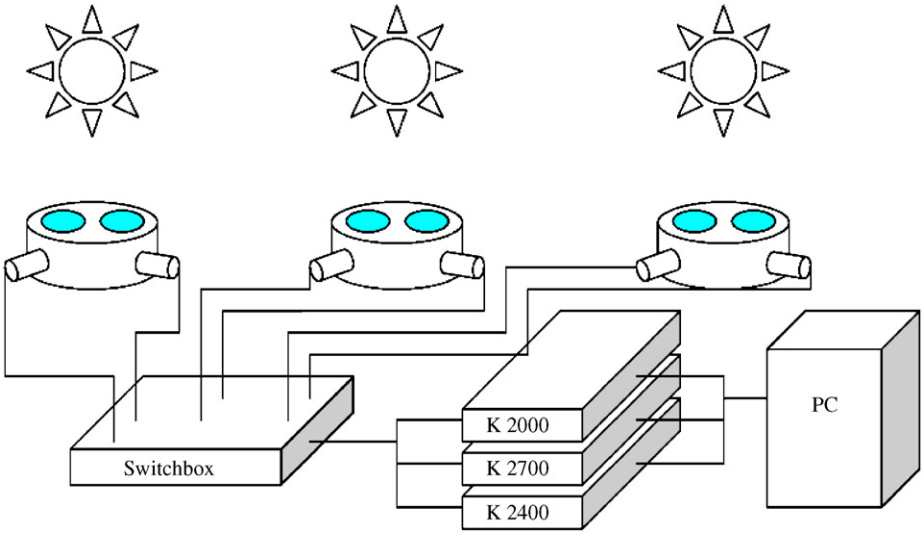

Fig. 6. Schematic drawing of the PC-controlled Keithley 2400 SMU and multiplexing unit Keithley 2700.

somewhat partly because a small part of the radiation is absorbed in the quartz windows, and partly because the window aperture is limited (inner diameter 36.4 mm) such that essentially only the direct light reaches the devices. If the outside lamp intensity is adjusted to 1 sun (1000 W m^{-2}, AM1.5G) then the measured intensity that the devices receive is only $\frac{1}{3}$ sun (330 W m^{-2}) as measured using a KG5 filtered Hamamatsu S1133 photodiode. Degradation of devices may depend on the wavelength of the radiation and optical filters can be placed above the quartz windows. UV-filters (Thorlabs inc., FGL400S) were used to exclude UV radiation below 400 nm from reaching the devices.

2.3. High-temperature version of the atmospheric chamber

It is sometimes desirable to test devices at elevated temperature to accelerate the degradation.

For this purpose a chamber was heated using a heating block while the external cooling fans were switched off. With the current setup that employs cooling water to remove heat in conjunction with external cooling fans and a heating block the accessible temperature range is 25–85 °C.

2.4. Complex system for lifetime measurements

A complex system for systematic *IV* data measurements has been developed for decay studies. The entire setup has three identical solar simulators with three ACs capable of measuring a total of six solar cells and three pyranometers or silicon diodes to monitor the light intensity changes. Lifetime measurements are performed by taking *IV* diode characteristics at short intervals for >1000 h. In principle this could be accomplished by assigning a source-measurement unit (SMU) to each of the cells and the pyranometers/silicon diodes. A more economic solution is to use one single SMU (a Keithley 2400) for all measurements and use a switchboard controlled by a Keithley 2700 unit equipped with a 7705 control module with 40 relays. The intensity of the lamps is measured using an empty slot on the switchboard, the Keithley 2700 and a multimeter (Keithley 2000). This multiplexing setup is shown schematically in Fig. 6 below.

A computer is used to control the multiplexing unit so that the individual cells are connected to the SMU at regular intervals by opening and closing appropriate relays. When the cells are not being measured, they are connected to a load, which in this case was a short circuit. Other options are open circuit, a resistor or an active load, e.g. with a bias voltage to apply an electrical stress to the cell. The layout of the switch matrix is shown in Fig. 7 and was chosen to minimize electrical interference. Other connection matrices can be made with 40 relays such that up to 10 channels are available with load switching but with increased electrical interference and possible cross-talk.

The SMU is also computer controlled to run the *IV*-curve where the current is measured as a voltage is sourced to the device in typical voltage steps of 10–20 mV from −1 to +1 V. Interfacing the computer with the instruments is accomplished through a general-purpose interface bus (GPIB). When the *IV*-curve is measured instead of just a single current and/or voltage at each data point it is possible to extract the the short-circuit current (I_{sc}), open-circuit voltage (V_{oc}), fill factor (FF) and maximum power point at each time step. Information relating to the different decay processes in the device can be extracted from the *IV*-curve. Separate files are created to hold each of these parameters as well as the individual files containing the *IV* measurements. The automated program also has options for notifying the user via electronic mail when the device efficiency falls below a certain threshold or if the sun simulator lamp should fail.

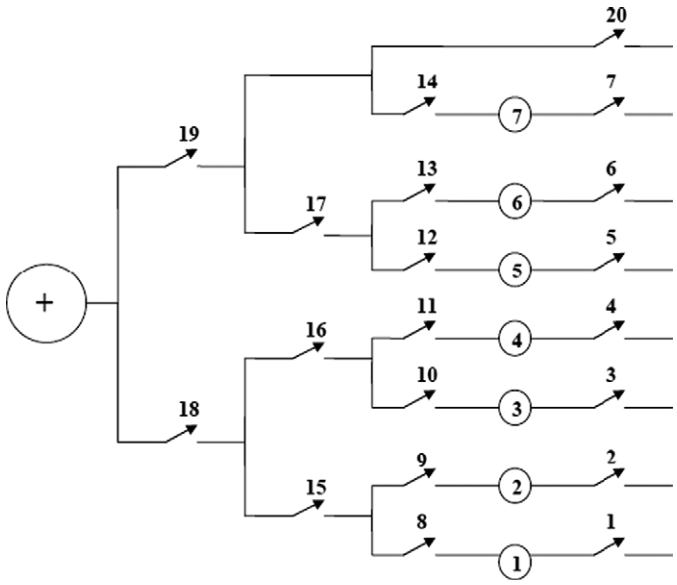

Fig. 7. The positive part of the switch matrix. The cells are marked as circles with numbers 1–7. Switches are marked 1–20. To measure cell 1 switches 8, 15 and 18 have to be closed to connect to the positive port of the SMU. Similarly, switches 28, 35 and 38 have to be closed to connect with the negative port of the SMU. Switches 1, 2, 3, 4, 5, 6 and 7 are connected to the load and are closed when the cell in question is not subject to measurements. The negative part of the switch matrix is not shown, but is otherwise identical to the positive switch matrix shown here.

2.5. Device preparation

A solution of PEDOT:PSS (Aldrich) was spin coated onto indium tin oxide (ITO)-covered glass slides (sheet resistance 8–12 Ω square^{-1}, Delta Technologies) and dried in an oven at (160 °C, 5 min). These substrates were then transferred to a glove-box environment where the active layer of P3HT/PCBM (1:1) (25 g mL^{-1} each in xylene) was spin coated. Finally, a layer of aluminum metal was evaporated on top. The final devices had an active area of 3 cm^2. All devices were subjected shortly to the ambient atmosphere for annealing at 150 °C for 6 min and characterization of the PV response. The solar cells were then mounted on holders (see Fig. 5) and placed inside the ACs (either in the atmosphere or in the glove-box environment). P3HT was prepared via the McCollough route [45] and the product had a regioregularity of 97% as established by 1H NMR. The polymer data were $M_w = 35\,600$, $M_n = 18\,700$, $M_p = 33\,900$, PD = 1.9.

3. Results and discussion

Eight lifetime experiments have been carried out in duplicate with the devices prepared above under ambient or nitrogen atmospheres at 25±1, 43±1, 63±1 or 83±1 °C. In the experiments with ambient atmosphere the humidity was measured to be 30±5% RH, while in the case of the nitrogen atmosphere the humidity was less than 0.1% RH and the oxygen level less than 2 ppm. The *IV* characteristics were recorded every 5 min for up to 200 h.

Table 1
Initial photovoltaic parameters for the glass/ITO/PEDOT:PSS/P3HT-[60]PCBM/Al devices employed here

Atmosphere	Temperature (°C)	V_{oc} (V)	I_{sc} (mA cm^{-2})	FF (%)	PCE (%)
Ambient	25±1	0.55	8.4	0.33	1.5
		0.55	7.8	0.31	1.3
	43±1	0.55	8.4	0.37	1.7
		0.55	8.2	0.33	1.5
	63±1	0.55	7	0.43	1.6
		0.57	6.5	0.47	1.7
	83±1	0.56	7.75	0.34	1.5
		0.55	8.1	0.32	1.4
Nitrogen	25±1	0.56	10.3	0.38	2.2
		0.56	10.5	0.37	2.1
	43±1	0.56	10.3	0.37	2.1
		0.56	10.6	0.36	2.1
	63±1	0.57	6.8	0.4	1.5
		0.55	6.9	0.44	1.6
	83±1	0.57	10	0.36	2.1
		0.56	10.6	0.35	2

The experiment at each temperature was performed for two independent cells. The device performance was recorded at and incident light intensity of 1000 W m^{-2}, AM1.5G, 72±2 °C, 35±5% relative humidity, ambient atmosphere. The active area of the devices was 3 cm^2.

From these data I_{sc}, V_{oc}, FF and relative power conversion efficiency (η) were calculated for each point in time.

Short circuit conditions were maintained while the devices were not being measured. The initial PV parameters varied somewhat between the devices as shown in Table 1. The major variation in the initial performance of the devices was in the short circuit current, whereas the V_{oc} was quite similar. We ascribe the small differences in V_{oc}, I_{sc}, FF and PCE to variations during device preparation and variation in film morphology.

The devices were subjected to continuous illumination at the specified temperature and atmosphere in the chambers. Devices operated in the ambient atmosphere degraded much faster than in inert nitrogen atmosphere as expected and also faster at higher temperature than at lower temperature.

In Fig. 8 the lifetime tests in the ambient atmosphere and in inert nitrogen at 43 °C are compared. The decay curves show a fast decay during the first few hours of testing and then stabilize to a constant decay that can be fitted with a linear or single exponential function. In this case where we employed relatively short test periods of a few hundred hours we chose a linear fit. The initial stabilization period could be due to an initial degradation mechanism involving the aluminum cathode that becomes less predominant after a short period of time. Since we observe it for cells tested in both ambient and inert atmospheres it could be linked to an oxidization of aluminum at the aluminum–polymer interface or it could be due to the reaction with water or oxygen introduced during initial testing. The curves obtained for the two devices in each test were more or less superimposable (not shown for clarity) with only slight variation indicating that the reproducibility of the

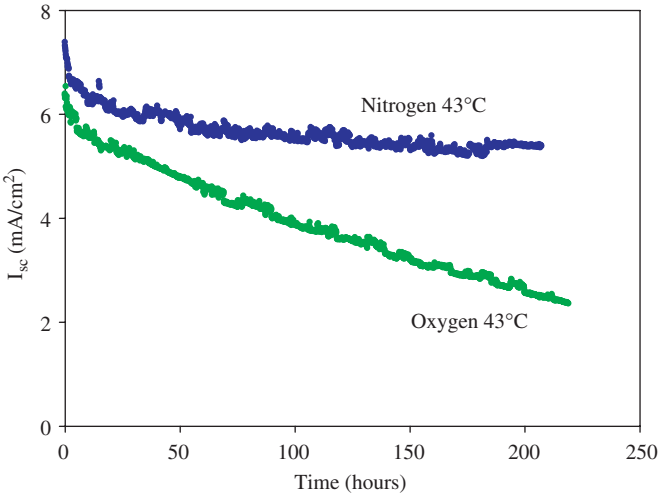

Fig. 8. Comparing the lifetime curves for devices in ambient atmosphere and in nitrogen at 43 ± 1 °C. The decay curves for the devices under the same conditions were quite similar and show a fast initial decay followed by region with a constant decay that can be fitted with a linear or an exponential function.

measurement of the decay curve was quite good. A reasonably fast decay was observed for the devices maintained in ambient atmosphere, which degraded to 50% of the initial performance after 150 h. A much slower decay was observed for the devices maintained in the nitrogen atmosphere that remained above 70% of the initial current after 200 h, which is consistent with earlier findings [46]. Similar relations between results in ambient atmosphere and nitrogen were seen also for other temperatures (25, 63 and 83 °C). The degradation of a PV device is characterized by a degradation constant that is obtained by fitting a suitable function to the decay curve for a device that shows the decay. The device current was chosen here and as mentioned above it can be fitted with either a linear (Eq. (1)) or a single exponential function (Eq. (2)). In our case the curves exhibit at least two regions where the rate of degradation is different. We chose the constant region observed after 15 h and fitted a linear function (Eq. (1)). Our reason for this is that it seems to be the typical constant behavior of the devices. Assuming that the degradation constant (k_{deg}) depends on the temperature (T) given by the Arrhenius equation (Eq. (3)), an acceleration factor (K) can be derived from Eq. (4) by fitting the values for k_{deg}. Fig. 9 shows acceleration factor (K) plotted against $1/T$ for both ambient atmosphere and nitrogen and the exponential fit to the calculated values. The calculated rate constants (k_{deg}) for each device, the acceleration factors and the activation energies are shown in Table 2

$$I_{sc}(t) = I_{sc}(t_0)(1 - k_{deg}t) \quad (1)$$

$$I_{sc}(t) = I_{sc}(t_0)\exp(-k_{deg}t) \quad (2)$$

$$k_{deg} = A\exp\left(\frac{-E_a}{k_B T}\right) \quad (3)$$

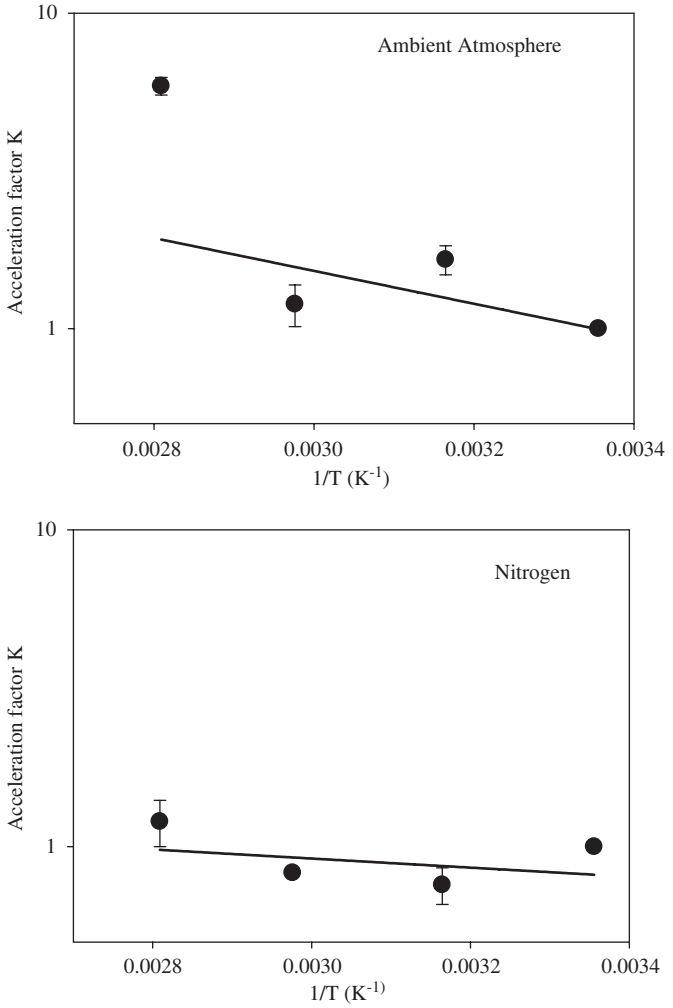

Fig. 9. Log scale plots of the acceleration factor, K, relative to 25 °C (298 K). The data were fitted using Eq. (4) and the parameters for the activation energy and the acceleration factor were obtained as shown in Table 2. The illumination intensity was $\frac{1}{3}$ sun (330 W m^{-2}).

$$K = \frac{k_{deg}(T_2)}{k_{deg}(T_1)} = \exp\left[\frac{E_a}{k_B}\left(\frac{1}{T_1} - \frac{1}{T_2}\right)\right]. \quad (4)$$

The activation energy has been extracted from the curves using Eq. (4) and in the case of ambient atmosphere it is rather low (103 meV), which might be due to fact that the data at 63 °C is an outlier. There is naturally a certain degree of experimental variation due to the fact that we could not prepare and run all eight experiments at the same time but had to run the experiments in three consecutive batches. The calculation of activation energy with omission of the point at 63 °C gives an activation energy that is 3 times higher than the one we obtain. This however underlines the difficulty in obtaining a value for the activation energy from one experiment and then generally applying it. Schuller et al. [43] performed accelerated measurements on devices based on MDMO-PPV and PCBM using both Ca/Ag and Al cathodes and obtained a value for the activation energy of 300–350 meV. This

Table 2
Rates of degradation, activation energy and acceleration constants obtained

Atmosphere	Temperature (°C)	k_{deg} (h^{-1})10^{-3}	K^a	E_a (meV)
Ambient	25±1	1.95	1	103
		0.96	1	
	43±1	2.16	1.48	
		2.67	1.83	
	63±1	1.7	1.17	
		1.78	1.22	
	83±1	8	5.5	
		9.1	6.25	
Nitrogen	25±1	0.92	1	29
		0.93	1	
	43±1	0.8	0.86	
		0.6	0.65	
	63±1	0.78	0.84	
		0.75	0.81	
	83±1	1.3	1.4	
		0.94	1.1	

[a] K was obtained by dividing each corresponding k_{deg} by average of k_{deg} values at 25 °C (except for values of K at 25 °C, which were simply normalized to one).

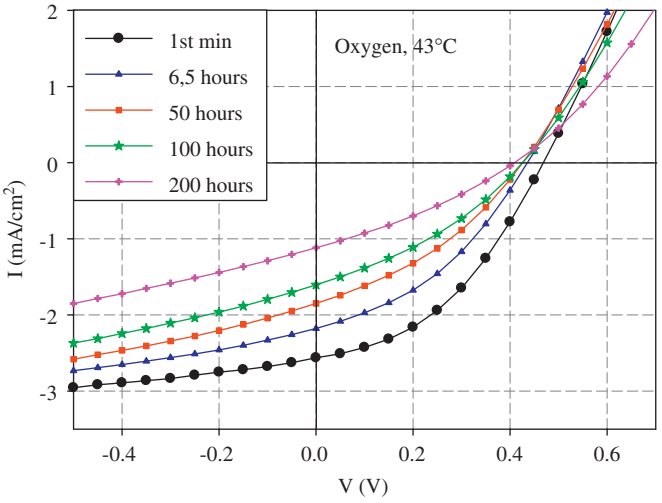

Fig. 10. Evolution of *IV*-curves during decay at 43 °C and ambient atmosphere (under $\frac{1}{3}$ sun illumination).

value was later employed by De Bettignies et al. [42] for a different polymer system P3HT to predict the operational lifetime under normal condition based on accelerated lifetime measurements. The lifetime under normal operational conditions was however not verified. In our case we employed the same material combination ITO, PEDOT:PSS, P3HT, [60]PCBM and aluminum. In our experiment we varied the light intensity, employed a UV-filter and did not have a LiF barrier layer between the active material and the cathode. Under inert conditions we obtain a totally different value for the activation energy and as a consequence a much slower acceleration factor indicating that there is no real acceleration of the degradation under inert conditions (albeit at lower light intensity and in the absence of UV-light). However, it is clear that the degradation proceeds much faster in the ambient atmosphere where oxygen and humidity are allowed to diffuse into the devices. This corroborates the results from several other studies on the degradation of polymer solar cell devices [16,20,42,43]. The degradation processes that take place in the presence of oxygen and humidity are most likely chemical processes involving the active polymer and perhaps the electrode materials. It is not so clear what causes the acceleration factor in our case to be much slower under nitrogen conditions. The limited data indicates that the process is not speeded up by increasing the temperature suggesting simple zero-order kinetics. This could happen if the rate of the process only depended on say the light intensity and not on the concentration and diffusion of molecular entities like oxygen and water. Further improvements to the setup would include the ability to increase and vary the light intensity in a larger range to investigate this issue.

The simple two-parameter exponential fit of the high-temperature degradation in ambient air does not describe the data completely. There seems to be two recognizable regions in the plot (Fig. 8): a rapid decrease in the first few hours followed by a more or less linear decay. This is consistent with earlier findings [17]. Using linear models for these two regions a better fit would of course be obtained in these regions and the acceleration factor would then be seen to change over time. The implications of this finding is that one has to exercise caution when estimating acceleration factors from decay curves that change over time as this may give rise to wrong estimates of operational lifetimes. Our results also strongly suggest that the determination and use of acceleration factors will only be applicable for one particular device constitution. This implies that even changing one constituent or interface layer is enough for the results not being useful. While we see accelerated studies as a useful means to characterize polymer and organic solar cells we also see it as limited to a particular device technology that cannot be extended to other systems without verification of the generality. The general degradation we observed for the devices were as expected with a decrease in mainly the I_{sc} but also the FF as the devices degraded as shown in Fig. 10 where the change of the *IV*-curve is shown for the devices maintained in ambient atmosphere at 43 °C.

As a further complication to the problem of obtaining an accurate stability measure for a given device technology we observed an unusual effect at the higher temperatures where atypical behavior sets in after a period of typically 50–100 h where a fast exponential decay was observed as shown in Fig. 11. At first we thought that this was due to a leak in the case of experiments studied under nitrogen but the observation was also made in ambient air. We currently have no explanation for this but consider this degradation path as a different one that is not linked to chemical changes in the material itself but perhaps to the macroscopic

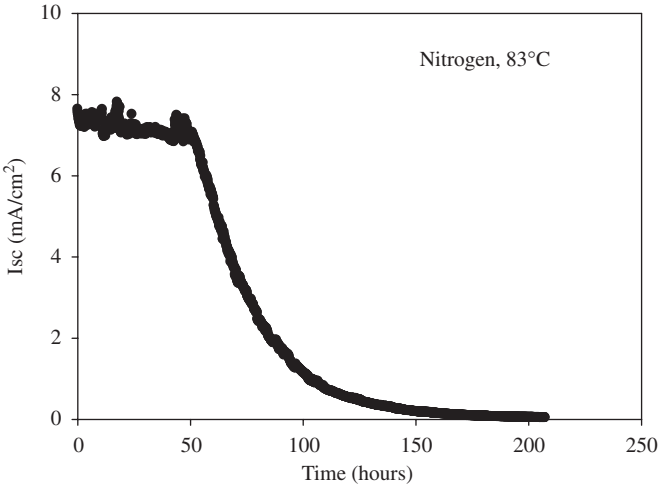

Fig. 11. Sudden fast decay behavior that we observed on occasion.

device. A likely explanation is incompatibility between the thermal properties of the individual layers in the multilayer device giving rise to a mechanical degradation.

Since we did not generally observe it and the onset of the fast degradation mechanism did not take place at a particular time we view it as a possible mechanical failure mechanism where the system delaminates or contact is lost between layers or at an interface. We did not include this behavior in the present study and only used the data that did not exhibit this behavior. We, however, chose to show the data here to underline the complexity of lifetime measurements and show that many processes may be in play that are not necessarily predictable.

4. Conclusion

An experimental setup for studying the lifetime and degradation of polymer solar cell devices has been described. This includes details of ACs that allow full control over the critical parameters that affect the decay of these devices with time. The setup consists of three ACs, where devices are connected to a single source meter through a computer-controlled switch matrix. Full *IV*-curves were recorded at 5-min intervals and the solar cell parameters of I_{sc}, V_{oc}, FF and η were extracted.

In the present paper the ACs and experimental setup were used to study the decay of ITO/PEDOT:PSS/P3HT-[60]PCBM/Al solar cell devices in ambient and nitrogen atmosphere at 25, 43, 63 and 83 °C. A rapid decay was recorded for the devices maintained in the ambient atmosphere with the presence of oxygen and water that could be fitted to a linear decay equation. An acceleration factor of about 6 was obtained by a ~60 °C increase in temperature. The decay mechanisms for devices maintained in ambient atmosphere can be ascribed to chemical reactions of the active layer and/or electrodes with oxygen and water that diffuse into the devices. The results from devices maintained in a nitrogen atmosphere showed that decay is much slower by more than one order of magnitude. What is more surprising is that no significant acceleration was found by increasing the temperature. The data are limited, but may suggest that the decay mechanism in this case is quite different, possibly only dependent on the light intensity or UV-light. The results also show that the decay of polymer solar cell devices is complicated and that several mechanisms operate. When the lifetime becomes sufficiently long it is not practical or possible to measure the whole decay curve until the devices are no longer operational. A few groups have resorted to accelerated tests where the temperature is increased to stress the devices and speed up the decay. The results in the present work show that the acceleration factor depends very much on the actual working conditions. It may also change value during the lifetime study if more than one mechanism is in operation. Accelerated studies may be necessary, but it is important that the exact experimental conditions are given; otherwise the results will be impossible to reproduce and interpret. Finally, results from accelerated lifetime testing cannot be viewed as generally applicable to other device geometries than the one tested as different materials and different device constitutions may give widely different responses to accelerated test conditions.

Acknowledgments

This work was further supported by the Danish Strategic Research Council (DSF 2104-05-0052 and DSF-2104-07-0022). Torben Kjær is acknowledged for technical assistance.

References

[1] C.J. Brabec, N.S. Sariciftci, J.C. Hummelen, Adv. Funct. Mater. 11 (2001) 15.
[2] H. Spanggaard, F.C. Krebs, Sol. Energy Mater. Sol. Cells 83 (2004) 125.
[3] K.M. Coakley, M.D. McGehee, Chem. Mater. 16 (2004) 4533.
[4] H. Hoppe, N.S. Sariciftci, J. Mater. Res. 19 (2004) 1924.
[5] S. Günes, H. Neugebauer, N.S. Sariciftci, Chem. Rev. 107 (2007) 1324.
[6] C. Winder, N.S. Sariciftci, J. Mater. Chem. 14 (2004) 1077.
[7] E. Bundgaard, F.C. Krebs, Sol. Energy Mater. Sol. Cells 91 (2007) 954.
[8] B.P. Rand, J. Genoe, P. Heremans, J. Poortmans, Prog. Photovoltaic Res. Appl. 15 (2007) 659.
[9] G. Li, V. Shrotriya, J. Huang, Y. Yao, T. Moriarty, K. Emery, Y. Yang, Nat. Mater. 4 (2005) 864.
[10] W. Ma, C. Yang, X. Gong, K. Lee, A.J. Heeger, Adv. Funct. Mater. 15 (2005) 1617.
[11] J.Y. Kim, K. Lee, N.E. Coates, D. Moses, T.–Q. Nguyen, M. Dante, A.J. Heeger, Science 317 (2007) 222.
[12] L.J.A. Koster, V.D. Mihailetchi, P.W.M. Blom, Appl. Phys. Lett. 88 (2006) 093511.
[13] M.C. Scharber, D. Mühlbacher, M. Koppe, P. Denk, C. Waldauf, A.J. Heeger, C.J. Brabec, Adv. Mater. 18 (2006) 789.
[14] M. Jørgensen, K. Norrman, F.C. Krebs 92 (2008) 696–724, this issue; doi:10.1016/j.solmat.2008.01.005.
[15] H. Neugebauer, C. Brabec, J.C. Hummelen, N.S. Sariciftci, Sol. Energy Mater. Sol. Cells 61 (2000) 35.

[16] K. Kawano, R. Pacios, D. Poplavskyy, J. Nelson, D.D.C. Bradley, J.R. Durrant, Sol. Energy Mater. Sol. Cells 90 (2006) 3520.
[17] F.C. Krebs, J.E. Carlé, N. Cruys-Bagger, M. Andersen, M.R. Lilliedal, M.A. Hammond, S. Hvidt, Sol. Energy Mater Sol. Cells 86 (2005) 499.
[18] M. Lira-Cantu, F.C. Krebs, Sol. Energy Mater. Sol. Cells 90 (2006) 2076.
[19] J. Alstrup, K. Norrman, M. Jørgensen, F.C. Krebs, Sol. Energy Mater. Sol. Cells 90 (2006) 2777.
[20] K. Norrman, F.C. Krebs, Sol. Energy Mater. Sol. Cells 90 (2006) 213.
[21] K. Norrman, N.B. Larsen, F.C. Krebs, Sol. Energy Mater. Sol. Cells 90 (2006) 2793.
[22] K. Norrman, J. Alstrup, M. Jørgensen, F.C. Krebs, Surf. Interface Anal. 38 (2006) 1302.
[23] M. Lira-Cantu, K. Norrman, J.W. Andreasen, F.C. Krebs, Chem. Mater. 18 (2006) 5684.
[24] C.W.T. Bulle-Lieuwma, W.J.H. van Gennip, J.K.J. van Duren, P. Jonkheijm, R.A.J. Janssen, J.W. Niemantsverdriet, Appl. Surf. Sci. 203 (2003) 547.
[25] C.W.T. Bulle-Lieuwma, J.K.J. van Duren, X. Jang, J. Loos, A.B. Sieval, J.C. Hummelen, R.A.J. Janssen, Appl. Surf. Sci. 231 (2004) 274.
[26] F.C. Krebs, K. Norrman, Prog. Photovoltaic: Res. Appl. 15 (2007) 697.
[27] K. Emery, C. Osterwald, Sol. Cells 17 (1986) 253.
[28] K. Emery, C. Osterwald, Current Topics in Photovoltaics, vol. 3, Academic, London, 1988 (Chapter 4).
[29] K. Emery, in: A. Luque, S. Hegedus (Eds.), Handbook of Photovoltaic Science and Engineering, Wiley, Chichester, UK, 2003 (Chapter 16).
[30] Standard IEC 60904-3, Measurement Principles for Terrestrial PV Solar Devices with Reference Spectral Irradiance Data, International Electrotechnical Commission, Geneva, Switzerland.
[31] Standard IEC 60904-1, Photovoltaic Devices, Part 1: Measurement of Photovoltaic Current–Voltage Characteristics, International Electrotechnical Commission, Geneva, Switzerland.
[32] ASTM Standard G159, Standard Tables for Reference Solar Spectral Irradiances: Direct Normal and Hemispherical on 37° Tilted Surface, American Society for Testing and Materials, West Conshocken, PA, USA.
[33] ASTM Standard G173, Standard Tables for Reference Solar Spectral Irradiances: Direct Normal and Hemispherical on 37° Tilted Surface, American Society for Testing and Materials, West Conshocken, PA, USA.
[34] Standard ASTM E948, Standard Test Method for Electrical Performance of Non-Concentrator Photovoltaic Cells Using Reference Cells, American Society for Testing and Materials, West Conshocken, PA, USA.
[35] C.R. Osterwald, Sol. Cells 18 (1986) 269.
[36] Standard ASTM E1021, Standard Test Methods for Measuring Spectral Response of Photovoltaic Cells, American Society for Testing and Materials, West Conshocken, PA, USA.
[37] Standard ASTM E1328, Standard Terminology Relating to Photovoltaic Solar Energy Conversions, American Society for Testing and Materials, West Conshocken, PA, USA.
[38] J. Rostalski, D. Meissner, Sol. Energy Mater. Sol. Cells 61 (2000) 87.
[39] J.M. Kroon, M.M. Wienk, W.J.H. Verhees, J.C. Hummelen, Thin Solid Films 403 (2002) 223.
[40] V. Shrotriya, G. Li, Y. Yao, T. Moriarty, K. Emery, Y. Yang, Adv. Funct. Mater. 16 (2006) 2016.
[41] E.A. Katz, S. Gevorgyan, M.S. Orynbayev, F.C. Krebs, Eur. Phys. J.: Appl. Phys. 36 (2006) 307.
[42] R. de Bettignies, J. Leroy, M. Firon, C. Sentein, Synth. Met. 156 (2006) 510.
[43] S. Schuller, P. Schilinsky, J. Hauch, C.J. Brabec, Appl. Phys. A 79 (2004) 37.
[44] http://www.valleydesign.com/pyrexpic.htm.
[45] R.D. McCullough, R.D. Lowe, M. Jayaraman, D.L. Anderson, J. Org. Chem. 58 (1993) 904.
[46] X. Yang, J. Loos, S.C. Veenstra, W.J.H. Verhees, M.M. Wienk, J.M. Kroon, M.A.J. Michels, R.A.J. Janssen, Nanoletters 5 (2005) 579.

ARTICLE

Water-Induced Degradation of Polymer Solar Cells Studied by $H_2{}^{18}O$ Labeling

Kion Norrman, Suren A. Gevorgyan, and Frederik C. Krebs*

Risø National Laboratory for Sustainable Energy, Technical University of Denmark, Frederiksborgvej 399, DK-4000 Roskilde, Denmark

ABSTRACT Water-induced degradation of polymer photovoltaics based on the active materials poly(3-hexylthiophene) (P3HT) or poly[2-methoxy-5-(2′-ethylhexyloxy)-1,4-phenylenevinylene] (MEHPPV) was studied. The solar cell devices comprised a bulk heterojunction formed by the active material and [6,6]-phenyl-C_{61}-butyric acid methyl ester (PCBM) in a standard device geometry. The use of $H_2{}^{18}O$ in conjunction with time-of-flight secondary ion mass spectrometry enabled mapping of the parts of the device that were induced by water. A comparison was made between the two active materials and between devices that were kept in the dark and devices that had been subjected to illumination under simulated sunlight. Devices that were exposed to ambient humidity were compared to devices exposed to saturated humidity. Finally, a comparison was made between results obtained using $H_2{}^{18}O$ and earlier work involving $^{18}O_2$. Water was found to have behavior similar to but not identical with molecular oxygen.

KEYWORDS: polymer solar cells • degradation • failure mechanism • TOF-SIMS • P3HT • MEH-PPV

INTRODUCTION

The exploitation of polymer materials for converting sunlight into electricity through polymer solar cells (1−6) for direct consumption or later usage through external storage is believed to convey several advantages such as lightweightedness, flexibility, environmental friendliness, a low thermal budget, low cost, and most notably very fast modes of production by printing techniques. The research has focused on low-band-gap materials (7, 8), morphology control (9−11), and stability (12) in order to achieve as good performance as possible. The power conversion efficiency currently reaches ∼5% for single junctions (13, 14) and 6.5% for tandem cells (15). The operational stability has reached thousands of hours under laboratory conditions (16−19) and up to a year under outside conditions (20, 21). Production issues are slowly starting to be addressed, and the production of very large area plastic solar cell modules up to 1000 cm^2 has been reported (22−24). Production experiments have shown that it is highly feasible with existing technology to mass produce polymer solar cells at a very low cost. While the operational stability has been addressed, an area that has received very little attention is the mechanisms that cause degradation and thus poor stability. All polymer solar cell devices are to some extent unstable and degrade over time. The archetypical polymer solar cell devices based on poly(*p*-phenylenevinylene) (PPV) materials are notoriously unstable under illumination and/or heating. The polythiophenes are more stable, and the current state-of-the-art polythiophenes employ morphologically stable bulk heterojunctions of regioregular poly(3-hexylthiophene) (P3HT) as the donor material and the soluble fullerene material phenyl-C_{61}-butyric acid methyl ester (PCBM) as the acceptor material. Stable device operation for 1000 h has been documented for this system (17). Stable operation for more than 10 000 h has been reported for bilayer heterojunctions between regiorandom poly(3-carboxydithiophene) (P3CT) and Buckminster fullerene (C_{60}) (18). One could argue that there has been a lot of progress within the areas of processability, efficiency, and stability and that the most serious obstacle for commercialization is the lack of a material that possesses a sufficient degree of all of these vital properties.

In this paper, the stability issue is addressed through studies of degradation. When organic materials are exposed to sunlight, they are subject to photochemical reactions, i.e., intramolecular, intermolecular, or reactions between the constituents of the device and the atmosphere (i.e., oxygen and/or water). Under illumination of organic materials, degradation is inevitable albeit slower under inert conditions. The materials degrade and, as a consequence, so do in many instances their physical, electrical, and mechanical properties. Photovoltaic devices that rely on the delicate interplay between the electronic structure of the material and the energy levels in external electrodes connecting the functional material in the device to the outside world are highly sensitive to even small degrees of degradation. Light absorption and charge-carrier transport properties take place throughout the bulk of the material and at the interfaces. All the processes that are affected by these reaction products in the bulk and at the interfaces will thus lead to degradation of the device performance. The transfers of charges at electrodes or between domains are interface phenomena that are sensitive to impurities or degradation phenomena. The transport of charges in the bulk is also very sensitive to impurities (25). For an electronic device based on organic materials that rely on both bulk and interface phenomena,

* E-mail: frederik.krebs@risoe.dk.
Received for review September 8, 2008 and accepted October 27, 2008
DOI: 10.1021/am800039w

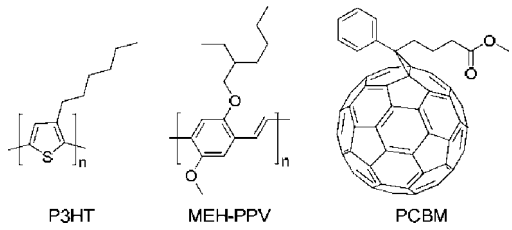

FIGURE 1. Molecular structures of the active materials used in this study. P3HT: regioregular poly(3-hexylthiophene) (donor material). MEH-PPV: poly[2-methoxy-5-(2′-ethylhexyloxy)-1,4-phenylenevinylene] (donor material). PCBM: phenyl-C_{61}-butyric acid methyl ester (acceptor material).

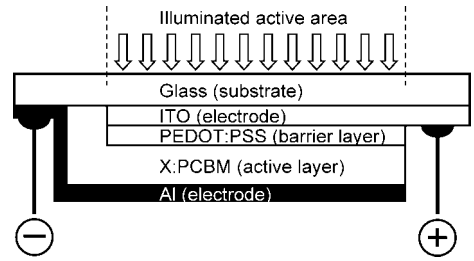

FIGURE 2. Schematic drawing of the device configuration (Al/X: PCBM/PEDOT:PSS/ITO) used for the two active materials (X = P3HT or MEH-PPV). The active area is ∼3 cm². The illustration is not drawn to scale.

it is clear that degradation constitutes a serious problem, and must be removed or at least minimized to optimize the lifetime of the device.

Earlier reports from this laboratory focused on the degradation of polymer solar cells induced by molecular oxygen (18, 26−33). By exposure of polymer solar cell devices to dry $^{18}O_2$, it was possible, by use of time-of-flight secondary ion mass spectrometry (TOF-SIMS) (34), to map the degradation processes induced by molecular oxygen during illumination. In this paper, the study is expanded to degradation induced by water, which is carried out by exposure of the polymer solar cell devices to $H_2{}^{18}O$ during illumination and subsequently analysis of the devices using TOF-SIMS methodologies. The study involves a comparative study of water-induced degradation of a bulk heterojunction between P3HT and PCBM and between poly[2-methoxy-5-(2′-ethylhexyloxy)-1,4-phenylenevinylene] (MEH-PPV) and PCBM (Figure 1). The following comparisons are made: (i) a comparison of the two active materials, (ii) a comparison of devices that were kept in the dark and devices that had been subjected to illumination under simulated sunlight, (iii) a comparison of devices that were exposed to ambient humidity and devices that were exposed to saturated humidity, and (iv) a comparison of the result obtained in this study and results obtained in earlier work involving $^{18}O_2$ (18, 26, 28, 31, 32). Detailed knowledge on the degradation mechanisms during illumination and/or storing is vital in the search for finding ways to remove or at least diminish degradation, so that stability will no longer be an issue and an obstacle for the commercialization of polymer solar cells.

EXPERIMENTAL METHODS

Photovoltaic Preparation and Characterization. P3HT and MEH-PPV with weight-average molecular weights (M_w) of 35 600 and 65 600 g mol^{-1} and polydispersities (PD) of 1.9 and 4.1 were prepared according to the methods described in the literature (35, 36). Solutions were prepared by dissolving P3HT (25 mg mL^{-1}) and PCBM (25 mg mL^{-1}) in xylene and MEH-PPV (10 mg mL^{-1}) and PCBM (40 mg mL^{-1}) in dichlorobenzene followed by microfiltration through a 1 μm filter. Devices were prepared by spin coating (2800 rpm) an 1.3 wt % aqueous PEDOT:PSS solution onto indium/tin oxide (ITO)-covered glass slides followed by drying at 180 °C for 10 min. The P3HT or MEH-PPV solutions were subsequently spin-coated (800 rpm) onto the PEDOT:PSS layer. Thin (∼100 nm) aluminum electrodes were hereafter evaporated onto the multilayer structure at a pressure of 2×10^{-6} mbar, resulting in the following device configuration: Al/X:PCBM/PEDOT:PSS/ITO (X = P3HT or MEH-PPV; Figure 2). The aluminum electrode needs to be thin in order to facilitate peeling of the electrode from the device and to reduce the sputtering time in TOF-SIMS experiments, where depth profiles were obtained by sputtering through the aluminum electrode. The electrode thicknesses were measured using atomic force microscopy (AFM). The final P3HT-based devices were annealed at 150 °C for 5 min. The active areas of the devices were ∼3 cm². The device geometry has been described earlier (37). The system was purged with argon during removal of the samples for testing. A solar simulator from Steuernagel Lichttechnik GmBH providing AM1.5G illumination conditions was employed for all lifetime measurements under simulated sunlight.

The spectral distribution and quality of the solar simulator were monitored using an AvaSpec 2048 spectrometer from Avantes, and a Precision pyranometer from Eppley Laboratories was used to monitor the total power that was set to the desired incident power. The electrical measurements were performed using Keithley 2400 sourcemeters. The photovoltaic performance and stability of the illuminated devices were studied by recording the IV curves at certain times during the experiment.

$H_2{}^{18}O$ Labeling Studies. The influence of the atmosphere was established by illumination in a chamber equipped with a quartz window, allowing for control of the atmosphere as described in the literature (37). The freshly prepared solar cells were introduced into the test chamber. $H_2{}^{18}O$ (90%, 5 mL, ∼20 mmol) was then added to the test chamber. The entire system has a volume of 2.5 L, resulting in a saturated isotopically labeled atmosphere. Light was subsequently admitted to half of the devices (the other half were wrapped in aluminum foil), and the short-circuit current (I_{sc}) was recorded in order to monitor the device degradation. After 250 h, the devices had degraded and were removed from the chamber and kept in the dark while they were transferrred to the TOF-SIMS analysis chamber. Part of the aluminum electrodes were peeled off by attaching 3M tape to the aluminum electrode followed by removal. This neatly adhered to the aluminum and separated it from the active layer.

Characterization Using TOF-SIMS Methodologies. The TOF-SIMS analyses were performed using a TOF-SIMS IV (ION-TOF GmbH, Münster, Germany). TOF-SIMS mass spectra were acquired using 30 ns pulses of 25 keV Bi_3^+ that were bunched to form ion packets with a nominal temporal extent of <0.9 ns at a repetition rate of 10 kHz, yielding a target current of 300 fA. These primary ion conditions were used to scan $100 \times 100\ \mu m^2$ areas of the sample surfaces for 30 s corresponding to an ion dose of 6×10^{11} ions cm^{-2} (below the static limit). TOF-SIMS images were acquired with equivalent conditions using a lateral resolution of ∼2 μm over $500 \times 500\ \mu m^2$ areas of the sample surfaces for 393 s corresponding to a ion dose of 7×10^{12} ions cm^{-2} (below the static limit). Depth profiling was performed using equivalent conditions with respect to the analysis ions (produced by an analysis gun). For the sputter part of the TOF-SIMS depth profiling, 1.5 kV Xe^+ (sputter ions produced by the sputter gun) was used, resulting in a target current of 14 nA. A

Table 1. Experimental Conditions for the Six Solar Cell Devices That Were Investigated in This Study[a]

device no.	active material	relative humidity (%)	temperature (°C)	illumination (W m^{-2})
1	P3HT	90 ± 5	42 ± 2	0
2	P3HT	90 ± 5	42 ± 2	330
3	P3HT	25 ± 5	72 ± 2	1000
4	MEH-PPV	90 ± 5	42 ± 2	0
5	MEH-PPV	90 ± 5	42 ± 2	330
6	MEH-PPV	25 ± 5	72 ± 2	1000

[a] The content of molecular oxygen ($^{16}O_2$) in the atmosphere was ~20% during all experiments.

Table 2. Photovoltaic Parameters for Solar Cell Devices That Were Measured in the Ambient Atmosphere Prior to the Degradation Experiment (25 ± 5% Relative Humidity; 72 ± 2 °C) Using AM1.5G Illumination (1000 W m^{-2})[a]

active material	J_{sc} (mA cm^{-2})	V (V)	FF	power conversion efficiency (%)
MEH-PPV	3.9 ± 0.03	0.83 ± 0.002	0.41 ± 0.01	1.33 ± 0.02
P3HT	9.7 ± 0.3	0.56 ± 0.002	0.31 ± 0.01	1.7 ± 0.1

[a] Average values are shown with corresponding standard deviations.

400 × 400 μm^2 area of the surface was sputtered, and the same area (400 × 400 μm^2) was analyzed. In the subsequent treatment of the data, only the central part was used and possible particles in the material were bypassed in order to exclude nonrepresentative phenomena in the resulting depth profiles. Electron bombardment (20 eV) was used to minimize charge buildup at the surface. Desorbed secondary ions were accelerated to 2 keV, mass analyzed in the flight tube, and postaccelerated to 10 keV before detection.

RESULTS AND DISCUSSION

Six solar cell devices were constructed: three with an Al/P3HT:PCBM/PEDOT:PSS/ITO configuration and three with an Al/MEH-PPV:PCBM/PEDOT:PSS/ITO configuration. Four of the devices were placed in a chamber with a saturated $H_2{}^{18}O$ atmosphere. The remaining two devices were placed in ambient air. One of each device type (P3HT or MEH-PPV) in the chamber was wrapped loosely in aluminum foil to exclude light but not the atmosphere. The temperatures of the devices in the chamber were similar because of the forced circulation of the atmosphere through a heat exchanger (37). The four devices in the chamber were then exposed to AM1.5G illumination (330 W m^{-2}). However, because one of each device type was wrapped in aluminum foil in the chamber, only one of each device type was actually illuminated. The two devices in ambient air were also exposed to AM1.5G illumination (1000 W m^{-2}). Table 1 shows what conditions each device was exposed to during the experiment. The degradation of the photovoltaic response was monitored as I_{sc} during illumination, and normalized decay parameters were extracted using a fitting procedure for all illuminated cells.

IV Characteristics and Degradation. Table 2 presents the key photovoltaic parameters for solar cell devices that where tested in the ambient atmosphere (25 ± 5% relative humidity; 72 ± 2 °C) using AM1.5G illumination (1000 W m^{-2}), and Figure 3 shows the corresponding IV curves measured immediately after device fabrication and prior to stability measurements. Figure 4 shows the short-circuit current−density decay curves for devices measured under different conditions (nos. 2, 3, 5, and 6 in Table 1). The curves in Figure 4 clearly demonstrate a significant impact of humidity on the stability of the solar cells. Devices exposed to ~90% relative humidity and ~42 °C showed significantly faster decay compared to the solar cells exposed

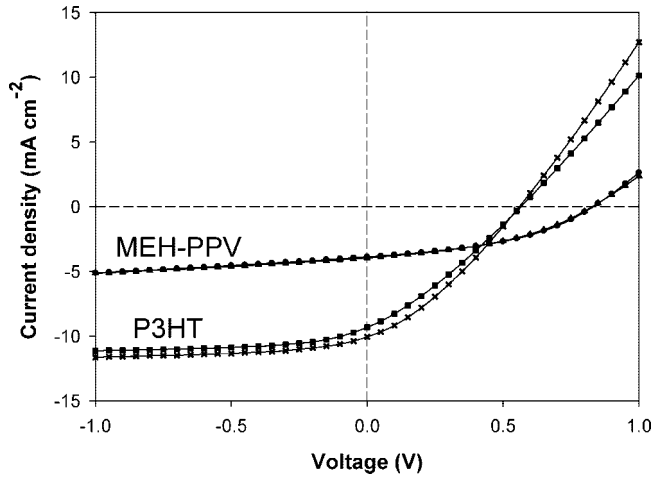

FIGURE 3. IV curves for solar cell devices that where tested in the ambient atmosphere (25 ± 5% relative humidity; 72 ± 2 °C) using AM1.5G illumination (1000 W m^{-2}). Filled squares and crosses correspond to the P3HT:PCBM devices. Filled circles and triangles correspond to the MEH-PPV:PCBM devices.

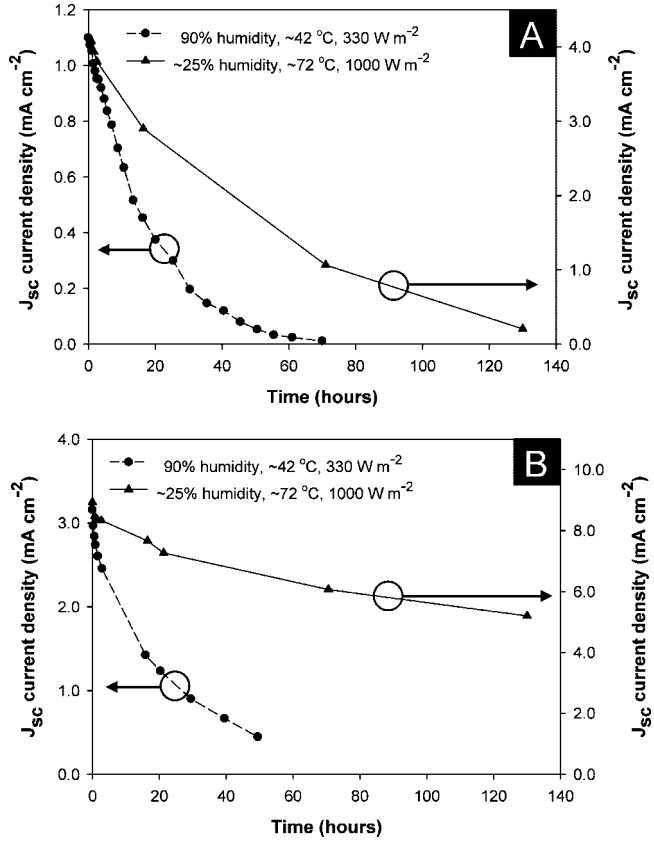

FIGURE 4. Short-circuit current−density decay curves for the MEH-PPV (A) and P3HT (B) devices.

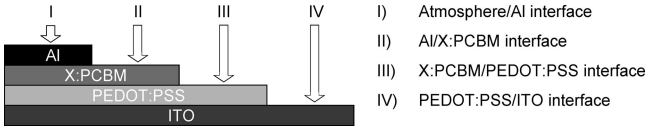

FIGURE 5. Schematic drawing of a cross-section of a polymer solar cell with the configuration Al/X:PCBM/PEDOT:PSS/ITO showing all the relevant interfaces. X is P3HT or MEH-PPV. The device is not drawn to scale.

to ~25% relative humidity and ~72 °C in spite of the fact that the samples at ambient humidity were subject to a temperature that is ~30 °C higher and subject to a factor of 3 stronger luminous intensity compared to the conditions of the solar cells in the chamber with ~90% relative humidity. The photovoltaic parameter that changed most was the short-circuit current (see the Supporting Information).

Characterization Using TOF-SIMS Methodologies. A polymer solar cell is a multilayer thin film and thus a complex object to analyze. The thin nature (<500 nm) of the device (not considering the substrate) makes it possible to use TOF-SIMS depth profiling to analyze the in-depth (i.e., vertical) and in-plane (i.e., lateral) distribution of chemistry in the device; i.e., three-dimensional information is obtained. However, there are certain problematic phenomena associated with the depth-profiling process that make it wise to consider an additional approach. During the depth-profiling analysis, the surface is bombarded with positively charged sputter ions of such high flux that the charge buildup cannot be adequately compensated for. The consequence is a dramatically reduced sensitivity. Furthermore, the sputter-ion bombardment degrades most of the molecular information, leaving only fragment ions to be analyzed. For example, C_{60} (or PCBM) will only be detected as a series of $C_mH_n^{\pm}$ ions when sputtering is involved but will additionally produce molecular ions ($C_{60}^{\pm}$) when only primary analysis ions are used. Finally, the sputter process causes interlayer mixing, which becomes increasingly worse for longer sputter times. Interlayer mixing makes it difficult (but not impossible) to analyze the interfaces in the multilayer film using depth profiling.

The interfaces in a polymer solar cell could be analyzed using nondestructive techniques such as spectroscopic ellipsometry or X-ray reflectivity (38). However, these provide structural information, and this study focuses primarily on chemical degradation, i.e., water-induced degradation of polymer solar cells, so chemical characterization is preferred such as TOF-SIMS or alternatively X-ray photoelectron spectroscopy. The best additional alternative to analyze the interior of a polymer solar cell with respect to chemistry is thus to systematically remove each layer in the device and analyze the exposed interfaces (II–IV in Figure 5). Only the four polymer solar cell devices that where exposed to isotopically labelled ~90% relative humidity (nos. 1, 2, 4, and 5 in Table 1) were studied using TOF-SIMS methodologies. The solar cell devices were disassembled on only part of the active area, leaving space for depth-profiling analysis through the entire device. The aluminum electrode layer was removed by applying adhesive tape and peeling it off, thus exposing the Al/X:PCBM interface (II in Figure 5) and enabling surface analysis. The X:PCBM layer was removed by gently swabbing a cotton stick soaked in chloroform multiple times across the surface, consequently exposing the X:PCBM/PEDOT:PSS interface (III in Figure 5). The PEDOT:PSS/ITO interface (IV in Figure 5) was exposed in the same way but using a cotton stick soaked in water instead.

All of the interfaces on the four devices were subjected to TOF-SIMS imaging, and a TOF-SIMS depth profile was performed through each device starting from the outer aluminum surface (I in Figure 5) and ending in the glass substrate. The combined results are presented and discussed in the following.

Figure 6 shows depth profiles of the four devices in question starting from the outer aluminum electrode surface (I in Figure 5) and ending somewhere in the active material. It took ~13 h under the given conditions to sputter through the entire device, ending in the glass substrate. However, only the first 1.4 h is informative, so only this part of the depth profiles is shown. Three types of profiles are shown: one for the AlO_2^- intensity (marker for the aluminum electrode, or rather the aluminum oxide part of the aluminum electrode), one for the C_4^- intensity (shared marker for each of the components in the active material X:PCBM), and finally the $^{18}O/^{16}O$ ratio. The AlO_2^- profiles (Figure 6a–d) inform us (not surprisingly) that there is a layer of aluminum oxide on each side of the aluminum electrode. In addition, a logarithmic AlO_2^- intensity scale (Figure 6b) reveals that aluminum oxide is present all the way through the aluminum electrode.

C_4^- is a shared marker for PCBM,P3HT, and MEH-PPV and is observed (as expected) to increase at the Al/X:PCBM interface. The C_4^- profiles have a maximum in the aluminum oxide region. This is due to a matrix effect caused by the vicinity of the oxide. The AlO_2^- and C_4^- profiles are consistent with previous experiments on a similar system using $^{18}O_2$ instead of $H_2{}^{18}O$ (18, 26, 28).

Figure 7 represents an example of how nonideal conditions can be used to extract pseudo depth profiles from a TOF-SIMS ion image. When the sputter-ion beam is rastered over an area, the outcome should ideally be a perfectly box-shaped hole. Instead, the hole is rounded off at the edges, and if the sputtering continues on for a long time, the effect becomes so pronounced that it becomes possible to detect the individual layers in the multilayer device from a subsequent TOF-SIMS imaging analysis over an area that extends the sputter hole. Line profiles can then be extracted from the ion image, e.g., at the dashed white line in Figure 7a, which should qualitatively represent pseudo depth profiles. The depth resolution is, however, even worse than the one obtained from the traditional depth profiling, so this alternative approach has limited applicability. An obvious advantage, however, is an increased sensitivity due to the absence of the parallel sputter process that is a natural part of the depth-profiling procedure. The sputter process incorporates positively charged sputter ions in the surface (i.e., charge buildup) that significantly decreases the signal intensity and thus decreases the sensitivity. After the sputter process and

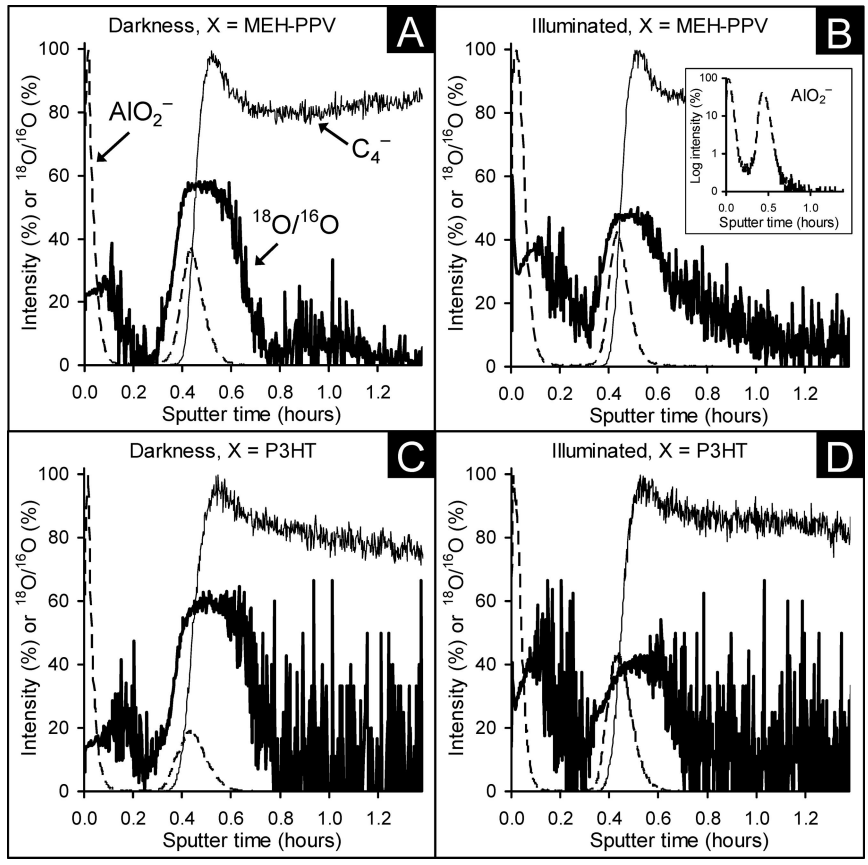

FIGURE 6. TOF-SIMS depth profiles for the devices that were exposed to ~90% relative humidity (nos. 1, 2, 4, and 5 in Table 1). The figures display $^{18}O/^{16}O$ ratios and normalized intensities for selected mass spectral markers as a function of the sputter time. AlO_2^- is a marker for the aluminum electrode, and C_4^- is a marker for the active material X:PCBM (X is P3HT or MEH-PPV). The inset in part B shows the AlO_2^- profile using a logarithmic intensity scale.

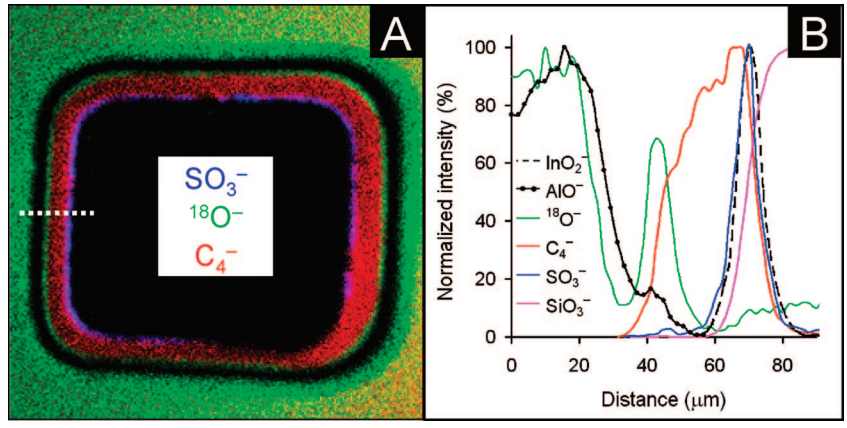

FIGURE 7. (A) TOF-SIMS ion image (500 × 500 μm^2) covering an entire sputter hole (~400 × 400 μm^2) after a depth-profiling analysis (Figure 66) of a device with the configuration Al/P3HT:PCBM/PEDOT:PSS/ITO. C_4^- is a marker for P3HT:PCBM, SO_3^- is a marker for PEDOT:PSS, and $^{18}O^-$ is a marker for ^{18}O incorporation or for natural ^{18}O. (B) Line profiles acquired from the dashed white line in the ion image. SiO_3^- is a marker for the glass substrate, InO_2^- is a marker for ITO, and AlO^- is a marker for the aluminum electrode. The color black in part A is not representative of a particular species; it simply means no intensity.

prior to the imaging analysis, this charge buildup will have had plenty of time to be neutralized.

The $^{18}O/^{16}O$ ratio profiles provide information on the in-depth incorporation of $H_2{}^{18}O$. The natural $^{18}O/^{16}O$ ratio is 0.2 %, so if the measured ratio is higher than this value, it must mean that incorporation of water ($H_2{}^{18}O$) occurred during and only during the experiment; i.e., incorporation of $H_2{}^{16}O$ during fabrication and handling is ignored. The marker $^{18}OH^-$ cannot be used because of a mass spectral peak overlap with the intense F^- peak that is always present (contamination). The TOF-SIMS analysis takes place in an ultrahigh vacuum chamber (10^{-10} mbar without a sample and 10^{-8}–10^{-9} mbar with a sample) so no nonreacted water is present during the analysis; i.e., it is the fixated (reacted) water that is detected.

It is evident from Figure 6a–d that $H_2{}^{18}O$ has been incorporated extensively in the aluminum oxide; i.e., some of the ^{16}O atoms have been replaced with ^{18}O atoms on the

outer aluminum electrode as well as in the aluminum oxide at the Al/X:PCBM interface. This phenomenon was also observed on a similar system using 1 atm of $N_2/^{18}O_2$ (80:20) for approximately the same period of time (25). However, the only significant difference is the extent of incorporation; in the previous experiment, the detected $^{18}O/^{16}O$ ratio did not exceed ~5% (compared to ~60% in this experiment), which suggests that water is incorporated more efficiently in aluminum oxide compared to molecular oxygen and/or reacts more readily with metallic aluminum. At this point, it can be concluded that water under the given conditions penetrates the aluminum electrode during illumination as well as in darkness. Incorporation of ^{18}O into the bulk of the aluminum oxide has presumably no effect on the photovoltaic properties assuming that it is purely a substitutional phenomenon. However, if the oxygen concentration increased in the bulk of the aluminum electrode during the experiment, then the barrier would have increased, which would have affected the photovoltaic properties. No effort was made to clarify whether molecular oxygen (not isotopically labelled) was added to the aluminum electrode during the experiment. It is far more interesting to learn whether $H_2{}^{18}O$ incorporates into the active materials (X:PCBM) at the Al/X:PCBM interface and to see how far into the device $H_2{}^{18}O$ is incorporated.

The right sides of the $^{18}O/^{16}O$ ratio profiles at the Al/X:PCBM interface in Figure 6a–d are rather informative. After ~0.7 h of sputtering (i.e., past the AlO_2^- profile), incorporation presumably occurs in the X:PCBM material. If the $^{18}O/^{16}O$ ratio profile in Figure 6a is compared with the one in Figure 6b, a distinct difference is observed. The $H_2{}^{18}O$ incorporation is clearly more pronounced in MEH-PPV:PCBM for the illuminated device compared to the one that was stored in darkness; i.e., illumination increases the water-induced degradation. This was the same conclusion made in the previous experiments using $^{18}O_2$ (26). For both P3HT devices, the $^{18}O/^{16}O$ ratio profiles are almost nonexistent after ~0.7 h of sputtering because of a significantly high signal-to-noise ratio caused by and an extremely low intensity of $^{18}O^-$. It is now possible to conclude that $H_2{}^{18}O$ degrades MEH-PPV:PCBM in darkness and during illumination in particular. Care should be taken when comparing $^{18}O/^{16}O$ ratios between devices with different configurations. One should consider the "natural" ^{16}O content of the materials. For example, P3HT contains no oxygen but MEH-PPV contains two oxygens per monomer unit (Figure 1). However, in this case, the ^{16}O contribution will only have dampened the effect observed for MEH-PPV in Figure 6a,b; i.e., the conclusions are still valid.

In summary, from the depth-profiling analysis, it was possible to extract information that shows that water diffuses into the device through the aluminum electrode regardless of whether it is illuminated or not. The depth profiles suggest that water is incorporated more efficiently in aluminum oxide compared to molecular oxygen. Water incorporation is observed to be more pronounced in the MEH-PPV:PCBM layer for the illuminated device compared to the one that was stored in darkness; i.e., illumination increases the water-induced degradation, consistent with earlier observations using $^{18}O_2$ (26).

Table 3. TOF-SIMS $^{18}O/^{16}O$ Ratios (in %) Measured on the Outer Aluminum Electrode and in Each of the Interfaces for Polymer Solar Cells with the Configuration Al/X:PCBM/PEDOT:PSS/ITO (X = P3HT or MEH-PPV)[a]

condition	position analyzed[b]	X = P3HT[c] (%)	X = MEH-PPV[c] (%)
darkness	I	26.4 ± 0.6	26.2 ± 2.6
illuminated	I	27.4 ± 0.3	24.1 ± 1.2
darkness	II	3.9 ± 0.3	11.1 ± 0.3
illuminated	II	5.6 ± 0.9	24.0 ± 0.8
darkness	III	2.3 ± 0.5	4.0 ± 0.1
illuminated	III	3.6 ± 0.3	3.6 ± 0.2
darkness	IV	4.1 ± 0.4	4.3 ± 0.1
illuminated	IV	3.5 ± 0.1	4.5 ± 0.3

[a] Each $^{18}O/^{16}O$ ratio is an average of five measurements on different surface locations. [b] The positions refer to Figure 5. [c] X refers to Figure 2 or 5.

On the basis of the signal-to-noise ratios observed in Figure 6a–d at 1.3 h of sputtering, it is tempting to conclude that $H_2{}^{18}O$ incorporation does no exude much further into the device. This is, however, far from the truth; the noisy $^{18}O/^{16}O$ ratio profiles are a consequence of the poor sensitivity caused by the sputter process. TOF-SIMS mass spectra were thus acquired on the outer aluminum electrode surface (I in Figure 5) and in each of the exposed interfaces (II–IV in Figure 5) in order to ascertain how far into the device $H_2{}^{18}O$ incorporation occurs under the given circumstances. Table 3 lists the $^{18}O/^{16}O$ ratios extracted from the TOF-SIMS mass spectra. The values from the outer aluminum electrode (I in Figure 5) should, in principle, be the same but are observed to differ slightly. The errors indicated are standard deviations based on five measurements on different surface locations. However, these are not necessarily representative for the possible sample-to-sample variation. Furthermore, the values in Table 3 for the outer aluminum electrode should not be compared with the values indicated in the $^{18}O/^{16}O$ ratio profiles in Figure 6. There are no zero values in the profiles because the depth-profiling process (unfortunately) begins with the sputter step instead of the analysis step.

When the $^{18}O/^{16}O$ ratios between the P3HT and MEH-PPV devices in the Al/X:PCBM interface (II in Figure 5) are compared, there are convincing differences. $H_2{}^{18}O$ reacts much more efficiently with MEH-PPV:PCBM compared to P3HT:PCBM. If the corresponding ratios for the illuminated devices are compared with the ones stored in darkness, it becomes clear that illumination enhances the $H_2{}^{18}O$ degradation. These observations are consistent with the conclusions made from Figure 6. It is now possible to set up a relative order of water stability for the four devices (or donor/acceptor materials) in question: P3HT:PCBM (darkness) > P3HT:PCBM (illuminated) > MEH-PPV:PCBM (darkness) > MEH-PPV:PCBM (illuminated).

At the X:PCBM/PEDOT:PSS interface (III in Figure 5), there are (as expected) no significant differences except for

a discrepancy between the two devices stored in darkness. The values differ significantly (2.3 ± 0.5 versus 4.0 ± 0.1). A possible explanation could be due to insufficient removal of MEH-PPV:PCBM at the interface.

At the PEDOT:PSS/ITO interface (IV in Figure 5), $H_2{}^{18}O$ incorporation is evident; i.e.; $H_2{}^{18}O$ has in all cases penetrated through the entire device to the ITO layer. There are no significant differences in $^{18}O/^{16}O$ ratios between the devices, which suggests either that diffusion through the X:PCBM layer is the same and/or that an equilibrium has had time to be established during the experiment. In a previous experiment (18) using $^{18}O_2$, incorporation was also observed in the ITO, however, with a factor of 10 lower efficiency. Water is apparently more efficiently incorporated into ITO compared to molecular oxygen. The same conclusion was made earlier in this paper for aluminum oxide. A similar experiment (31, 32) was previously performed on a hybrid solar cell with the configuration Ag/MEH-PPV/Nb_2O_5/ITO, where it was shown that ^{18}O (from $^{18}O_2$) only incorporates into the outer monolayer of oxygen in Nb_2O_5. It was, furthermore, shown that in the absence of oxygen in the atmosphere the oxygen is depleted at the MEH-PPV/Nb_2O_5 interface (i.e., the outer oxygen monolayer on the Nb_2O_5 surface), causing the photovoltaic properties to degrade until oxygen was added to the atmosphere, whereafter the outer oxide layer was reestablished at the Nb_2O_5 surface and the photovoltaic properties were reviewed.

In summary, by comparison of mass spectra from all interfaces of the four devices, it was possible to conclude that water diffuses through all layers in the device all the way to the counter electrode (ITO) and that water reacts much more efficiently with MEH-PPV:PCBM compared to P3HT:PCBM. Previous conclusions on the fact that illumination accelerates water-induced degradation are supported by the mass spectral data from the interfaces. The mass spectral investigation of the interfaces enabled a relative order of water stability to be set up for the four devices (or donor/acceptor materials) in question: P3HT:PCBM (darkness) > P3HT:PCBM (illuminated) > MEH-PPV:PCBM (darkness) > MEH-PPV:PCBM (illuminated).

In order to juxtapose our findings with previous work (18, 26), we examined data for isotopic labeling studies at the Al/C_{60} interface using $^{18}O_2$ under both light and dark conditions. One point of reservation is that the two experiments (18, 26) had a different underlying geometry while the Al/C_{60} interface and the conditions of labeling $^{18}O_2$ were similar to this work. Figure 8 shows TOF-SIMS $^{18}O/^{16}O$ ratio images from this previous work (18, 26). The image in Figure 8a was acquired from an Al/C_{60} interface in a device with the configuration Al/C_{60}/P3CT/ITO after having been stored in darkness for 800 h in a $N_2/^{18}O_2$ (80:20) atmosphere after degradation in vacuum. The image in Figure 8b was also acquired from an Al/C_{60} interface that was part of a device with the configuration Al/C_{60}/C_{12}—PSV/PEDOT:PSS/ITO after having been illuminated for 45 h in a $N_2/^{18}O_2$ (80:20) atmosphere. The circularly oriented incorporation in the lateral plane was shown to be a consequence of microscopic

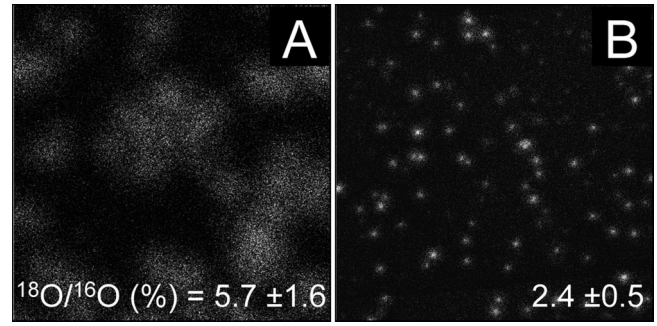

FIGURE 8. TOF-SIMS $^{18}O/^{16}O$ ratio images (500 × 500 μm^2) of two different devices: (A) Al/C_{60} interface in a device with the configuration Al/C_{60}/P3CT/ITO [P3CT corresponds to poly(3-carboxydithiophene)]; (B) Al/C_{60} interface in a device with the configuration Al/C_{60}/C_{12}—PSPV/PEDOT:PSS/ITO [C_{12}—PSV corresponds to polydidodecylstilbenylenevinylene]. The ratio scale is normalized such that black is zero ratio, gray is some ratio, and white is maximum ratio.

holes in the aluminum electrode. $^{18}O_2$ diffuses vertically through the holes and expands in all lateral directions, reacting with C_{60}, whereafter ^{18}O becomes fixated in degradation products. One should bear in mind that the experimental conditions were different (different exposure times, darkness and illumination, and different thicknesses of the aluminum electrode); however, it is still valid to compare the qualitative differences. The spots in Figure 8b are smaller and more intense than the large blurry spots in Figure 8a. The small intense spots suggest that molecular oxygen reacts faster when illuminated. In other words, molecular oxygen reacts in close vicinity to the holes in the lateral plane. In contrast, the device stored in darkness reacts relatively slower and has time to diffuse further in the lateral plane, resulting in bigger but more blurred circular spots. The circular spots were also found in the C_{12}—PSV/PEDOT:PSS interface for the Al/C_{60}/C_{12}—PSV/PEDOT:PSS/ITO device but were not found in the C_{60}/P3CT interface for the Al/C_{60}/P3CT/ITO device (P3CT was shown to be practically inert toward $^{18}O_2$). However, homogeneous ^{18}O incorporation was observed in the ITO surface for both devices, which led to the conclusion that it cannot be ruled out that there is a contribution from the diffusion of $^{18}O_2$ through the grains in the aluminum electrode.

Figure 8 distinguishes incorporation of ^{18}O under dark-light conditions for the Al/C_{60} interface using molecular oxygen ($^{18}O_2$) as the source of isotopically labelled oxygen. In contrast, Figure 9 presents TOF-SIMS $^{18}O/^{16}O$ ratio images acquired for the four different experiments carried out here with water ($H_2{}^{18}O$) as the source of isotopically labelled oxygen. The device configuration in this study was Al/X:PCBM/PEDOT:PSS/ITO. The images are obtained in the Al/X:PCBM interface (II in Figure 5). As is evident from all four images, no circular spots are observed except for some slight inhomogeneities. The tiny white dots in Figure 9a,b are mostly normalized noise. These observations suggest that $H_2{}^{18}O$ diffuses efficiently/rapidly through the aluminum grains in the aluminum electrode, causing homogeneous incorporation/degradation. In this case, all electrodes have the same thickness (100 nm). The corresponding images for the remaining interfaces have also practically homogeneous

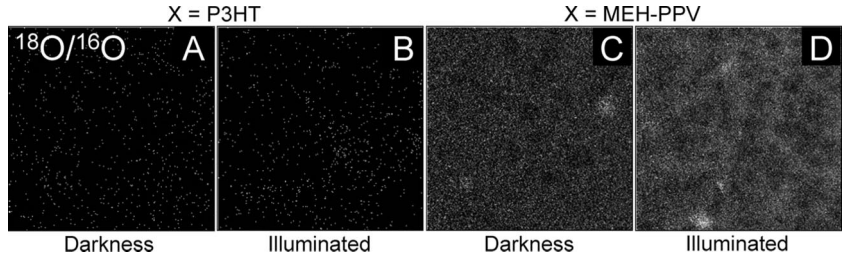

FIGURE 9. TOF-SIMS $^{18}O/^{16}O$ ratio images (500 × 500 μm^2) in the Al/X:PCBM interface (II in Figure 5) of the four devices with the configuration Al/X:PCBM/PEDOT:PSS/ITO. X is P3HT or MEH-PPV. The ratio scale is normalized such that black is zero ratio, gray is some ratio, and white is maximum ratio.

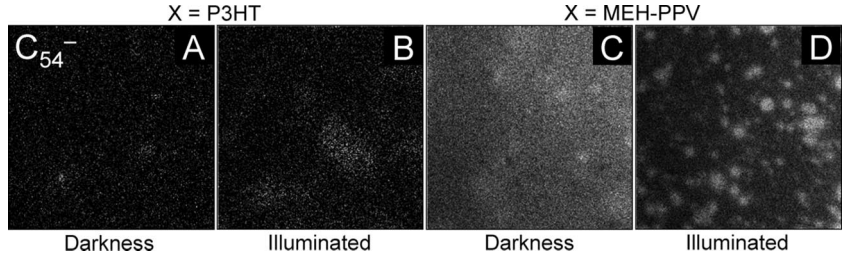

FIGURE 10. TOF-SIMS ion images (500 × 500 μm^2) in the Al/X:PCBM interface (II in Figure 5) of the four devices with the configuration Al/X:PCBM/PEDOT:PSS/ITO. X is P3HT or MEH-PPV. C_{54}^- is a marker for degraded PCBM. The intensity scale is normalized such that black is zero intensity, gray is some intensity, and white is maximum intensity.

$^{18}O/^{16}O$ ratio distributions (not shown). Compared to molecular oxygen, water seems to behave differently with respect to diffusion through the aluminum electrode. However, it could be argued that water could have diffused into the device from the side instead of through the aluminum electrode. This is unlikely because of the extreme ratio between the thicknesses of the various layers (~100 nm) and the width and length of the device (centimeters). The diffusion from the edges is thus expected to be extremely slow (even when the exposure time of 250 h is considered) compared to diffusion through the aluminum electrode.

In summary, the results from an imaging analysis of all interfaces for all four devices suggest that water diffuses efficiently/rapidly through the aluminum electrode between the aluminum grains, causing homogeneous incorporation/degradation in all interfaces. This is a behavior opposite to that of molecular oxygen, which has been shown to at least mainly diffuse through the microscopic pinholes in the aluminum electrode, causing circularly oriented incorporation/degradation, i.e., inhomogeneous incorporation/degradation.

The molecular ion of PCBM (Figure 1) is not sufficiently stable during ionization under the analysis conditions in question; however, the fragment C_{60}^- is (or C_{60}^+ for positively charged secondary ions), so C_{60}^- is used as a specific marker for PCBM. If a freshly prepared Al/X:PCBM interface (II in Figure 5) is analyzed, then only C_{60}^- is detected in the high mass region (not shown). The mass spectra for the corresponding interfaces for the exposed (light + heat + $H_2{}^{18}O$ or heat + $H_2{}^{18}O$) devices include peaks corresponding to degraded C_{60}; i.e., the C_{60} part of PCBM shows signs of degradation after exposure. These mass spectral peaks correspond mainly to C_{60-2n}^- ($n = 1-4$); i.e., no oxygen-containing ions are detected. The in-plane distribution of one of these fragment ions (C_{54}^-) is shown in Figure 10 for the Al/X:PCBM interface for each of the four devices in question. Parts a–c of Figure 10 show fairly homogeneous distributions, but Figure 10d shows a pronounced inhomogeneous C_{54}^- distribution of the same pattern type like the ones shown in Figure 8 for the $^{18}O/^{16}O$ ratio distribution. The C_{60}^- distribution corresponding to Figure 10d is complementary to the C_{54}^- distribution (not shown). From Figure 9, it is fairly certain that $H_2{}^{18}O$ diffuses through the aluminum electrode in a homogeneous manner, i.e., between the aluminum grains. The C_{54}^- distribution in Figure 10d thus suggests that it is the combination of light and molecular oxygen (ambient $^{16}O_2$) that is accelerating the C_{60} degradation. The devices used in this work were exposed to ambient air during fabrication and during transportation to and from equipment. At least molecular oxygen seems to be involved in the degradation mechanism regarding the C_{60} part of PCBM.

The Al/X:PCBM interfaces (II in Figure 5) were additionally analyzed with respect to positive secondary ions. The distribution patterns for Na^+ revealed an interesting phenomenon. The P3HT devices have more or less homogeneous distribution patterns, but the MEH-PPV devices have not. In Figure 11c, the sodium is distributed everywhere with an elevated intensity at circular-shaped spots (potassium is concentrated at the dark circular spots). In Figure 11d, the Na^+ intensity is even more elevated in the circular spot areas. In addition, the sodium seems to have vanished from the center of the circular spots, leaving rings of sodium. MEH-PPV is probably more hydrophilic after degradation/oxygenation, which would increase the affinity toward Na^+ and possibly induce migration of Na^+ into the degraded parts of the device. It was not possible to find an explanation as to why Na^+ is not present in the center parts of the degraded areas that were presumably degraded by molecular oxygen. There are two possible sodium sources. (i) The obvious one is that it was leftover from the synthesis (i.e., of PCBM, P3HT, or MEH-PPV) because of insufficient purification. (ii) The other source is the PEDOT:PSS layer. PEDOT:PSS typically

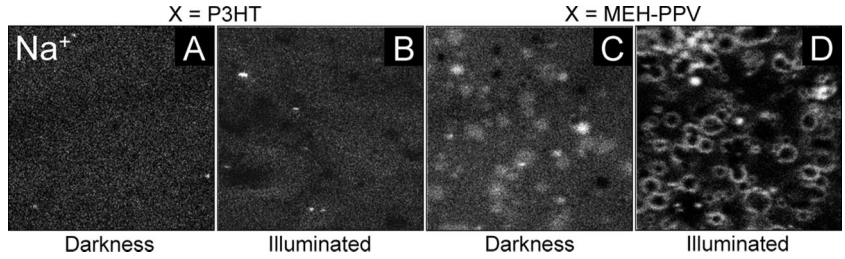

FIGURE 11. TOF-SIMS ion images (500 × 500 μm^2) in the Al/X:PCBM interface (II in Figure 5) of the four devices with the configuration Al/X:PCBM/PEDOT:PSS/ITO. X is P3HT or MEH-PPV. The intensity scale is normalized such that black is zero intensity, gray is some intensity, and white is maximum intensity.

contains a few hundred parts per million of sodium that could have segregated through the active layer to the Al/X:PCBM interface. PEDOT:PSS contains a small excess of PSS that could have acted as a counterion and thus migrated together with Na^+. However, PSS was not detected in the interface, which would otherwise have supported the theory that sodium originates from the PEDOT:PSS layer. It is not known what the presence of (or migration of) Na^+ has on the photovoltaic properties. The sodium phenomenon is a good example of the fact that an overwhelming amount of (desired and undesired) processes take place during operation of a polymer solar cell. It is impossible to guess how many undesired processes that are still not discovered.

Particle formation in polymer solar cell devices is an area that has received almost no attention. It is thus unknown to what extent particles affect the photovoltaic properties. In previous work from this laboratory, an attempt was made to identify the mechanism for particle formation in an incomplete device (28). The molecular identity of the particles is the key to understanding how the particles are formed. However, to establish the identity of the particles, it is necessary to gain access to them, and that is problematic. The washing procedure used in this work removes the individual layers and thus possible particles located in the bulk of the layers, and possible particles located in the interface will most likely be washed away. Depth profiling is an obvious alternative, but the method suffers from the fact that the sputter process destroys the molecular identity, leaving only small pieces of the puzzle. The particles are visible from the acquired images during a depth-profiling analysis so at least they can be bypassed by software methods as a post-treatment of the data. Possible particle areas were therefore disregarded in the depth profiles presented in Figure 6 in order to avoid nonrelevant complex contributions to the depth profiles.

Possible particles are expected to be formed either in the bulk X:PCBM layer or at the X:PCBM/PEDOT:PSS interface with respect to the devices from this work. In an attempt to image the particles in the device, the following experiment was performed on the illuminated MEH-PPV device starting from the Al/MEH:PCBM interface (II in Figure 5). The images from a depth-profiling analysis were monitored during acquisition. When the images started to show weak signs of particles, the analysis was stopped and the analysis parameters were adjusted to increase the intensity, which caused the acquisition time to increase. To compensate for the increased acquisition time the sputter area size was reduced to ~200 × 200 μm^2 in order to increase the sputter-

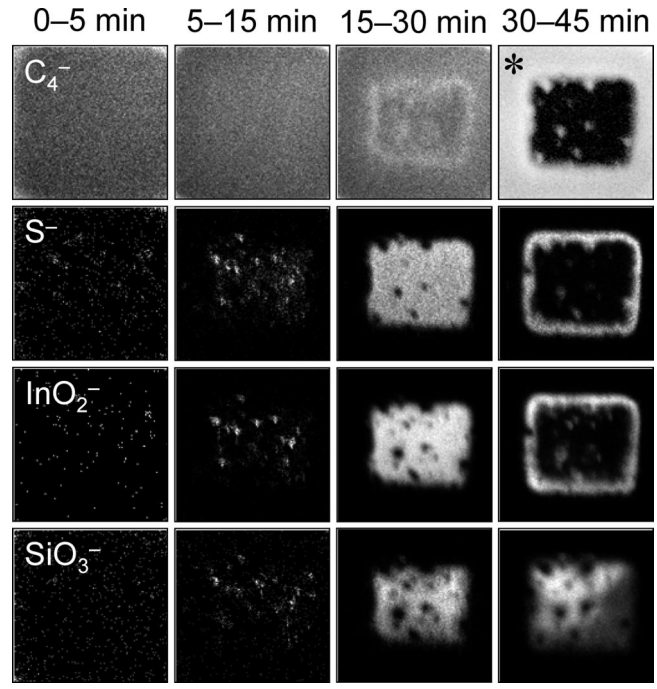

FIGURE 12. TOF-SIMS ion images (200 × 200 μm^2) over a sputter hole performed in the Al/MEH-PPV:PCBM interface (II in Figure 5) of a device with the configuration Al/MEH-PPV:PCBM/PEDOT:PSS/ITO that was illuminated. C_4^- is here a shared marker for P3HT, MEH-PPV, and PEDOT:PSS. S^- is a marker for PEDOT:PSS. InO_2^- is a marker for ITO. SiO_3^- is a marker for the glass substrate. The intensity scale is normalized such that black is zero intensity, gray is some intensity, and white is maximum intensity. The image marked with an asterisk has a logarithmic intensity scale.

ion flux (reduces the depth resolution), which reduced the sputter time and thus the acquisition time. Relevant images are shown in Figure 12 for various relevant sputter time windows. At 5−15 min, particles are detected containing at least sulfur, indium, and silicon. At 15−30 min, particles are indirectly visible as dark spots. The interesting observation is that these particles have a different distribution pattern compared to the ones at 5−15 min. Finally, at 30−45 min, it becomes more or less clear that the second set of particles contains at least carbon, sulfur, and perhaps indium. The observations suggest that PEDOT:PSS and ITO are involved in the particle formation. C_4^- is a shared marker for MEH-PPV, PCBM, and PEDOT:PSS, so it is not possible to conclude whether the active layer is involved or not. One could argue that the observed phenomenon could be due to uneven sputtering; however, such sputter-induced surface/interface irregularities would probably occur on a smaller scale. Care should be taken when interpreting these kinds of images

(Figure 12). A particle is likely to be eroded (by the sputter process) at a different rate than the surroundings, which would induce uneven sputtering that would continue on. Particle formation in polymer solar cells is rarely commented on in the literature, probably because so little is known about the phenomenon. There is only one example in the literature that describes the phenomenon (28).

In summary, it was possible to extract information from the in-plane and in-depth distribution of some mass spectral markers that were not isotopically labeled. The mass spectral imaging data originating from PCBM suggest that it is the combination of light and molecular oxygen (i.e., not water) that is accelerating the degradation of the C_{60} part of PCBM. The imaging results from the MEH-PPV:PCBM interfaces suggest that sodium possibly segregates to locations with a relatively large extent of degradation (caused by molecular oxygen) possibly because of the higher hydrophilicity. For the illuminated MEH-PPV:PCBM interface, sodium had vanished from the center part of the degraded areas. No explanation was found for this phenomenon. An in-depth analysis of selected nonisotopically labeled mass spectral markers suggests that at least two types of particles are found in at least the illuminated MEH-PPV device. One type of particles contains at least sulfur, indium, and silicon. The other type contains at least carbon, sulfur, and perhaps indium. The observations regarding particles suggest that PEDOT:PSS and ITO are involved in the particle formation. It was not possible to conclude whether the active layer is involved in particle formation or not. It was not possible to conclude anything about to what extent particles influence the photovoltaic properties.

CONCLUSIONS

Water-induced degradation of polymer solar cells with the configuration Al/X:PCBM/PEDOT:PSS/ITO (X = P3HT or MEH-PPV) was studied. The use of $H_2{}^{18}O$ in conjunction with TOF-SIMS methodologies enabled mapping of the parts of the device that were induced by water. A comparison was made between P3HT:PCBM and MEH-PPV:PCBM and between devices that were kept in the dark and devices that had been subjected to illumination under simulated sunlight. Furthermore, devices that were exposed to ambient humidity were compared to devices exposed to saturated humidity. The current result obtained using $H_2{}^{18}O$ was compared with earlier work involving $^{18}O_2$.

Short-circuit current−density decay curves of solar cell devices that were exposed to a saturated water atmosphere during operation revealed a significant degradation of the stability when compared to the corresponding devices exposed to ambient humidity.

A depth-profiling analysis showed that water diffuses into the device through the aluminum electrode regardless of whether it is illuminated or not. Water appears to be incorporated more efficiently in aluminum oxide compared to molecular oxygen. Water incorporation is observed to be more pronounced in the MEH-PPV:PCBM layer for the illuminated device compared to the one that was stored in darkness; i.e., illumination increases the water-induced degradation, consistent with earlier observations using $^{18}O_2$.

Possible incorporation of ^{18}O in the various interfaces was determined from the $^{18}O/^{16}O$ ratio extracted from the mass spectral data. On the basis of these findings, it was possible to conclude that water diffuses through all layers in the device all the way to the counter electrode (ITO). Furthermore, it was found that water reacts much more efficiently with MEH-PPV:PCBM compared to P3HT:PCBM and that illumination accelerates water-induced degradation, consistent with the depth-profiling results. The mass spectral investigation of the interfaces suggests that the relative stability of the donor/acceptor materials in question is P3HT:PCBM (darkness) > P3HT:PCBM (illuminated) > MEH-PPV:PCBM (darkness) > MEH-PPV:PCBM (illuminated).

An imaging analysis of all interfaces for all four devices suggests that water diffuses efficiently/rapidly through the aluminum electrode between the aluminum grains, causing homogeneous incorporation/degradation in all interfaces. This is a behavior opposite to that of molecular oxygen, which has been shown to at least mainly diffuse through the microscopic pinholes in the aluminum electrode, causing circular oriented incorporation/degradation, i.e., inhomogeneous incorporation/degradation.

An imaging analysis based on mass spectral markers that were not isotopically labeled showed that it is the combination of light and molecular oxygen (i.e., not water) that is accelerating the degradation of the C_{60} part of PCBM. The imaging results from the MEH-PPV:PCBM interfaces suggest that sodium possibly segregates to locations with a relatively large extent of degradation (caused by molecular oxygen) possibly because of the higher hydrophilicity. For the illuminated MEH-PPV:PCBM interface, sodium had vanished from the center part of the degraded areas. No explanation was found for this phenomenon. An in-depth imaging analysis of selected nonisotopically labeled mass spectral markers suggests that at least two types of particles are found in at least the illuminated MEH-PPV device. The observations regarding particles suggest that at least PEDOT:PSS and ITO are involved in the particle formation. It was not possible to conclude anything about to what extent particles influence the photovoltaic properties.

Acknowledgment. This work was supported by the Danish Strategic Research Council (DSF 2104-04-0030, 2104-05-0052, and 2104-07-0022).

Supporting Information Available: Evolution of the IV curves as a function of time/degradation and plots of TOF-SIMS depth profiles showing the level of ^{18}O incorporation in the bulk of the aluminum electrode on a logarithmic scale. This material is available free of charge via the Internet at http://pubs.acs.org.

REFERENCES AND NOTES

(1) Brabec, C. J.; Sariciftci, N. S.; Hummelen, J. C. *Adv. Funct. Mater.* **2001**, *11*, 15–26.
(2) Spanggaard, H.; Krebs, F. C. *Sol. Energy Mater. Sol. Cells* **2004**, *83*, 125–146.

(3) Coakley, K. M.; McGehee, M. D. *Chem. Mater.* **2004**, *16*, 4533–4542.
(4) Hoppe, H.; Sariciftci, N. S. *J. Mater. Res.* **2004**, *19*, 1924–1945.
(5) Günes, S.; Neugebauer, H.; Sariciftci, N. S. *Chem. Rev.* **2007**, *107*, 1324–1338.
(6) Krebs F. C. *Polymer Photovoltaics a Practical Approach*; SPIE Press: Bellingham, WA, 2008.
(7) Winder, C.; Sariciftci, N. S. *J. Mater. Chem.* **2004**, *14*, 1077–1086.
(8) Bundgaard, E.; Krebs, F. C. *Sol. Energy Mater. Sol. Cells* **2007**, *91*, 954–985.
(9) Thompson, B. C.; Fréchet, J. M. J. *Angew. Chem., Int. Ed.* **2008**, *47*, 58–77.
(10) Hoppe, H.; Sariciftci, N. S. *J. Mater. Chem.* **2006**, *16*, 45–61.
(11) Yang, X.; Loos, J. *Macromolecules* **2007**, *40*, 1353–1362.
(12) Jørgensen, M.; Norrman, K.; Krebs, F. C. *Sol. Energy Mater. Sol. Cells* **2008**, *92*, 686–714.
(13) Li, G.; Shrotriya, V.; Huang, J.; Yao, Y.; Moriarty, T.; Emery, K.; Yang, Y. *Nat. Mater.* **2005**, *4*, 864–868.
(14) Ma, W.; Yang, C.; Gong, X.; Lee, K.; Heeger, A. J. *Adv. Funct. Mater.* **2005**, *15*, 1617–1622.
(15) Kim, J. Y.; Lee, K.; Coates, N. E.; Moses, D.; Nguyen, T. Q.; Dante, M.; Heeger, A. J. *Science* **2007**, *317*, 222–225.
(16) Krebs, F. C.; Spanggaard, H. *Chem. Mater.* **2005**, *17*, 5235–5237.
(17) Yang, X.; Loos, J.; Veenstra, S. C.; Verhees, W. J. H.; Wienk, M. M.; Kroon, J. M.; Michels, M. A. J.; Janssen, R. A. J. *Nano Lett.* **2005**, *5*, 579–583.
(18) Krebs, F. C.; Norrman, K. *Prog. Photovoltaics* **2007**, *15*, 697–712.
(19) Bjerring, M.; Nielsen, J. S.; Siu, A.; Nielsen, N. C.; Krebs, F. C. *Sol. Energy Mater. Sol. Cells* **2008**, *92*, 772–784.
(20) Katz, E. A.; Gevorgyan, S.; Orynbayev, M. S.; Krebs, F. C. *Eur. Phys. J. Appl. Phys.* **2007**, *36*, 307–311.
(21) Hauch, J. A.; Schilinsky, P.; Choulis, S. A.; Childers, R.; Biele, M.; Brabec, C. J. *Sol. Energy Mater. Sol. Cells* **2008**, *92*, 727–731.
(22) Krebs, F. C.; Spanggaard, H.; Kjær, T.; Biancardo, M.; Alstrup, J. *Mater. Sci. Eng. B* **2007**, *138*, 106–111.
(23) Krebs, F. C.; Alstrup, J.; Spangaard, H.; Larsen, K.; Kold, E. *Sol. Energy Mater. Sol. Cells* **2004**, *83*, 293–300.
(24) Lungenschmied, C.; Dennler, G.; Neugebauer, H.; Sariciftci, N. S.; Glatthaar, M.; Meyer, T.; Meyer, A. *Sol. Energy Mater. Sol. Cells* **2007**, *91*, 379–384.
(25) Liu, A.; Zhao, S.; Rim, S. B.; Wu, J.; Könemann, M.; Erk, P.; Peumans, P. *Adv. Mater.* **2008**, *20*, 1065–1070.
(26) Norrman, K.; Krebs, F. C. *Sol. Energy Mater. Sol. Cells* **2006**, *90*, 213–227.
(27) Alstrup, J.; Norrman, K.; Jørgensen, M.; Krebs, F. C. *Sol. Energy Mater. Sol. Cells* **2006**, *90*, 2777–2792.
(28) Norrman, K.; Larsen, N. B.; Krebs, F. C. *Sol. Energy Mater. Sol. Cells* **2006**, *90*, 2793–2814.
(29) Norrman, K.; Alstrup, J.; Krebs, F. C. *Surf. Interface Anal.* **2006**, *38*, 1302–1310.
(30) Lira-Cantu, M.; Krebs, F. C. *Sol. Energy Mater. Sol. Cells* **2006**, *90*, 2076–2086.
(31) Lira-Cantu, M.; Norrman, K.; Andreasen, J. W.; Krebs, F. C. *Chem. Mater.* **2006**, *18*, 5684–5690.
(32) Lira-Cantu, M.; Norrman, K.; Andreasen, J. W.; Casan-Pastor, N.; Krebs, F. C. *J. Electrochem. Soc.* **2007**, *154*, B508—B513.
(33) Norrman, K.; Krebs, F. C. *Proc. SPIE* **2005**, *5938*, 59380D.
(34) Vickerman J. C.; Briggs D. *TOF-SIMS Surface Analysis by Mass Spectrometry*; IM Publications and Surface Spectra Ltd.: West Sussex, U.K., 2001.
(35) Neef, C. J.; Ferraris, J. P. *Macromolecules* **2000**, *33*, 2311–2314.
(36) McCullough, R. D.; Lowe, R. D.; Jayaraman, M.; Anderson, D. L. *J. Org. Chem.* **1993**, *58*, 904–912.
(37) Gevorgyan, S. A.; Jørgensen, M.; Krebs, F. C. *Sol. Energy Mater. Sol. Cells* **2008**, *92*, 736–745.
(38) Andreasen, J. W.; Gevorgyan, S. A.; Schlepütz, C. M.; Krebs, F. C. *Sol. Energy Mater. Sol. Cells* **2008**, *92*, 793–798.

AM800039W

23rd European Photovoltaic Solar Energy Conference, 1-5 September 2008, Valencia, Spain

REVERSIBLE DEGRADATION OF CONJUGATED POLYMER/FULLERENE SOLAR CELLS

Gevorgyan S. A.[1], Katz E. A[2]. and Krebs F. C.[1]
[1]Risø National Laboratory for Sustainable Energy, Technical University of Denmark, Frederiksborgvej 399, DK-4000 Roskilde, Denmark.
[2]Dept. of Solar Energy and Environmental Physics, J. Blaustein Institutes for Desert Research, Ben-Gurion University of the Negev, Sede Boker Campus 84990 Israel.

ABSTRACT: Recent studies of out-door operation of encapsulated conjugated polymer/fullerene bulk heterojunction and bi-layered solar cells with improved long-term stability revealed effect of recovery of PV parameters when the cells were kept in the dark overnight. The first short circuit current *Isc* and open circuit voltage *Voc* measurements every morning yielded the highest values compared to those during the rest of a day. It was suggested that in addition to the nonreversible photochemical degradation of the plastic cell some reversible mechanisms could be in play. Here we report experimental evidence of the reversible degradation and the restoration effect for non-encapsulated in-door characterized solar cells based on P3HT/PCBM and native polythiophene/PCBM bulk heterojunctions. We suggest that the underlying mechanism of the observed reversible degradation of *Voc* can involve the effect of temperature, while recovery of *Isc* is a result of persistent internal photopolarization in the cell photoactive layer.

Keywords: organic solar cells, bulk heterojunction, degradation, photopolarization.

1 INTRODUCTION

Along with the growing number of reports on stability and degradation of polymer-based solar cells the reported lifetimes of devices are being extended further reaching values that bring the plastic photovoltaics rather close to commercialization. 1000 hours of stability for both indoor [1] and outdoor [2] conditions have been recently reported and a number of interesting works has been devoted to explanation of the degradation process in the organic solar cells [1-7]. However, due to the unclear and almost unpredictable degradation behavior of different organic devices [8, 9] it is still hard to give an exact and precise scenario for the decay mechanisms that take place in the active layer of the cells.

Presented work is a complementary to our earlier published article that described the outdoor testing of stability of different organic solar cells and discussed the recorded reversible degradation of the cell photovoltaic parameters [8]. In this paper current work we present the further attempts of explanation of the aforementioned reversible degradation by providing some additional experimental data and suggesting a physical mechanism responsible for the effect.

2 EXPERIMENTAL

2.1 Device preparation

Solar cells were prepared according to traditional guidelines. A solution of PEDOT:PSS (Aldrich) was spin coated onto indium tin oxide (ITO)-covered glass slides (sheet resistance 8–12Ωsquare^{-1}, Delta Technologies) and dried in an oven at (150 ^{o}C, 5 min). These substrates were then transferred to a glove-box where the active layer of P3HT/PCBM (1:1) (25 mgmL^{-1} each in xylene) was spin coated. Finally, the device was transformed into evaporator and the back electrode (Aluminum) was evaporated. The final cells had an active area of 3 cm^2.

2.2 Photovoltaic characterization

The photovoltaic performance was tested under a solar simulator. The spectrum during characterization of the solar cell efficiency was AM1.5G with an incident light power of 1000 W m^{-2}. The solar simulator is Class AAA from 400-800 nm with uniform illumination over the area of the cell and for the duration of the experiment. The continuous measurement of the photovoltaic parameters (*Voc* and *Isc*) under different bias conditions were performed using Keithley 2400 controlled by PC.

3 RESULTS AND DISCUSSIONS

Fig. 1 presents our previously reported data of open circuit voltage *Voc* and short circuit current *Isc* for an encapsulated traditional P3HT/PCBM bulk heterojunction solar cell measured under real sun AM1.5G outdoor conditions [8].

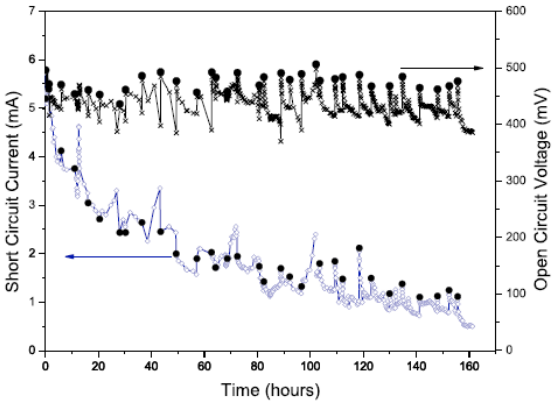

Figure 1: *Voc* and *Isc* as a function of additive time of the sunlight exposure for the P3HT/PCBM cell [8]. Solid circles indicate the very first measurements every day (from 15.03.2006 to 16.05.2006). *Isc* was normalized to the standard irradiance value of 1000 Wm^{-2}.

With the each start of the day the first measurements were giving the highest values with subsequent decay of the parameter along the day (the first measurement of the day is indicated by solid circles). Similar experiments were carried out on nonencapsulated cells with similar

configuration and structure under indoor conditions while measuring the temperature right on the back electrode of the device. Fig. 2 presents the variation of *Voc* and cell temperature while the cell was being subjected to light and dark and subsequently to 2V forward bias.

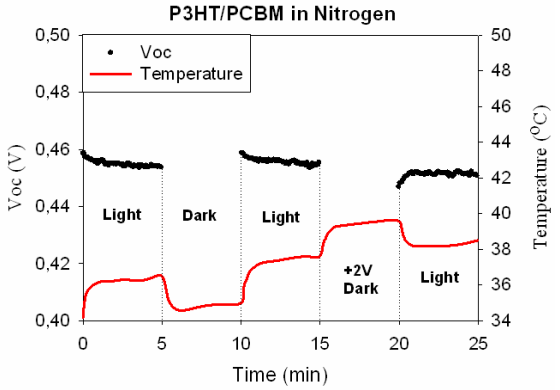

Figure 2: Measurements of *Voc* and temperature, while applying voltage and light to the cell at different times. The cells were kept in a nitrogen atmosphere. The cell configuration: Glass/ITO/PEDOT:PSS/P3HT:PCBM/ Al. The steps were the following:
0-5 min – cell is illuminated, no external field applied,
5-10 min – cell is in dark, no external field applied,
10-15 min – cell is illuminated again, no external field applied,
15-20 min – cell is in the dark, forward bias applied to the cell (+2V),
20-25 min – cell is illuminated, forward bias is released.

The temperature change clearly resembles the change of *Voc* with opposite direction. The temperature of the cell is rising, when forward bias is being applied, which is due to the high current density flow through the device. The data is reproducible on different samples. Based on obtained data one can assume that the earlier reported *Voc* recovery (Fig. 1) can be originated from the temperature variation in the device.

However, there is a different trend in *Isc* behavior. From Fig. 1 it is clear that *Isc* shows similar behavior to *Voc*. We should also stress that the *Isc* recovery effect becomes more pronounced with ageing of the cell. Since the current increases with rising temperature [10] the effect can not be attributed to the temperature change. Therefore, we suggest that there might be some photoinduced charge traps that decrease the photocurrent and disappear in the dark. In 1996 Katz et al. [11] studied the phenomenon of persistent photoconductivity (PPC) [12] in C_{60} thin films. The authors found that after exposing the film to light it takes 5 days for the conductivity of the film to reach the initial value. Along with PPC the authors recorded another phenomenon of persistent internal photopolarization (PIPP) in C_{60} thin films, which is shown in Fig. 3. After applying a voltage (time: 0 - t_2) and light (time: 0 - t_1) to the film and releasing both light and then voltage a change of current direction in the film was found (time: t_2- t_3). Further illumination of the film (time: t_3 - t_4) increased the negative current without any external electric field. It was suggested that during the first irradiation period an internal field with opposite direction to the bias field is generated in the sample, due to a movement of photo-excited electrons and holes in opposite directions under the action of the external field, and their subsequent trapping at defect centers near the electrodes. I.e. the sample was photopolarized. This internal field leads to a change of the current sign after switching off the external field and to the "negative" photocurrent flow after turning on the light the second time.

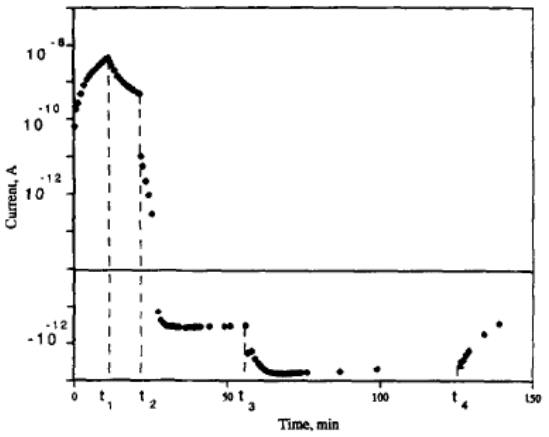

Figure 3: Kinetics of the current change in C60 thin film characteristic for PIPP effect [11]. t = 0 is the moment of turning the light on, t1 is the moment of turning the light off, t2 is the moment of turning the voltage bias off, t3 and t4 are the moments of second turning the light on and off, respectively.

A year after there was another report, where Zou et al. studied the degradation process in light emitting diodes (LEDs) and recorded recovery effect of current density and luminescence of the devices after applying external field to the device [13]. The authors suggested that when a forward bias is being applied to the device the ionic impurities in the material start to diffuse to the electrodes, the positive ions to one direction and cations to the other, creating an internal field, which is opposite to the external field. Thus, the internal field reduces the effective electric field for carrier injection. Once the forward bias is released the internal field decreases due to the depolarization of ionic impurities. As a matter of fact, the discovered recovery effect in LEDs and the earlier reported PIPP seemed to have similar nature.

Our first attempts to record recovery effect on photocurrent for freshly prepared nonencapsulated cells revealed no recovery phenomenon. However, after repeating the measurements on the one month old cell, the restoration of photocurrent was demonstrated clearly (Fig. 4). This finding is completely consistent with the recovery recorded by the outdoor measurements (Fig. 1) and confirms that the recorded phenomenon is reproducible also for nonencapsulated cells under indoor testing conditions. In addition, similar results were obtained for devices based on native polythiophene (PT)/PCBM bulk heterojunction (the route of device preparation is described elsewhere [14]). Therefore, based on the earlier reports and the currently obtained results we suggest that the PIPP in the photoactive layer of the bulk heterojuction solar cells can cause the observed reversible degradation of the cell under illumination. When the cell is kept in the dark for certain period the sample is depolarized and the internal field decreases. As a result, at a very first stage of cell illumination the photocurrent gives the highest value with subsequent decay within the time. The older the cell is, the more is the concentration of defects in the active

layer and the stronger is the internal filed.

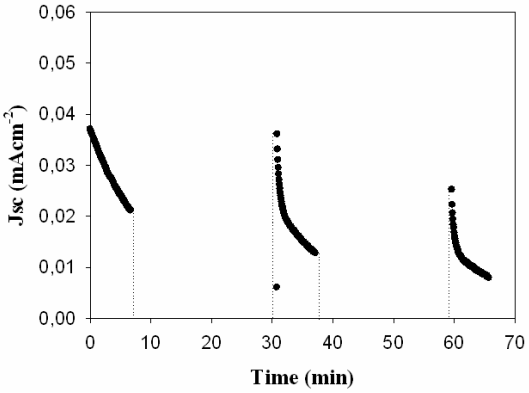

Figure 4: Short circuit current density Jsc versus time while the cell is being periodically exposed to 1sun irradiation and dark.

4 CONCLUSIONS

The further investigations of the reversible degradation effect in polymer solar cells confirmed that the phenomenon is observed independently on testing conditions and device configuration. The detailed studies showed that the recovery of *Voc* can be resulted from temperature change in the device active layer. While the nature of the *Isc* recovery resembles the earlier studied effect of photoinduced internal photopolarization (PIPP) and the effect becomes more apparent with ageing of the cell. These findings could further elucidate the decay processes that take place in the cell.

5 AKNOWLEDGMENTS

This work was further supported by the Danish Strategic Research Council (DSF 2104-05-0052 and DSF-2104-07-0022). Mikkel Jørgensen is acknowledged for PC software assistance.

6 REFERENCES

[1] X. Yang, J. Loos, S. C. Veenstra, W. J. H. Verhees, M. M. Wienk, J. M. Kroon, M. A. J. Michels and R. A. J. Janssen, Nano Letters, 5 (2005) 579.
[2] J. A. Hauch, P. Schilinsky, S. A. Choulis, R. Childers, M. Biele, C. J. Brabec, Solar Energy Materials & Solar Cells, 92 (2008) 727.
[3] F. C. Krebs, H. Spanggaard, Chemistry of Materials, 17 (2005) 5235.
[4] F. C. Krebs, K. Norrman, Progress in Photovoltaics: Research and Applications, 15 (2007) 697.
[5] M. Bjerring, J. S. Nielsen, A. Siu, N. C. Nielsen, F. C. Krebs, Solar Energy Materials & Solar Cells, 92 (2008) 772.
[6] H. Neugebauer, C. Brabec, J.C. Hummelen, N.S. Sariciftci, Solar Energy Materials & Solar Cells 61 (2000) 35.
[7] K. Kawano, R. Pacios, D. Poplavskyy, J. Nelson, D.D.C. Bradley, J.R. Durrant, Solar Energy Materials & Solar Cells 90 (2006) 3520.
[8] E.A. Katz, S. Gevorgyan, M.S. Orynbayev and F.C. Krebs, European Physical Journal – Applied Physics, 36 (2006) 307.
[9] S. A. Gevorgyan, M. Jørgensen, F. C. Krebs, Solar Energy Materials & Solar Cells 92 (2008) 736.
[10] N. Camaioni, G. Ridolfi, G. Casalbore-Miceli, G. Possamai and M. Maggini, Advanced Materials, 14 (2002) 1735.
[11] E.A. Katz, V.M. Lyubin, D. Faiman, S. Shtutina, A. Shames and S. Goren, Solid State Communications, 100 (1996) 781.
[12] H. Kallmann and B. Rosenberg, Physical Review, 97 (1955) 1596.
[13] D. Zou, M. Yahiro, T. Tsutsui, Synthetic Metals, 91 (1997) 191.
[14] S. A. Gevorgyan and F. C. Krebs, Chemistry of Materials, 20 (2008) 4386.

Advanced Processing of New Materials for Extended Operational Lifetime of Polymer Solar Cells

S.A. Gevorgyan and F.C. Krebs, Risø National Laboratory for Sustainable Energy, Roskilde, Denmark

ABSTRACT

Lifetimes of over one year have been reported for traditional organic solar cell devices using various buffer layers and encapsulation techniques. Yet the new types of thermocleavable polymers might offer a possibility of producing devices that can operate without encapsulation. In addition, changing the device structure can significantly affect the operational stability of the device under different environmental conditions. The method is also fully roll-to-roll compatible and demonstrates that it is possible to manufacture devices in large scale with reasonable photoconversion efficiencies (PCE) and lifetimes using vacuum free coating steps only. PCEs in excess of 2% have been achieved for roll-to-roll coated cells and up to 3% for small model devices. Exceptional resilience towards oxygen and water has been shown for different structures.

INTRODUCTION

There are three key issues that represent the essence of the OPV field: photovoltaic conversion efficiency (PCE), device lifetime and large scale processing. Most of the research has been focusing on optimization of the PCE [1,2], but in recent years also the lifetime [3-5] and the large scale production [6,7] of the devices have received some attention. Both the PCE and the lifetime have been optimized independently and brought to values reasonable for commercial applications and very recently there have been a number of reports on large scale production of organic solar cells. Yet, there has been no report on a device that posses all three optimized parameters at the same time, while it is an essential requirement that must be fulfilled in order to bring the OPV technology to the commercial market.

The current manuscript discusses new approaches for producing organic solar cells that bring them closer to the desired universal device. As a first step utilization of a new type of thermocleavable polymers is discussed, which show promising stability under atmospheric conditions. The second part discusses the application of an inverted device geometry, which allows processing using full roll-to-roll coating techniques and also results in different degrading behaviors of the photovoltaic parameters.

THERMOCLEAVABLE POLYMERS

One of the steps during the syntheses of conjugated polymers for photovoltaic applications involves the attachment of the side chains in order to make the material soluble in various solvents, which allows using solution processing technique for thin film production. However, after casting the film the side chains are of no use anymore, since they are occupying a significant part of the film (up to 40%) and yet they do not contribute in photoconversion effect in any way. Moreover the side chains make the polymer soft and therefore exposed to morphological instabilities. The idea behind the thermocleavable polymers is that during the synthesis of the polymer carboxylic groups are attached to the main rings of the polymer and the side chains are attached to the carboxylic groups. It gives the possibility to cleave the polymer at high temperatures resulting in removal of the side chains and decarboxylation. After this the film becomes insoluble.

Two thermocleavable polymers with different optical band gaps have been tested for stability in organic solar cell devices manufactured at Risø DTU National Laboratory. While comparing with traditional P3HT based devices it was shown that thermocleavage results in very rigid film and thus significantly improves the stability of the polymer. One can find the detailed description of the synthesis routes and the device production as well as the testing results elsewhere [8,9].

INVERTED GEOMETRY

More and more interest is generated towards the use of various metal oxides, such as ZnO, TiO_2 etc., as a barrier layer between metal and active layer interface, which also allows manufacturing an inverted structure, when the front transparent electrode acts as a cathode. One of the common inverted structures has the following combination:

Glass (or PET)/ITO/ZnO/Active Blend/PEDOT:PSS/Ag

The use of high work function silver electrode gives possibility to apply roll-to-roll coating process for production of cells with this geometry, since an Ag paste is commercially available for printing. As a result it is possible to produce fully roll-to-roll processed devices. In case of normal geometry a low work function metal such as aluminium is used, which is not useful as a paste.

 505/856-7188
52nd Annual Technical Conference Proceedings, Santa Clara, CA, May 9–14, 2009 ISSN 0737-5921

Organic solar cell devices with both normal and inverted geometries have been produced at Risø DTU National Laboratory using regular spin coating and metal evaporating techniques for model devices or vacuum free roll-to-roll coating approach for large scale devices (the later one was applied only for inverted geometry) [10]. In case of the roll-to-roll coated devices PCEs over 2% have been achieved with shelf lifetime of nonencapsulated cells exceeding one year. The complete cells have been tested for stability under various atmospheric conditions and illumination:

1. Nitrogen (water < 1 ppm, oxygen < 1 ppm)
2. Humid nitrogen (water ~90 ± 5% rh, oxygen < 1 ppm)
3. Oxygen (water < 1 ppm, oxygen ~100%)
4. Ambient atmosphere (water ~20 ± 5% rh, oxygen ~20%)

The results revealed that devices with normal geometry are rather stable in nitrogen and pure oxygen, while degrade quickly in humid environment. On a contrary, the cells with inverted devices showed good stability in 90% humid environment and degraded in pure oxygen atmosphere [10]. The results point out that using the same active layer, but different combinations and layer sequence in the device structures it is possible to achieve stability in atmosphere with high concentration of water or oxygen. Therefore, choosing the right materials and the right combination one can possibly produce a device with high stability in any environment.

CONCLUSIONS

It can be concluded that thermocleavable materials are rather promising for photovoltaic applications and the further optimization of these polymers might lead to efficient solar cell devices that will have long lifetime and will not require any encapsulation.

The approach following an inverted device geometry gives the possibility for fully roll-to-roll processed devices with efficiencies higher than 2% and shelf lifetimes exceeding one year without encapsulation. Furthermore, the inverted geometry reveals new features of degradation process in organic solar cells showing that by choosing different combinations and geometries of the device it is possible to get cells that would be stable in humid environment or in oxygen.

ACKNOWLEDGEMENT

This work was supported by the Danish Strategic Research Council (DSF 2104-05-0052 and 2104-07-0022).

REFERENCES

1. G. Li, V. Shrotriya, J. Huang, Y. Yao, T. Moriarty, K. Emery, Y. Yang, "High-efficiency solution processable polymer photovoltaic cells by self-organization of polymer blends", *Nat. Mater.*, 4, 864, 2005.

2. W. Ma, C. Yang, X. Gong, K. Lee, A. J. Heeger, "Thermally Stable, Efficient Polymer Solar Cells with Nanoscale Control of the Interpenetrating Network Morphology", *Adv. Funct. Mater.*, 15, 1617, 2005.

3. M. Jørgensen, K. Norrman, F.C. Krebs, "Stability/degradation of polymer solar cells", *Sol. Energy Mater. Sol. Cells*, 92, 686, 2008.

4. K. Norrman, F.C. Krebs, "Lifetimes of Organic Photovoltaics: Using TOF-SIMS and 18O2 Isotopic Labelling to Characterise Chemical Degradation Mechanisms", *Sol. Energy Mater. Sol. Cells*, 90, 213, 2006.

5. C. Lungenschmied, G. Dennler, H. Neugebauer, N.S. Sariciftci, M. Glatthaar, T. Meyer, A. Meyer, "Flexible, long-lived, large-area, organic solar cells", *Sol. Energy Mater. Sol. Cells*, 91, 379, 2007.

6. C.J. Brabec, J.R. Durrant, "Solution-processed organic solar cells", *MRS Bulletin*, 33, 670, 2008.

7. F.C. Krebs, "Fabrication and processing of polymer solar cells: A review of printing and coating techniques", *Sol. Energy Mater. Sol. Cells*, doi:10.1016/j.solmat.2008.10.004, 2008.

8. S.A. Gevorgyan, F.C. Krebs, "Bulk Heterojunctions Based on Native Polythiophene", *Chem Mater.*, 20, 4386, 2008.

9. M.H. Petersen, S.A. Gevorgyan, F.C. Krebs, "Thermocleavable Low Band Gap Polymers and Solar Cells Therefrom with Remarkable Stability toward Oxygen", *Macromol*., 41 (23), 8986, 2008.

10. F.C. Krebs, S.A. Gevorgyan, J. Alstrup, "A roll-to-roll process to flexible polymer solar cells: model studies, manufacture and operational stability studies", *J. Mat. Chem*., DOI: 10.1039/b823001c, 2009.

Available online at www.sciencedirect.com
ScienceDirect
Solar Energy Materials & Solar Cells 92 (2008) 793–798
Solar Energy Materials and Solar Cells
www.elsevier.com/locate/solmat

Applicability of X-ray reflectometry to studies of polymer solar cell degradation

Jens Wenzel Andreasen[a,*], Suren A. Gevorgyan[a], Christian M. Schlepütz[b], Frederik Christian Krebs[a]

[a]*Polymers for Energy Technology, Risø, National Laboratory for Sustainable Energy, Technical University of Denmark, Frederiksborgvej 399, DK-4000 Roskilde, Denmark*
[b]*Swiss Light Source, Paul Scherrer Institut, CH-5232 Villigen-PSI, Switzerland*

Received 4 December 2007; received in revised form 20 February 2008; accepted 20 February 2008
Available online 3 April 2008

Abstract

Although degradation of polymer solar cells is widely acknowledged, the cause, physical or chemical, has not been identified. The purpose of this work is to determine the applicability of X-ray reflectometry for *in situ* observation of physical degradation mechanisms. We find that the rough interfaces of the polymer solar cell constituent layers seriously obstruct the sensitivity of the technique, rendering it impossible to elucidate changes in the layer/interface structure at the sub-nanometer level.

Keywords: Organic; Polymer; X-ray reflectivity; Stability; Degradation

1. Introduction

It has become apparent in recent years of research in organic photovoltaics (PVs) that the realization of organic solar cells, which are at the same time efficient and stable, is a major challenge [1–3]. Consensus appears to have been reached on the requirements for efficient organic solar cells, i.e. a well-dispersed hetero-junction on the size scale of the exciton and good contact between the active layer and the electrodes [4]. The procedure to meet these requirements is optimized by trial and error for different systems and comprises choice of solvent, casting temperature and annealing of the cast film [5,6]. The film structure of the pristine cell is therefore, determined by a combination of the chosen processing parameters and of the molecular weights of the hetero-junction components. The characterization of the cells is, however, often limited to PV performance, i.e. *IV*-curves and microscopy, mainly a combination of AFM, SEM and TEM, all of which are localized and surface-specific probes. There is, consequently, little physical evidence for the correlation between PV efficiency, the nano-scale structure of the bulk hetero-junction, and the interface structure of the electrodes and active layer. Recently, however, *in situ* studies of the layer and interface structure of polymer solar cells by energy-dispersive X-ray reflectometry have been reported [7,8]. Inspired by this work, we have studied the layer and interface structure of glass/ITO/PEDOT:PSS/MEH-PPV/Al solar cells during operation with high-resolution angle-dispersive synchrotron X-ray reflectometry.

2. Experimental

2.1. Sample preparation

Samples representing different combinations of polymer solar cell layers were prepared as outlined in Table 1. Indium tin oxide (ITO) covered glass slides (sheet resistance 8–12 $\Omega\,sq^{-1}$, Delta Technologies) were ultrasonically cleaned in isopropanol and milli-Q water each for 10 min. A solution of PEDOT:PSS (Aldrich) was spin coated onto 3 samples and dried in an oven at 160 °C for 5 min. One of them was transported into a glove-box atmosphere, where an active layer of MEH-PPV (10 mg/mL

*Corresponding author.
E-mail address: jens.wenzel.andreasen@risoe.dk (J.W. Andreasen).

0927-0248/$ - see front matter © 2008 Elsevier B.V. All rights reserved.
doi:10.1016/j.solmat.2008.02.011

Table 1
Structure of prepared samples

3	Glass/ITO/PEDOT:PSS/MEH-PPV/Al
4	Glass/ITO/PEDOT:PSS/Al
5	Glass/ITO/PEDOT:PSS
7	Glass/ITO

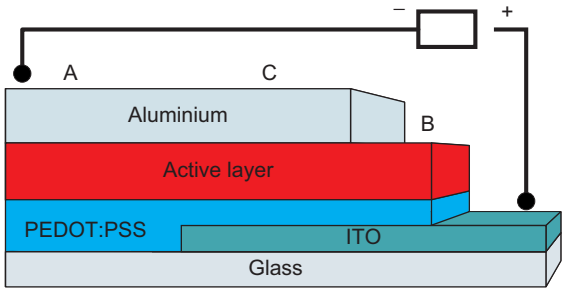

Fig. 1. The complete device structure. The points marked A and B mark the positions where reflectivity curves were acquired to facilitate the construction of the model used for fitting the data representing the full cell structure (as measured at C).

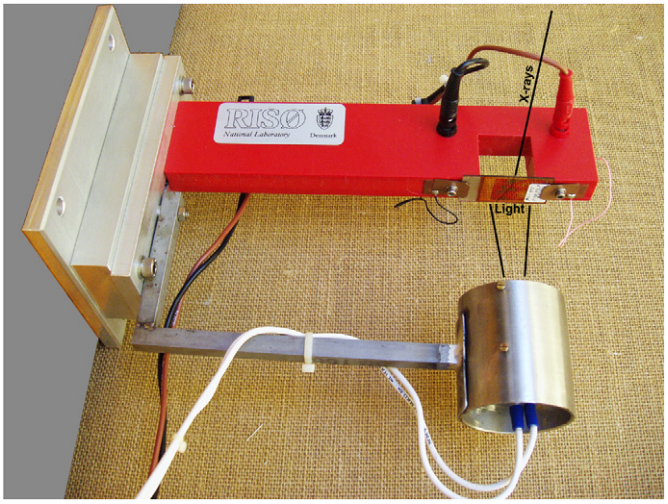

Fig. 2. The sample-holder designed for *in situ* reflectivity measurements. The solar cell is seen mounted just above the word "Light", held in place by clamps ensuring contact with the electrodes for measuring *IV* characteristics.

in chlorobenzene) was spin coated. As a final step, the Al electrode was evaporated on top and the final device (# 3 in Table 1) was annealed in the oven at 150 °C for 5 min. The geometrical architecture of the full solar cell, which had an active area of 3 cm^2, is shown in Fig. 1.

After *IV*-curve measurements, the samples were packed in diffusion and light tight bags made from a composite foil (70 μm polyethylene/9 μm Al/20 μm polyamide) inside the glove-box and transported to HASYLAB, Hamburg, for the X-ray reflectometry studies.

2.2. Lifetime measurements

IV diode characteristics were measured for the device ♯3 (Table 1) simultaneously with reflectometry studies in order to record the rate of the decay process inside the solar cell. The cell was mounted on a holder designed for *in situ* measurements, which provides the necessary contacts for the *IV* characterization and keeps the cell surface accessible for X-ray reflectivity measurements. A spotlight halogen lamp (OSRAM Decostar IRC 20W 12 V) is fixed approximately 10 cm below the holder to illuminate the cell (Fig. 2). After the cell was removed from the sealed bag and mounted on the setup, initial reflectivity measurements on the cell were carried out in a dark room for about 5 h. Then the spotlight was turned on and *IV* data were collected using a source-measuring unit (Keithley 2400 and computer) connected to the cell, while continuing the reflectometry analyses.

2.3. X-ray reflectometry

The X-ray reflectivity profiles were measured at the BW2 beam line at HASYLAB, using the Risø *Z*-axis diffractometer. The beam coming from the wiggler insertion device was monochromatized to a wavelength λ of 1.2398 Å, by a fixed exit, double Si 1 1 1 monochromator. The specularly reflected intensity was recorded using a Cyberstar point detector at scattering vectors $q = 4\pi \sin\theta/\lambda$ ranging from 0.015 to 0.600 $Å^{-1}$, corresponding to incidence angles θ from 0.08° to 3.4°, and covered up to 8 orders of magnitude in reflected intensity. It was found to be crucial to correct for misalignment during illumination because of heating by the light source. Full reflectivity profiles were acquired in the dark at positions **A**, **B** and **C** (Fig. 1, positions corresponding to cell without back or top electrode, and the full cell) and during illumination (up to 5 h). Each full reflectivity scan took about 39 min. The data were normalized to the calculated Fresnel reflectivity for the substrate below the critical angle and fitted with a box model using the dynamical formalism of Parratt [9] implemented in a set of MATLAB® routines. The optimization was performed as a combination of a genetic algorithm and a constrained non-linear least-squares minimization (the latter to ensure local convergence to the minimum). Thin boxes of intermediate density were included between the boxes corresponding to major layers of the structure, to adequately represent diffuse or graded interfaces. Above $q \sim 0.2\ Å^{-1}$ the reflected intensity followed a simple power law decay, and the actual fitting was therefore, restricted to scattering vectors below 0.2 $Å^{-1}$ to reduce computation time. In addition to the density profile, the effective footprint and correction for absorption were fitted to the data. The reflectivity profile calculated from the fitted model was smeared using an empirical model for the instrumental resolution. The data points were weighted by an estimated relative error of 4%, because the main source of uncertainty is systematical errors in the mechanical setup and not counting statistics.

3. Results and discussion

Fig. 3 presents the decay of short-circuit current density of the cell measured within ~6 h and a double exponential fit normalized to the experimental data according to the following equation [10] in order to more clearly illustrate the degradation process

$$\left|\frac{J_{sc}(t)}{J_{sc}(0)}\right| = Ae^{-bt} + Ce^{-dt} + \cdots \quad (1)$$

The normalized decay parameters of the fit are collected in Table 2. The decay of this device type is consistent with earlier findings for ITO/PEDOT:PSS/MEHPPV/Al homojunctions [10]. One can see that after 20 min of illumination the current dropped to 50% of its initial value. This fast decay is ascribed to the combination of a high intensity of the spotlight (measured irradiation was about 2 sun) and overheating of the tested cell by the lamp (the temperature of the cell during measurements reached 92 °C). Future experiments will involve forced air cooling of the sample.

The reflectivity profiles representing different processing stages in cell preparation are shown in Fig. 4 with indications of the salient features. It is apparent that the dominant feature of the reflectivity profiles is the Kiessig thickness fringes [11] from the ITO layer. However, below the critical angle for total reflection from ITO, i.e. where the ITO layer does not contribute to the interference signal, we observe the much weaker fringes from the polymer layer(s). For the glass/ITO/PEDOT:PSS sample, we can also distinguish the critical angle for total reflection from the PEDOT:PSS surface (red curve at $Q_z \sim 0.026\,\text{Å}^{-1}$). The critical angles for the polymer layers are hidden, where the top layer is Al because of the much higher electron density of the latter (blue and green curves in Fig. 4). In these cases, we observe the interference signal from the polymer layers mainly in the region between the critical angles for total reflection of Al and ITO ($0.034\,\text{Å}^{-1} < Q_z < 0.05\,\text{Å}^{-1}$, see inset of Fig. 4). Repeated measurements revealed no changes to the reflectivity data as a function of exposure to the X-ray beam (“beam damage”).

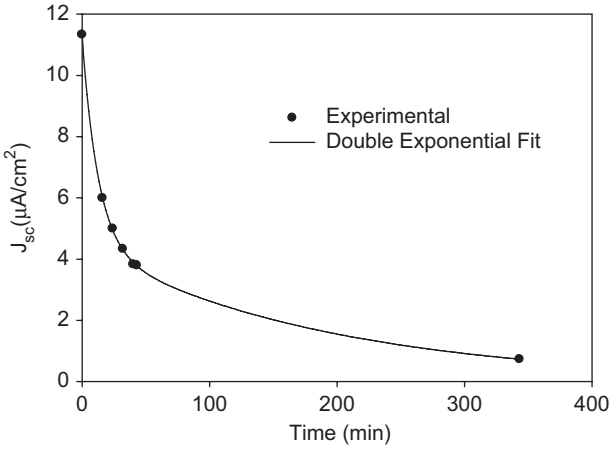

Fig. 3. Experimental data (●) and double exponential fit (—) of short-circuit current density measured for 6 h under 2 sun irradiation for the cell with geometry ITO/PEDOT:PSS/MEH-PPV/Al.

Table 2
Normalized data parameters of the fit describing the PV performance decay according to Eq. (1)

a (%)	b (s^{-1})	c (%)	d (s^{-1})	J_o (μA/cm^2)
6.9	79×10^{-3}	4.4	5.3×10^{-3}	11.3

From fits of the partial cell sample reflectivity profiles and profiles acquired at positions **A** and **B** of the full cell (glass/PEDOT:PSS/MEH-PPV/Al and glass/ITO/PEDOT:PSS, respectively, see Fig. 1), we obtained reasonable starting parameters for fitting the data from the full cell, before and during illumination (Fig. 5). Qualitatively, it is possible to distinguish some small changes in the interference pattern after about 3-h illumination (marked by arrows in the inset of Fig. 5), but after 5 h, no further change is observed, i.e. the reflectivity profiles after 3 and 5 h illumination are virtually indistinguishable. The final fit parameters are summarized in Table 3.

It is apparent from Fig. 6, showing the scattering length density (SLD) profiles of the fitted model, that there are some small but distinctive differences before and after the onset of illumination. It is tempting to ascribe the observed changes to some real physical changes in the constituting materials. For example, it has been proposed that PEDOT:PSS is unstable at elevated temperatures (i.e. above $T_g \sim 50$ °C) because of residual solvent [12], or as in the case of MEH-PPV, because of substantial thermal expansion [13]. However, we emphasize that for thick, complex layer sequences as the full solar cell structures studied here, the analysis of reflectivity data is highly ambiguous [14]. As in most X-ray scattering experiments, the observations are scattered intensities proportional to the modulus of the structure factor (in this case the absolute square of the amplitude reflectivity), which does not preserve the phase information [15]. The practical consequence is that the data cannot be inverted by Fourier transformation to directly produce the scattering length density profile, but must be fitted by optimization of analytically calculated model profiles. For complex structures with high roughness interfaces the minima on the χ-statistic surface are wide and shallow and a multitude of slightly different SLD profiles may therefore be obtained, which fit the observed data equally well. As an example of this, we regard the increase in density at the glass/ITO interface, obtained from the model fit of the reflectivity data before illumination, but not after 3-h illumination, as likely unphysical. The fits presented here are the best that we could obtain, but as explained above, several other fits of nearly the same statistical quality yielded different density profiles, e.g. less or no change in Al thickness, larger density of the PEDOT:PSS layer during illumination, lower density at the PEDOT:PSS/MEH-PPV interface and larger thickness of the MEH-PPV layer. In fact,

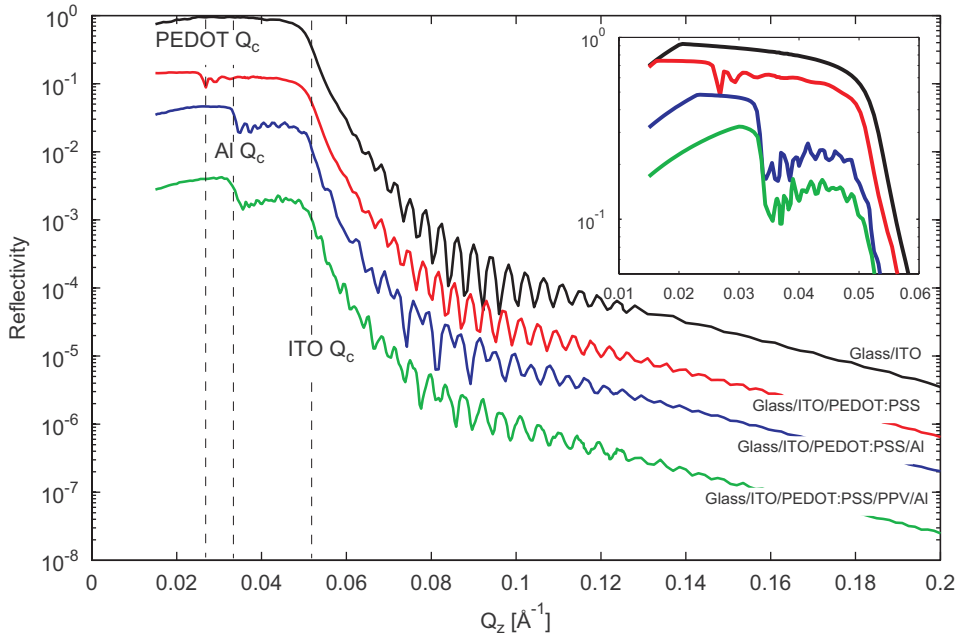

Fig. 4. (color online) Reflectivity profiles of glass/ITO (top/black), glass/ITO/PEDOT:PSS (2nd/red), glass/ITO/PEDOT:PSS/Al (3rd/blue), and a full solar cell structure, glass/ITO/PEDOT:PSS/PPV/Al (4th, green). The inset shows details of the region around the critical angles for total reflection for different top layers.

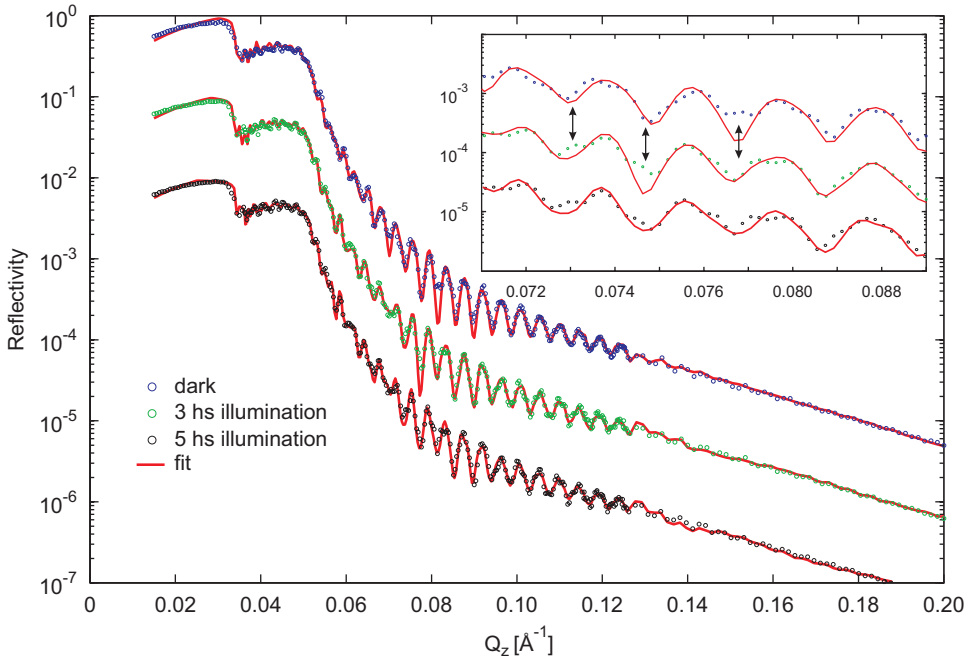

Fig. 5. (color online) Reflectivity data from glass/ITO/PEDOT:PSS/MEH-PPV/Al before illumination (top/blue circles, "dark") and during illumination (green circles, 3-h illuminated, black circles, 5-h illuminated, respectively offset by 1 and 2 decades for clarity), with calculated profiles for the fitted scattering length density profiles shown as red lines. The inset shows the detail where we qualitatively observe the largest differences.

the difference in quantified parameters is as large between data that are qualitatively completely similar (3 and 5 h illumination) as between data with small but distinct differences (before and during illumination, see inset of Fig. 5). The only parameter that consistently refines to the same value is the thickness of the ITO layer. This is not surprising because the thickness fringes from this layer completely dominate the reflectivity profiles, because of the high electron density of ITO. This, together with the fact that the interfaces of the studied solar cell are quite rough, although relatively smooth compared to real hetero-junction cells (e.g. PPV–PCBM, P3HT–PCBM), seriously

Table 3
Reflectivity fit parameters, thicknesses (d) with r.m.s. roughness, σ in parenthesis, from the box fits of the partial samples and the full cell, in the dark and during illumination (all figures in Ångstrøm)

Sample no.	$d(\sigma)$ [Å]					
	7	5	4	3	3(illuminated for 3 h)	3(illuminated for 5 h)
Al-top interface	–	–	56(49)	99(48)	135(70)	88(23)
Al	–	–	927(49)	775(30)	858(20)	774(32)
MEH-PPV-top interface	–	–	–	58(24)	119(39)	117(27)
MEH-PPV	–	–	–	1407(31)	1400(27)	1472(34)
PEDOT:PSS-top interface	–	97(39)	128(49)	84(33)	107(32)	90(75)
PEDOT:PSS	–	798(45)	773(25)	521(34)	428(23)	506(30)
ITO-top interface	67(33)	90(30)	97(33)	95(16)	104(21)	66(25)
ITO	1191(28)	1249(41)	1201(39)	1107(31)	1109(32)	1105(32)
ITO-bottom interface	–	–	–	92(58)	91(16)	93(23)
χ-Statistic (%)	1.97	0.41	1.51	1.56	1.23	1.26

The fit criterion, χ statistic is calculated as $\sum_{i=1}^{k}(y_i^{obs}-y_i^{cal}/y_i^{err})$ for the observed and calculated intensities, y^{obs} and y^{cal} and standard error of the observed intensities, y^{err}.

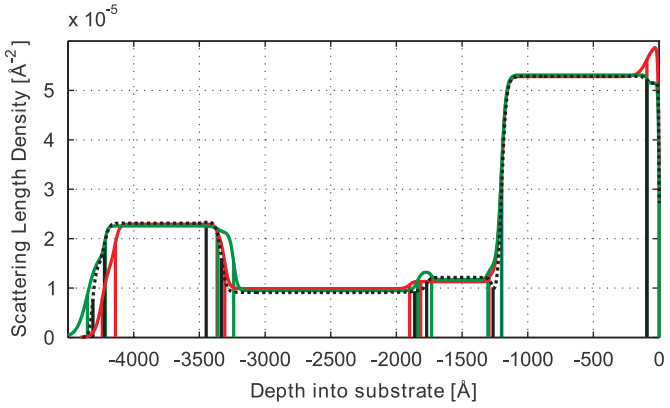

Fig. 6. Fitted scattering length density profiles for the glass/ITO/PEDOT:PSS/MEH-PPV/Al solar cell, before (RED) and during illumination (GREEN, 3 h, BLACK/broken, 5 h). Vertical lines indicate the extent of boxes used in the model.

limits the information detail obtainable, especially at the interfaces. In contrast to the results reported by Paci et al. [7,8], we cannot relate the fast degradation of the cell to a substantial morphological change, quantifiable by X-ray reflectometry. We did expect that an apparent increase in Al electrode thickness by oxidation at the polymer–Al interface would proceed to a greater extent when the cell was exposed to air during operation [2] as compared to the N_2 atmosphere used by Paci et al. [7,8], but this does not appear to be the case.

4. Conclusion

We have shown that even high-resolution angle-dispersive synchrotron X-ray reflectivity data, seemingly well fitted by detailed models, still leaves much uncertainty regarding the interpretation of the obtained density profiles. Although small changes in the reflectivity profile are observed, repeated model fits do not provide a consistent result. We obtained no statistical significant change at the interface between polymer and Al electrode, but emphasize that the comparatively rough interface, even for a model system as studied here, seriously inhibits the observation of small changes, like the formation of a thin (sub-nm) interfacial oxide layer. We cannot exclude that such a change or other morphological changes takes place, especially because a difference in reflectivity profiles before and during illumination is qualitatively observed, but the non-linear model fit cannot provide an unequivocal scattering length density profile of sufficient statistical validity. On these grounds, we regard it as near impossible to detect such changes in more realistic devices, e.g. bulk hetero-junctions of P3HT–PCBM or PPV–PCBM for which we have observed much higher interfacial roughness than for the model system homo-junction studied in the work presented here.

Acknowledgments

We acknowledge HASYLAB for providing beamtime and DANSYNC for financial support. This work was further supported by the Danish Strategic Research Council (DSF 2104-05-0052 and DSF-2104-07-0022). Prof. Martin Meedom Nielsen is acknowledged for providing the Matlab routines for fitting the reflectivity data and for assistance with its application. Torben Kjær is acknowledged for the technical assistance, and Jan Kehres is acknowledged for assistance with the data acquisition at HASYLAB.

References

[1] M. Jørgensen, K. Norrman, F.C. Krebs, this issue.
[2] F.C. Krebs, K. Norrman, Prog. Photovoltaics: Res. Appl. 15 (2007) 697.
[3] F.C. Krebs, Refocus 6 (2005) 38.
[4] S. Günes, H. Neugebauer, N.S. Sariciftci, Chem. Rev. 107 (2007) 1324.

[5] G. Li, V. Shrotriya, J. Huang, Y. Yao, T. Moriarty, K. Emery, Y. Yang, Nat. Mater. 4 (2005) 864.
[6] W. Ma, C. Yang, X. Gong, K. Lee, A.J. Heeger, Adv. Funct. Mater. 15 (2005) 1617.
[7] B. Paci, A. Generosi, V.R. Albertini, P. Perfetti, B. de Bettignies, M. Firon, J. Leroy, C. Sentein, Appl. Phys. Lett. 87 (2005) 194110.
[8] B. Paci, A. Generosi, V.R. Albertini, P. Perfetti, B. de Bettignies, M. Firon, J. Leroy, C. Sentein, Appl. Phys. Lett. 89 (2006) 043507.
[9] L.G. Parratt, Phys. Rev. 95 (1954) 359.
[10] F.C. Krebs, J.E. Carlé, N. Cruys-Bagger, M. Andersen, M.R. Lilliedal, M.A. Hammond, S. Hvidt, Sol. Energy Mater. Sol. Cells. 86 (2005) 499.
[11] H. Kiessig, Ann. Phys. 5. Folge, Band 10 (1931) 788.
[12] J.Y. Kim, J.H. Jung, D.E. Lee, J. Joo, Synth. Met. 126 (2002) 311.
[13] G.R. Webster, W.J. Mitchell, P.L. Burn, R.K. Thomas, G. Fragneto, J.P.J. Markham, I.D.W. Samuel, J. Appl. Phys. 91 (2002) 9066.
[14] A. van der Lee, F. Salah, B. Harzallah, J. Appl. Crystallogr. 40 (2007) 820.
[15] M. Tolan, X-ray Scattering from Soft-Matter Thin Films, Springer, Berlin, 1999.

Risø DTU is the National Laboratory for Sustainable Energy. Our research focuses on development of energy technologies and systems with minimal effect on climate, and contributes to innovation, education and policy. Risø has large experimental facilities and interdisciplinary research environments, and includes the national centre for nuclear technologies.

Risø DTU
National Laboratory for Sustainable Energy
Technical University of Denmark

Frederiksborgvej 399
PO Box 49
DK-4000 Roskilde
Denmark
Phone +45 4677 4677
Fax +45 4677 5688

www.risoe.dtu.dk